Enhanced process development by simulation of ultrasonic heavy wire bonding

zur Erlangung des akademischen Grades DOKTOR DER

INGENIEURWISSENSCHAFTEN (Dr.-Ing.) der Fakultät für

Maschinenbau

der Universität Paderborn

genehmigte

DISSERTATION

von

Reinhard Schemmel, M. Sc.

aus Paderborn

Tag des Kolloquiums: 9. Februar 2022
Referent: Prof. Dr.-Ing. habil. Walter Sextro
Korreferent: Prof. Dr.-Ing. habil. Gunter Kullmer

Geleitwort

Neue technische Entwicklungen entstehen heute immer öfter an den Grenzen zwischen den Disziplinen, wo verschiedene Denkweisen sich begegnen und miteinander wechselwirken. Die Entwicklung neuer mechatronischer oder intelligenter technischer Systeme setzt ein interdisziplinäres Denken und Handeln voraus.

Mechatronische Systeme bestehen aus einer mechanischen Grundstruktur, die durch Integration von Sensoren und Aktoren sowie durch informationsverarbeitende Komponenten ein hohes Maß an Flexibilität und Leistungsfähigkeit gewinnt. Die Mechatronik stellt somit eine interdisziplinäre Kombination der Fächer Maschinenbau, Elektrotechnik und Informatik dar.

Der Lehrstuhl für Dynamik und Mechatronik gehört der Fakultät für Maschinenbau der Universität Paderborn an. In Forschung und Lehre befassen wir uns mit der Modellierung, Simulation, Zuverlässigkeit, Optimierung, Betrieb, Überwachung, Diagnose und Prognose von mechanischen, mechatronischen und intelligenten technischen Systemen. Die Forschungsschwerpunkte liegen in den Bereichen Nichtlineare Dynamik, Kontaktmechanik, Reibung, Condition Monitoring, Data Analytics, Reliability Engineering, Sensorik, Aktorik und Ultraschalltechnik. Sie spiegeln sich in den Bänden dieser Schriftenreihe, in denen Ergebnisse unserer Forschung veröffentlicht werden. Die Schriftenreihe soll dazu beitragen, den Wissenstransfer zwischen der Universität und der praktischen Anwendung zu verbessern.

Die rein experimentelle Prozessentwicklung beim Ultraschallbonden ist erfahrungsgemäß durch komplexe Wechselwirkungen zwischen vielen Prozessparametern und Bondqualität mit einem hohen experimentellen Aufwand verbunden. Mit dem von Herrn Schemmel entwickelten Verfahren lässt sich der Bondprozess effizient simulieren. Dies führt zur Verringerung des experimentellen Aufwands im Auffinden optimaler Bondparameter. Das entwickelte Simulationsverfahren konnte von Herrn Schemmel validiert und innerhalb von recht aufwendigen Versuchsreihen erfolgreich angewendet werden. Mit Hilfe des entwickelten Prozessmodells kann die aktuelle Prozessentwicklung beim Dickdrahtbonden zukünftig deutlich verbessert werden. Parameterstudien können nun statt experimentell simulativ durchgeführt werden, zudem wird die Optimierung unter Einbeziehung verschiedenster Parameter und Ziele möglich.

Paderborn, im Februar 2022

Prof. Dr.-Ing. habil. Walter Sextro

Vorwort

Die vorliegende Dissertation entstand während meiner Tätigkeit als wissenschaftlicher Mitarbeiter am Lehrstuhl für Dynamik und Mechatronik der Universität Paderborn im Zeitraum von 2017 bis 2021. Mein Dank gilt Herrn Prof. Dr.-Ing. habil. Walter Sextro für die gewährte Freiheit und das Vertrauen bei der Wahl meiner Forschungsschwerpunkte, für die wertvollen fachlichen Anregungen und für die Gelegenheit im internationalen Umfeld forschen zu dürfen. Durch die wissenschaftlichen und projektbezogenen Arbeiten habe ich in meiner persönlichen Entwicklung sehr profitiert. Bei Herrn Prof. Dr.-Ing. Gunter Kullmer bedanke ich mich für die freundliche Übernahme des Korreferats. Ebenso gilt mein Dank Herrn Prof. Dr.-Ing. Werner Homberg und Herrn Dr.-Ing. Tobias Hemsel für das Mitwirken in der Promotionskommission als Vorsitzender bzw. Beisitzer.

Meinen Kolleginnen und meinen Kollegen am Lehrstuhl für Dynamik und Mechatronik danke ich für die stets sehr angenehme Arbeitsatmosphäre. Besonders möchte ich mich bei allen Mitarbeitern aus der Fachgruppe „Sensorik, Aktorik und Ultraschalltechnik“ für die hervorragende Zusammenarbeit und die vielen fachlichen Diskussionen bedanken. Mein besonderer Dank gilt hierbei Dr.-Ing. Tobias Hemsel; durch seine Erfahrung und vielfältige Unterstützung bis zum Schluss meiner Promotion habe ich stark profitiert und das weiß ich sehr zu schätzen.

Den vielen Studierenden danke ich für das Vertrauen in die Begleitung ihrer Abschlussarbeiten und für die Zusammenarbeit am Lehrstuhl. Dabei gebührt mein Dank insbesondere Ludger Klahold, Katharina Ranert, Viktor Krieger und Nico Müller, die einen wesentlichen Beitrag zu dieser Arbeit geleistet haben.

Mein größter Dank gilt meiner Mutter Anna. Ohne deine stetige Föderung und Zuspruch von Beginn an hätte ich diesen Weg nicht eingeschlagen und ohne deine Unterstützung gewiss nicht erfolgreich begangen.

Paderborn, im Februar 2022

Reinhard Schemmel

Abstract

Ultrasonic heavy wire bonding with aluminium wire is a standard process to produce electrical contacts in power semiconductor modules. The increasing demands on the efficiency and reliability of the modules have led to technological developments and copper wires with significantly better electrical and thermal properties are used more often nowadays. This results in new challenges in process development due to higher process forces and ultrasonic power; for this purpose, a simulation model is developed to improve process development.

Ultrasonic wire bonding tests with 400 µm aluminium and copper wires were carried out to investigate the influence of the process parameters on the bond quality; these results and additional measurements of wire deformation and vibrations were used to define the requirements for the model and validate the results of the simulation.

A process model based on a co-simulation was developed between *MATLAB* and *ANSYS*; the physical phenomena such as ultrasonic softening of the wire material, bond formation and dynamic behaviour of the components were considered.

Based on a tensile-compression testing machine, a test rig was developed to identify the model parameters. In additional compression tests with the wires with and without ultrasonic excitation, the reduction of the forming forces under ultrasonic influence was characterised.

With the developed process model, the parameter studies from the ultrasonic wire bond tests were simulated and directly compared with the experimental results; a relative good agreement between simulation and measurement could be achieved for both aluminium and copper.

Kurzfassung

Das Ultraschall-Dickdrahtbonden mit Aluminiumdraht ist ein Standardverfahren zur elektrischen Kontaktierung von Leistungshalbleitermodulen. Die steigenden Anforderungen an die Effizienz und Zuverlässigkeit der Module haben zu technologischen Weiterentwicklungen geführt und es werden vermehrt Kupferdrähte mit wesentlich besseren elektrischen und thermischen Eigenschaften eingesetzt. Hieraus resultieren durch höhere Prozesskräfte und Ultraschallleistung neue Herausforderungen bei der Prozessentwicklung; hierfür wird ein Simulationsmodell zur Verbesserung der Prozessentwicklung entwickelt.

In Ultraschall-Drahtbondversuchen mit 400 µm Aluminium und Kupfer Drähten wurde der Einfluss der Prozessparameter auf die Bondqualität untersucht; diese Ergebnisse und zusätzliche Messungen der Drahtdeformation und Schwingungen wurden für die Formulierung der Anforderungen und zur Validierung der Ergebnisse des Simulationsmodells genutzt.

Es wurde ein Prozessmodell, basierend auf einer Co-Simulation zwischen *MATLAB* und *ANSYS*, entwickelt; hierbei wurden die phyiskalischen Phänomene wie die Ultraschall Werkstoffentfestigung, der Verbindungsaufbau und die dynamischen Systemeigenschaften abgebildet.

Basierend auf einer Zug-Druck-Prüfmaschine wurde ein Prüfstand zur Identifikation der Modellparameter entwickelt. In zusätzlichen Druckversuchen mit den Bonddrähten mit und ohne Ultraschallanregung wurde die Reduktion der Umformkräfte unter Ultraschalleinfluss untersucht.

Mit dem entwickelten Prozessmodell wurden die Parameterstudien aus den Ultraschall-Drahtbondversuchen simuliert und direkt mit den experimentellen Ergebnissen verglichen, wobei sich eine relativ gute Übereinstimmung zwischen Simulation und Messung sowohl für Aluminium, als auch für Kupfer, erzielen ließ.

Prior Publications

Parts of this thesis have already been published in the following journals, conferences or book contributions.

Journal Articles

Schemmel, R. ; Hemsel, T. ; Dymel, C. ; Hunstig, M. ; Brökelmann, M. ; Sextro, W.: Using complex multi-dimensional vibration trajectories in ultrasonic bonding and welding. In: *Sensors and Actuators A: Physical* (2019), Volume 295, pp. 653-662

Schemmel, R. ; Krieger, V. ; Hemsel, T. ; Sextro, W.: Co-simulation of MATLAB and ANSYS for ultrasonic wire bonding process optimization. In: *Microelectronics Reliability* (2021), Volume 119, pp. 114077

Reviewed Conference Proceedings

Schemmel, R. ; Althoff, S. ; Sextro, W. ; Unger, A. ; Hunstig, M. ; Brökelmann, M.: Effects of different working frequencies on the joint formation in copper wire bonding. In: *10th International Conference on Integrated Power Electronics Systems (CIPS).* Stuttgart, Germany, 2018

Schemmel, R. ; Hemsel, T. ; Sextro, W.: Numerical and experimental investigations in ultrasonic heavy wire bonding. In: *6th European Conference on Computational Mechanics (ECCM).* Glasgow, UK, 2018

Schemmel, R. ; Eacock, F. ; Dymel, C. ; Hemsel, T. ; Hunstig, M. ; Brökelmann, M. ; Sextro, W.: Impact of multi-dimensional vibration trajectories on quality and failure modes in ultrasonic bonding. In: *International Symposium on Microelectronics (IMAPS).* Boston, USA, 2019

Schemmel, R. ; Krieger, V. ; Hemsel, T. ; Sextro, W.: Co-simulation of MATLAB and ANSYS for ultrasonic wire bonding process optimization. In: *21st International Conference on Thermal, Mechanical and Multi-Physics Simulation and Experiments in Microelectronics and Microsystems (EuroSimE).* Cracow, Poland, 2020

Schemmel, R. ; Scheidemann, C. ; Hemsel, T. ; Kirsch, O. ; Sextro, W.: Experimental analysis and modelling of bond formation in ultrasonic heavy wire bonding. In: *11th International Conference on Integrated Power Electronics Systems.* Berlin, Germany, 2020

Schemmel, R. ; Müller, N. ; Klahold, L. ; Hemsel, T. ; Sextro, W.: Experimental parameter identification and validation of a process model for ultrasonic heavy wire bonding. In: *International Symposium on Microelectronics (IMAPS).* San Diego, USA, 2021

Unger, A. ; Schemmel, R. ; Meyer, T. ; Eacock, F. ; Eichwald, P. ; Althoff, S. ; Sextro, W. ; Brökelmann, M. ; Hunstig, M. ; Guth, K.: Validated Simulation of the Ultrasonic Wire Bonding Process. In: *IEEE CPMT Symposium Japan (ICSJ).* Kyoto, Japan, 2016

Eichwald, P. ; Althoff, S. ; Schemmel, R. ; Sextro, W. ; Unger, A. ; Brökelmann, M. ; Hunstig, M.: Multi-dimensional Ultrasonic Copper Bonding - New Challenges for Tool Design. In: *International Symposium on Microelectronics (IMAPS).* Raleigh, USA, 2017

Dymel, C. ; Schemmel, R. ; Hemsel, T. ; Brökelmann, M. ; Hunstig, M. ; Sextro, W.: Experimental investigations on the impact of bond process parameters in two-dimensional ultrasonic copper bonding. In: *Proceedings of 8th Electronics IEEE CPMT Symposium Japan (ICSJ)* Kyoto, Japan, 2018

Dymel, C. ; Eichwald, P. ; Schemmel, R. ; Hemsel, T. ; Brökelmann, M. ; Hunstig, M. ; Sextro, W.: Numerical and statistical investigation of weld formation in a novel two-dimensional copper-copper bonding process. In: *Proceedings of 7th Electronics System-Integration Technology Conference (ESTC).* Dresden, Germany, 2018

Book Contributions

Sextro, W. ; Broekelmann, M. ; Unger, A. ; Meyer, T. ; Hunstig, M. ; Althoff, S. ; Kirsch, O. ; Schemmel, R.: *Intelligente Herstellung zuverlässiger Kupferbondverbindungen. In: Springer Vieweg Verlag.* 2019, ISBN 978-3-662-55145-5

Contents

Nomenclature

This list includes symbols that are used multiple times.

α	Model coefficient for the cleaning state τ
α_{BT}	Opening angle of the v-groove of the bonding tool
β	Model coefficient for the bonding state γ
Δx	Side length in x-direction of the partial surfaces of the discretized contact model
Δy	Side length in y-direction of the partial surfaces of the discretized contact model
$\Delta\sigma_{\mathrm{f}}$	Flow stress change
$\dot{\epsilon}$	Strain rate
$\dot{\epsilon}_0$	Constant strain rate of the testing machine during tensile or compressions testing
$\dot{x}_{\mathrm{BT}}$	Wire velocity
$\dot{x}_{\mathrm{S}}$	Substrate velocity
$\dot{x}_{\mathrm{W}}$	Wire velocity
ϵ	Strain
ϵ_{p}	Plastic strain
γ	State of bonded areas in the bond formation model
$\hat{\epsilon}$	Strain amplitude of harmonic strain oscillation
$\hat{q}$	Eigenvector
$\hat{v}_{\mathrm{US}}$	Ultrasonic velocity amplitude
$\hat{x}_{\mathrm{US}}$	Ultrasonic displacement amplitude
μ_{Met}	Coefficient of friction of pure metal/metal contact without contaminations
μ_{Ox}	Coefficient of friction of metal/metal contact with contaminations like oxide layers
μ_{TW}	Coefficient of friction between bonding tool and wire
μ_{WS}	Coefficient of friction between wire and substrate
μ_i	Coefficient of friction of the i-th partial area element of discretized friction model
ω	Angular frequency
$\overline{\sigma}$	Mean stress under cyclic loading
ρ	Material density

σ Stress

σ_0 Static stress without ultrasonic excitation

σ_f Flow stress

σ_S Shear strength of bond connection measured from the shear test results

σ_USS Stress with ultrasonic excitation, typically reduced due to ultrasonic softening effect

σ_Y Yield stress

τ State of cleaned areas in the bond formation model

τ_S Material shear strength

$\tilde{()}$ Index for reduced model order, such like the reduced mass matrix $\underline{\tilde{M}}$

$\underline{\Delta}$ Modal damping matrix

$\underline{\Omega}$ Diagonal matrix with the squared natural frequencies

$\underline{\xi}$ Vector of modal coordinates

$\underline{A}$ System matrix of the state space model

$\underline{B}$ Input matrix of the state space model

$\underline{C}$ Output matrix of the state space model

$\underline{f}$ Force vector with dimension $(n_\mathrm{DOF}, 1)$

$\underline{K}$ Stiffness matrix with dimension $(n_\mathrm{DOF}, n_\mathrm{DOF})$

$\underline{M}$ Mass matrix with dimension $(n_\mathrm{DOF}, n_\mathrm{DOF})$

$\underline{Q}$ Modal matrix

$\underline{q}$ Vector of coordinates with dimension $(n_\mathrm{DOF}, 1)$

$\underline{T}$ Transformation matrix

$\underline{x}$ State vector

a Parameter of the ultrasonic softening model

$A_\mathrm{Activated}$ Activated area

A_Bonded Bonded area

$A_\mathrm{C,TW}$ Contact area between bond tool and wire

$A_\mathrm{C,WS}$ Contact area between wire and substrate

A_S Shear area

b Parameter (exponent) of the ultrasonic softening model

$c_\mathrm{t,TW}$ Coupling stiffness between bond tool and wire to model form fit

$c_{\mathrm{t,WS},i}$ Tangential stiffness between wire and substrate of the i-th partial area element of discretized friction model

$c_{\mathrm{t,W}}$ Tangential stiffness of the wire

D_j Modal damping of the j-th mode

D_{W} Wire Diameter

DR Deformation ratio between the width of the wire bond and the wire diameter

E Youngs modulus

F_{BN} Bond normal force

$F_{\mathrm{N,BT}}$ Normal force in the contact between bonding tool and wire.

$F_{\mathrm{N},i}$ Normal force of the i-th partial area of the discretized friction model

F_{N} Normal force

$F_{\mathrm{N}}(x, y)$ Normal force distribution in the contact between wire and substrate

F_{S} Shear force

f_{S} Excitation frequency of the shaker used in the low frequency test rig

$F_{\mathrm{t,TW}}$ Tangential contact force between bonding tool and wire

$F_{\mathrm{t,WS}}$ Tangential contact force between wire and substrate

F_{TD} Touchdown force

f_{T} Excitation frequency of the ultrasonic transducer

G Shear modulus

h_{I} Interface layer height

i_{T} Excitation current of ultrasonic transducer

k Magnification factor of the bond normal force in the contact between bond tool and wire

k_{TSC} Reduction factor for bond formation after tool/substrate contacts

k_{USS} Softening factor which specifies the amount of reduction of the yield stress due to ultrasonic softening

L Length of the wire bond

m_{D} Wire mass

n_{disc} Number of elements in the discretised friction model

n_{DOF} Number of degrees of freedom

n_{Modes} Number of eigenmodes

n_{Osc} n-th oscillation cycle

n_{x} Number of partial areas in x-direction of the discretized friction model

n_{y} Number of partial areas in y-direction of the discretized friction model

$P_{\mathrm{US,I}}$ Ultrasonic power intensity

t Time

t_{B} Bond duration

t_{I} Interval duration

$T_{\mathrm{P},n_{\mathrm{Osc}}}$ Period length of the n-th oscillation cycle of the bond duration

T_{P} Period length

t_{R} Ramp duration

t_{Sim} Simulation duration

u_{T} Excitation voltage of ultrasonic transducer

W Width of the wire bond

W_{f} Dissipated energy due to frictional work

W_{s} Specific ultrasonic energy

x_{BT} Displacement of the bond tool tip

x_{H} Displacement of the ultrasonic transducer horn tip

x_{S} Displacement of the substrate at the reference point

x_{W} Displacement of the wire mass

z_{TR} Vertical position of the traverse from the test-rig

$z_{\mathrm{WD,max}}$ Maximum vertical displacement of the bonding tool at the end of the bond process

$z_{\mathrm{WD,TSC}}$ Critical vertical position of the bond tool, at which tool/substrate contacts occur

z_{WD} Vertical displacement of the bonding tool

1 Introduction

Since about 1954 an abrupt change of the connecting technology in microelectronics industry occurred when the mesa transistor was developed which lead to a significantly decreased size of the contact areas and new interconnection techniques needed to be developed. At first, Bell Labratories [5] published in 1957 wire bonding results using a heated bonding tool without ultrasonic energy and in 1960 Sonobond received the first patent for ultrasonic metal welding [138]. In the following decades, packaging technology was constantly developed further. Today, in particular wire bonding technology still plays a major role due to its versatility and cost-effectiveness.

The wire bonding process is divided into three categorical processes: thermo compression bonding (TC) with only heat energy, thermosonic bonding (TS) with combined heat and additional ultrasonic energy, and ultrasonic bonding (US) with only ultrasonic energy; a distinction is made between fine wire (diam. 12 µm to 75 µm) and heavy wire (diam. 75 µm to 500 µm) and between ball-wedge and wedge-wedge wire bonding, see table 1.1. In fine wire bonding, TC, TS, and US bonding are used, depending on the application; in heavy wire bonding, only US bonding is used in production, although thermosonic heavy wire bonding experiments have been reported lately [53].

Table 1.1: The three different process technologies of wire bonding [66].

Wire bond form / Diameter	Processes	Typical Materials	Energy
Ball-Wedge (12.5 µm$< D_{\mathrm{W}} <$ 75 µm)	TC or TS	Au	Heat
Wedge-Wedge (17.5 µm$< D_{\mathrm{W}} <$ 75 µm)	TS or US	Au, Cu, AlSi1	Heat / US
Wedge-Wedge (75 µm $< D_{\mathrm{W}} <$ 600 µm)	US	Al, Cu	US

Approximately 93% of all semiconductor packages are manufactured using ball-wedge bonding method as nearly all dynamic random access memory (DRAM) chips and most ICs are assembled by ball bonding [66]. In addition, fine wire bonding in general is used for low-current connections in devices like lead-frame packages, antenna designs on CMOS chips where the antenna is designed by the loop of the wire bond, or disk drives [19, 88, 58].

Although most of the annually produced wire bonds are made by ball-wedge bonding processes, heavy wire bonding is part of the important growing market of power modules to connect the upper side of chips to substrates and connect substrates to terminals. From an application point of view, more than half of the market is in industrial motor drives, followed by traction power supplies. Strongly growing market segments are power modules for renewable energies (wind turbines and solar modules) and automotive applications where in particular, converters and chargers for electric vehicles (EV) require the continued development of packaging technology in terms of higher efficiency, lower weight and construction volume [123, 83]. In particular, the market potential for SiC

and also GaN technologies, which have been developed beside the Si IGBTs in the recent past, is very high due to the potential to increase the efficiency and thus the range of EVs, see figure 1.1.

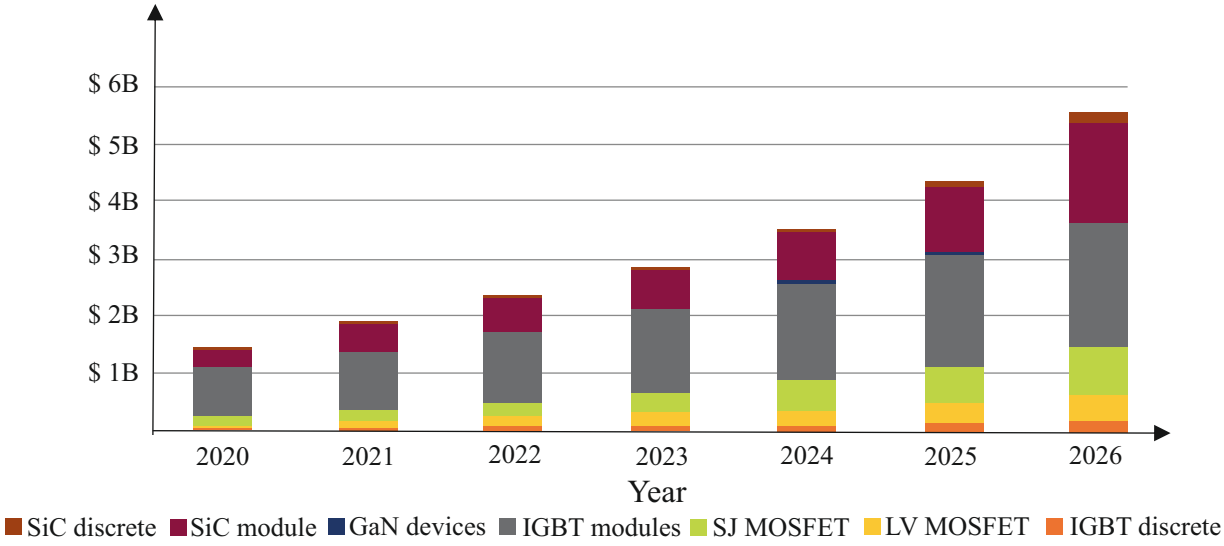

Figure 1.1: According to Yole [146] the power electronics market for EVs - especially the IGBT and SiC modules - will steadily increase and almost triple from 2020 to 2026; redrawn from [146].

For power modules, new challenges are the rising demands on the electrical connections with larger junction temperatures because of higher electrical power of the new technology generations. To adapt on these demands, the packaging technology is steadily further developed; for example, the back sides of semiconductors are mostly no longer soldered, but sintered, as the soldered interconnection tended to break. As a consequence, the typically used pure aluminium heavy wire bonds at the top became the weak spot of the system, as lift offs and heal cracks under cycling temperature loads can occur, which can lead to an electrical failure of the whole module [112]. In process development, the wire material and diameter are adapted to the specifications in terms of maximum current, switching frequency and temperature of the application. One alternative to aluminium wire is copper which has better electrical and thermal conductivity and higher mechanical strength and is used lately for packaging of power modules mainly on semiconductors with a thin copper metallization on top, [104, 23], see figure 1.2.

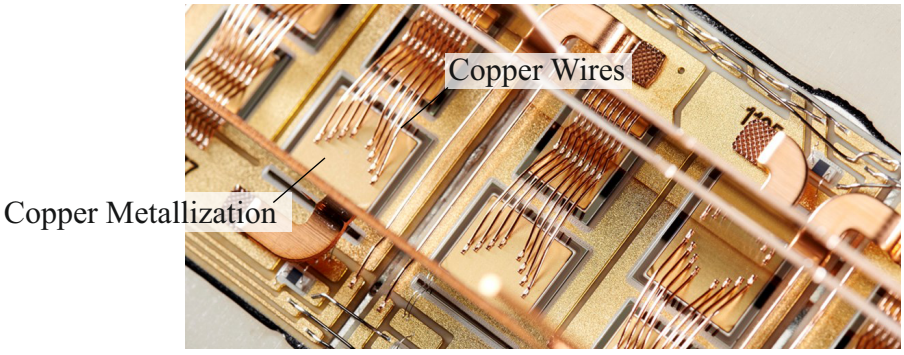

Figure 1.2: Inside view of a semiconductor module with copper heavy wire bonds on semiconductors with copper metallization; image from [23].

Although copper wires offer advantages in applications with high electrical power, using pure copper increases the risk that the metallization of the semiconductor is damaged during the bonding process, thus the yield of power modules is reduced. In direct comparison, there are also advantages in using aluminium wires: due to the higher ductility of the wire, the process windows are at lower bond normal force, lower ultrasonic power and shorter bond duration, thus the risk of metallization damage is less. Although the conductivity of aluminium is only around 60 % of copper, it is one third the weight and can therefore conduct twice as much electricity when compared with copper of the same weight [12].

Thus, the choice of wire material is always based on the requirements of the application which are derived in the process design step during the process development shown in figure 1.3. Different factors have to be considered, such as the choice of process parameters, which differ strongly between the wire materials and also depend on the target values like shear force, strength and thermal stability in power cycling tests. In conventional process development, the process parameters are determined in the experimental process characterization step using methods of statistical experiment design such as the Design of Experiment; although the ultrasonic heavy wire bonding process appears to be quite simple - as only a bond normal force and an ultrasonic excitation need to be provided for a short time - determination of process parameters often becomes a very challenging time and cost consuming task. The small dimensions of the components, highly complex contact dynamics during bond formation, and the different process parameters that have an impact on bond quality and failure modes make it very difficult to understand the wire bond process. In the process optimization step, suitable parameter combinations are then selected from the experimentally determined correlations of process parameters and target variables, such as shear force, strength and other parameters, in order to achieve the targets previously defined during process design step. If these goals are not achieved, appropriate actions must be taken again in the process design step and the process development loop starts again.

To reduce time and costs but efficiently determine optimized process parameters, process design, characterization, and optimization should be enhanced by simulation. In the past, several researchers [85, 34, 29, 108, 86] showed that the effects of bond formation in ultrasonic wire bonding can be investigated using simulation tools like thermal and mechanical finite element simulation and process models. But an encompassing model for the simulation of parameter studies with different wire materials - such like aluminium and copper - for the ultrasonic heavy wire bond process is still missing.

Based on such a model, the effects of the process parameters on bond quality could be investigated early in the process design phase. Results of the experimental process characterization could be combined with simulation results for the interpretation of effects of process parameters on bond quality and thus to reduce the overall amount of needed experimental parameter combinations and additional measurements. By that the amount of experimental effort and thus time and costs could be reduced significantly.

1.1 Objectives

The main objective is to develop a simulation model for copper and aluminium heavy wire bonding, which enables the simulation of parameter studies in order to improve

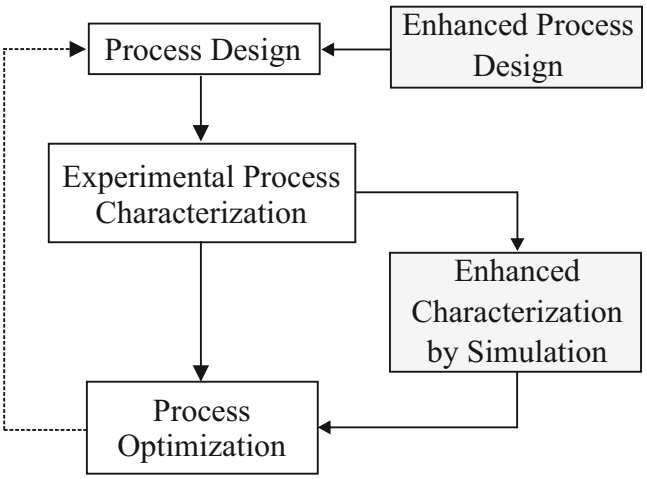

Figure 1.3: Process development steps for ultrasonic wire bonding, enhanced by simulation.

the current process development in heavy wire bonding. The specific objectives of this research are:

1. Carrying out ultrasonic bonding tests with 400 µm aluminium and copper wire to:
   - investigate the impact of touch down force on shear force and strength,
   - determine the main effects diagrams for shear force and strength,
   - investigate the impact of bonding frequency on shear force and substrate vibration,
   - perform additional measurements of bond tool vibration amplitude and vertical wire deformation,

   thus defining requirements and generating a database for the bond model and later comparison between experimental and simulated results.
2. Development of a simulation model based on the requirements derived from the ultrasonic bonding tests, that represents the essential physical phenomena which influence bond formation in ultrasonic wire bonding and is suitable in terms of computing performance for carrying out parameter studies.
3. Experimentally determine the fundamental model parameters, which can not directly be identified from the ultrasonic bonding tests.
4. Carrying out simulation-based parameter studies for aluminium and copper wire, comparing the results from the simulations and experiments for validation of the bond model, and analyse the bond formation with additional simulation results, which can not be determined by experiments because of technical limitations.

1.2 Thesis Outline

Chapter 2 provides a summary of the state of the art on the mechanisms of bond formation and the impact of the main process parameters on the bond quality. A summary of the known findings on the so-called ultrasonic softening effect is given, as it has a significant impact on wire deformation and bond formation. In addition, the known model

approaches, for simulating bond formation, ultrasonic softening and the wire bond process are summarised. Finally, the knowledge gaps for ultrasonic heavy wire bonding are identified, which will be investigated in this thesis.

Chapter 3 presents the results from the experimental bonding tests with 400 µm aluminium and copper wire on DCB substrates to determine the influence of bond normal force, bond duration and ultrasonic power on the shear force and strength, which are summarised in the main effects and interactions diagrams. Additionally, the shear codes and tool/substrate contacts have been determined from microscopy images of the sheared areas. Since the impact of the touchdown force on shear force and shear strength was unknown for ultrasonic heavy wire bonding so far, pre-screening tests with varied touch down force have been carried out and evaluated. In additional experiments the influence of the bonding frequency on the substrate vibrations and the shear force over the bonding duration has been investigated, as it was known from thin wire bonding that high frequencies can have beneficial effects on the bond quality, which had not yet been proven for heavy wire bonding before.

Chapter 4 presents a multi-scale model approach, based on a co-simulation between the two software tools *MATLAB* and *ANSYS*. First, the physical subsystems are discussed, followed by the technical implementation of the program, including high performance computing to simulate parameter studies of the bond parameters in parallel.

Chapter 5 describes the identification of the model parameters. A test rig based on a universal tensile-compression testing machine has been extended by dynamic excitation either with a shaker up to 1 kHz or with an ultrasonic transducer at 20 kHz, so that friction coefficients and force-displacement characteristics with and without superimposed ultrasonic excitation can be measured. The force-displacement characteristics are needed to determine the material models (stress-strain curves) for copper and aluminium for the finite element method in *ANSYS*.

In chapter 6, the results from the simulated parameter studies for the aluminium and copper wire are presented and directly compared with the experimental results from chapter 3 for validation of the bond model. In addition, selected simulation results are discussed, which provide additional insights into the details of bond formation.

Lastly, chapter 7 provides a conclusion and outlook to proposed future work.

2 State of the art

In section 2.1, a phenomenological description of the bond formation in ultrasonic wire bonding is given on the basis of published research results. During process development, several parameters such as touchdown force, bond duration, ultrasonic frequency and many more have to be taken into account; the already known influence of these parameters is summarised in section 2.2. An important effect in ultrasonic wire bonding is the wire deformation which is influenced by the so-called ultrasonic softening effect; due to the great importance of this effect, it is described separately in section 2.2.3. The methods of process development and the equipment and test methods for determining bond quality, e.g. by shear tests, are an essential basis for wire bonding experiments and are summarised in chapter section 2.3. The simulation of the bonding process and thus also the bond formation is a core task of this thesis; the modelling approaches known so far are summarised in section 2.4. In section 2.5, the identified knowledge gap is derived from the previous sections.

2.1 Phenomenological description of the bond formation process

In figure 2.1 the schematic structure of the ultrasonic transducer system and exemplary trajectories for the bond normal force F_{BN} and ultrasonic voltage u_{T} with two intervals are shown. Both, the bond normal force and the voltage can vary over the bond duration t_{B}; for this, interval and ramp durations can be set at the bonding machine. In this example, the bond normal force F_{BN} begins at the value of the touch down force F_{TD} and then increases to a higher level during the ramp duration and is held constant for the rest of the first interval time. During the second interval, the bond normal force is held constant and the voltage is reduced to reduce the ultrasonic power at the end of the bond process.

Ultrasonic heavy wire bonding is a solid-state joining process, where the induced oscillating shear between the faying surfaces is mainly responsible for the metallurgical bond formation. During bond formation, different processes take place, thus the bond process is typically divided into different phases, [35, 77].

In the first phase (Pre-Deformation Phase) a static touchdown force F_{TD} is applied to the wire which is clamped by the bond tool, an initial contact area is created, and oxide layers and other contaminants can be cracked which enhances the following cleaning process. Cracking and detachment of oxide layers differs significantly for aluminium and copper wire. The hard and brittle oxide Al_2O_3 shows very little aluminum and oxygen diffusion, limiting its thickness to a few nanometers. The two copper oxides, Cu_2O and CuO on the other hand are both very soft and grow with a continuous oxide growth over time [40]. The aluminium oxide Al_2O_3 has proved to crack under the bonding load and aids in the cleaning phase as an abrasive. This enhances the bond formation [75] whereas

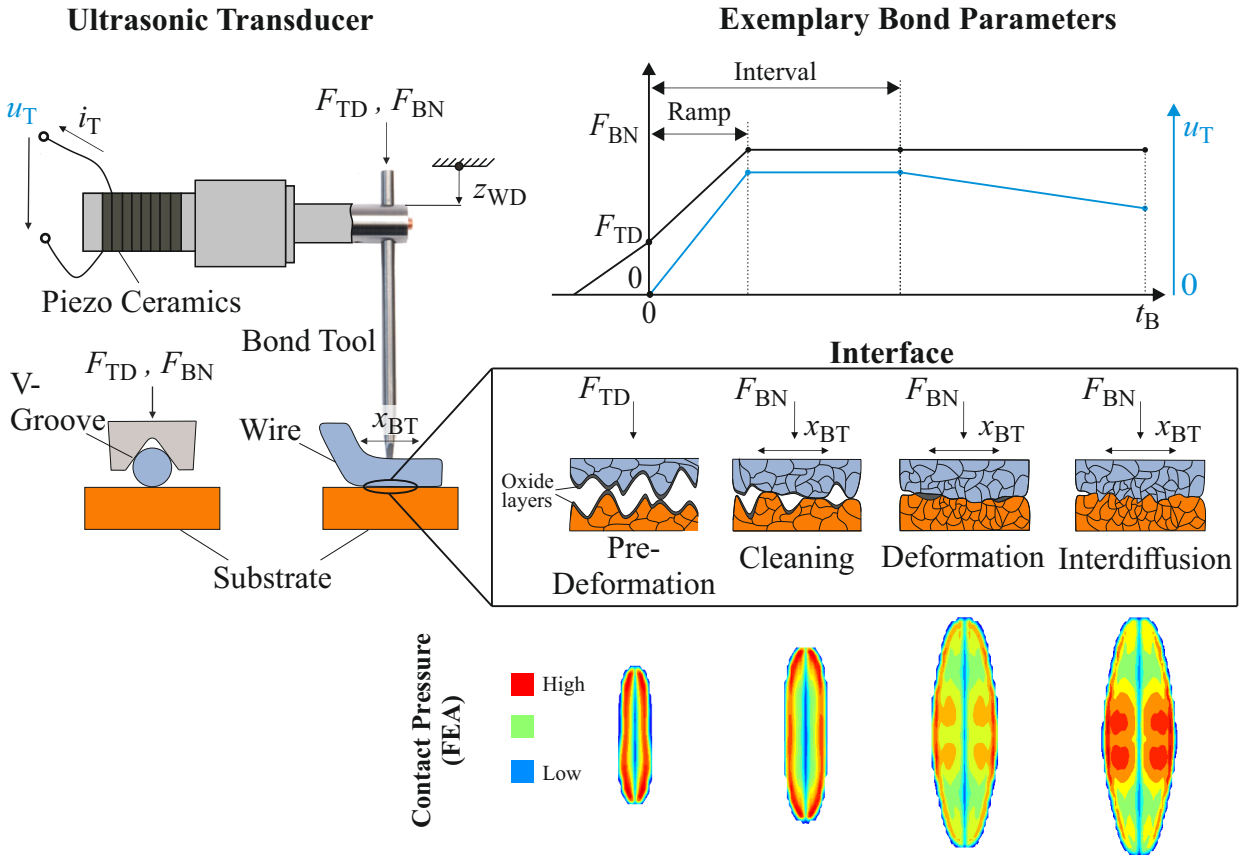

Figure 2.1: **Left:** Ultrasonic transducer, driven by the oscillating voltage u_T and the bond tool tip with the v-groove, clamping the wire by the bond normal force F_{BN}. The wire is excited by the bond tool amplitude x_{BT}. **Right:** Trajectories of the main bond parameters (F_{BN}, u_T) over the bond duration and the changing interface conditions during the four bond phases. The Finite Element Analysis (FEA) results show, that during the bond formation, the contact area increases and the contact pressure distribution changes.

the ductile copper oxides are smeared over the surface and cannot entirely crack due to the touchdown force [31].

In the next phase (Cleaning Phase), the ultrasonic vibration x_{BT} and the bond normal force F_{BN}, which can differ from F_{TD}, are applied to the wire. When the induced oscillating shear forces are large enough to overcome the sticking-force between the wire and substrate, sliding occurs. The oxide layers and other contaminations are then detached from the faying surfaces and are transported to the peripheral contact region [76]. Long et al. reported in [75] for bonding 400 µm Al wire that oxide removal process takes four steps: cracking, detaching, milling and transporting; cracking of the oxide layers occurs already in the pre-deformation phase and the first few milliseconds of the cleaning phase. Detachment is caused by vibration and the shear forces at the beginning of the ultrasonic excitation. The detached oxides are then milled to small particles by relative movement between wire and substrate and transported to the outside of the contact surface. Lum et al. reported in [80] that bonding tests with aluminium wire on copper substrate made without ultrasonic energy but having a deformation comparable to ultrasonically bonded wires did not lead to bond formation. This demonstrates that deformation alone cannot result in bonding and it was concluded, that wearing the relatively ductile copper ox-

ide by ultrasonic energy is mandatory for creating clean metal to metal contact, which results in bonding.

In the following phase (Deformation Phase), high plastic deformation of the wire and the interface region of the substrate dominates the bond process, even though the normal force F_{BN} is not increased significantly. Apparent reduction of yield stress of the wire by ultrasonic excitation known as the *Ultrasonic Softening Effect* enhances the deformability of the wire, which is mandatory for transportation of detached oxide particles, increase of the real contact area between wire and substrate, and grain refinement and recrystallization. Material flow of the wire combined with unevenly distributed normal stress and relative motion between wire and substrate lead to oxide flow to the peripheral interface region [75].

Once microwelds are formed, interdiffusion begins between wire and substrate in the last phase (Interdiffusion Phase). The material flow occurs without melting the materials and is induced by the oscillating shear stress and plastic strain in the interface [108]. The material flow leads to a metallic connection between wire and substrate; as the two metals are not molten, dissimilar metals with different melting temperatures can be bonded forming Intermetallic compounds (IMCs) [28, 148, 24]. Pedersen et al. investigated in [97] the bond formation for 400 µm Al wire bonded to IGBT chips by micro-sectioning of the wire and SEM combined with FIB to characterize the grain refinement of the interface. The grain structure of the wire can be divided into three primary regions in the interface: the refinement- the deformation-, and the original region. During the bonding process, dynamic recrystallization and recovery take place at the region close to the interface. It results in a polycrystalline interface where the grain size is much smaller than that before bonding [63]. According with decreasing grain size at the interface the increasing number of grain boundaries enhances diffusion and finally the bond formation.

Although the four bond phases are presented sequentially in figure 2.1 for a phenomenological description of the bond formation process, the deformation and interdiffusion phases in particular cannot be clearly separated in reality, as these two phases strongly interact with each other at the same time.

2.2 Factors affecting bond quality

The first step before process optimization is to figure out the main factors influencing the target value to be investigated. Cause-effect diagrams are suitable for determining the factors influencing a target value. Such diagrams were developed by Tsai et al. [129] for ball-wedge bonding of copper and by Kaestle [56] for aluminium and copper heavy wire bonding; however, the influencing factors are individual for each process. In figure 2.2 the key influencing variables focused on the ultrasonic heavy wire bonding process are listed; they are divided into *Parameter*, *Disturbance* and *Requirement*.

Parameters are all adjustable process parameters which can be set specifically and reproducibly. Derks [65] grouped those factors into the *machine parameters* and *system parameters*; machine parameters are directly settable at the bonding machine (such as F_{BN}, F_{TD}, u_{T}, and t_{B}) whereas the system parameters have to be chosen during process development, e.g. setting the bonding frequency f_{T} by choosing a bonding head.

Disruptive factors are uncontrollable influencing factors and need to be reduced. For example, Han et al. [43] found that the tightening torque of the screw for clamping the

bond tool can have an impact on the vibration form of the bond tool and influence the bond quality. As a consequence, the screw should always be tightened with a calibrated torque spanner before the bonding tests. Other factors are wear of the bonding tool and contaminations on the substrate; parameters such as the temperature and humidity of the environment can not be avoided and should be observed and kept as constant as possible, [117].

Requirements are for example know-how and experience of process development engineers that are needed to interpret results such as machine data, shear force values, shear codes and further measurements to evaluate the quality of the bonds. The experts also plan the experiments and ensure that the settings are kept constant, which results in higher process accuracy and precision.

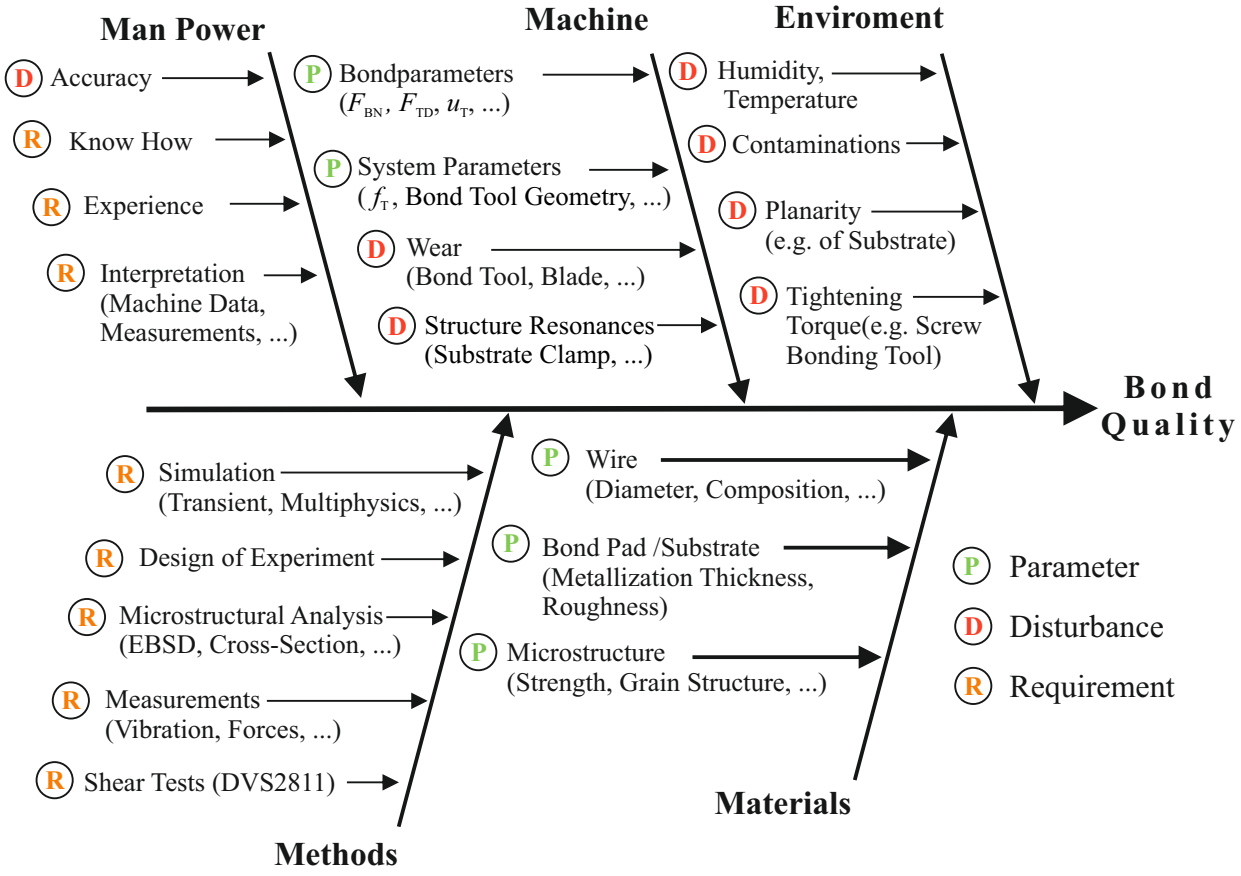

Figure 2.2: Cause-effect diagram for the ultrasonic heavy wire bonding process; the factors affecting the bond quality are grouped into directly adjustable *Parameters*, uncontrollable *Disturbance* factors and *Requirements*.

This PhD thesis is focussed on the the impact of *Parameters* (machine and system parameters) on the bond quality. Therefore the following subsections summarize scientific publications on this topic. Among the system parameters, the frequency f_T is discussed in particular. Other system parameters, such as the geometry of the bond tool or the material of the substrate and wire, are not specifically varied, but have been defined as the basis for this PhD and are kept constant for the experiments.

2.2.1 Machine parameters

One of the most studied machine parameter is the ultrasonic power which is related to the actual vibration amplitude x_{BT} and is set differently depending on the manufacturer and type of bonding machine; in case of the bonding machine *Hesse Mechatronics* Bondjet BJ939 used for all experiments in this PhD thesis, the ultrasonic voltage u_{T} is set. With other machine types from different manufactures, also the current i_{T} or the ultrasonic power (measured in W, digits or %) are used. In addition to the ultrasonic power, the bond normal forces F_{TD} and F_{BN} are also bond parameters with a significant influence on the bond quality and have been studied by several scientists. The choice of ultrasonic power and the bond normal forces are strongly interrelated, as the ultrasonic power influences the ultrasonic softening effect and the normal force in turn also influences the wire deformation.

In addition, the bond normal force influences the friction forces between wire and substrate, thus higher normal forces in turn require higher ultrasonic power to achieve sliding friction between wire and substrate. Therefore, the influence of ultrasonic vibration and bond normal force is studied together in section 2.2.1.1. The impact of the touch down force F_{TD} is discussed in section 2.2.1.2. Except the touch down force, all machine parameters can vary over bond duration t_{B} by setting up different intervals defined by t_{I}. The impact of the different durations is summarized in section 2.2.1.3.

2.2.1.1 Bond normal force and ultrasonic power

Lum et al. investigated in [79, 80] the impact of the bond normal force and the ultrasonic power on bond formation in thermosonic wedge-wedge bonding experiments with aluminium wires of 25 µm diameter on copper substrate. In experiments, the ultrasonic power was varied from 0 mW to 260 mW and the bond normal force from 0.34 N to 0.64 N. The bonding results for the different bond normal forces and ultrasonic power values were classified, whether the bonds lifted off or were bonded to the substrate (in percentage of ten samples for each parameter combination) and if micro slip or gross sliding occurred, see figure 2.3. Without ultrasonic excitation and for all three bond normal forces, no fretting in the footprint was found, meaning no micro slip or gross sliding occurred and all bonds lifted off. With ultrasonic power of 65 mW, for all three bond normal normal forces micro slip but no gross sliding was observed, so all bonds lifted off. Increasing the ultrasonic power to 135 mW first leads to gross sliding for the lowest bond normal force (0.34 N) and for ultrasonic power 195 mW to 260 mW gross sliding occurs for all investigated normal forces. The SEM pictures of foot prints for bond normal force 0.34 N show for 65 mW minimal fretting in the peripheral interface but no bonding areas. For 160 mW, minimal bonding was found but not all fretted areas lead to bonding. For 195 mW the bonded area was increased except of an elliptical band in the contact periphery. For 260 mW the largest footprint with more adhering aluminium after shearing was found indicating the strongest bond. The results show, that the minimum ultrasonic power needed for gross sliding and bonded wires (those which didn't lift off) is strongly influenced by the bond normal force and strong interaction between both parameters exists. In summary, an increased bonding power is required for an increased normal bonding force in order to achieve gross sliding and, hence, increased bond strength.

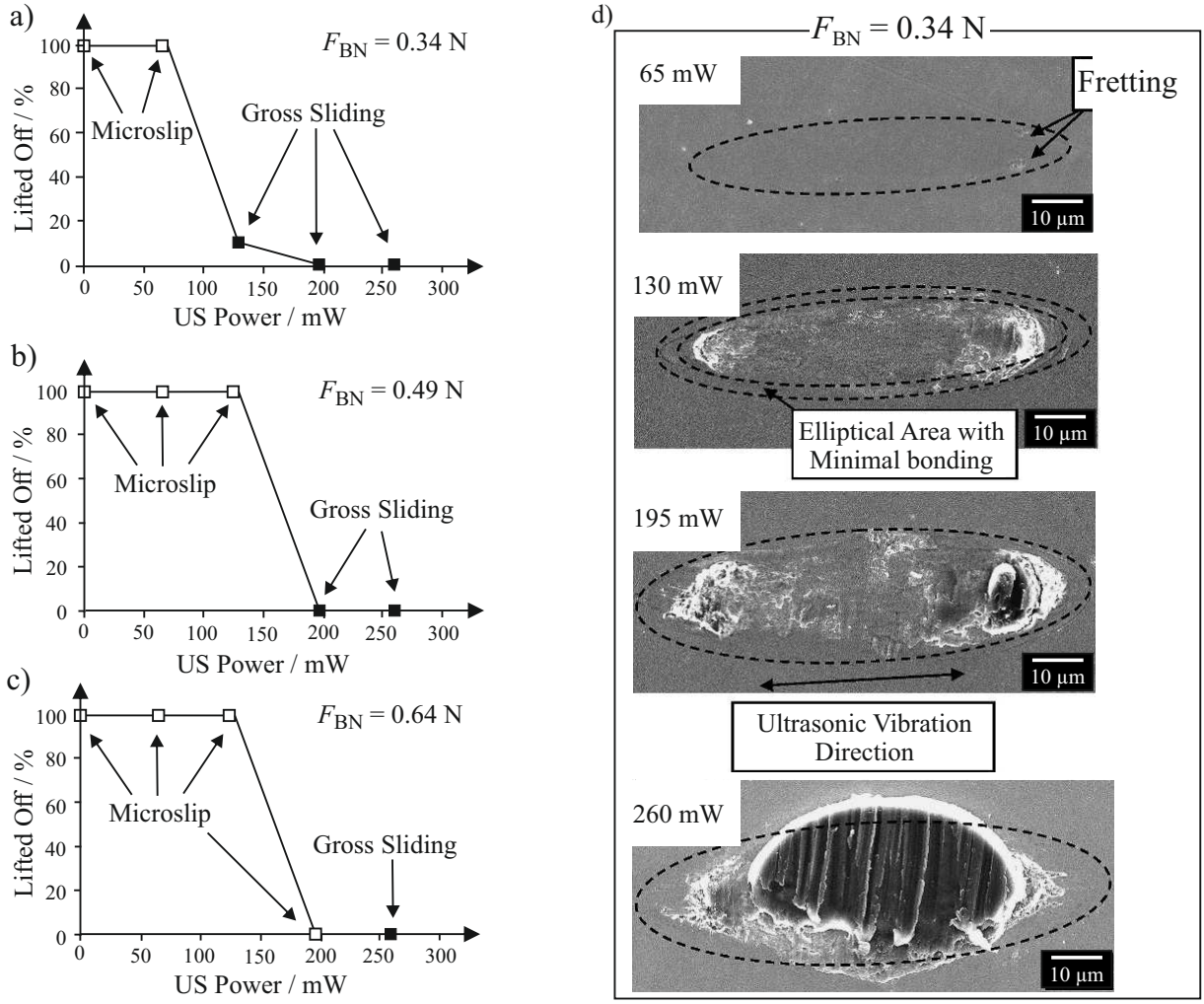

Figure 2.3: On the left side, the amount of lift off's in % for a) 0.34 N, b) 0.49 N and c) 0.64 N bond normal force and different ultrasonic powers. In d) bond footprints made with 0.34 N bond normal force at various ultrasonic powers are shown. Redrawn results from Lum et al. [80].

Goehre et al. investigated in [36] the impact of bond normal force and ultrasonic power on wire bond reliability by active power cycling for 400 µm aluminium wire bonding. From active power cycling experiments it was found that the lifetime of the bonds was increased by a factor from 1.5 up to 3.0 just by increasing the ultrasonic power. The bond normal force on the other side increased the lifetime only by a factor of maximum 1.3. Kästle and Franke [57] determined process parameter windows for ultrasonic power and bond normal force for 300 µm Al and Cu wire bonding. The Al wire bonding process was influenced most significantly by the bond normal force while the Cu wire bonding process was mainly driven by the ultrasonic power. Unger et al. [131] found for 500 µm copper wire bonding that the evaluated shear force is more sensitive to ultrasonic power than to the applied bond normal force.

Ding et al. [29] investigated in finite element simulations the impact of bond normal force on the contact pressure distribution between wire and substrate for ultrasonic wedge bonding of an Au-wire with 25.4 µm diameter. The simulation results showed that the maximum of contact pressure occurred always at the periphery and the minimum in

the central region of the contact area for all investigated bond normal forces. The real contact area increased linearly with increased bond normal force. Frictional energy was calculated from contact pressure distribution; results showed that the total frictional energy in the interface increases linearly with bond force.

2.2.1.2 Touchdown force

The influence of touchdown force on bond quality has rarely been systematically investigated but is known to have an effect on the bond formation process and therefore on bond quality. Unger et al. [132] investigated the pre-deformation process of 500 µm copper wire; a linear relationship between touchdown force and the contact area between wire and surface was found. Osterwald [92] stated that a greater touch down force results in a longer oxide removal process as a larger contact area between wire and substrate is generated. Althoff et al. [4] found that a large touch down force is preferred when the substrate material is softer than the wire material and vice versa. Especially for brittle oxides like aluminium oxide (Al_2O_3), cracks are generated by the application of the touch down force which greatly facilitate the subsequent removal process of the oxides in the cleaning phase [113].

2.2.1.3 Bond and ramp duration

A rarely investigated parameter is the bond duration t_B and the ramp/interval duration t_R and t_I. Kaestle et al. [57] found for heavy wire bonding of aluminium and copper wire, that the bond duration has a linear effect on the pull and shear force results; the ramp duration has no significant effect. For the aluminium wire, the bonding time was significantly shorter than for the copper wire (155 ms compared to 500 ms) in order to achieve optimal results. Xu et al. [141] investigated the formation of microwelds by observing the footprints obtained at different bonding times for ball wedge bonding with an 20 µm Au wire on aluminium metallization pads. The dimension of contact area increased quickly at the early stage of bonding, then grew very slowly with longer bonding time. The bond duration has a significant influence on the number of lift-offs and should not be below a critical value. Shah et al. [114] investigated the impact of resonance effects from the substrate structure on the bond formation; they found that longer bond durations may be used to improve bond quality in some cases when substrate vibrations due to resonances effect the bond process.

2.2.2 System parameters (transducer frequency)

Since the 1960s, 60 kHz was used as bonding frequency in ultrasonic wire bonding which resulted in transducers and tools that were appropriate to microelectronic dimensions [44]. However, in the past several decades researchers reported about advantages of high-frequency bonding in terms of less substrate vibrations, less wire deformation, larger process windows, and higher bond strength:

Bonding on supple substrates: Heinen et al. concluded in [47] that for bonding on integrated circuits with assembled test chips on a polymeric dielectric with a frequency of 120 kHz provides additional process reliability and a larger process window. The high working frequency leads to more focused ultrasonic energy that does not penetrate deeply

into the chip. When bonding on soft polymers such as Teflon or unreinforced polyimide the bonding quality is improved with higher bonding frequency.

Process window: Pang et al. reported in [96] for thermosonic ball bonding of gold stud bumps (Au-wire with 25.4 µm diameter) that the bond process window of the ultrasonic power and bond normal force was generally larger for bonding frequency 109 kHz compared to 63 kHz. Pan et al. found similar results in [95] for thermosonic ball-wedge bonding of 25.4 µm Au-wire: a larger process window was found for 120 kHz bonding frequency compared to 60 kHz and bonding with 120 kHz required less ultrasonic power than bonding at 60 kHz. It was concluded, that the higher ultrasonic frequency transfers ultrasonic power more efficiently to the interface between wire and bonding pad. Charles et al. reported in [18] and [17] for thermosonic ball-wedge bonding of Au-wire with 25.4 µm diameter that bonds made with 100 kHz on gold metallization appeared to be consistently stronger than bonds made at 60 kHz. On AlSi metallization, the results were not clear and the bond strength at 60 kHz was slightly larger than for 100 kHz and the 100 kHz bonding window (ultrasonic power and bond duration) appeared to be smaller and sharper than the 60 kHz window. So the choice of frequency in this case was dependent on the type of metallisation.

Wire deformation: Onuki et al. reported in [90] that bonding Al wires with 500 µm diameter on transistor chips with 110 kHz raises the bond strength and decreases the deformation ratio between wedge to the wire diameter B/D_{W} of the Al-wire compared to 60 kHz. Chan et al. [16] found for thermosonic wedge-wedge bonding of 25.4 µm Au-wires on a PCB bond pad with two bonding frequencies at 62 kHz and 138 kHz that bonding with 138 kHz leads to a larger bond process window (bond pad temperature and ultrasonic power) and bond strength. The deformation ratio B/D_{W} was consistently less at 138 kHz compared to 62 kHz while the pull strength was consistently higher. Levine explained in [68] the effect of higher bonding frequency on the deformation behaviour of the wire by higher strain rate: lower bonding frequencies (here 60 kHz) lead to an initially softened wire by the slip of local dislocations. When deformation occurs, the material hardens and the vibration energy is transmitted to the interface between the wire and bond pad. At higher frequencies (here 120 kHz) the wire is initially hardened due to the simultaneous shift of whole lattice planes and the vibration energy is directly transmitted to the interface with little deformation leading to more efficient transition of ultrasonic energy to the interface between wire and substrate.

Frequency depended substructure behaviour: Mayer and Huang presented in [84] results of a harmonic frequency response calculated with a finite element model of 25 µm Au-wire for ball bonding on a metallization layer on a Si-chip that is embedded in a dielectric layer stack. The tangential force F_{US} acting on the interface was evaluated for bonding frequencies up to 700 kHz and constant excitation amplitude $\hat{x}_{\mathrm{BT}}$ of 559 nm; additionally, they investigated three different tool geometries with varying main taper angels (MTA) of the capillary. In figure 2.4 a) the frequency depended tangential force is shown and in figure 2.4 b) the first three lateral resonances are listed. Typical bonding frequencies for fine wire bonding lie nowadays in the range of 130 kHz to 140 kHz which is within the first range in figure 2.4. The simulation results show that in this range the tangential force F_{US} remains relatively flat in the frequency response; this behaviour is assumed to be robust for industrial application. A second range has been identified in the frequency range from 380 kHz to 420 kHz above the second set of resonances. In order to compare the two ranges, the amplitude $\hat{x}_{\mathrm{BT}}$ was evaluated in figure 2.4 c), which is necessary to

achieve a tangential force of 258 mN. Depending on the MTA, a reduction of up to 76 % in ultrasonic vibration amplitude could be achieved by using the higher frequency range at 400 kHz. It can be assumed that the mechanical load on the bondpad is lower at the higher frequency.

a)

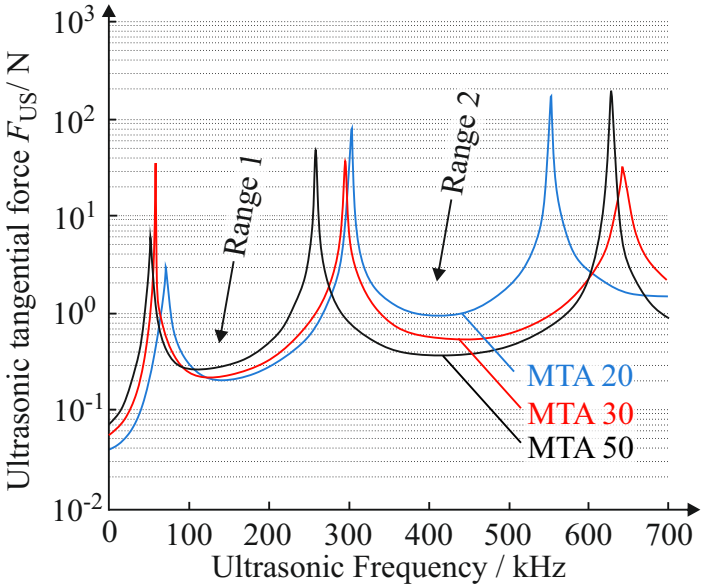

b)

MTA	1st	2nd	3rd
20°	72 kHz	305 kHz	556 kHz
30°	61 kHz	295 kHz	646 kHz
50°	50 kHz	257 kHz	632 kHz

c)

	Main Taper Angle		
Frequency	20°	30°	50°
130 kHz	642 nm	565 nm	497 nm
400 kHz	154 nm	229 nm	363 nm
Reduction	-76 %	-59 %	-27 %

Figure 2.4: Results of harmonic analysis from finite element model with three different main taper angels (MTA): a) the frequency depended tangential force, b) the first three resonance frequencies and c) the required amplitude to achieve tangential force F_{US} equal to 258 mN. Results redrawn from [84].

2.2.3 The ultrasonic softening effect

Ultrasonic excitation can cause the deformation behaviour of metals to differ significantly from static deformation behaviour in such a way that the material appears softer, which is why the effect is also called *Ultrasonic Softening Effect* and has been part of research for decades, [67, 25, 116, 139, 50]. To characterize the material softening, typically stress-strain diagrams are measured in tensile or compression tests, and an additional ultrasonic excitation is superimposed during the quasi-static deformation; a schematic representation of such a stress-strain diagram with phase-wise ultrasonic superposition is shown in figure 2.5. When ultrasound is superimposed during the tension-compression test, a stress drop $\Delta\sigma_f$ compared to the static stress-strain curve is observed which increases with increased ultrasonic power [105, 137, 149]. This effect is used for reducing forming forces and increasing surface quality in numerous manufacturing processes like milling, microforming, deep drawing, and wire drawing [73, 143, 81, 71]. Compared to the softening generated by heat, much less energy is needed to achieve a certain degree of softening which makes it more efficient and interesting for applications mentioned above.

Although the ultrasonic softening effect has been known for decades - Langenecker et al. [67] were one of the first to study the effect on aluminium samples in 1966 - the exact mechanisms have not yet been conclusively clarified. The most challenging aspect of characterising the ultrasonic softening is that there are a number of different influencing

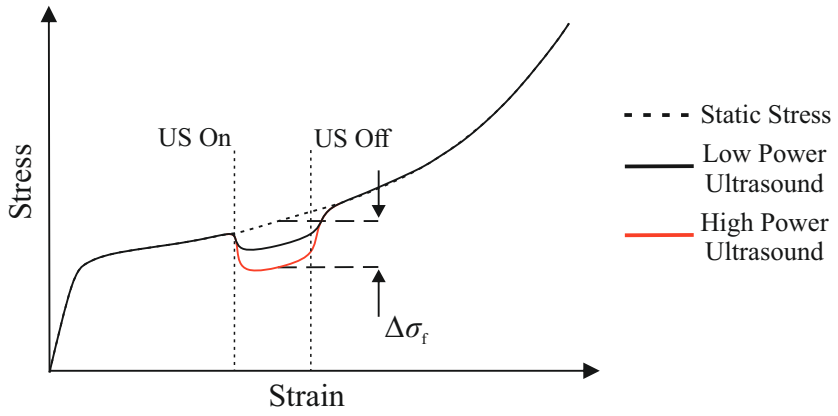

Figure 2.5: Schematic representation of a stress-strain diagram with phase-wise ultrasonic superposition and flow stress change $\Delta\sigma_f$ for "low ultrasonic power" (black) and "high ultrasonic power" (red).

factors, depending on external conditions such as the test rig and the environment, but also on the material itself. From previous studies, it is known that the following process parameters have an effect on the flow stress reduction:

- vibration amplitude [67, 105, 133, 149, 52],
- vibration frequency [16, 149],
- material microstructure [1].

The ultrasonic softening effect itself is, according to the current state of science, based on three mechanisms: stress superposition (section 2.2.3.1), ultrasonic friction reduction (section 2.2.3.2), and metallurgical effects (section 2.2.3.3), which are described in the following sections.

2.2.3.1 Stress Superposition

The stress superposition has been analysed experimentally and analytically by different researchers in [59, 111, 15, 121, 50]. The superimposed vibration of the strain in the plastic region causes a cyclic loading and unloading in addition to the quasi-static loading of the material, resulting in a time-averaged reduction of the stress level, see figure 2.6. Starting from the quasi-static load (a), the vibration first increases the plastic deformation while the stress is limited by the plastic stress-strain characteristics. After the vibration reaches its peak (b), unloading starts; stress and strain reduce according to the elastic characteristics (c) and reach point (d) when the strain is further reduced to the minimum of the vibration. Correspondingly, the time average mean value of the stress $\overline{\sigma}$ is lower than the quasi-static applied stress σ resulting in an apparent overall stress reduction. Within the elastic range, the stress reduces during unloading by the same amount as it increases during loading, thus no overall stress reduction occurs here.

The principle of stress superposition was modelled by Kirchner et al. [59] for low frequency oscillations for strain rate dependent and independent materials:

$$\Delta\sigma_f = E\left(\hat{\epsilon} + \frac{\dot{\epsilon}_0}{4\,f}\right). \tag{2.1}$$

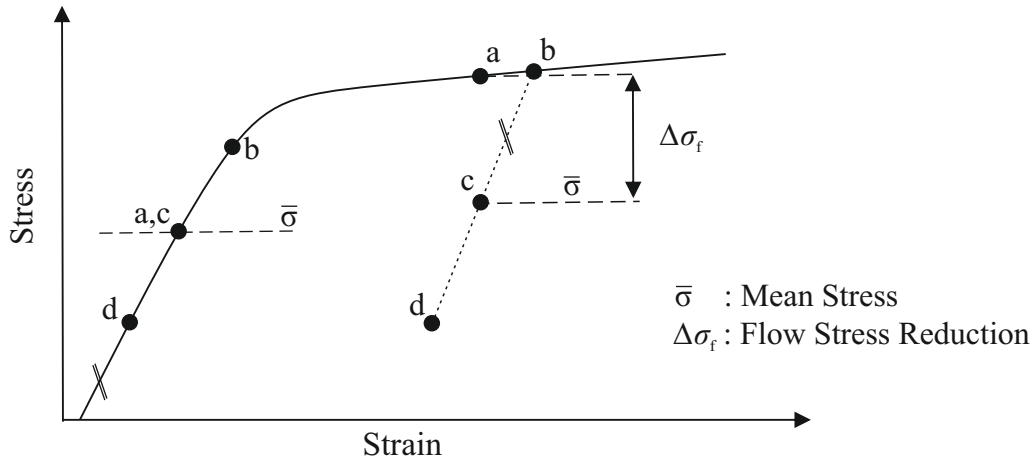

Figure 2.6: Schematic illustration of the stress superposition in the elastic (left) and plastic (right) range of the stress-strain curve.

In equation 2.1, E is the modulus of elasticity, $\hat{\epsilon}$ the strain amplitude, $\dot{\epsilon}_0$ the constant strain rate of the testing machine during the measurement of the strain-stress curve, and f is the oscillation frequency. When neglecting the term $\frac{\dot{\epsilon}_0}{4\,f}$ for small $\dot{\epsilon}_0$ and comparatively high frequency f, the equation equals the mean stress reduction $\Delta\sigma_\mathrm{f}$ in figure 2.6. Kirchner et al. investigated a low frequency (0.5 Hz to 1 Hz), medium frequency (10 Hz to 50 Hz), and ultrasonic frequency (20 kHz) excitation force during static compression tests with aluminium alloys to validate equation 2.1 (and an extended equation for strain hardening materials). The analytical model was well validated for low frequency experimental tests and therefore it was concluded that the mechanism of mean flow stress reduction would be similar for ultrasonic frequencies. Although, this was not verified by experimental measurements, because of the inability to measure the oscillatory response at the higher frequencies.

2.2.3.2 Ultrasonic friction reduction

The effect of ultrasonic friction reduction describes an apparent reduction of the quasi-static friction force that can occur when an additional oscillation is applied to a system with friction, [98, 70, 64, 122, 116, 105, 139, 82]. In fact, the friction in the system is not really reduced, but an outwardly apparent reduction of the frictional force is achieved. Friction reduction by means of ultrasonic superimposition thus differs from methods such as lubricating the friction contact to reduce friction. Although friction reduction does not directly influence material behaviour, frictional contacts play a role in many forming processes such as deep drawing and wire drawing. A reduction of the frictional force makes it easier for the material to flow into the forming tool, so that the quasi-static forming forces are reduced. In ultrasonic wire bonding, there is frictional contact between the bonding tool and the wire with sliding friction during the bonding process, as the wire material flows into the v-groove of the bonding tool.

There are in general three ways to superimpose a harmonic vibration $\hat{v}\,\cos(\omega\,t)$ on a body moving at a constant speed $v_\mathrm{B,c}$: perpendicular and parallel to the sliding direction and also in direction of the applied normal force (z-direction). The mechanisms of superimposed ultrasonic vibration perpendicular (y-direction) and parallel (x-direction) to the sliding direction - which are most relevant for the ultrasonic wire bonding process

- are shown in figure 2.7. When an oscillation parallel or perpendicular to the sliding direction of the moving body is applied, the direction and amplitude of the tangential force $\widetilde{F}_{\mathrm{T,x}}$ is time-dependent due to the superimposed oscillation.

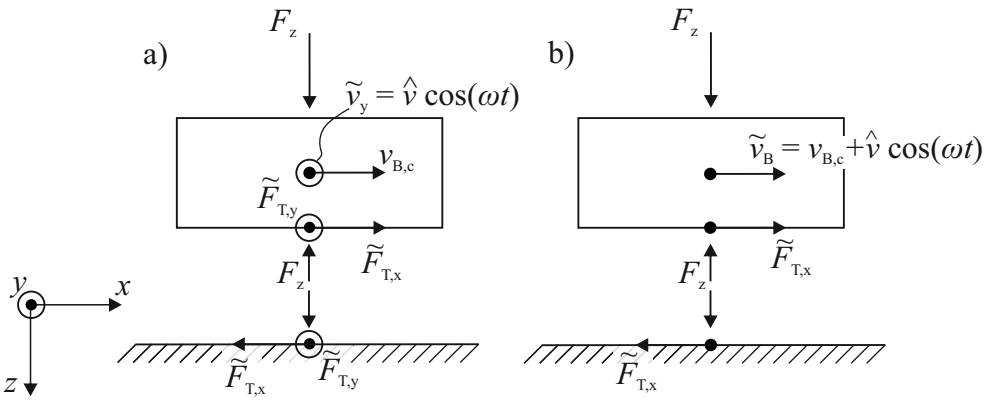

Figure 2.7: The two directions of vibration superimposition: a) perpendicular and b) parallel to the constant velocity $v_{\mathrm{B,c}}$ of the sliding body.

Littmann et al. [70] and Storck et al. [124] calculated the reduction of the coefficient of friction for perpendicular and parallel oscillation superimposition using analytical models. They defined the velocity ratio ξ between the superimposed vibration amplitude $\hat{v}$ and the constant sliding velocity $v_{\mathrm{B,c}}$ of the body in x-direction and the reduced coefficient of friction $\mu_{\parallel}$ and $\mu_{\perp}$ for parallel and perpendicular oscillation superimposition:

$$\begin{aligned} \xi &= \frac{v_{\mathrm{B,c}}}{\hat{v}} \\ \mu_{\parallel,\perp} &= \frac{\bar{F}_{\mathrm{T,x}}}{F_{\mathrm{T,x,static}}}. \end{aligned} \tag{2.2}$$

In equation 2.2, $F_{\mathrm{T,x,static}} = \mu_{\mathrm{static}}\, F_{\mathrm{z}}$ is the static friction force with the static friction coefficient μ_{static} and $\overline{F}_{\mathrm{T,x}}$ is the time-averaged friction force calculated by integrating $\widetilde{F}_{\mathrm{T,x}}$ over one period length:

$$\bar{F}_{\mathrm{T,x}} = \frac{1}{T}\int_0^T \widetilde{F}_{\mathrm{T,x}}(t)dt = \frac{1}{2\pi}\int_0^{2\pi} \widetilde{F}_{\mathrm{T,x}}(\tau)d\tau. \tag{2.3}$$

Taking the Coulomb's law of friction and harmonic excitation for the solution of equation 2.3, the friction reduction for parallel oscillation superimposition can be calculated by the following equation:

$$\mu_{\parallel} = \begin{cases} 1 & \forall\, \xi \geq 1 \\ \frac{2}{\pi}\arcsin(\xi) & \forall\, \xi \in [0,1) \end{cases} \tag{2.4}$$

From equation 2.4, it follows that for $\xi \geq 1$ no friction reduction occurs: this is only the case for $\xi \in [0,1)$ where the sliding direction is reversed and by this also the direction of $\widetilde{F}_{\mathrm{T,x}}$, thus the time average value of $\bar{F}_{\mathrm{T,x}}$ is reduced.

For the perpendicular vibration superimposition, a closed solution cannot be determined

directly; the result for $\mu_\perp$ is the elliptical integral:

$$\begin{aligned} \mu_\perp &= \frac{2}{\pi}\xi k \int_0^{\frac{\pi}{2}} \frac{1}{\sqrt{1-k^2 \cdot sin^2(\tau)}} d\tau \\ k &= \frac{1}{\sqrt{\xi^2+1}}, \end{aligned} \tag{2.5}$$

which needs to be solved numerically, e.g. with *MATLAB* and its build in function *ellipticF*, [127]. In equation 2.5, there is no case distinction depending on ξ; this is, because the perpendicular oscillation immediately changes the direction of the tangential friction force even for low values of $\hat{v}$, thus the absolute value of $\widetilde{F}_{\mathrm{T,x}}$ is reduced in time-average even for $\xi \geq 1$.

The results from equation 2.4 and equation 2.5 are shown in figure 2.8. For the perpendicular superimposition, for $\xi = 1$, already a friction reduction to $\mu_\perp = 0.83$ occurs.

For ultrasonic wire bonding, especially the superposition of a vibration perpendicular to the sliding direction is relevant, as the bonding tool is sinking in the vertical direction during bonding and at the same time an ultrasonic vibration is superimposed in the axial direction of the wire - perpendicular to the sliding direction of the bonding tool.

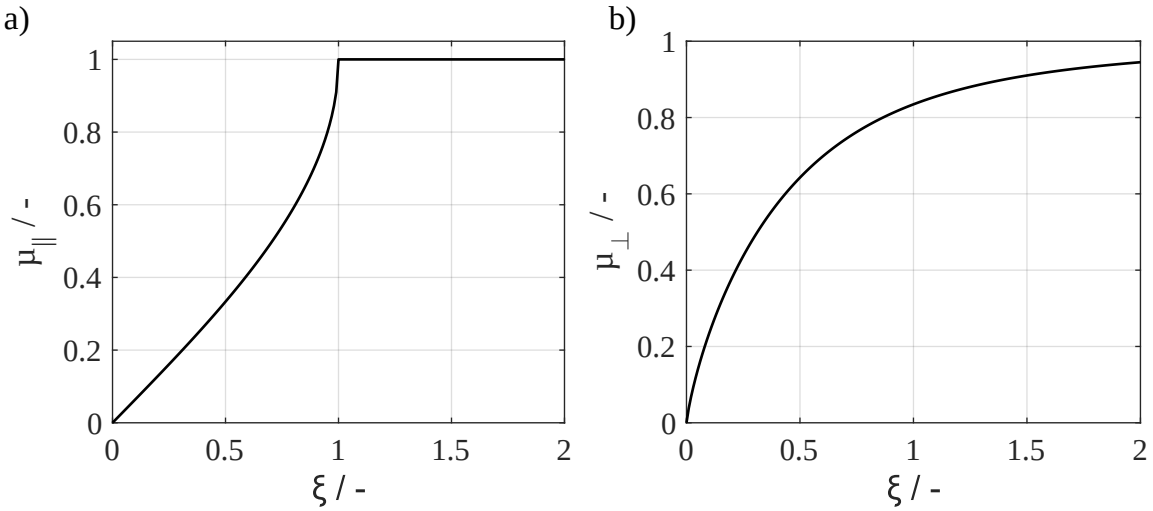

Figure 2.8: Reduction of the coefficient of friction for a) parallel and b) perpendicular vibration superimposition.

2.2.3.3 Acoustic softening: metallurgical effects

Although friction reduction and stress superposition can explain a significant part of the overall stress reduction, it is also necessary to consider the effects at the microstructure level under ultrasonic excitation - the so called acoustic softening - for a complete description of the ultrasonic softening effect, [25, 119, 118, 27, 51, 69].

All real crystals like copper and aluminium contain deviations from the ideal crystal structure, called *defects*. There are three major types of crystallographic defects [78]: point defect around a single lattice point involving only a few atoms, line defects that

extend along a row of many atoms, and planar defects that cover a whole plane of atoms. The most important line defects in crystals are *dislocations*, and it is up to now universally accepted that plastic deformation at room temperature in crystals result from the movement of dislocations [55]. The movement of dislocation occurs on certain crystal planes in direction of the close-packed planes. In figure 2.9 the movement of an edge dislocation along the slip plane is shown; in order to move, each atom needs to move the atomic distance and as long as the stress is maintained, the dislocation can move to the next position and so on; When the dislocation reaches the crystal boundary, slip will have occurred on the entire slip plane [78]. The movement of dislocations is hindered at the grain boundaries, so that with increasing plastic deformation a hardening of the material is typically observed. When dislocations gather at the grain boundaries, dense dislocation walls (DDWs) develop; these DDWs can transform into sub-boundaries separating individual subgrains leading to grain refinement [11].

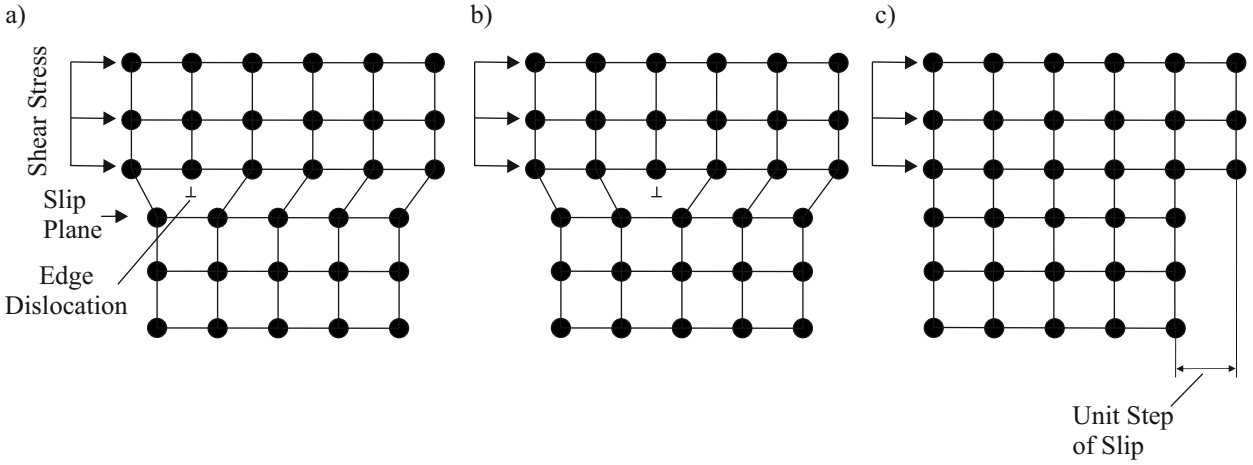

Figure 2.9: Dislocation motion along the slip plane under a shear stress load according to [78].

In summary, the plastic deformation of metals is largely influenced by lattice imperfections such as the density of the dislocations. Consequently, these properties are influenced by ultrasonic excitation, since the ultrasonic softening effect influences the plastic deformation behaviour. Several scientists have verified that ultrasound has a significant influence on the microstructure. Langenecker [67], who used tensile tests of high purity aluminium single crystals to investigate the ultrasonic softening effect, proposed that the ultrasonic vibration can increase the dislocation density and increase the mobility of dislocation. He also observed that, compared to heated samples, much less acoustic energy is needed to achieve a certain degree of softening compared to thermal energy and assumed, that acoustic energy is absorbed at dislocations and grain boundaries only, which makes it more efficient. Application of ultrasound caused residual hardening of the aluminium specimen, while heat caused permanent softening. Liu et al. [74] found in ultrasonic-assisted upsetting process using copper rods, that the ultrasonic vibration enhanced grain refinement from an initial grain size of approx. 50 µm to a range from 100 nm to 300 nm, which is significantly less compared to conventional deformed specimen without ultrasound. Zhou et al. [149] reported that the ultrasonic vibration not only refined the grains but also changed the grain orientation in ultrasonic assisted compression tests with aluminium an titanium samples. Siu et al. [119] compared the microstructures of samples deformed by vertical indentation with and without ultrasonic

excitation. They found that enhanced subgrain formation occurred due to the application of ultrasound; also, by comparing samples deformed while being heated, the enhanced subgrain formation by the ultrasound is proved to be larger than that due to the heat.

2.3 Equipment and methods of process development in heavy wire bonding

In figure 2.10 a) a typical modern fully automated heavy wire bonding machine and the bond head are shown. The bond head has four degrees of freedom and applies the normal force and ultrasonic excitation to the wire, guides the wire to the v-groove of the bond tool, cuts the wire, and forms the loop. The ultrasonic excitation frequency of the bond head is fixed to the resonance frequency of the transducer and the manufacturer typically provides different types of bond heads to adapt the frequency by changing the bond head. During the bond formation process, sensor data (typically u_T, i_T, f_T, and z_{WD}) are measured and stored for each bond. The gained sensor data can be used for online quality control as described in [42] or for offline interpretation by process operators.

With the bonding machine, two types of bond forms shown in figure 2.10 b) can be produced. The first form is the bond loop which is formed by bonding the first bond (source bond), forming the bond loop by travelling of the bond head along a specific trajectory and bonding the second bond (destination bond); after bonding the destination bond, the wire is cut off. The bond loop form is used in all packaging applications to produce an electrical interconnection between two positions. When producing the single bond, only one bond connection is produced and directly cut off without forming a loop. The single bond form is used to investigate specifically the bond formation process without the impact of loop forming process on the bond quality; additionally, less space on the substrate is required for a specific amount of wire bonds; in this PhD, the single bond form is used in all wire bond experiments.

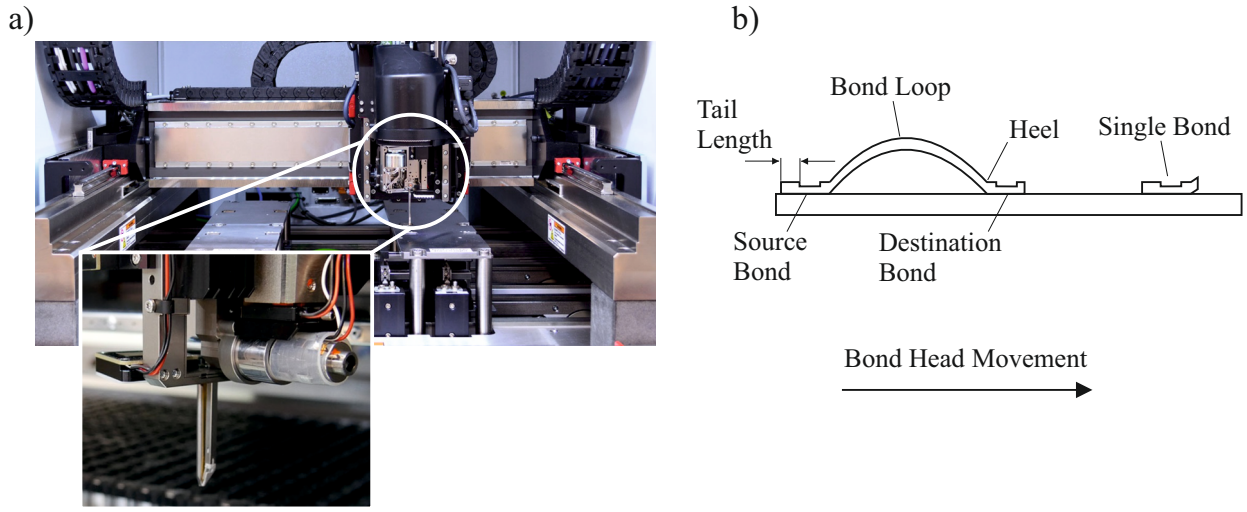

Figure 2.10: a) Operation area of a bonding machine (Hesse Mechatronics Bondjet BJ985) with a detail view on the bond head [49] and b) the two wire bond forms of a bond loop and a single bond.

The most discussed machine settings are the bonding parameters, namely the normal

forces F_{TD}, F_{BN}, the ultrasonic driving voltage u_T or current i_{T}, and the durations t_{B} and t_{I}, but besides these parameters numerous settings that have an impact on the behaviour of the bonding machine and affect the bond quality can be made at the bonding machine; a selection of these settings are:

- The vertical velocity of the bonding head approaching the bond position is crucial to prevent overshooting of the touch down force [132, 100] and a proper value for the trailing of the bond head after detection of touch down contact is important to achieve high accuracy of the applied touch down force.
- The cutting depth into the wire determines the remaining wire cross section for wire break off. Too high cutting depth leads to inconsistent wire feed underneath the tool; too less cutting depth can damage the destination bond.
- The tail length shown in figure 2.10 b) mainly affects the source bond; if the tail is too short and the bonding tool bends under loading condition, the wire can slip underneath the bonding tool.
- The loop forming parameters have to be determined empirically by setting up the coordinates of the loop trajectory of the bonding head leading to the desired loop form. The bending load during loop forming can affect the bond strength of the source bond, especially in the heel area.

In conventional process development of wire bonding, the key stages generally include initial process design, experimental process characterization, as well as process optimization shown in figure 1.3.

In the *process design* step, the first task is to define the goals for the process development; therefore, the materials of the metallisation and the wire, the wire diameter, bond-loop geometry, ultrasonic frequency, definition of limits for the minimum shear force/strength must be specified. In addition to electrical conductivity and mechanical strength, thermal conductivity also plays a role in the selection of the wire material in order to reduce the thermal mismatch of the entire structure, [66, 56]. The equipment for carrying out the bonding tests and the subsequent testing of the wire bonds must be determined during process design step. This includes the choice of bonding machine, bonding tool and shear/pull tester and additional equipment for reliability analysis such as active power cycling and thermal cycling [110] and dynamic mechanical vibration loading [21]. The related information to select suitable equipment and choose sufficient materials must be obtained from laboratory studies, published literature, as well as from experiences of the process development engineers [66] and can be summarized using case-effect diagrams as shown in figure 2.2.

During *experimental process characterization*, methods of *Design of Experiment* (DoE) are used to characterise the newly developed wire bond process to determine the process window. For ultrasonic heavy wire bonding, typically the bond duration, ultrasonic power and bond normal force are varied; if required, additional parameters such like the ramp duration and touch down force must also be investigated. For each parameter combination, a suitable number of wire bonds must be produced (typically 30 bonds for each parameter combination for destructive shear and pull tests) and then evaluated using main effects and interaction diagrams to interpret the results. During wire bonding tests, additionally measurements directly at the bonding machine are stored for further analysis. Parameters like the tail length, the velocity of the bond head approaching the bond position and cutting depth are usually not varied during the DoE and are determined based on experience of the process engineers prior to the tests. However, to

ensure that these influencing variables do not affect the results, they must be continuously monitored during the tests and adjusted if necessary.

In the *process optimization* step, the results from the experimental process characterization are analysed to determine optimal process parameters in terms of high bond strength, low variance, short process time, and additional goals like the process capability index C_{PK} which evaluates the bond process by including standard deviation, mean value and lower/upper limits for e.g. the measured shear force values; limits for those quality criteria must be defined by the process engineers or can be found in guide lines like the technical bulletin *DVS 2811* [30]. If the objectives of the design step process are not achieved, the loop must be repeated at the first step and appropriate actions taken.

For the experimental process characterization, the method for determination of the bond quality is one of the most important tasks. The term "bond quality" is linked to the reliability and mechanical strength of the bond connection. The reliability can be tested by cyclic loading of the bond connections either by temperature cycling or vibrational loading. The test methods for temperature cycling are *active power cycling* (APC) and *thermal cycling* (TC). In APC a current profile is applied to the electrical circuit including the wire bond connections which leads to temperature changes in the bond connection [37] and in TC the wire bonds are exposed to an alternating temperature profile within environmental chambers [9]. For vibrational loading, Czerny et al. [22] recently presented a method called *BAMFIT* which induces mechanical cyclic shear stresses in order to initiate fatigue fracture until lift-off failure at the bond interface. As high vibration frequencies in the ultrasonic range are used, the test duration is highly accelerated compared to TC and APC.

The mechanical strength can be determined by pull or shear tests. In the pull test, a hook shaped tool is positioned underneath the bond loop and pulls the loop in vertical direction until either the bond connection or the bond loop itself breaks. In the shear test, a sharp-edged chisel moves horizontal against the bond perpendicular to the direction of the wire axis until the bond connection breaks [30]. In this PhD, shear tests are used to determine the correlation between bond process parameters and bond quality in terms of mechanical strength of the bond connection because single bond connections without a bond loop are investigated; thus, no pull tests can be performed for single bonds.

The shear test procedure is shown in figure 2.11: the shear testing machine continuously moves a chisel in horizontal direction against the bond contact at a defined height – the shear height - which should be 10 µm to maximum 10 % of the wire diameter and with a set speed in the range of 100 µm/s to 500 µm/s, [30]. The reaction force F_{S} is measured until failure of the bond connection is detected by decreasing reaction force; the maximum force after failure of the joint is the shear force value for further evaluation. As recommended in the technical bulletin *DVS 2811* [30], the shear force should be converted to the shear strength σ_{S}; therefore the deformation width B and length L of the bonded wire before shear test or the area of the sheared surface must be measured using optical microscopy to determine the area A_{S} and calculate the shear strength:

$$\tau_{\mathrm{S}} = \frac{F_{\mathrm{S}}}{W\ L} = \frac{F_{\mathrm{S}}}{A_{\mathrm{S}}} \tag{2.6}$$

Besides the shear force value and shear strength, the failure mode of the shear test has to be taken into account; it provides information on the location of the defect and its appearance. The four *shear codes* are determined by the criteria of the residue of original

bond remaining on the substrate (shear nugget) [10, 41, 57, 30]; exemplary shear codes are shown at the bottom of figure 2.11. The division into the four shear codes is made as followed [30]:

- Shear code 1: the shear nugget covers less than 25 % of the interface area.
- Shear code 2: the shear nugget covers 25-50 % of the interface area.
- Shear code 3: the shear nugget covers 50-75 % of the interface area.
- Shear code 4: the shear nugget covers more than 75 % of the interface area.

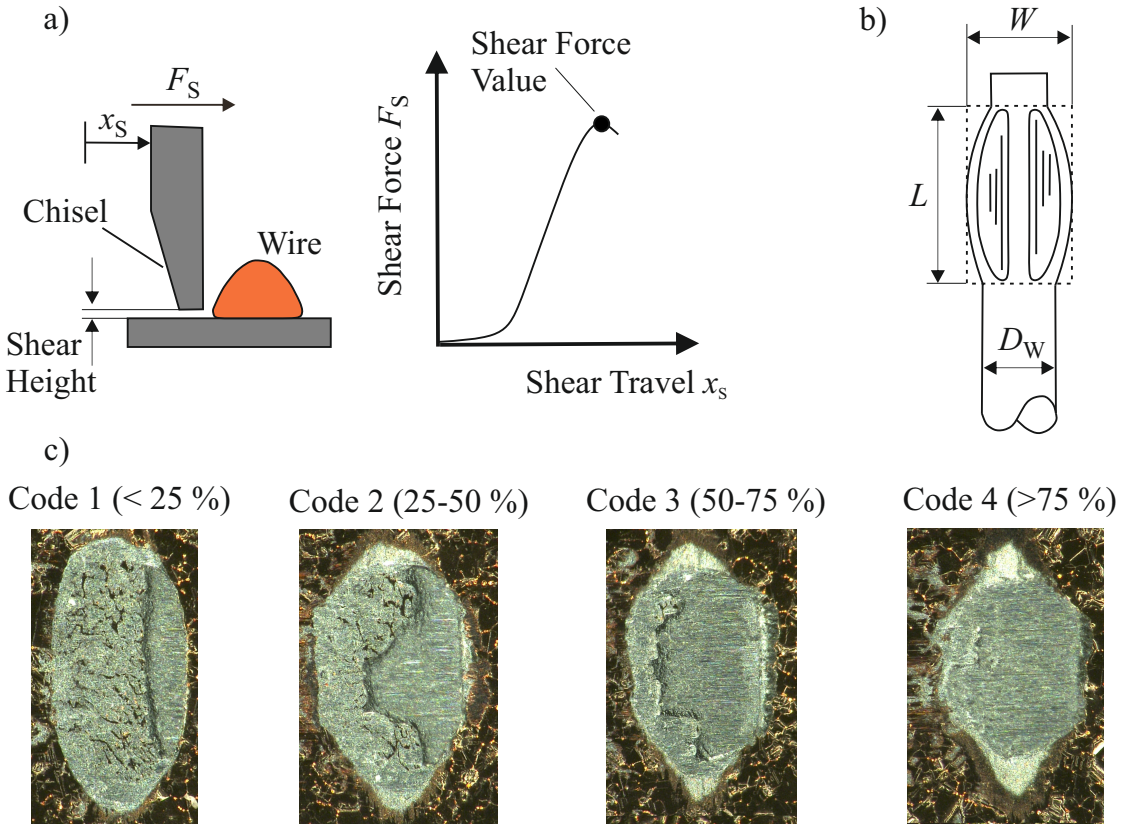

Figure 2.11: Shear test procedure: a) chisel shearing the bond connection and measuring the shear force F_S, b) measurement of the wire deformation (width W and length L of the bond) and c) the four shear codes according to DVS-2811 guide lines [30].

While for fine wire bonding recommendations for quality criteria are given in [26, 10, 30] no general standards for qualification of heavy wire bonds exist. To overcome this issue, industry standards of companies producing heavy wire bond connections have been developed in the past based on the standards for fine wire bonding, [48]. The criteria of these norms are summarized as follows:

- The ratio of the width W to the wire diameter D_W should not exceed the value 1.6.
- At least 50 % of the interface area should be residual wire bond material (shear code 3 or 4).
- The shear force value should be as high as possible and the process variation as low as possible.
- No tool/substrate contacts should occur.

2.4 Modelling and simulation of the wire bond process

2.4.1 Modelling the bond formation

Ultrasonic wire bonding is mainly driven by friction and deformation. Thus, several researchers [108, 4, 86, 131, 38] modelled the bond formation, by taking these processes into account. Different approaches were published to model the effects of cleaning, deformation and bond formation based on modified friction models.

Mayer and Schwizer modelled the Au ball bond process (25 µm) in [85] based on a friction model approach:

$$\begin{aligned} F_{\mathrm{T}}(t) &= [1-\gamma(t)]\ \mu\ F_{\mathrm{BN}} + \gamma(t)\ \tau_{\mathrm{S}}\ S \\ \frac{d\gamma}{dt} &= \frac{\beta\ P_{\mathrm{f}}(t)\ [1-\gamma]}{S}. \end{aligned} \tag{2.7}$$

In equation 2.7 F_{T} is the maximum tangential force, γ is the ratio of welded areas and the whole interface area S, μ is the coefficient of friction, F_{BN} is the bond normal force, and τ_{S} is the shear strength of the material. The tangential force F_{T} in this model is the sum of the friction force and shear strength of bonded areas in the interface. The coefficient γ is a measure of bond quality in this model and can be calculated by the given differential equation in equation 2.7, where P_{f} is the frictional power in the interface between wire and substrate and β is a material constant for bond growth. It is assumed, that the interface area remains constant over bond duration and the initial size is calculated from geometrical data of the free air ball.

Gaul [33] modelled the wedge/wedge bond process with AlSi1 wire (25 µm) similar to Mayer and Schwizer:

$$\begin{aligned} F_{\mathrm{T}}(t) &= ([1-\gamma(t)]\ \mu_{\mathrm{ox}} + \gamma(t)\ \mu_{\mathrm{met}})\ F_{\mathrm{BN}} \\ \gamma &= \frac{\beta}{S(t)} \int_0^t P_{\mathrm{f}}(t)\ [1-\gamma]\ \mathrm{d}t + \gamma_0 \\ \frac{\mathrm{d}\gamma}{\mathrm{d}t} &= -\frac{1}{S}\ \frac{\mathrm{d}S}{\mathrm{d}t}[\gamma-\gamma_0] + \frac{\beta\ P_{\mathrm{f}}(t)\ [1-\gamma]}{S(t)} \end{aligned} \tag{2.8}$$

where μ_{ox} is the friction coefficient between wire and substrate with oxide layers and μ_{met} the friction coefficient in cleaned pure metal/metal contact (instead of the shear strength τ_{S} in equation 2.7). The ratio γ of cleaned areas to the contact area $S(t)$ can have an initial value γ_0; it is assumed, that after touch down broken oxide layers lead to already cleaned surfaces in the interface. The differential equation for the cleaning coefficient is extended with a term taking into account, that γ is reduced, when the interface area $S(t)$ increases because uncleaned areas are added to the interface. Therefore, the time dependent value of $S(t)$ has to be known; when a constant contact area is assumed ($\frac{dS}{dt} = 0$), than γ can be calculated the same way like in equation 2.7.

In both approaches, the coefficient γ describes the amount of pure metal/metal contact, which is assumed to be directly bonded when cleaned; the cleaning process to increase γ is influenced by frictional power P_f and the material coefficient β. The deformation behavior of the wire and its impact on bond formation with rising contact area S is not considered; in equation 2.8 rising contact area S could be considered but is neglected because the behaviour of $S(t)$ during bond formation is typically unknown. Recently,

Gogh et al. [38] modified the model presented by Mayer and Schwitzer in equation 2.7 using the Archard wear model to simulate oxide removal; additionally they integrated an lumped parameter model for the ultrasonic transducer system that allows the analysis and comparison between the transverse force F_T on the bond tool for different electrical input powers.

2.4.2 Modelling the ultrasonic softening effect

In order to calculate the material behaviour under ultrasonic influence, different approaches have been developed in the past. For a uniform representation in the following, the factor k_USS is defined by the following equation

$$k_\mathrm{USS} = \frac{\sigma_\mathrm{USS}}{\sigma_0} \tag{2.9}$$

in which $\sigma_\mathrm{USS} = \sigma_0 - \Delta\sigma_\mathrm{f}$ is the stress reduced by the amount of $\Delta\sigma_\mathrm{f}$ due to ultrasonic softening effect (see figure 2.5) and σ_0 is the static stress without ultrasonic excitation.

Several researchers such as Lin et al. [69] and Verma et al. [135], used an extended version of the Johnson-Cook material model to model the stress-strain curve depending on the ultrasonic excitation.

Chen et al. [20] modelled the ultrasonic welding process of aluminium and copper sheets with finite element method under consideration of the ultrasonic softening effect using the equation

$$\begin{aligned} k_\mathrm{USS} &= e^{n_2 W_\mathrm{s}} \\ W_\mathrm{s} &= \frac{W}{V} \end{aligned} \tag{2.10}$$

in which n_2 is a material specific parameter and W_s is the specific ultrasonic energy W in the specimen with the volume V measured in $\mathrm{J/m^3}$. The material parameters were identified from compression tests under ultrasonic excitation. Good agreement between simulation and measurement of the vertical displacement of the sonotrode were found.

Siddiq and El Sayed [116, 115] proposed an analytical model to predict the flow stress reduction by ultrasonic excitation represented as

$$\begin{aligned} k_\mathrm{USS} &= (1 - d\ I_\mathrm{US})^e \\ I_\mathrm{US} &= \rho\ c\ \hat{v}_\mathrm{US}^2 \end{aligned} \tag{2.11}$$

with $\hat{v}_\mathrm{US}$ being the velocity amplitude of the ultrasonic excitation, I_US the ultrasonic intensity measured in $\mathrm{W/m^2}$ and c being the velocity of sound in the material; d and e are model parameters, which need to be identified from experiments.

Yao et al. [144] derived an exponential equation, which was further used by Zha et al. [147] for simulation of ultrasonic assisted micro-square cup deep drawing and by Wang et al. [137] to model ultrasonic assisted tension test of copper foil:

$$k_{\mathrm{USS}} = 1 - \frac{\beta\, M\, \hat{\tau}}{\sigma_0} \left(\frac{E_{\mathrm{US}}}{\hat{\tau}}\right)^m \qquad (2.12)$$
$$E_{\mathrm{US}} = \rho\, \hat{v}_{\mathrm{US}}^2.$$

In this equation β is a material specific parameter, M is the Taylor factor and $\hat{\tau}$ is a material property named mechanical threshold, which can be considered as the shear strength of a metal at absolute zero (0 K); m is a model parameter. The input of the equation is the specific ultrasonic energy E_{US} measured in J/m^3.

All three approaches use an exponential approach to calculate the softening factor k_{USS}, but with different input variables. Chen et al. and Yao et al. used a specific energy related to the volume of the specimen, while Siddiq et al. used the ultrasonic intensity related to the radiating area of the ultrasound source. While Chen's approach in equation 2.10 only requires one parameter to be identified from measurements, the approach of Siddiq et al. requires two and that of Yao et al. four parameters, so that the identification of the model parameters becomes significantly more complex. All three approaches have in common that the material softening is covered as a function of the applied ultrasound energy (in the form of ultrasound intensity or ultrasound density), which is directly related to the ultrasound amplitude. It can be assumed that the specific ultrasonic energy is a suitable input variable for covering the ultrasonic softening effect approximately independently of the specimen size, since it is reasonable to assume that a larger specimen volume also requires a higher ultrasonic intensity for a certain softening, thus the parameters in equation 2.11 might also depend on the specimen size.

2.4.3 Modelling the heavy wire bonding process

In order to simulate the wire bonding process, modelling the bond formation alone using one single differential equation for the bonding state γ like in equation 2.7 and equation 2.8 is not sufficient to capture all relevant effects. The size of the contact area is highly influenced by the geometry of the v-groove, the material properties of the wire, the touch down and bond normal force, and the ultrasonic softening effect which is affected by the ultrasonic excitation. Additionally, the normal force is not evenly distributed in the interface between wire and substrate. All these effects influence each other, as for example the vibration amplitude has an impact on the ultrasonic softening effect and in combination with the bond normal force impacts the wire deformation; this can lead to early tool/substrate contacts which on the other hand affects the bond formation as a significant amount of the vibration power is transmitted into the substrate and not into the interface between wire and substrate. Thus, the essential relationships between the process parameters, the wire deformation and the bond formation must be captured to perform a simulation based DoE.

Althoff et al. [3] presented a friction based approach for modelling the bond formation using a discretised friction model which was used by Unger et al. [131, 130] and Meyer et al. [86] for simulation of the ultrasonic wire bonding process; the program structure of the simulation model is shown in figure 2.12. The bond formation is modelled using the modelling approach of Gaul et al. described in section 2.4.1 using the discretised friction model, which is capable to simulate the bond formation depending on the contact

pressure distribution in the interface between wire and substrate. The complete model was programmed within *MATLAB*; before the simulation in the pre-processing step, a finite element simulation is carried out to simulate the pressure distribution, depending on the vertical bond tool position z_{WD}. The ultrasonic softening effect is modelled, using a machine learned model [133] which is trained with measured time series of the vertical tool position z_{WD} from the bonding machine for different levels of the ultrasonic voltage u_{T} and bond normal force F_{BN}; the bonding experiments have to be carried out before the simulation is performed. The ultrasonic softening model is capable to predict the vertical position z_{WD} for the input parameters u_{T} and F_{BN} in the range of the training data and has limitation to correctly predict z_{WD} for other input parameters, different wire materials, other bond tool geometries or ultrasonic frequencies which have not been used to produce the training data.

For simulation of the bond formation, the discretised friction model and a simplified single point contact model are used. The discretised friction model is used to update the friction coefficient of the simplified friction model at specific time points of the simulation, to reduce the simulation time. Within these updating time steps, the discretised friction model calculates the bond formation distribution in the contact area, based on the local friction energy.

Unger et al. [131] presented for ultrasonic wire bonding with 500 µm copper wire on DCB substrate simulation results of the process window for the bond parameters u_{T} and F_{BN} and the shear force values F_{S} as the result. Good agreement between the simulated and experimental determined process windows could be observed; also the tool/substrate contacts were simulated with good accuracy.

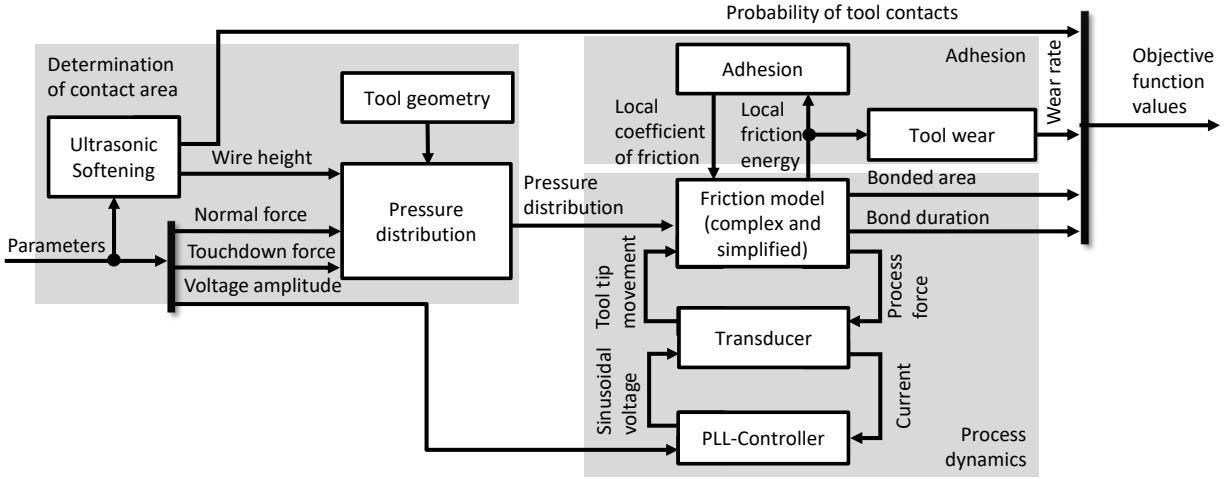

Figure 2.12: Program structure of the wire bond process model presented in [86].

2.5 Knowledge gap in ultrasonic heavy wire bonding

Many process parameters described in section 2.2 are known to have an impact on the wire bond quality measured as shear forces and strength. At the same time, a knowledge gap exists for the impact of the touch down force and the ultrasonic frequency on the bond quality in ultrasonic heavy wire bonding, as most of the reported research results

summarized in section 2.2.1.2 and section 2.2.2 are only valid for thin wire bonding, which often are thermosonic wire bonding processes.

Additionally the ultrasonic softening effect plays an important role in wire bonding, as the wire deformation is mandatory for the bond formation. The material behaviour under ultrasonic excitation has been investigated by several researchers in the past, but experiments with the wire materials and sample sizes used in heavy wire bonding have not been reported yet.

Mayer et al. [85] and Gaul et al. [34] modelled the bond formation for thin wire bonding using a differential equation with the frictional power in the interface as the input. As the contact area between wire and substrate increases significantly during bond formation for heavy wire bonding, this assumption is not valid any more. Althoff et al. [3] and Meyer et al. [86] presented a process model for ultrasonic heavy wire bonding, which considers the ultrasonic softening effect by machine learning. With this model, Unger et al. [131] simulated parameter studies for 500 µm copper wire bonding. With the machine learning model, wire bonding experiments are still mandatory before the simulation of the parameter studies and only parameters within the range of the data basis can be varied in the simulation. For example, when the touch down force has not been varied in the experiments to parametrize the machine learning model, then this parameter can not be investigated in the simulation model as its impact on the wire deformation is not captured.

3 Ultrasonic heavy wire bonding experiments

Many process parameters described in section 2.2 are known to have an impact on the wire bond quality, thus bonding experiments are essential to determine the correlation between the different parameters and the shear forces and strengths. For some process parameters like the touch down force and the ultrasonic frequency also a knowledge gap was identified in section 2.5. Additionally, for modelling the heavy wire bonding process, it is necessary to generate a data base for validation of the simulation results but also to identify model parameters. Therefore, results from ultrasonic bonding tests with 400 µm copper and aluminium wire are presented in this chapter.

In section 3.1, the impact of the touch down force on the bond quality is investigated. In section 3.2, the results from parameter studies varying the main machine parameters - the ultrasonic voltage, bond normal force and the bond duration - are presented and compared to each other. In section 3.3 the impact of the bond frequency on the bond formation and substrate vibrations is investigated, using three different working frequencies. The planning and performance of the parameter studies in section 3.1 section 3.2 was carried out in collaboration with Ranert [102].

3.1 Impact of the touchdown force

In this section, the ratio F_{TD} / F_{BN} between the touchdown force and the bond normal force is varied in the range from 40 % to 100 % for the 400 µm copper and aluminium wire; the wire characteristics are specified in table 3.2. For each wire material, two levels of the ultrasonic voltage and for the lower ultrasonic voltage, three levels of the bond normal forces were investigated, see table 3.1. The ratio F_{TD} / F_{BN} was then varied for the higher ultrasonic voltage for one level of F_{BN} to verify the "low power" results. For each parameter combination, shear force was evaluated 30 times and shear strength three times; the ramp duration was 15 ms and the bond duration 200 ms for all experiments.

In figure 3.1 the main effects plot of shear force and shear strength at different levels of the ratio $F_{\mathrm{TD}}/F_{\mathrm{BN}}$ is shown. The main effects plot shows the mean values of shear force and strength values of the categorical variable (here $F_{\mathrm{TD}}/F_{\mathrm{BN}}$) for all groups (here u_{T} and F_{BN}). For example, to calculate the point at 40 % for the copper wire, all shear force values bonded with $F_{\mathrm{TD}}/F_{\mathrm{BN}}$ equal to 40 %, and 30 V and 20 N, 26 N and 32 N, and 50 V and 32 N are combined into one average value at 40 % [87]. For copper, clearly a main effect of the touch down force on the shear force value and the shear strength occurs. A linear decreasing trend occurs and the ratios $F_{\mathrm{TD}}/F_{\mathrm{BN}}$ equal to 40 % and 60 % are beneficial to increase the shear force and the shear strength as these values lay above the dashed line of the overall mean value. For the aluminium wire, the shear force values remain almost constant in the range between 1815 cN to 1875 cN for the four different

Table 3.1: Levels of the ultrasonic voltage u_T and bond normal force F_{BN} for investigation of the impact of the touch down force for the copper and aluminium wire; for each parameter combination, the ratio F_{TD} / F_{BN} is varied in the range from 40 % to 100 %

	Copper			**Aluminum**		
u_T / V	30			20		
F_{BN}/ N	20	26	32	9	15	21
u_T / V	50			40		
F_{BN}/ N	32			15		

ratio levels; the shear strength shows a decreasing trend, which is not as significant as for copper wire.

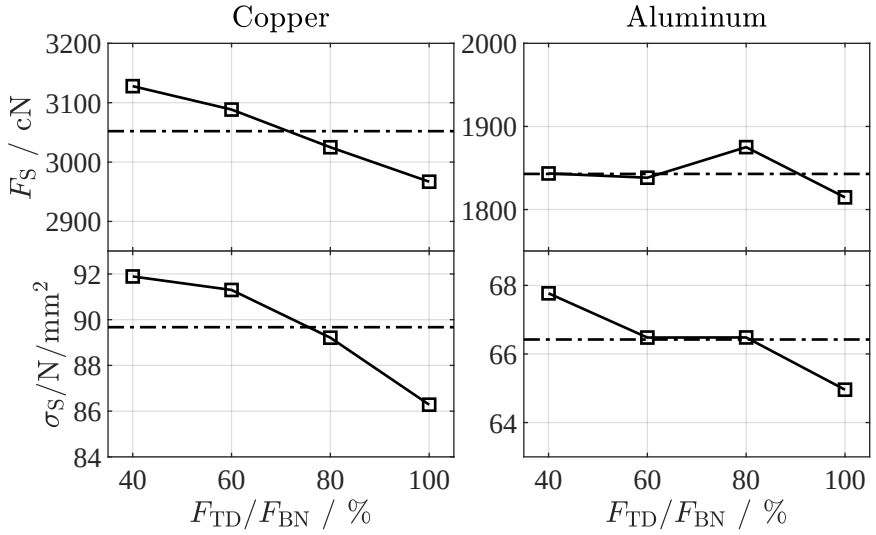

Figure 3.1: Main effects diagrams of shear force and shear strength for copper and aluminium wire for different ratios F_{TD}/F_{BN}.

In figure 3.2 the vertical displacement z_{WD} measured by the bonding machine is shown for the copper wire. For all levels of F_{BN} and u_T, the vertical displacement increases with decreasing touchdown force F_{BN}. The level of the ratio F_{TD} / F_{BN} has an impact on the slope of the curves at the beginning stage of the bond process. The ramp duration t_R was set to 15 ms for all levels of the bond parameters; with lower ratio F_{TD} / F_{BN} the deformation of the wire starts earlier and the slope of the curves is larger within the ramp duration. For the ratio of 40 % the vertical deformation almost linearly increases until the end of the ramp duration; afterwards, the slope decreases and the curve is parallel to the curves for 60 % to 100 %.

Looking at the curves of the vertical displacement z_{WD} for the aluminium wire experiments in figure 3.3, in general, different deformation behaviour compared to the copper wire is observed. Most of the deformation occurs in the first 50 ms and the slope at the beginning, especially during the first 15 ms does not differ that much as for the copper wire experiments for the different ratio levels F_{TD} / F_{BN}, except for the lowest bond normal force level of 9 N. The overall deformation at the end of the bond process is again significantly influenced by the touchdown force: the highest deformation occurs

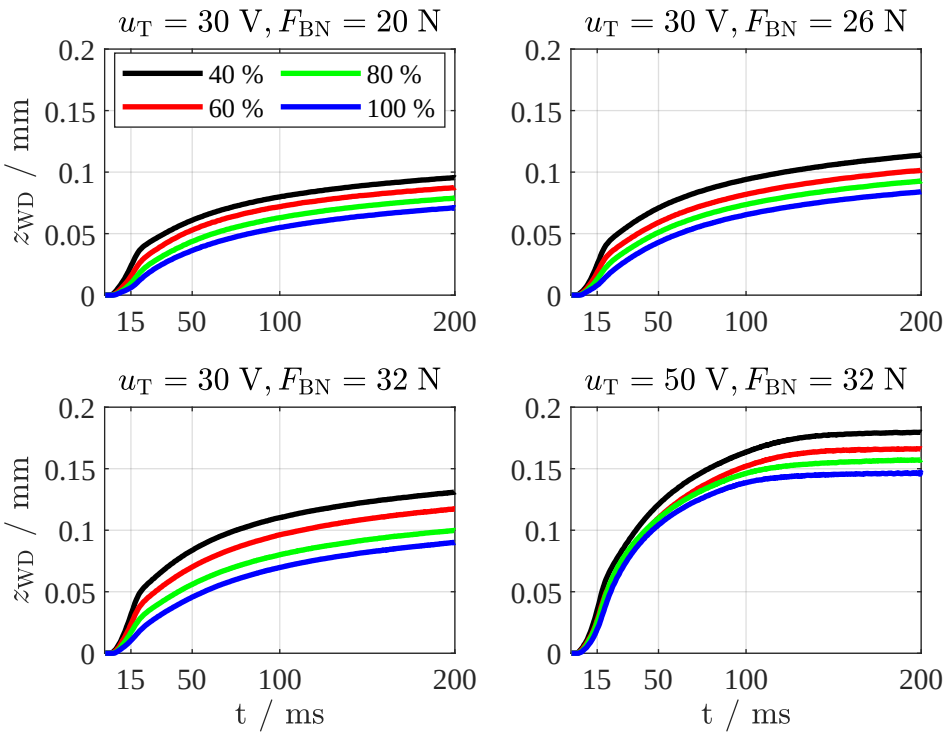

Figure 3.2: Copper wire: vertical displacement z_{WD} measured by the bonding machine for different ratios F_{TD} / F_{BN}.

for the lowest touchdown force for all investigated levels. The impact of the touchdown force on the overall vertical displacement of the bond tool is even higher as for copper, as the curves are more spread for the different ratios of F_{TD} / F_{BN}.

3.1.1 Discussion

The experiments showed that the touchdown force has a significant effect on the shear force and shear strength for copper wire. In the investigated range of F_{TD} / F_{BN} the ratio of 40 % should be chosen to increase the bond strength. For ratios lower than 100 %, the bond normal force is increased within the ramp duration from F_{TD} to F_{BN}, which leads to a quasi-static deformation independently from the ultrasonic softening effect which results into a larger slope of the curve of z_{WD} within the ramp duration. For the ratio of 100 %, this static deformation occurs within the pre-deformation phase before the bond formation starts and thus is not registered by the bonding machine. Therefore, the deformation for lower ratios of F_{TD} / F_{BN} seems to be higher compared to larger ratios. Lower touch down forces than the bond normal force are preferable, because the static deformation of the wire with superimposed ultrasonic excitation during ramping up the normal force enhances the cleaning phase for the copper wire, as the increasing wire deformation at the beginning stage of the bond formation improves the transportation of contaminations to the outside of the interface. Additionally, lower normal forces increase gross sliding in the beginning of the bond process, when the vibration amplitude is relatively low, which results in further enhancement of cleaning and activating the interface area.

For the aluminium wire, no significant impact of the touchdown force on the shear force

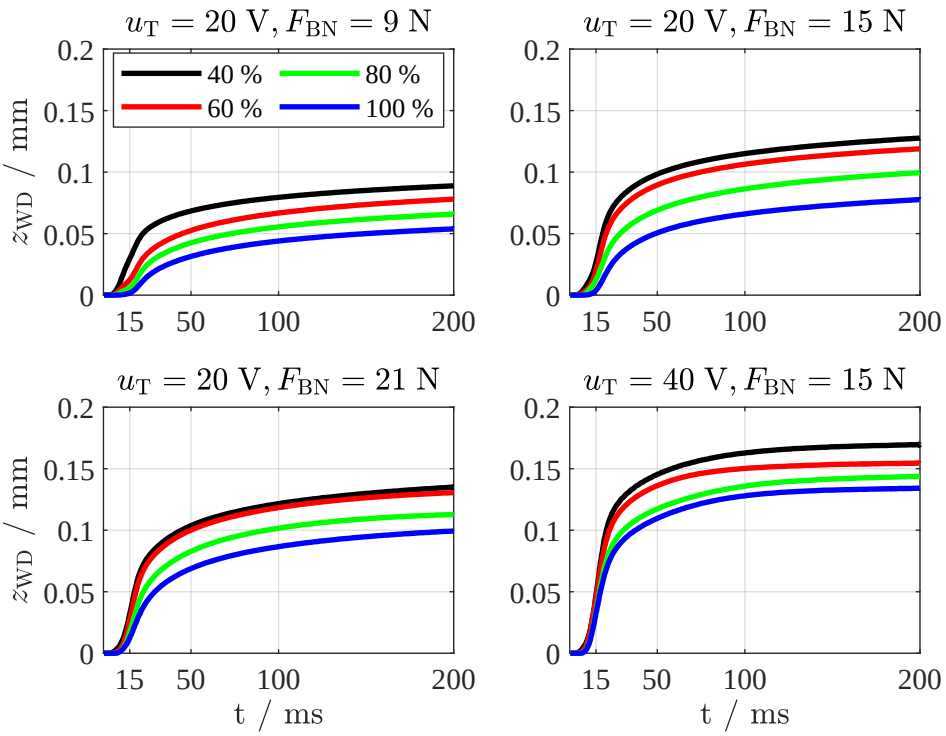

Figure 3.3: Aluminium wire: vertical displacement z_{WD} measured at the bonding machine for different ratios F_{TD} / F_{BN}.

and strength could be observed; nevertheless, the vertical deformation z_{WD} also increases for decreasing ratio of F_{TD} / F_{BN} with the same reason, that the pre-deformation of the wire is not measured by the bonding machine. The main differences between the copper and aluminium wire are the material strength and the brittle oxide layers of the aluminium wire compared to ductile oxide layers of the copper wire. Since the aluminium wire is softer, lower bond normal forces were investigated. Thus micro slip during the cleaning phase cannot be enhanced by lower touch down forces. Additionally, it was reported by Long et al. in [76] that cracking of the oxide layers of the aluminium wire is crucial for the cleaning process, but is not assisted by ultrasonic excitation. Thus, the variation of touchdown force does not affect shear force and strength.

3.2 Design of Experiment

For all wire bonding experiments, a *Hesse Mechatronics* Bondjet BJ939 bonding machine equipped with a standard bonding head for copper ribbon/heavy wire with a bonding frequency of 58 kHz and a bonding tool produced by *Small Precision Tools (SPT)* with the type number OSG7-16-M-3,18-2,733-G were used. For the substrate, DCBs with the dimensions of 55 mm x 39 mm x 0.9 mm were used; the copper layer on the top and bottom side has a thickness of approx. 0.3 mm with an Al_2O_3 ceramic in the middle layer. The DCB was clamped on an EPDM-plate by vacuum underneath the DCBs, see figure 3.4. Two different wire materials produced by *Heraeus* and *Tanaka* - copper and aluminium - were used; the wire characteristic are listed in table 3.2. For shear tests, a *Dage Series 4000* pull and shear tester was used with the shear height set to 15 µm

and the shear velocity set to 300 µm/s according to [30]. To evaluate the sheared area to determine the shear strength σ_S, a digital microscope *Keyence VHX-600* was used.

A simplified trajectory for the bonding parameters shown in figure 3.5 was set at the bonding machine to vary the levels of the touchdown force F_{TD}, bond duration t_B, and ultrasonic voltage u_T; one interval with the ramp duration $t_{R,1}$ and the interval duration $t_{I,1}$ is used. For the used bonding machine, either the ultrasonic voltage or the current can be set; for the experiments the mode for setting the ultrasonic voltage was chosen.

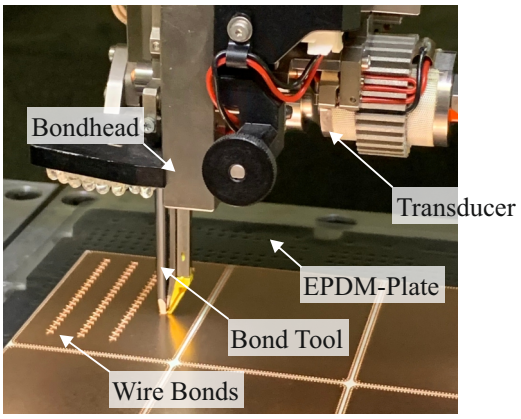

Figure 3.4: Setup of the wire bonding experiments.

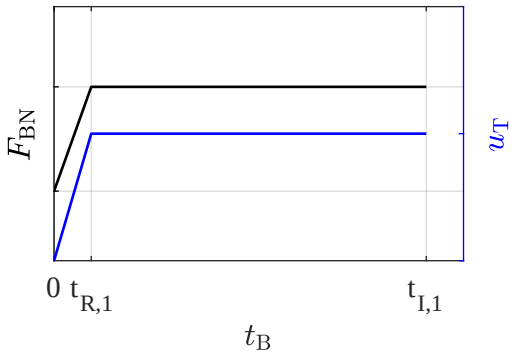

Figure 3.5: Schematic trajectories of the bonding parameters.

Table 3.2: Wire characteristics from the data sheet of the manufacturer.

Material	Manufacturer	Breaking load (cN)	Elongation (%)
Al	Tanaka	550-750	10-30
Cu	Heraeus	2300-3200	> 15

For all experiments in this section, for each investigated parameter combination, 80 destination wire bonds in four rows on one DCB were produced using the *single bond* mode (see figure 2.10) of the bonding machine and 40 bonds were sheared; from three sheared samples the sheared areas were determined to calculate the shear strength σ_S. The remaining 40 bonds were produced as a back up for further evaluations like microscopy pictures of the bonded wire for optical inspection.

Based on pre-screening tests, the limits for the bond normal force F_{BN}, ultrasonic voltage u_T and bond duration t_B were selected such that for the lower limit just no lift offs occur and for the upper limits tool/substrate contacts occur. Additionally, the ramp duration t_R was varied from 5 ms to 45 ms. No significant effect on the shear force was observed and 15 ms was found to be a suitable value for the ramp duration. Based on the results from section 3.1, the ratio F_{TD}/F_{BN} was set to 40 % for copper wire and to 60 % for aluminium wire. The ratio was set to 60 % for the aluminium wire, because the lowest touchdown force F_{TD} was than equal to 6 N, which still can be applied precisely by the used bond head; for even lower touchdown forces, a different bond head type would be needed. The chosen levels for the DoE in table 3.3 lead to 64 combinations for the copper wire and 48 combinations for the aluminium wire.

Table 3.3: Bond parameter levels for the parameter studies for copper and aluminium wire.

	Copper				**Aluminium**			
F_{BN}/ N	20	26	32	38	10	14	18	-
t_B/ ms	70	100	200	300	100	200	300	400
u_T/ V	30	40	50	60	20	25	30	35

3.2.1 Main effects and interaction diagrams

Copper wire

In figure 3.6 the main effects diagram for the copper wire is shown. For the bond normal force F_{BN}, first a small increase from approx. 3500 cN to 3800 cN is observed when increasing F_{BN} from 20 N to 26 N; for bond normal forces greater than 26 N, no significant effect of F_{BN} on the shear force values occurs. For the shear strength, a linear negative trend is observed; values greater than 26 N have a negative effect on the shear strength as they are smaller than the overall mean value.

The investigated levels of the bond duration t_B have a significant positive trend for both, the shear force and the shear strength; for values greater than 100 ms a steady increase of F_S and σ_S occurs and for t_B greater than 200 ms, the shear force and shear strength values are larger than the overall mean values. For 70 ms bond duration and ultrasonic voltage equal to 30 V, 100 % lift off's occurred for all bond normal forces, thus values equal to 0 cN were used for the shear force and strength at 70 ms for 30 V.

The ultrasonic voltage u_T showed to have the highest impact on the shear force and shear strength. For the shear force values, a linear positive trend over the whole range from 30 V to 60 V occurs and values of 50 V and 60 V have a positive effect on the shear force and shear strength, as the response lies above the overall mean level. For the shear strength a linear trend from 30 V to 50 V and a saturation from 50 V to 60 V occurs, but still with the maximum at 60 V.

In figure 3.7 the interactions diagram of the shear force F_S is shown; for t_B equal to 70 ms, 100 % lift off's occurred, thus no data points are plotted for this bond duration. For the different levels of the bond normal force F_{BN} (first row), no interaction can is identified neither for different bond durations nor for different ultrasonic voltages; all lines for the different levels of F_{BN} are grouped together. Independently from the investigated bond normal forces, increasing the bond duration and ultrasonic voltage has a positive effect on the shear force values.

For the bond duration t_B (second row), also no interaction with the other bond parameters is observed as all lines are parallel to each other for both, different bond normal forces and different ultrasonic voltages. Increasing the bond duration from 200 ms to 300 ms leads to a small improvement of the shear force values for both, different bond normal forces and ultrasonic voltages; the biggest step is observed for increasing the bond duration from 100 ms to 200 ms which is in good agreement with the main effects diagram in figure 3.6.

The lines for the different levels of the ultrasonic voltage u_T (third row) are also parallel to each other for both, different bond normal forces F_{BN} and different bond durations t_B and clearly a positive effect of increasing the ultrasonic voltage on the shear force values can

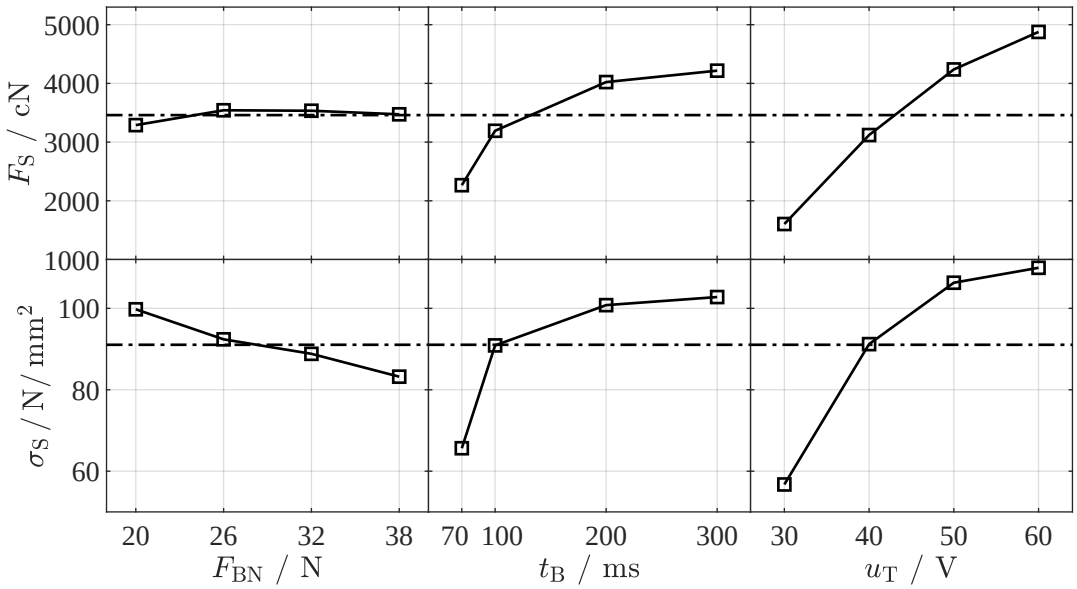

Figure 3.6: Copper wire: main effects diagram for the different levels of F_{BN}, t_B, and u_T for the responses of the shear force F_S and shear strength σ_S. The dashed line shows the overall mean value of F_S and σ_S.

be seen as the lines are shifted to higher levels of shear force values for increasing values of u_T. This means, independently from F_{BN} and t_B, increasing u_T leads to increased shear force values.

In figure 3.8 the interaction plot for the response of the shear strength is shown. The bond normal force (first row) has no significant interaction between the different levels of the bond duration and the ultrasonic voltages. Like for the shear force in figure 3.7, increasing the bond duration and the ultrasonic voltage leads to increased shear strength. In contrast to the results of the shear force values, the lines of different levels of F_{BN} are not grouped together: when decreasing the bond normal force from 38 N to 20 N, the shear strength increases, thus for the lowest bond normal force equal to 20 N, the highest shear strength is reached.

For all levels of t_B (second row), for increasing bond normal force the shear strength linearly decreases and the other way round, for increasing u_T the shear strength increases. Again, no significant interaction occurs, as all curves are parallel to each other.

For the different levels of u_T (third row), a slight interaction occurs, because the curve for u_T equal to 60 V is not fully parallel to the other curves of the lower levels of u_T. For increasing the bond duration, the shear strength is increased from 70 ms to 300 ms, except for u_T equal to 60 V; here, saturation is reached from 200 ms to 300 ms.

Aluminium wire

In figure 3.9 the main effects diagram for the aluminium wire is shown. In contrast to the copper wire, the different levels of the bond normal force F_{BN} have a significant effect on both, the shear force F_S and the shear strength σ_S: the shear force values increase from approx. 1800 cN to 2300 cN when increasing F_{BN} from 10 N to 18 N. The opposite behaviour is observed for the shear strength, as the values linearly decrease with increasing the bond normal force.

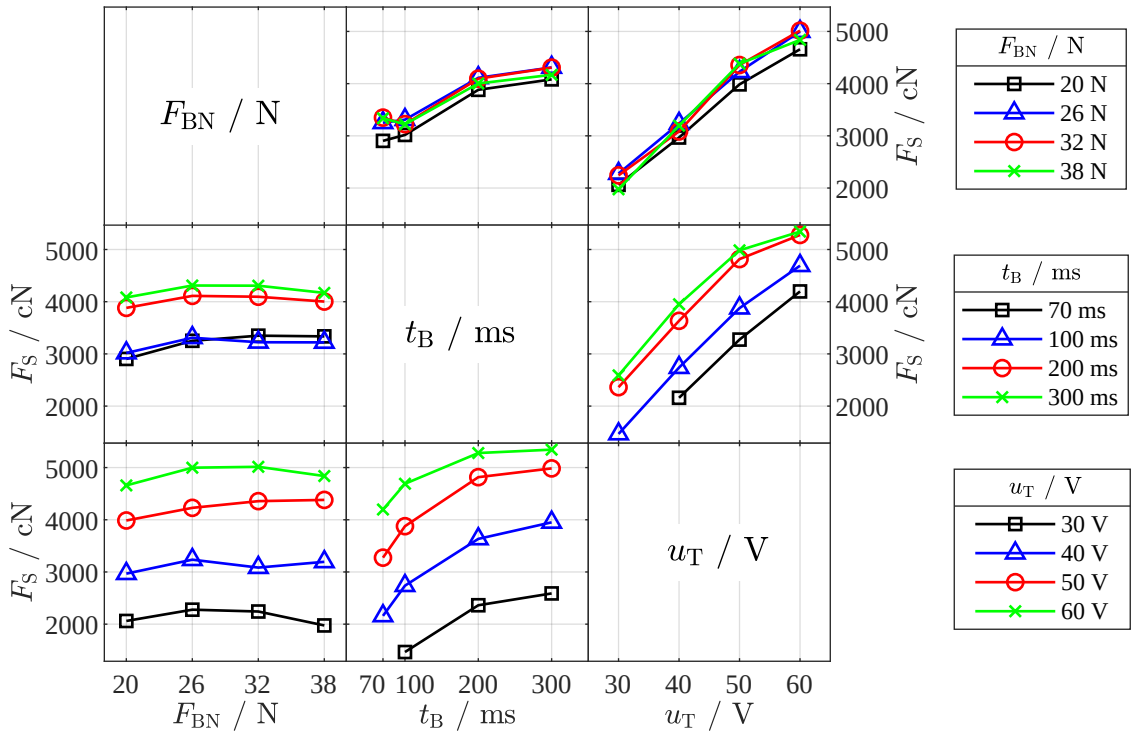

Figure 3.7: Copper wire: interactions diagram for the response of the shear force for the different levels of F_{BN}, t_B, and u_T.

For the bond duration t_B, a positive trend for the shear force is observed, which reaches saturation at 300 ms to 400 ms. The shear strength slightly deceases with increasing bond duration from σ_S equal to 75.4 N/mm^2 to 73.28 N/mm^2.

For the ultrasonic voltage u_T, first F_S increases with increasing ultrasonic voltage, reaches its maximum at 30 V and than decreases for u_T equal to 35 V. In contrast to the copper wire bonding experiments, the ultrasonic voltage has a negative impact on the shear strength: from 25 V to 35 V, σ_S linearly decreases.

In figure 3.10 the interactions diagram of the shear force F_S is shown. For the different levels of the bond normal force F_{BN} (first row), for 10 N to 14 N, the shear force values increase with increasing bond duration and no interaction occurs, but for F_{BN} equal to 18 N, the shear force values decrease from 200 ms to 300 ms. Thus a slight interaction between the different bond durations and the highest bond normal force of 18 N occurs. For different levels of ultrasonic voltage, also an interaction is observed: for the lowest bond normal force of 10 N increasing the ultrasonic voltage steadily increases F_S. For the bond normal force in the range from 14 N to 18 N, a maximum at u_T equal to 30 V occurs and for 35 V, the shear force decreases. For all levels of t_B and u_T, increasing the bond normal force leads to larger shear force values F_S.

For the bond duration t_B (second row), increasing the bond normal force F_{BN} from 10 N to 18 N leads to almost linearly increasing shear force values for 100 ms to 200 ms bond duration. For t_B equal to 300 ms to 400 ms, from 14 N to 18 N no significant difference between the shear force values occur; furthermore, the curves for the levels of 300 ms and 400 ms are almost identical. Increasing the ultrasonic voltage u_T leads to steadily increasing shear force values for 100 ms; for 200 ms to 400 ms, the maximum is reached for u_T equal to 30 V.

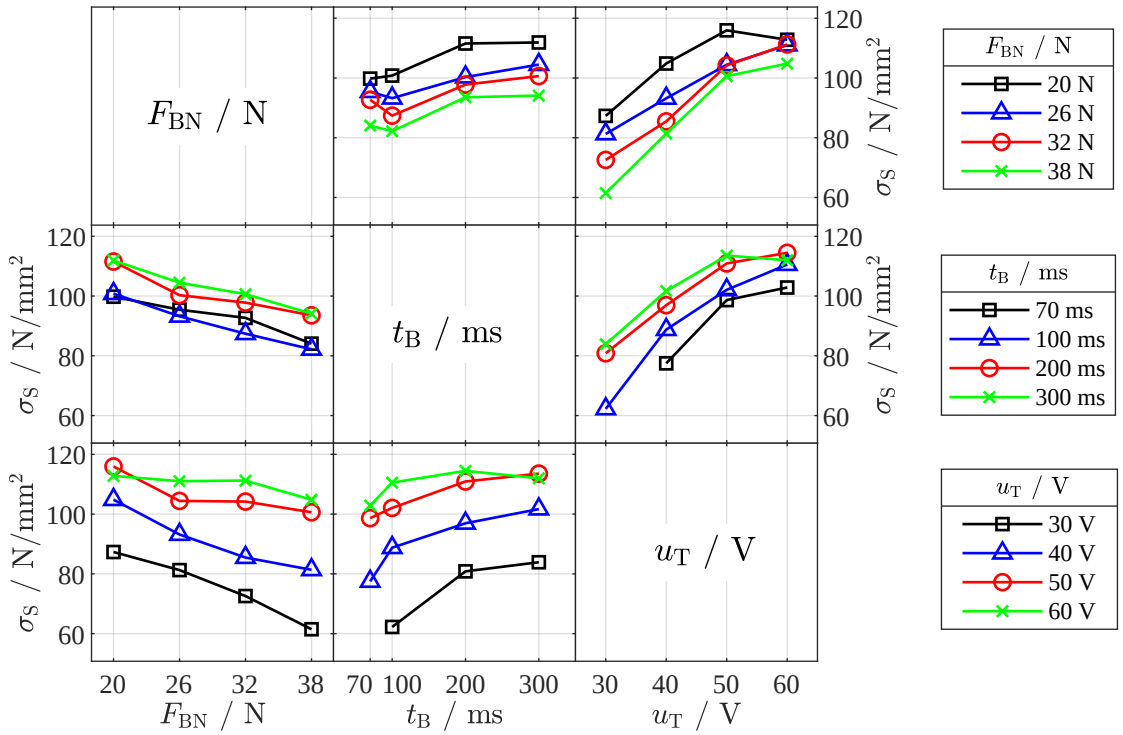

Figure 3.8: Copper wire: interactions diagram for the response of the shear strength for the different levels of F_{BN}, t_B, and u_T.

For the ultrasonic voltage u_T (third row) in the range from 20 V to 30 V the shear force increases when the bond normal force F_{BN} is increased from 10 N to 18 N; for u_T equal to 35 V, saturation is reached at F_{BN} equal to 14 N and the shear force value at 18 N is even lower compared to 25 V and 30 V. The bond duration t_B shows similar behaviour, as the shear force values increase for u_T from 20 V to 30 V, but for u_T equal to 35 V, the shear force value drops from 300 ms to 400 ms.

In figure 3.11 the interaction plot for the response of the shear strength is shown. For the bond normal force (first row) only small interaction is observed to the bond duration and ultrasonic voltage. The curve for F_{BN} equal to 10 N shows a different behaviour compared to the other bond normal forces; first, the shear strength increases until it reaches its maximum at 300 ms. For the larger bond normal forces, the shear strength decreases with increasing bond duration; this is in contrast to the shear force values shown in figure 3.10, which increase with increasing bond duration. With increasing ultrasonic voltage, the shear strength reaches a maximum at u_T equal to 25 V for F_{BN} in the range from 10 N to 14 N and for 18 N, the shear strength approximately linearly decreases. Comparing the results to the curves of the shear force in the first row in figure 3.11, it follows that the curves for the shear strength have an opposite order, meaning that the curves for F_{BN} equal to 10 N reaches the highest values and the curves for F_{BN} equal to 18 N the lowest.

For the levels of t_B (second row) from 200 ms to 400 ms, for increasing the bond normal force the shear strength decreases linearly; for 100 ms, the shear strength first remains constant for F_{BN} equal to 10 N and 14 N and then drops for F_{BN} equal to 18 N. Significant interaction between the bond duration and ultrasonic voltage occurs on the right side of the second row. When increasing the ultrasonic voltage u_T for 100 ms, the shear

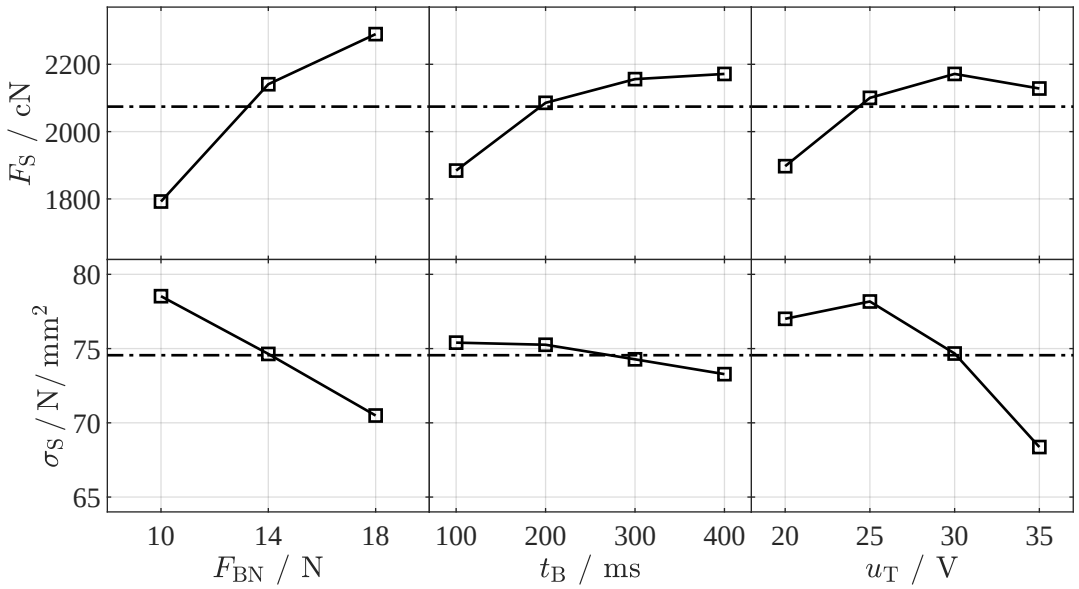

Figure 3.9: Aluminium bonding experiments: main effects diagram for the different levels of F_{BN}, t_B, and u_T for the responses of the shear force values F_S and shear strengths σ_S. The dashed line shows the overall mean value of F_S and σ_S.

strength increases to its maximum at 25 V to 30 V. For t_B equal to 200 ms, the maximum occurs at u_T equal to 25 V and for t_B equal to 300 ms to 400 ms, the maximum lies at u_T equal to 20 V; with rising bond duration, the maximum shear strength is reached with less ultrasonic voltage.

The different levels of u_T (third row) show significant interaction to the bond normal force and bond duration when comparing the curves of the levels for u_T equal to 20 V to 25 V to the others. For increasing the bond normal force, in general the shear strength decreases, but for u_T equal to 20 V, the shear strength decreases less and for u_T equal to 25 V, only from 14 N to 18 N a significant drop occurs. For different bond durations t_B, also a difference between the lower and the higher ultrasonic voltages occurs. For u_T equal to 20 V, the shear strength increases with increasing bond duration and for u_T equal to 25 V, the shear strength almost keeps constant. For u_T from 30 V to 35 V, the shear strength linearly decreases with increasing bond duration.

3.2.1.1 Conclusions from the main effects and interaction diagrams

In the main effect and interaction diagrams for the copper and aluminium wire, different behaviour between the two wire materials is observed. For the copper wire, following conclusions are drawn:

- In the investigated range of F_{BN} from 20 N to 38 N, the bond normal force has no significant impact on the shear force and affects the shear strength negatively; from the investigated parameters, F_{BN} equal to 20 N should be chosen for high shear force and strength.
- Independently from F_{BN} and u_T, increasing the bond duration increases the shear force and strength and from the investigated bond durations, 300 ms should be chosen.

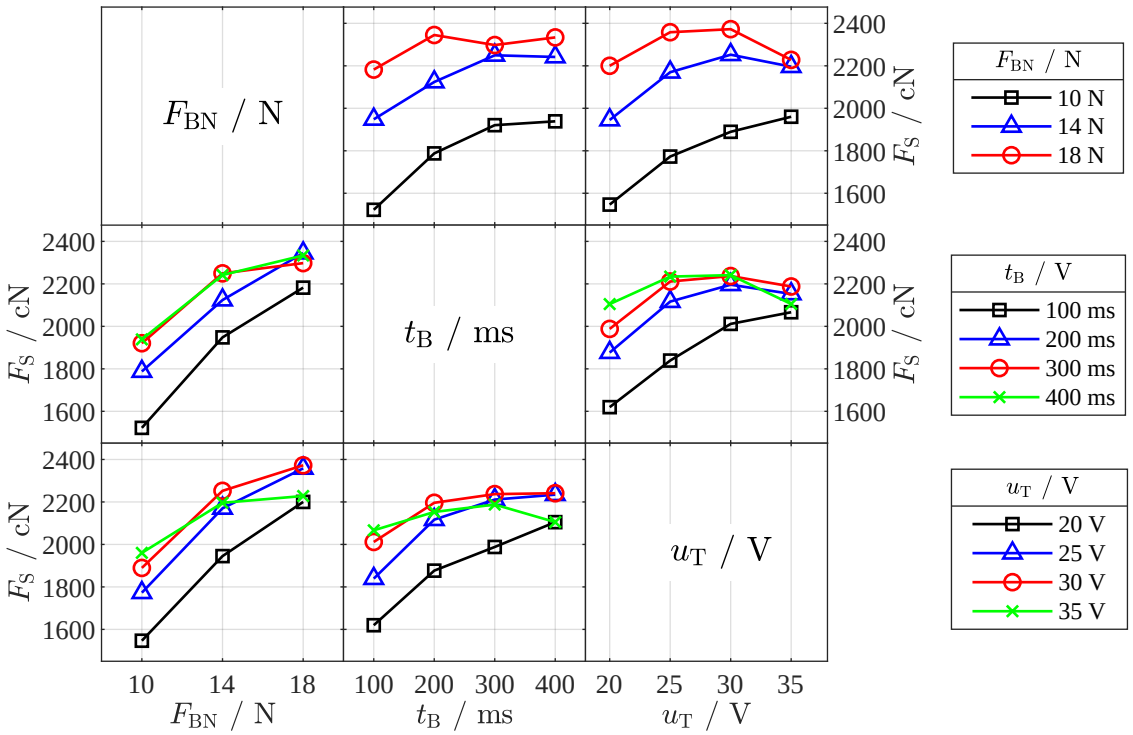

Figure 3.10: Aluminium wire: interactions diagram for the response of the shear force values.

- The ultrasonic voltage u_T has the highest impact on the shear force and strength; independently from the bond duration and bond normal force, increasing u_T increases the shear force and strength. In terms of increasing F_S and σ_S, the ultrasonic voltage should be chosen as high as possible; in this case u_T equal to 60 V results into the highest shear force and shear strength values; but further increasing u_T lead to tool/substrate contacts hindering the bond formation.

For the aluminium wire, following conclusions are drawn:

- In the investigated range of F_{BN} from 10 N to 18 N, the bond normal force has a significant positive effect on the shear force, but affects the shear strength negatively. Also, there is a significant interaction with the ultrasonic voltage, see figure 3.10 and figure 3.11. The smaller F_{BN} is set, the higher u_T needs to be chosen to increase the shear force and shear strength. So the bond normal force should not be chosen independently from the ultrasonic voltage.
- For the ultrasonic voltage u_T, significant interaction with the bond normal force and bond duration occurs. For u_T in the range from 20 V to 30 V, the shear force increases when increasing the bond normal force or the bond duration; only for u_T equal to 35 V the shear force keeps constant when increasing the bond normal force from 14 N to 18 N and even drops when increasing the bond duration from 300 ms to 400 ms. This was also observed in the main effects diagram, where the maximum of the shear force occurred at u_T equal to 30 V. In contrast to the copper wire, the shear strength decreases, when increasing u_T, except when increasing u_T from 20 V to 25 V.
- The bond duration has a positive effect on the shear force in the range between

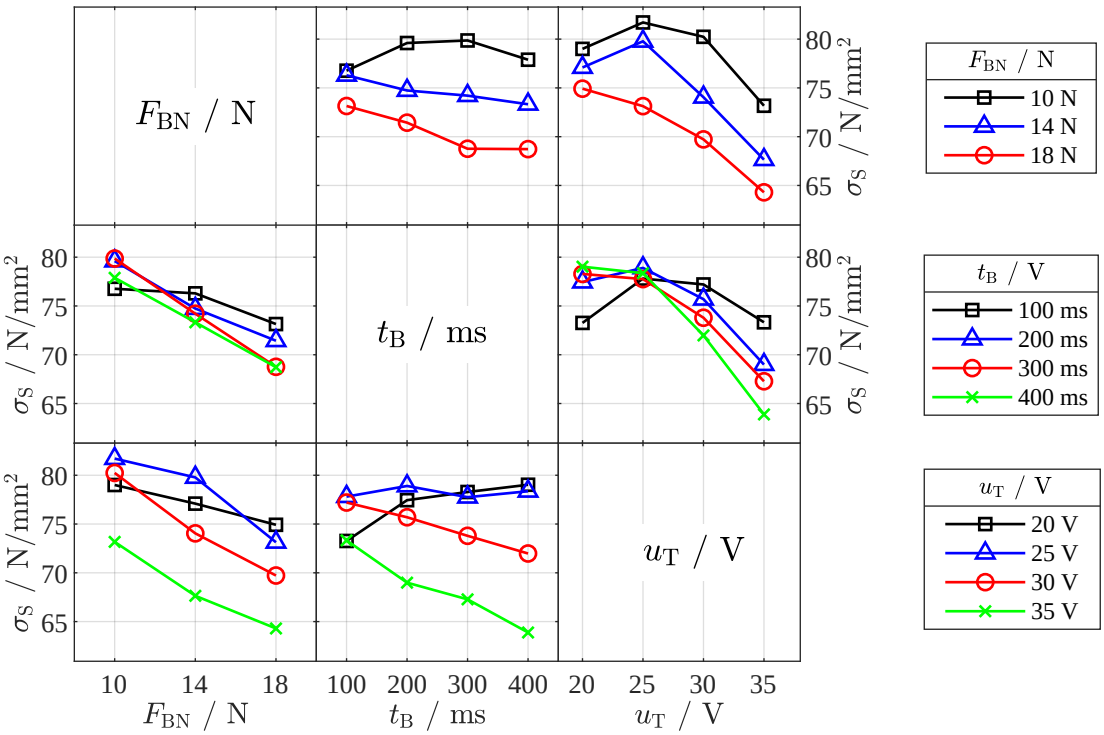

Figure 3.11: Aluminium wire: interactions diagram for the response of the shear strength values.

100 ms to 300 ms and only small improvement can be achieved when further increasing t_B to 400 ms. Since the bond duration has no significant effect on the shear strength, bond durations between 300 ms to 400 ms seem to be suitable to achieve high shear force without affecting the shear strength.

Although the material strength of the two wires is significantly different the preferable bond normal force for the two wire materials do not differ much. For copper, the bond normal force should be chosen equal to 20 N (or even lower), which is comparable to the bond normal force for aluminium wire which should be chosen in the range between 14 N to 18 N. To maximize the shear force and strength the ultrasonic voltage should be increased, which is known to increase the ultrasonic softening effect. For copper the ultrasonic voltage should be twice as high (60 V) as for aluminium (30 V).

Although the limits and levels of the bonding parameters were selected based on preliminary tests and experience, the results show that further tests would be necessary to determine optimal settings. This leads to further experimental effort and iterations from the experiments, evaluation and interpretation of the results. This clearly shows the potential of process development enhanced by simulation which is performed in chapter 6.

3.2.2 Shear codes

In this section, the microscopy images of the sheared surfaces from the copper and aluminium wire bonding experiments are discussed for two different levels of F_{BN} each: for the copper wire, sheared surfaces produced with F_{BN} equal to 20 N and 38 N and for the aluminium wire, produced with F_{BN} equal to 10 N and 18 N respectively are

shown; the shear codes for the remaining bond normal forces are shown in the appendix in section A.1.

Copper wire

For u_T equal to 30 V and t_B equal to 70 ms, 100 % lift off's occurred for all investigated bond normal forces, so no shear codes are shown for this parameter combination. In figure 3.12, the shear codes produced with F_{BN} equal to 20 N are shown. For u_T equal to 30 V and t_B equal to 100 ms, the sheared surface appears to be non homogeneously bonded; Unger et al. described in [131], that the shiny areas in between the stripe-shaped darker spots can be categorized to bonded parts of the sheared surface. With rising bond duration, the contact area and density of bonded areas increases but unbonded parts of the interface remain in the central part of the sheared area and mainly the outer area of the interface is bonded. This also correlates with the results for the shear force and shear strength described in section 3.2.1: with rising bond duration, both values increase. Similar results are found for u_T equal to 40 V; with rising bond duration, the size of the area increases and the interface seems to be more homogeneously bonded compared to 30 V. For u_T equal to 50 V, especially for t_B from 70 ms to 100 ms, the sheared area increases and than remains almost constant from 100 ms to 300 ms. Compared to the lower ultrasonic voltages, the sheared areas are in general larger for the different bond durations. For the highest ultrasonic voltage of 60 V, the most significant change in the appearance of the sheared area is the formation of shear nuggets. For bond duration equal to 200 ms shear code 3 and for bond duration equal to 300 ms shear code 4 is observed while for the lower ultrasonic voltages, only shear code 1 is observed. For bond duration equal to 200 ms, minor contact imprints of the bonding tool on the DCB substrate are observed at approx. 50 % of the sheared samples. For 300 ms bond duration, the imprints of the bonding tool on the substrate are more significant and occur at approx. 80 % of the sheared samples.

The impact of increasing ultrasonic voltage on the size of the sheared area is larger than that one of increasing bond duration. Especially for 30 V, the sheared areas are very small, indicating that the ultrasonic softening of the wire is insufficient for proper bond formation.

In figure 3.13, the shear surfaces produced with F_{BN} equal to 38 N are shown. For u_T equal to 30 V, for all bond durations, non homogeneously bonded sheared surfaces are observed. Similar results are found for u_T equal to 40 V as mainly the stripe-shaped darker spots appear in the sheared surfaces and additionally, the first minor tool/substrate contacts occur already with t_B equal to 200 ms. For u_T equal to 50 V, tool/substrate contacts occur beginning with t_B equal to 100 ms and for u_T equal to 60 V, imprints of the bonding tool on the substrate are observed for all investigated bond durations.

All sheared areas are non homogeneously bonded. Even for higher ultrasonic voltages and longer bond durations unbonded areas in the central region of the interface remain. For all levels of u_T and t_B, the sheared surfaces show shear code 1.

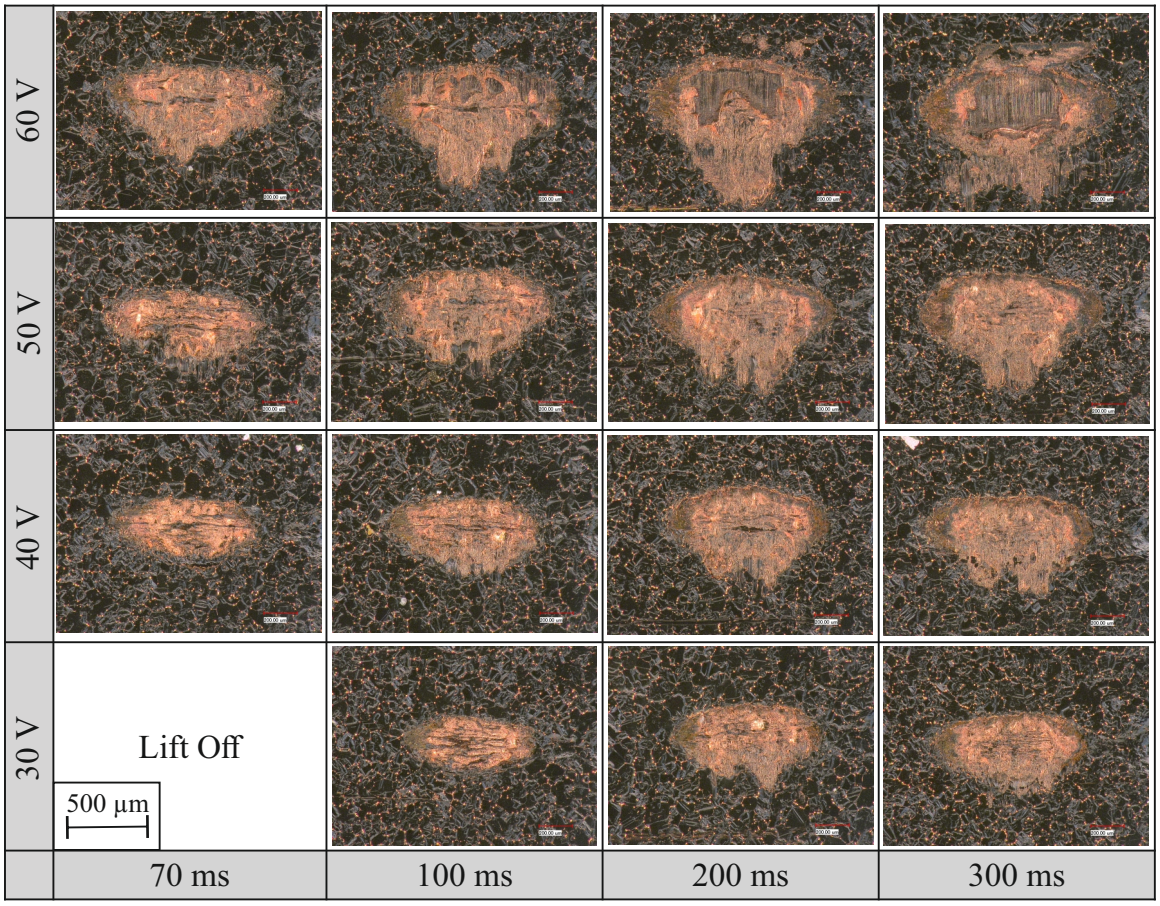

Figure 3.12: Copper wire: shear surfaces for F_{BN} equal to 20 N.

Aluminum wire

In figure 3.14, the sheared surfaces produced with 10 N bond normal force are shown. For u_{T} equal to 20 V and t_{B} equal to 100 ms, the sheared surface is non homogeneously bonded with many dark spots - copper that shines through the silver aluminium- within the interface area. With increasing bond duration from 200 ms to 400 ms, the sheared surface almost keeps constant, but the amount of bonded areas increases and at 400 ms, a shear nugget remains with less than 25 % of the sheared area (shear code 1). For u_{T} equal to 25 V, the size of the sheared surface is almost the same as for 20 V. The interface appears to be more homogeneously bonded, and beginning from 200 ms bond duration, a shear nugget remains with 25 % - 50 % of the sheared surface (shear code 2). For u_{T} equal to 30 V, the shear code 2 occurs for all bond durations. Between u_{T} equal to 25 V and 30 V, the sheared surface increases more significantly as between u_{T} equal to 20 V and 25 V. No further significant differences are observed between u_{T} equal to 30 V and 25 V. For u_{T} equal to 35 V, the most significant change in the appearance of the sheared surface is, that for t_{B} from 300 ms to 400 ms the shear code 4 is observed with a shear nugget larger than 75 % of the sheared surface.

In figure 3.15, the shear surfaces produced with F_{BN} equal to 18 N are shown. Overall, the size of the sheared surface is significantly increased compared to the shear surfaces produced with F_{BN} equal to 10 N. For u_{T} equal to 20 V and t_{B} equal to 100 ms, the sheared surface is non homogeneously bonded; with increasing bond duration from 200 ms to

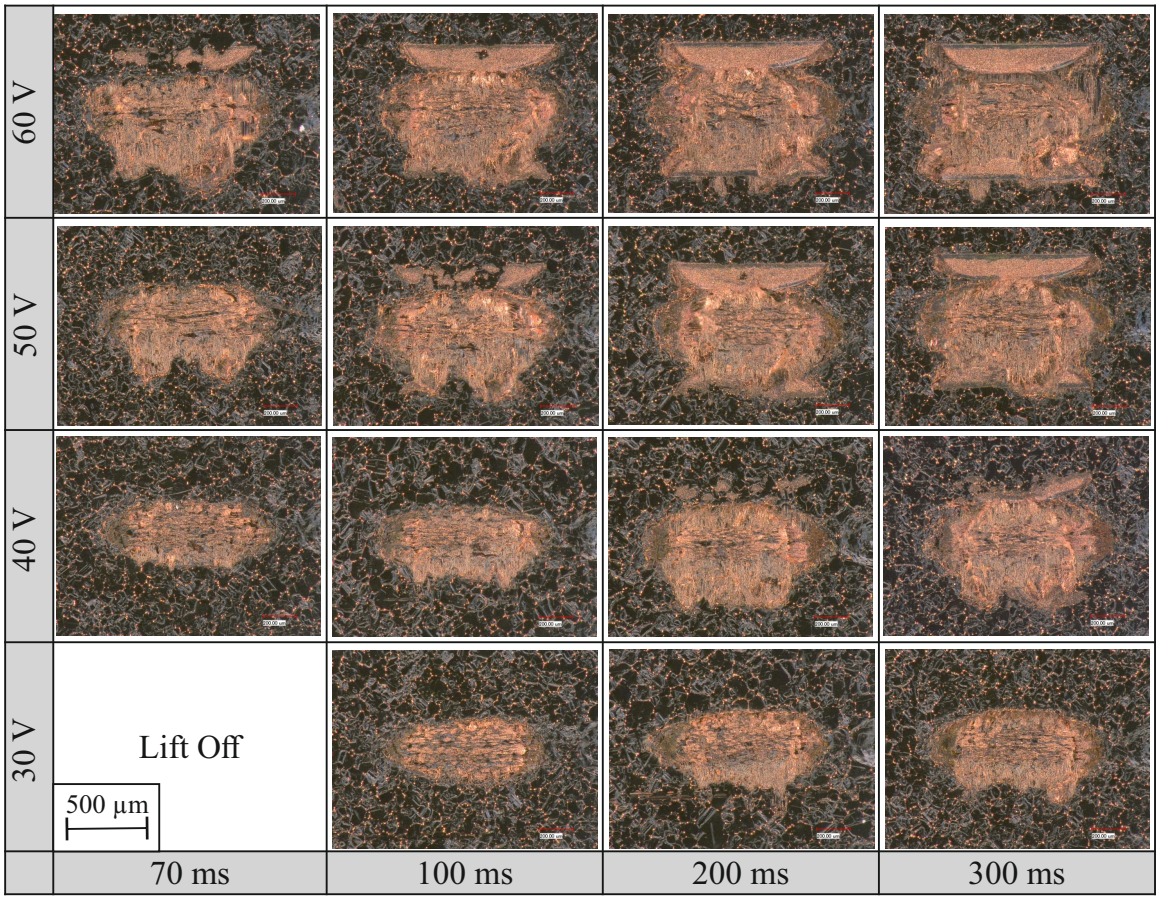

Figure 3.13: Copper wire: shear surfaces for F_{BN} equal to 38 N.

400 ms, the size of the sheared surface almost keeps constant and the density of bonded areas does not increase significantly. For all bond durations, a shear nugget remains but only shear code 1 is observed. For u_{T} equal to 25 V, the sizes of the sheared surfaces are increased slightly compared to 20 V and beginning from 200 ms bond duration, a shear nugget remains with 25 % - 50 % of the sheared surface (shear code 2). For u_{T} equal to 30 V, the shear code 2 occurs for all bond durations from 100 ms to 400 ms and the shear nugget is increased compared to 25 V; no further significant differences occur between 30 V and 25 V. For u_{T} equal to 35 V, for t_{B} from 300 ms to 400 ms, shear code 3 is observed with a shear nugget close to 75 % of the sheared surface which is shear code 3, but close to shear code 4; tool/substrate contacts occur from 200 ms to 400 ms.

3.2.2.1 Summary and conclusion from the shear codes and sheared surfaces

Copper and aluminium wire show significantly different results regarding shear codes and sheared surfaces. For copper wire, shear code 4 occurs only for the lowest bond normal force (20 N), the highest ultrasonic voltage (60 V), and the longest bond duration (300 ms), for this parameter combination, slight tool/substrate contacts were observed for most of the bonds. For lower ultrasonic voltages, only shear code 1 occurs, thus the high ultrasonic voltage is mandatory to achieve the preferred shear code 4.

For the aluminium wire, a shear nugget remains for almost all investigated parameter levels, except for the lowest ultrasonic voltage equal to 20 V and the lowest bond normal

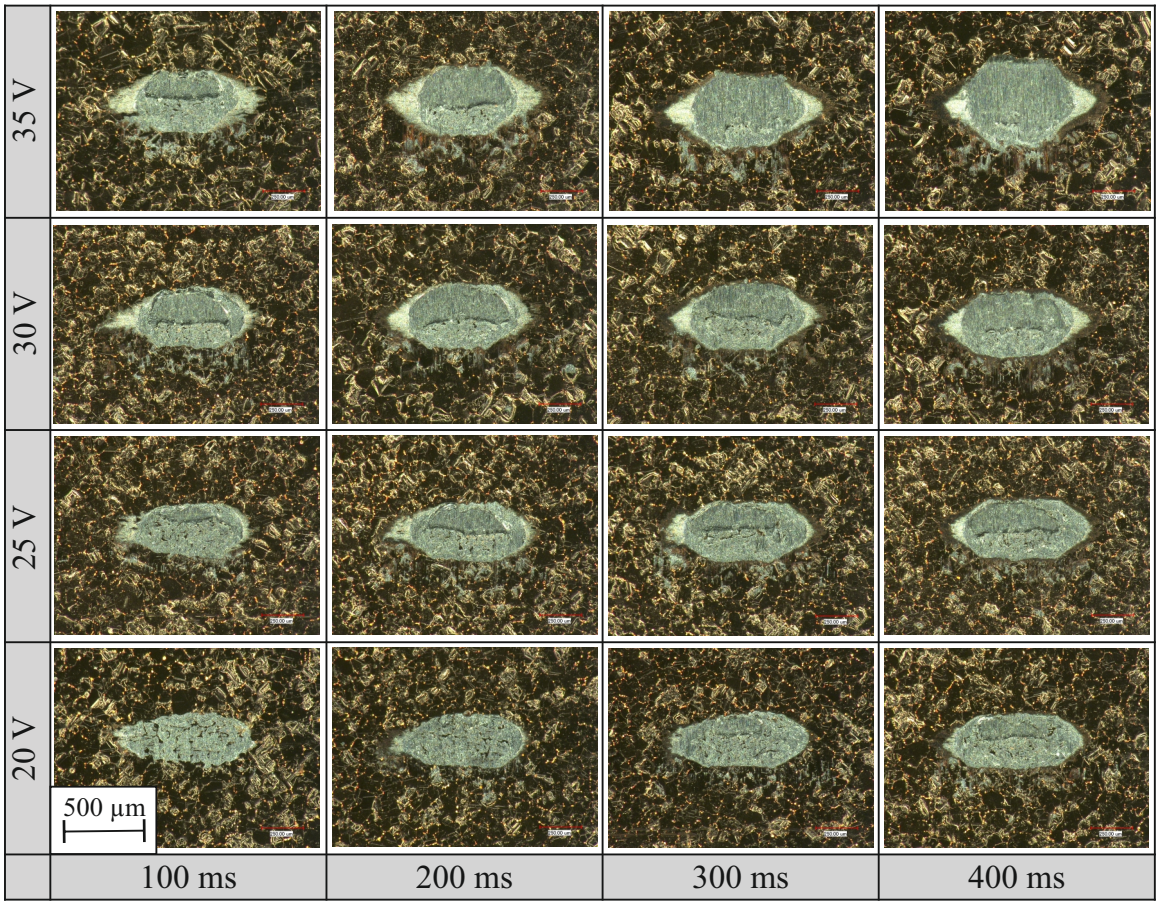

Figure 3.14: Aluminium wire: shear surfaces for F_{BN} equal to 10 N.

force equal to 10 N. For all three bond normal forces from 10 N to 18 N, for u_{T} equal to 60 V and t_{B} from 300 V to 400 V, shear code 4 is observed. For F_{BN} equal to 14 N, shear code 4 also occurs for 200 ms, see figure A.3. The shear codes are not influenced as negatively by increasing bond normal force as for the copper wire. Only for F_{BN} equal to 18 N, the shear nuggets are decreased slightly.

In comparison to the copper wire, shear codes higher than shear code 3 occur in a wider range of the bond parameter levels for the aluminium wire. For copper, the shear codes 3 and 4 only occur in a narrow window of the investigated bond parameters and only in combination with tool/substrate contacts, which indicates that the bond normal force should be further decreased to reduce chances of tool/substrate contacts. For the copper wire, the sheared surface is not significantly impacted by the bond normal force, which explains the low impact of F_{BN} on the shear force observed in section 3.2.1. The ultrasonic voltage has a significant positive effect on the size of the sheared area which results into increased shear forces. For the aluminium wire, the bond normal force has higher impact on the size of the sheared area compared to the ultrasonic voltage; this correlates with the results of the shear forces observed in the main effects and interaction diagrams in section 3.2.1 where also the highest impact was observed by the bond normal force.

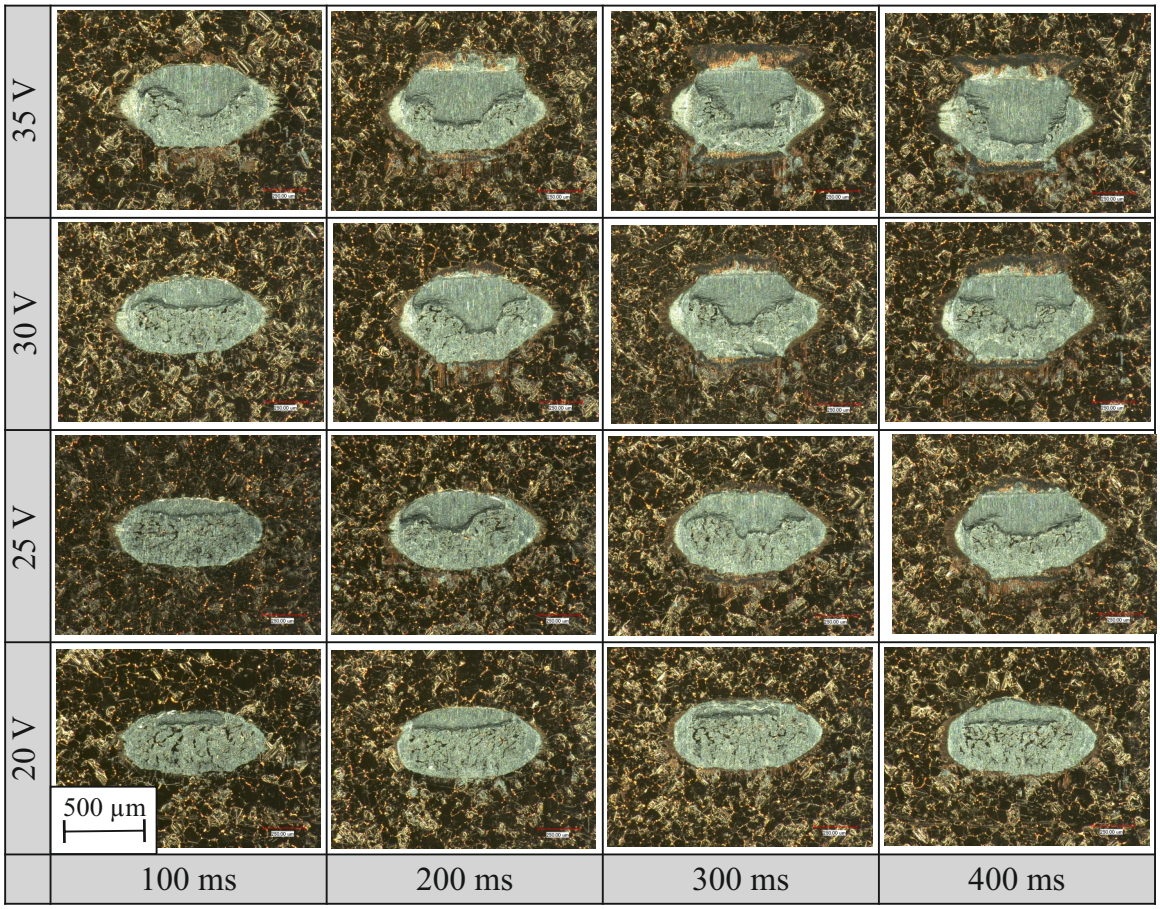

Figure 3.15: Aluminium wire: shear surfaces for F_{BN} equal to 18 N.

3.2.3 Process Windows

In this section, the process windows of the copper and aluminium wire are discussed. Therefore, contour plots of the shear force depending on the bond duration and ultrasonic voltage for the different levels of the bond normal force are utilized. Besides the shear force values, the shear code and tool/substrate imprints are important information to evaluate the process windows, thus these results are additionally plotted within the contour plots.

Copper wire

The contour plots for different levels of the bond normal force are shown in figure 3.16; the red dashed lines show the border between parameter combinations where no tool/-substrate contacts occur and higher parameters of u_{T} and F_{BN} in direction of the top right corner, where tool imprints on the substrate were observed. The black lines indicate the appearance of the different shear codes. Additionally, the three largest values of the shear forces are plotted with markers shown in the legend in figure 3.16.

The shear code 4 occurs only for F_{BN} from 20 N to 26 N and u_{T} equal to 60 V; furthermore the shear codes 2-4 only occur in combination with tool/substrate contacts. As mentioned in section 3.2.2, only for F_{BN} equal to 20 N the tool contacts could be tolerated for bonding on DCB-substrate, as only for approx. 50 % of the sheared samples

contacts were observed and the imprints were not as strong as for higher bond normal forces. When comparing the contour plots for the different levels of the bond normal force, only minor differences in the shape and location of the contour lines for the shear force occur. From the the main effects diagram discussed in section 3.2.1, it is already known that the bond normal force has no significant impact on the shear force, which is approved by the contour plots. On the other hand, the higher the bond normal force is, the earlier the tool/substrate contacts occur. The maximum shear force of 5470 cN was reached for F_{BN} equal to 26 N, equal to u_{T} 60 V, and t_{B} equal to 200 ms; as a quality criteria, the minimum shear force value is set to 90 % of the maximum value which leads to 4900 cN. This level is shown as a contour line in figure 3.16: for F_{BN} from 20 N to 26 N, this criteria can be reached without tool imprints on the substrate, and for F_{BN} from 32 N to 38 N, tool/substrate contacts occur alongside this level. Between u_{T}, t_{B} and the shear force, a parabolic correlation exists; with rising bond duration less ultrasonic voltage is needed to reach a certain level of the shear force value and in general the levels are shifted towards the upper right corner with increasing ultrasonic voltage. For F_{BN} from 26 N to 38 N, the level lines reach saturation from 200 ms to 300 ms bond duration, especially for 4900 cN; for 20 N, saturation is not reached for this level, thus increasing bond duration might further increased the shear force for a certain level of u_{T}.

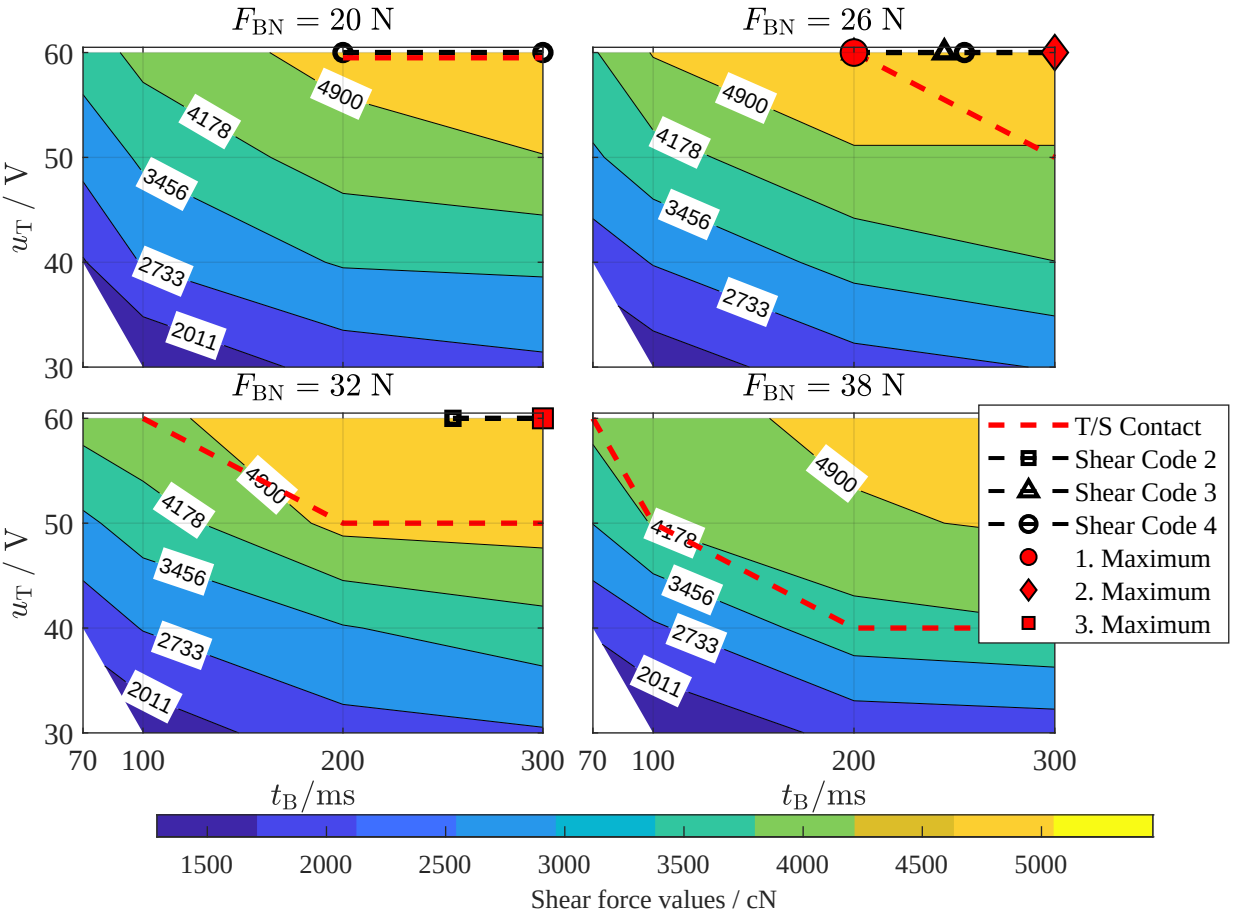

Figure 3.16: Copper wire: contour plot of the shear force. The shear codes 2-4 are indicated by the dashed black lines with markers. The dashed red line indicates tool/substrate contacts. Additionally, the three largest shear force values are plotted with the red markers.

Aluminium wire

In figure 3.17, the contour plot of the aluminium wire for the three investigated levels of F_{BN} is shown; the red dashed lines and the black lines indicate again the appearance of tool/substrate contacts and the different shear codes. The maximum shear force was measured at F_{BN} equal to 18 N, u_{T} equal to 25 V, and t_{B} equal to 300 ms; like for the copper wire, the quality criteria was set to 90 % leading to the level of approx. 2200 cN shown in figure 3.17.

The contour plots show significantly different behaviour for the aluminium wire compared to the copper wire. For F_{BN} equal to 10 N, the criteria of 2230 cN is not reached, but in contrast to the copper wire, the shear codes 2-4 occur even at this low level of shear force. Increasing F_{BN} to 14 N results into a different look of the contour plot: the quality criteria of 2200 cN is reached even at relatively low ultrasonic voltages of about 25 V. The shear code 4 occurs only for u_{T} equal to 35 V and t_{B} from 200 ms to 400 ms; from 300 ms to 400 ms, slight tool/substrate contacts were observed. In the area of the highest shear force value of 2293 cN and higher, the shear code 2-3 is observed. For F_{BN} equal to 18 N, the highest shear force values are reached and all of the three largest shear force values lay within the area of the level 2385 cN in the contour plot. In contrast to the copper wire experiments, the maximum shear force values are reached without any tool/substrate contacts. Furthermore, the area of shear forces larger than 2385 cN is surrounded by lower shear forces, except from the right side, thus, the optimal parameter combinations can be found within the boundaries of this area. For F_{BN} equal to 18 N, shear code 2 occurs at the upper boundary of the area with the level of 2385 cN and for 35 V, shear code 3 occurs from 200 ms to 400 ms in combination with tool/substrate contacts.

3.2.3.1 Summary and conclusion from the contour plots

The contour plots summarize the results of the shear codes and shear force measurements; for the copper and aluminium wire, different results were observed. For the copper wire, following conclusions can be made:

- As already shown in the interaction diagram in section 3.2.1, the parameters normal force, bond duration, and ultrasonic voltage seem to be almost independently selectable.
- The level lines have a parabolic shape and are almost parallel to each other. This means that with longer bond duration, the ultrasonic voltage required to achieve a certain shear force is reduced; on the other hand, the voltage must be increased for a certain bond duration to increase the shear force.
- The process windows for the three different bond normal forces look very similar, except for the position of the shear codes and tool/substrate contacts. As already observed in the main effects diagram, the bond normal force has only a small influence on the shear force values, but negatively affects the appearance of the tool imprints and the shear codes 3-4.
- As a tendency, a smaller bond normal force should be chosen in favour of longer bond duration and higher voltage to avoid tool/substrate contacts.

For the aluminium wire, following conclusions can be made:

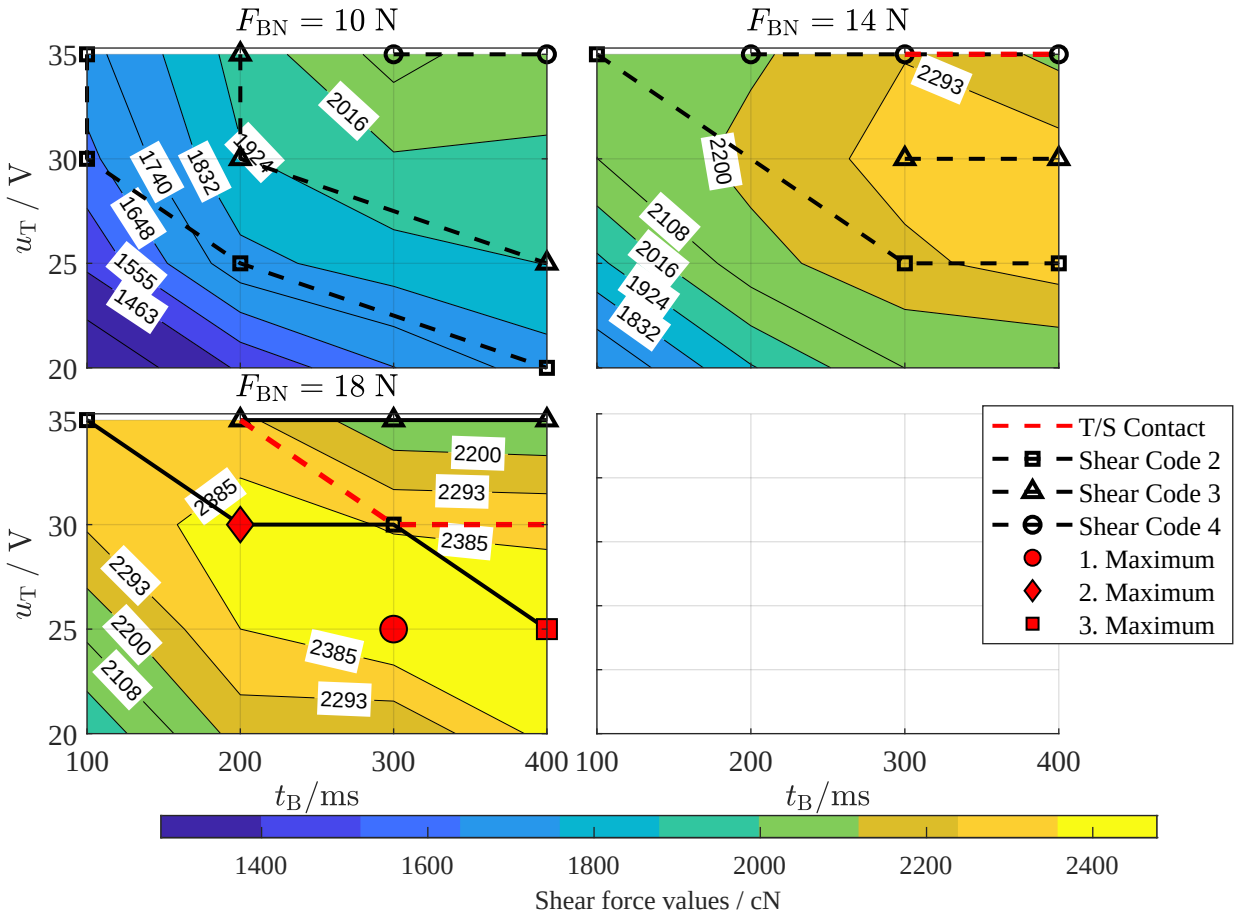

Figure 3.17: Aluminium wire: contour plot of the shear force. The shear codes 2-4 are indicated by the dashed black lines with markers. The dashed red line indicates tool/substrate contacts. Additionally, the three largest shear force values are plotted with the red markers.

- Especially for the aluminium wire it follows that the highest shear force values do not necessarily occur with the highest shear code, but rather together with shear code 2-3.
- As already shown in the main effects diagram in section 3.2.1, the bond normal force has a high influence on the shear force values. The three highest values occur all at F_{BN} equal to 18 N.
- In contrast to the copper wire, the maximum shear forces do not necessarily occur with the highest ultrasonic voltage; for F_{BN} equal to 18 N the optimum is rather at 25 V to 30 V and the longer the bond duration is selected, the lower the required ultrasonic voltage. For F_{BN} equal to 14 N the voltage must be increased to achieve the quality criterion of 2200 cN.

3.2.4 Additional measurements

3.2.4.1 Laser measurements

For the copper wire, the ultrasonic voltage has the highest impact on the shear force and strength. For aluminium, only approx. half of the ultrasonic voltage as for copper wire

is needed to produce wire bonds with sufficient strength. Since the ultrasonic voltage is directly related to the converted ultrasonic power and vibration amplitude at the tool tip during bonding, the vibration at the tool tip was measured as a supplementary measurement using a *Polytec* OFV-512 laser doppler vibrometer. The results for the copper wire are shown in figure 3.18. For all four levels of the bond normal force, the vibration amplitude approx. linearly increases with increasing ultrasonic voltage. The bond normal force has an impact on the vibration amplitude, as the line for F_{BN} equal to 20 N is shifted to higher level compared to the bond normal forces larger than 20 N. Looking at the envelopes for F_{BN} equal to 20 N (figure 3.18 b), different behaviour between 30 V and larger ultrasonic voltages occurs. For higher voltages the amplitude increases during the ramp and then drops down continuously. For u_T equal to 30 V the amplitude increases even after the ramp duration and decreases only slightly after 100 ms, which indicates less bond formation. This fits well to experience and knowledge about the bond formation; with rising bond strength the mechanical resistance increases and therefore the vibration amplitude decreases, because the ultrasonic voltage is constant.

For F_{BN} equal to 38 N (figure 3.18 c) and and all levels of u_T, the envelope is shaped similar to those for 20 N and 30 V; for the higher bond normal force (and higher touch down force) the ultrasonic excitation is not high enough to excite the wire to slide on the substrate and sticking avoids the tool tip vibration to increase as much as for the bond normal force equal to 20 N. Additionally, for 50 V and 60 V, the tool/substrate contacts decrease the amplitude suddenly at approx. 100 ms for u_T equal to 50 V and approx. 50 ms for u_T equal to 60 V.

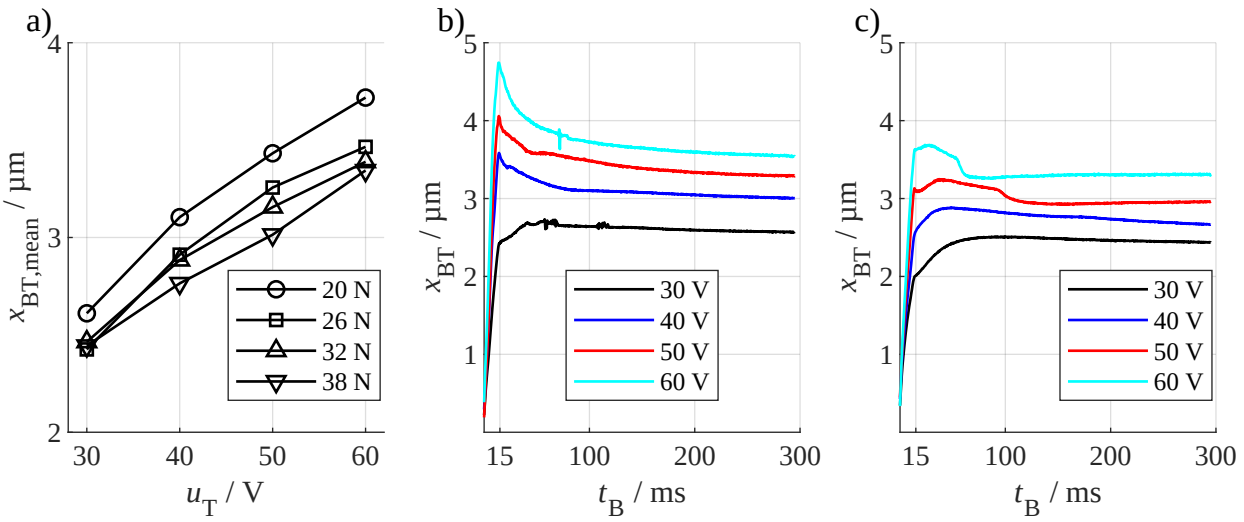

Figure 3.18: Copper wire: laser measurements at the bond tool tip for different ultrasonic voltages: a) mean vibration amplitude during bonding, b) envelope for F_{BN} equal to 20 N, and c) envelope for F_{BN} equal to 38 N.

The results of the laser measurements for the aluminium wire are shown in figure 3.19. The mean amplitudes are in the range from 1.4 µm to 2 µm; even the highest mean amplitude from the aluminium wire is lower than the smallest amplitude of the copper wire at 30 V and 20 N. The mean amplitudes for F_{BN} equal to 10 N are significantly higher than for the larger bond normal forces; nearly no difference occurs between 14 N and 18 N. In figure 3.19 b), the envelopes for F_{BN} equal to 10 N are shown. For all levels of the ultrasonic voltage, the vibration amplitude decreases directly after the ramp

duration. Similar behaviour is observed for F_{BN} equal to 18 N in figure 3.19 c); the shape of the envelopes is not affected by increasing F_{BN} that much as for the copper wire.

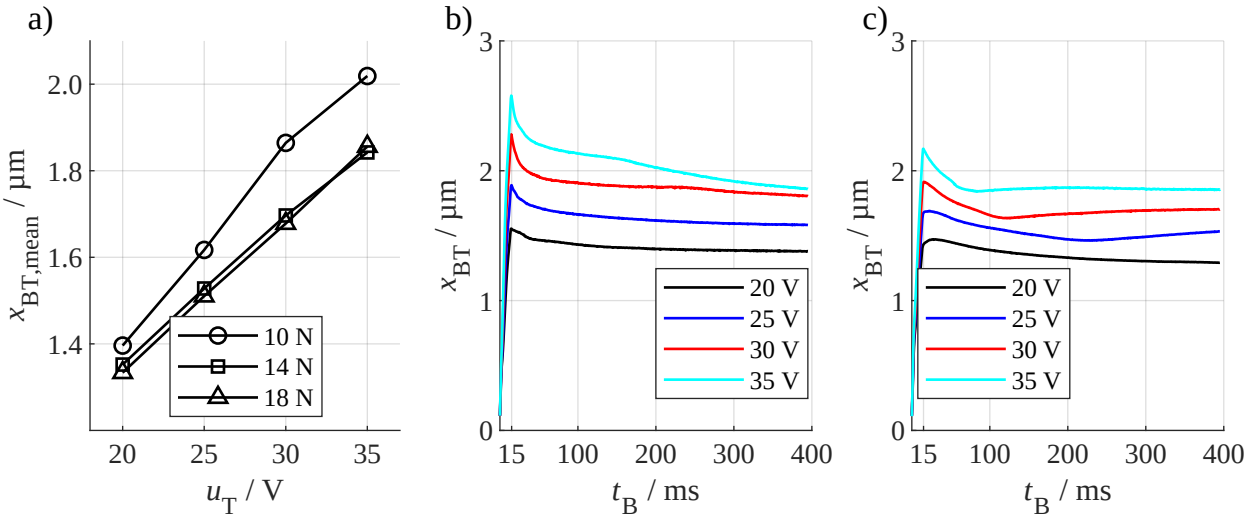

Figure 3.19: Aluminium wire: laser measurements at the tool tip for different ultrasonic voltages: a) mean vibration amplitude during bonding, b) envelope for F_{BN} equal to 10 N, and c) envelope for F_{BN} equal to 18 N.

In comparison to the copper wire, the vibration amplitude at the same ultrasonic voltage of 30 V is less for the aluminium wire: for aluminium, the mean amplitude is in the range from 1.7 µm to 1.9 µm for the three different bond normal forces and for copper, in the range from 2.5 µm to 2.7 µm, although the bond normal forces were significantly larger compared to aluminium. Since the same bond head, bond tool and substrate substructure were used for both wire materials, the mechanical resistance of the aluminium wire during bond formation must be different compared to the copper wire. Since the shear stiffness of the aluminium wire is less compared to the copper wire, either the material damping or the contact resistance due to form fit or higher coefficient of friction must be higher for the aluminium wire.

3.2.4.2 Wire deformation: vertical displacement of the bond tool

In figure 3.20, the vertical deformation z_{WD} during bonding at the different levels of F_{BN} and u_T are shown for the copper wire. For all bond normal forces the wire deformation increases with increasing ultrasonic voltage and the curves are shifted almost parallel to higher values. For F_{BN} equal to 20 N, no significant tool/substrate contacts occurred so that all curves have smooth and monotonously rising characteristics, which gradually saturates after half of the bond duration. For 26 N, tool/substrate contacts occurred for 60 V after about 100 ms bond duration; from this point, the curve has an almost flat horizontal trend. With further increasing bond normal forces, tool contacts occur at shorter bond durations and lower ultrasonic voltages. This trend continues for higher forces at lower voltages.

In figure 3.21, the wire deformation during bonding for the aluminium wire is shown; the axis scaling is the same as in figure 3.20 for the copper wire. The measured deformation in the z-direction during bonding is lower for the aluminium wire than for the copper wire. Since tool/substrate contacts occurred for F_{BN} equal to 18 N and the wire diameter

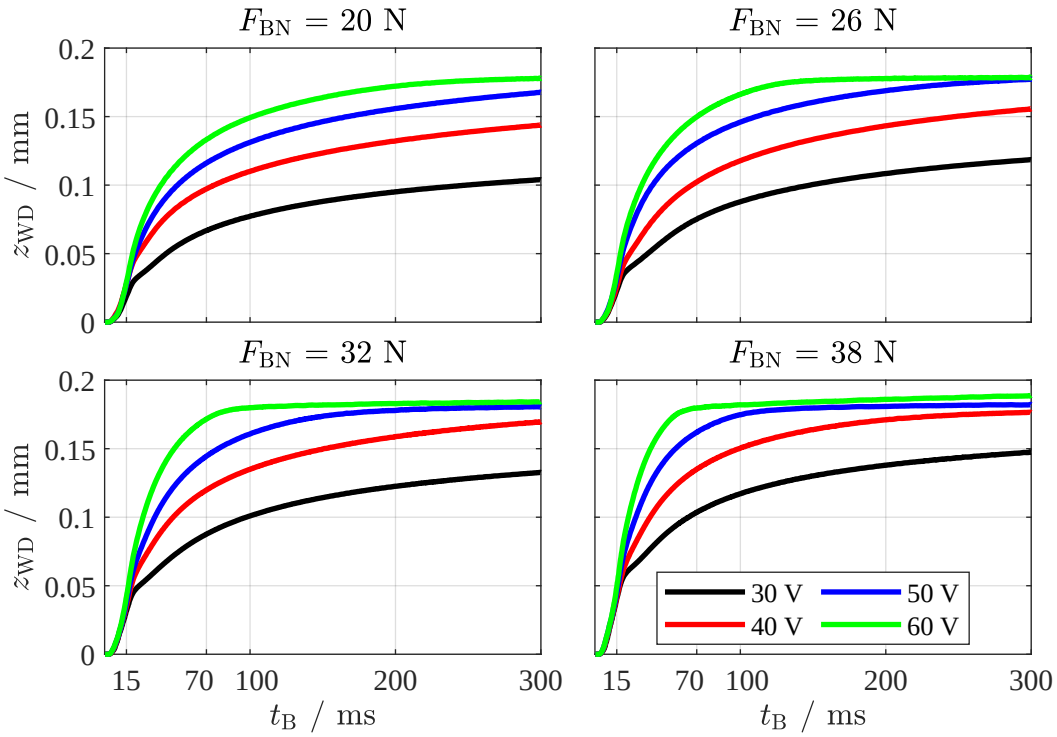

Figure 3.20: Vertical deformation z_{WD} during bonding for the copper wire.

and bond tool were the same for copper and aluminium, the bond tool moved the same distance z_{WD} from the first contact of the wire on the substrate to the tool/substrate contact as for copper wire. Nevertheless, the distance z_{WD} measured during wire bonding is smaller for aluminium, thus the pre-deformation before the measurement must have been larger for aluminium. The initial slope of the curves is higher for aluminium than for copper; in a direct comparison with the copper tests in figure 3.20, the majority of the deformation for aluminium takes place in the first 70 ms, while for copper a significant proportion of the deformation also takes place after 100 ms.

In figure 3.22, the maximum vertical displacement $z_{WD,max}$ at the end of the curves over the mean vibration amplitude $x_{BT,mean}$ is plotted. The lines for the aluminium wire are grouped together at significantly lower vibration amplitudes in the range from 1.4 µm to 2 µm compared to the copper wire in the range from 2.4 µm to 3.7 µm. The mean value of all values $z_{WD,max}$ is approx. 1.4 higher for the copper wire than for the aluminium wire.

3.3 Impact of substructure resonances and bond frequency

The question of the appropriate bonding frequency f_T for an optimum bonding result has not yet been answered in a general way in ultrasonic heavy wire bonding and usually also depends on the application itself. Various scientists have investigated the influence of the bonding frequency for fine wire bonding (see section 2.2.2) and there is an emerging trend that a higher bonding frequency is particularly suitable for soft and flexible substrates. However, there is still a lack of dynamic studies on how substrate vibrations during

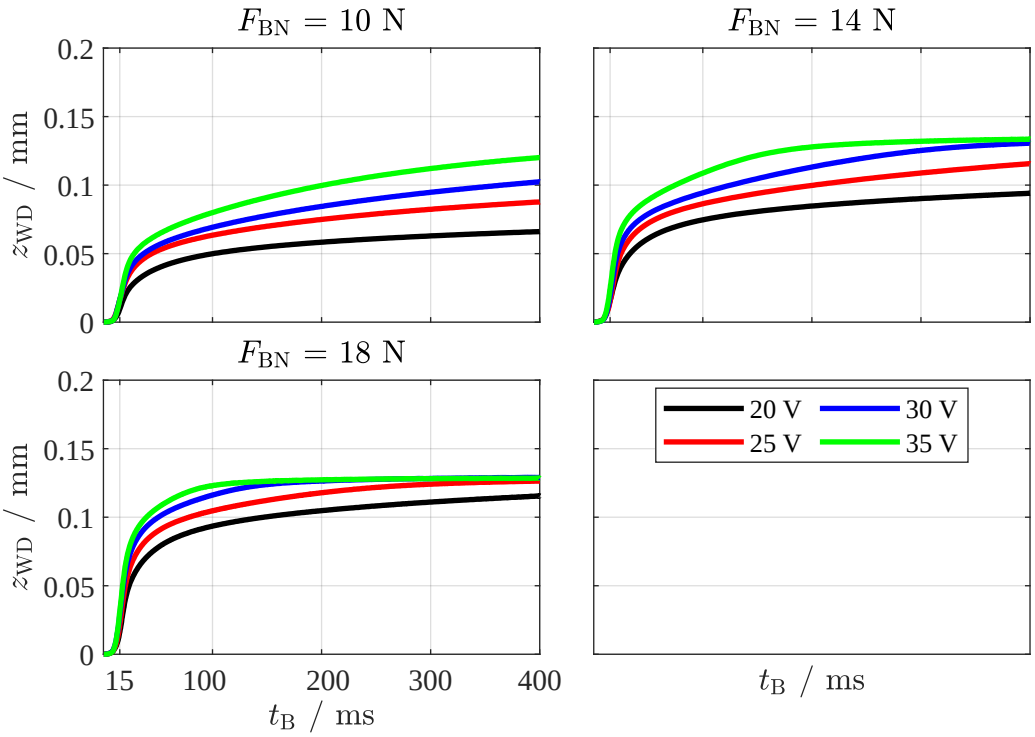

Figure 3.21: Vertical deformation z_{WD} during bonding for the aluminium wire.

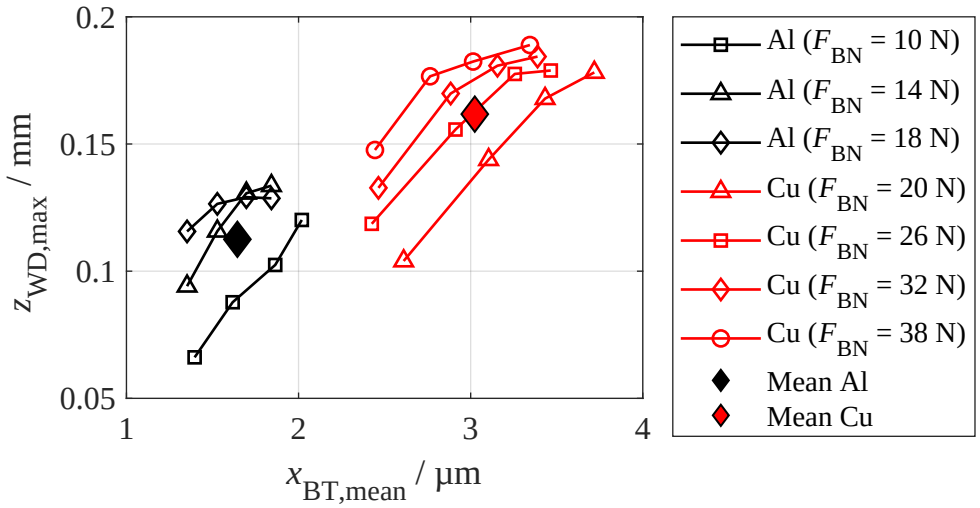

Figure 3.22: Maximum vertical displacement $z_{WD,max}$ for the copper and aluminium wire depending on the mean vibration amplitude $x_{BT,mean}$ of the bond tool tip.

bonding affect bond formation and how they can be influenced by the choice of bonding frequency.

In section 3.3.1, a principle experiment on a substructure with reduced geometrical complexity - a copper rod with variable height clamped in a vise - is used to investigate the dynamical behaviour of the substrate during bond formation using laser vibrometer measurements. This principle setup is not suitable for extensive experimental series because of the limited amount of wire bonds that can be placed on one copper rod. Therefore, in section 3.3.2 a DCB, which is fixed on a EPDM-plate by a vacuum suction, is used to

determine the shear force values, wire deformation and welded surfaces of bonds which have been produced with different bond frequencies. All bonding experiments were performed using 300 µm copper wire produced by *Heraeus* and a *Hesse Mechatronics BJ939* wire bonder, using different bondheads for different working frequencies.

3.3.1 Substructure resonances

The setup of the principle experiment with the copper rod clamped in the vise is shown in figure 3.23 a). The height h of the copper rod with a diameter of 1 mm can be varied to change the static stiffness as well as the resonance frequencies of the bending mode. For the experiment, two bond frequencies (37 kHz and 100 kHz) and two different heights (3.6 mm and 9.6 mm) were investigated.

The resonance frequencies of the copper rod at the two different heights were measured by impulse excitation. For the excitation, a spherical steel bullet with a diameter of 2 mm was rolled over a v-shaped slide against the top of the copper rod, see figure 3.23 b). The measured velocity response at the reference point M2 is then transformed into the frequency domain by the Fast Fourier Transform (FFT) in MATLAB. The upper frequency limit for this method depends on the mass of the bullet and its stiffness; the method is described in [103].

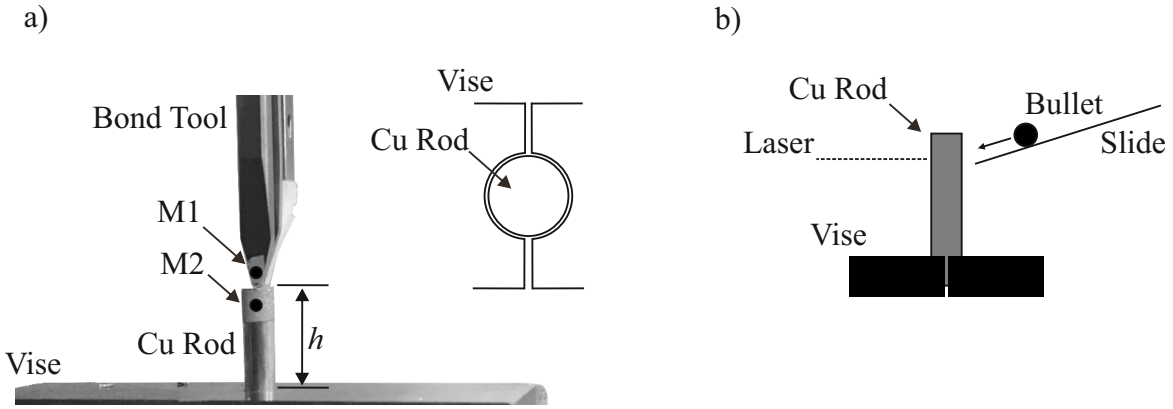

Figure 3.23: a) Clamped copper rod in a vise; the height h can be varied and the velocity amplitudes at the positions M1 (tool tip) and M2 (edge of the copper rod) are measured. b) Principle setup of the impulse excitation by spherical steel bullet.

In figure 3.24, the spectrum of the vibration of the copper rod at the two different heights are shown. At the height of $h = 3.6$ mm, two significant resonance frequencies at 45 kHz and 54 kHz occur, which have been identified to belong to two bending modes of first order. Two different resonance first bending modes occur due to the anisotropic stiffness of the vise. At the second height $h = 9.6$ mm, the bending modes appear at significantly lower frequencies (10 kHz and 11.5 kHz). Additionally a torsional mode at 48 kHz, and the second bending modes at 56 kHz and 60 kHz could be identified.

Depending on the height of the copper rod, there is the following significant difference for the system dynamics during bonding: for $h = 3.6$ mm, the bonding frequency 37 kHz lays below the first bending modes and the bonding frequency of 100 kHz above it. For $h = 9.6$ mm, the bonding frequency of 37 kHz is above the first bending mode of the copper rod and the bonding frequency of 100 kHz above the second bending mode.

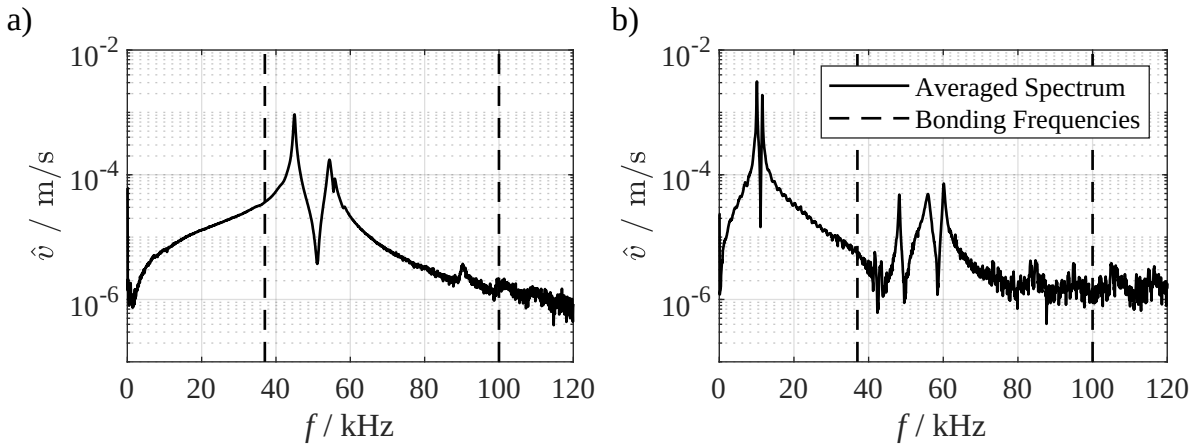

Figure 3.24: Resonance spectrum of principle setup with a) the height $h = 3.6$ mm and b) $h = 9.6$ mm. The averaged spectrum is based on five single measurements. The investigated bonding frequencies 37 kHz and 100 kHz are marked by the dashed lines.

The bonding tests on the copper rod were carried out with the bonding parameters from table 3.4; the parameters were not changed for the two heights. The voltage u_T was chosen in a way, that the velocity amplitude at the tool tip was approximately the same for the two bonding frequencies.

Table 3.4: Bond parameters for the two different bond frequencies.

	37 kHz	100 kHz
F_TD / N	5	
F_BN / N	15	
t_R / ms	50	20
t_B / ms	250	100
u_T / V	40	86

The results of the laser vibrometer measurements at the edge of the copper rod are shown in figure 3.25. The envelopes of the vibration amplitude $\hat{v}$ in figure 3.25 a) show that in case of the bonding frequency of 37 kHz and a height $h = 3.6$ mm, significantly higher velocity amplitudes occur compared to the remaining three setups. For $f_\mathrm{T} = 37$ kHz and $h = 3.6$ mm, the phase difference in figure 3.25 b) between the tool and substrate is approximately 0°; hence the higher substrate amplitudes are explained by the forced in-phase excitation of the substrate by the tool/wire vibration. When bonding with the same frequency of 37 kHz on the copper rod with the height of $h = 9.6$ mm the substrate amplitude is decreased to approximately 10% of the amplitude at $h = 3.6$ mm and the phase difference between tool and substrate movement reaches approximately 150°. The substrate amplitudes is lowered due to the absorbing character of the copper rod with a height of 9.6 mm when being excited over-critically with 37 kHz, even though the static stiffness of the rod is lower compared to the rod with $h = 3.6$ mm. In case of the excitation frequency equal to 100 kHz, for both heights the working frequency lies above the relevant resonance frequencies of the substructure and in both cases, the substructure behaves like an absorber for the dynamical excitation leading to low vibration amplitudes

of the copper rod.

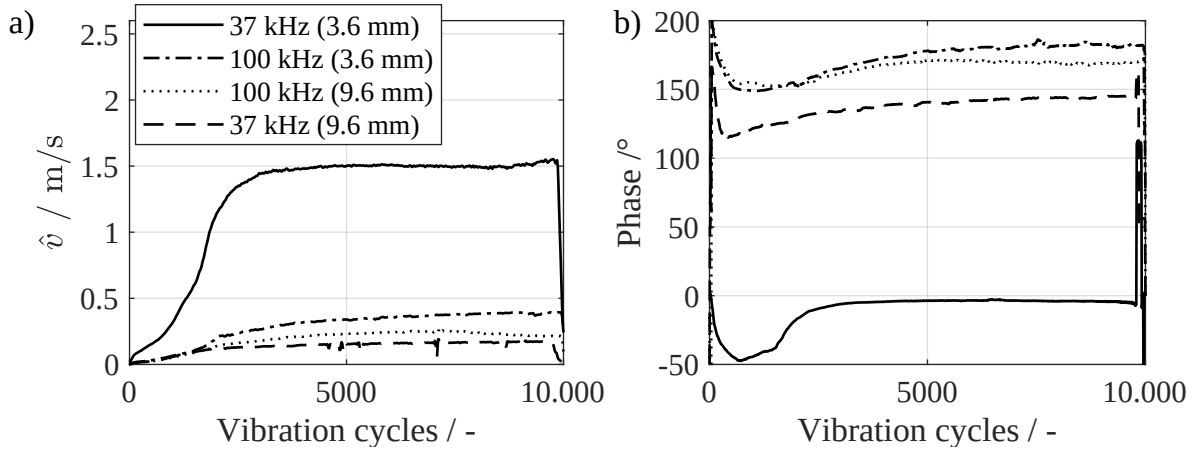

Figure 3.25: a) Velocity amplitude of the copper rod at the measurement position M2 b) Phase difference between the tool tip movement (M1) and substructure movement (M2).

The conclusions from the bonding tests on the copper rod are:

- The static stiffness of the substrate structure is not decisive for the resulting substrate vibration.
- If the substrate acts as an absorber, the substrate vibration can be reduced effectively. Therefore the bond frequency must be higher than the significant resonance of the substrate.
- The phase in the over-resonant case reaches up to 180°; this can have a positive effect on the transmitted friction energy in the interface, as it increases the slip between the wire and the substrate and the vibration energy is more effectively conducted into the contact.

3.3.2 Bond tests on DCB with 37 kHz, 60 kHz and 100 kHz

Choosing bond parameters at the different bonding frequencies to achieve comparable results is difficult without knowing which physical quantity (tool tip displacement or velocity amplitude? frictional energy or power in the wire-substrate interface?) is the leading parameter for bond formation. Bond tests with unaltered bond parameter settings cannot be successful. At least the ultrasonic voltage must be adjusted, as the transducers within the bond heads for different frequencies show different electro-mechanical characteristics. Preliminary bond tests were carried out to determine the bond parameters. The bond duration was chosen, such that the number of oscillations at the end of the bond formation is 10,000 for all three frequencies. An exception is the bond duration at 100 kHz, which was further extended during the test, as no saturation of the shear force values up to 100 ms could be observed as with the lower frequencies; thus, the bonding time was extended to 140 ms for 100 kHz until saturation was observed. For all three frequencies the same touch down force and bond normal force is used. The trajectory of the bond parameters was chosen like in the DoE in figure 3.5 with one interval and a ramp phase at the beginning. The voltage u_T was adapted to achieve approximately same shear force values at the end of bond formation after 10,000 vibration cycles. For

all three bonding frequencies, the same bond tool geometry was used. The bonding parameters for the experiments are listed in table 3.5.

Table 3.5: Bond parameter for the three different bond frequencies.

Bond frequency	37 kHz	60 kHz	100 kHz
F_{TD} / N	5		
F_{BN} / N	15		
t_{R} / ms	50	33	20
u_{T} / V	35	20	86

The shear force values and the wire deformation z_{WD} over the bond durations are measured at eight cut-off times which were chosen such that the number of oscillation cycles is the same for the three nominal bonding frequencies. Since the transducer frequency f_{T} is not constant during the bonding process as the frequency is controlled by the PLL, the real numbers of oscillation cycles differ slightly. For each cut-off time, 25 shear force values were measured at the destination bond position. The mean shear force values at the cut-off times are listed in table 3.6 and the vertical wire deformation z_{WD} and the shear force values during bond formation are shown in figure 3.26.

The trend of the deformation curve approximately follows the development of the shear values for the three bonding frequencies. For 60 kHz, the growth rate of shear force values is the largest, as $F_{\mathrm{S}} = 2504$ cN is reached after 3971 vibration cycles; for 37 kHz, 2654 cN is reached after 5628 cycles and for 100 kHz, 2560 cN is reached after 5982 cycles. For 100 kHz, in the beginning stages of bond formation up to approx. 4000 vibration cycles, the shear force values increase more slowly compared to the two lower frequencies. But when the saturation is reached for the shear force values and vertical wire deformation for 37 kHz and 60 kHz at approx. 6000 vibration cycles, these values further increase for 100 kHz; at 9982 vibration cycles, the mean shear force value is 3302 cN and no saturation of the curve of z_{WD} and F_{S} is observed. In extended bond tests, it was found that the saturation occurs shortly after 10,000 vibration cycles for 100 kHz; for 11998 cycles $F_{\mathrm{S}} = 3343$ cN and for 14014 cycles $F_{\mathrm{S}} = 3303$ cN were measured.

Table 3.6: Mean shear force values and the number of vibration cycles at the corresponding cut-off times.

37 kHz		60 kHz		100 kHz	
Vib. Cycles	F_{S} / cN	Vib. Cycles	F_{S} / cN	Vib. Cycles	F_{S} / cN
936	0	1007	0	990	0
1428	459	1482	438	1502	0
1872	833	1976	1255	2014	600
2808	1715	2964	2068	3006	1019
3744	2163	3971	2504	3998	1572
5628	2654	5928	3025	5982	2560
7500	2686	7904	3038	7999	2925
9372	2654	9918	3124	9982	3302

For further analysis, laser vibrometer measurements of the bond tool tip were carried out. The results for bond tool displacement and speed are shown in figure 3.27. For

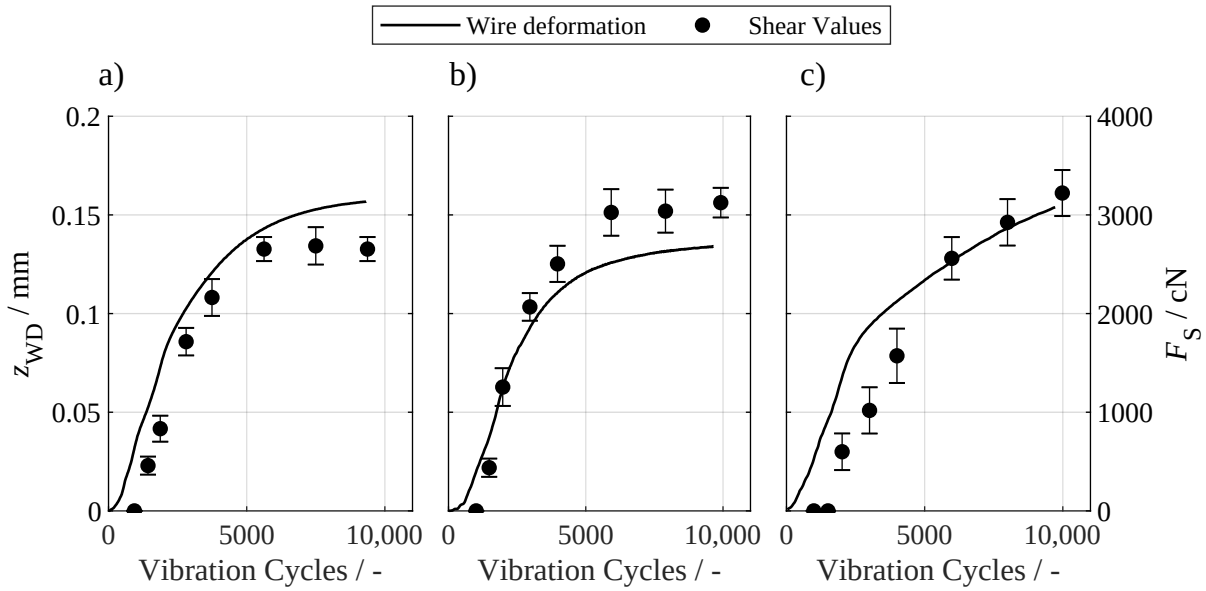

Figure 3.26: Shear values for a) 37 kHz, b) 60 kHz and c) 100 kHz at cut-off times with the same number of oscillations (mean and standard deviation values) and measured wire deformation (mean value).

37 kHz and 60 kHz, the mean value over bond duration of the bond tool amplitude x_{BT} is approximately the same (3.4 µm) and at 100 kHz there is a significantly lower amplitude (2.6 µm). For the velocity, however, the values for 60 kHz and 100 kHz are comparable (1.5 m/s), while for 37 kHz a significantly lower velocity (1.0 m/s) is reached.

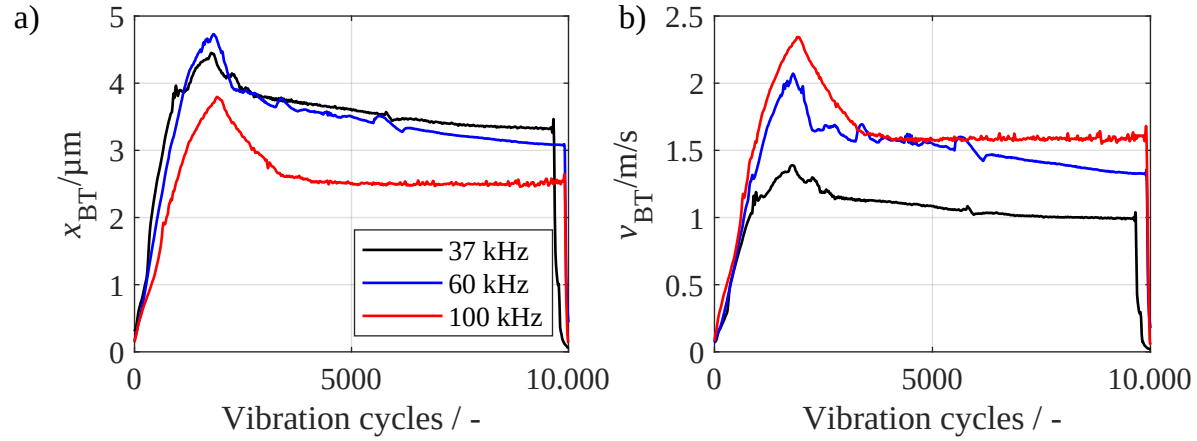

Figure 3.27: Laser measurements at the bond tool tip for the three bond frequencies. a) Envelope of the bond tool displacement x_{BT}. b) Envelope of the bond tool velocity v_{BT}.

In figure 3.28 exemplary microscope images of the wire deformation of the bonds themselves and micrographs of the cross sections for the three bond frequencies are shown. Optical inspection shows that the wire deformation for 100 kHz leads to a narrower bond: the bond is more elongated than for the lower frequencies. In table 3.7, the bond foot width W and the depth of immersion ID in the interface were measured and listed to quantify the deformation. The immersion depth is measured from the surface of the DCB

to the lowest point of grain refinement, see the cross section of 60 kHz in figure 3.28. Even though the recorded vertical wire deformation z_{WD} at the bonding machine at 100 kHz was higher than at 37 kHz and 60 kHz, the bond width W is 8 % and the immersion depth ID is 13 % less compared to 37 kHz.

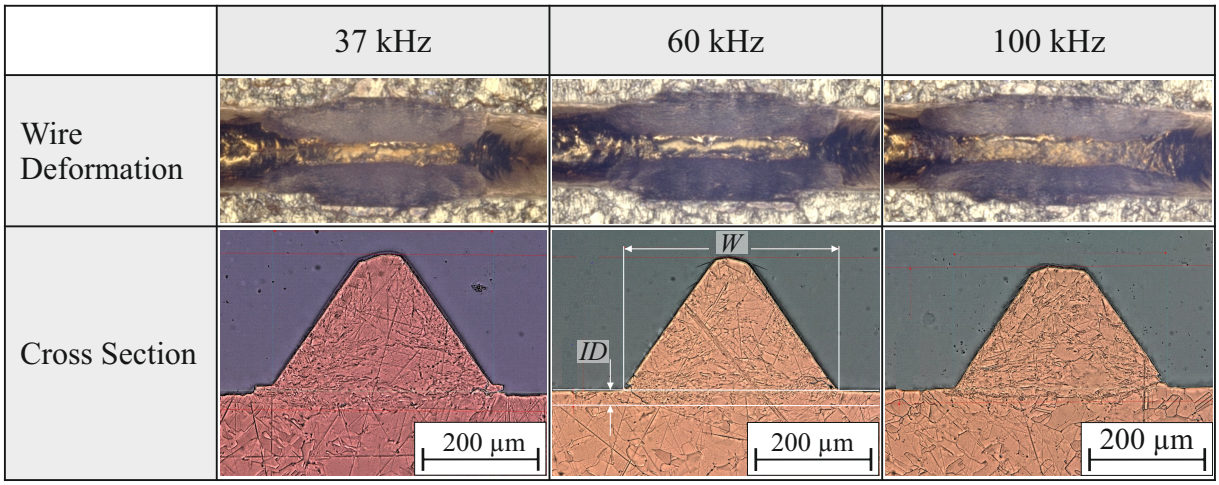

Figure 3.28: Images of the wire deformation and cross sections for the three different bond frequencies.

Table 3.7: Results from the cross sections: bond foot width W and immersion depth ID at the interface for the three different bond frequencies determined from the cross sections (mean values from five cross sections for each frequency).

Bond frequency	37 kHz	60 kHz	100 kHz
W / µm	381	369	352
ID / µm	36.8	38.6	28.2

In figure 3.29 results of image segmentation of the bond interface are shown to characterize the bond formation within the interface area. For this purpose, the bonds were peeled at the destination bond, resulting in a fracture surface in the joining zone. The fracture surface of 15 bonds is then analysed by an image segmentation algorithm using the RGB values to distinguish bonded and unbonded areas in the interface; from the 15 images, the distribution of bond probability in the interface area is calculated. Details on this segmentation algorithm are given in [131]. For 100 kHz the width of the elliptic interface is less compared to 37 kHz and 60 kHz. That corresponds to the measured width of the foot prints, table 3.4. The distribution of the micro welds shows, that for 100 kHz a more homogeneous welded area with an elliptic ring of high weld probability developed. For the working frequencies of 37 kHz and 60 kHz, the areas of high bond probability are aligned to the tool position and a less homogeneous welded interface arises.

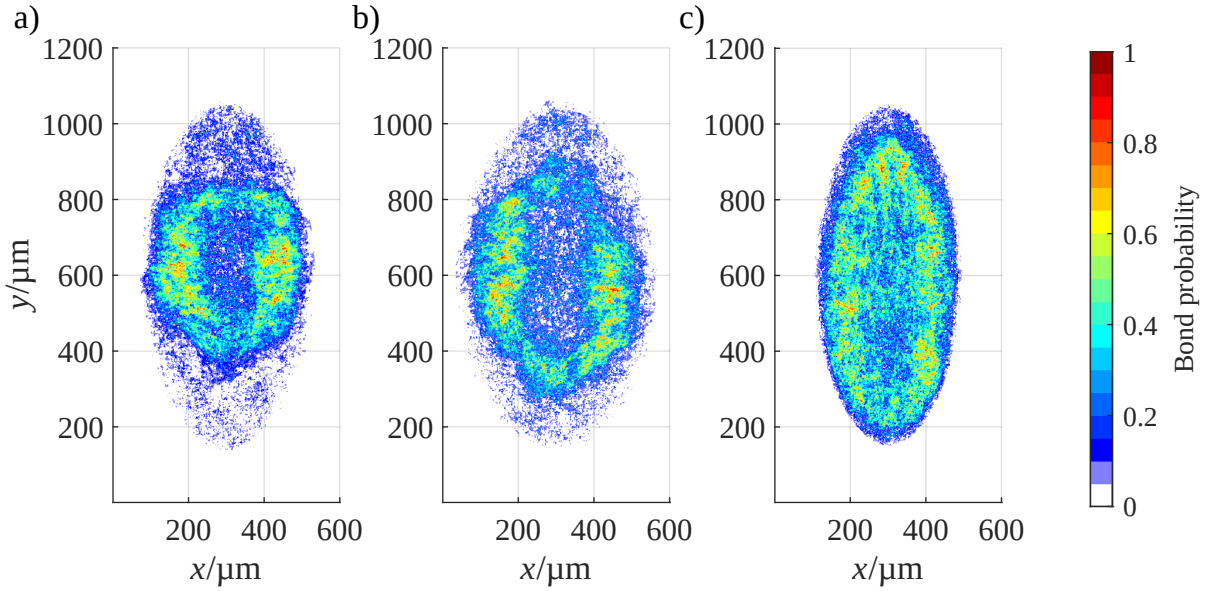

Figure 3.29: Results of image segmentation at 10.000 oscillation cycles of 15 pealed interface images for a) 37 kHz, b) 60 kHz and c) 100 kHz.

4 Multi scale model of the heavy wire bond process

From the wire bonding experiments in chapter 3 the following requirements for modelling the heavy wire bonding process are derived:

- For modelling the impact of touch down force, the pre-deformation of the wire needs to be modelled.
- The ultrasonic softening effect has to be modelled to capture the impact of bond parameters on the the wire deformation, which has an impact on the bond formation.
- From the experiments with different ultrasonic frequencies in section 3.3 it is known that the substrate dynamics play an important role. Thus, the substrate vibrations need to be modelled to include these effects.

To cover all relevant physical effects and to ensure the computationally efficient simulation of the bonding process, a multi scale model approach based on a co-simulation of *MATLAB* and *ANSYS* was chosen. The model setup is described in section 4.1. The Finite Element Model in *ANSYS* (section 4.1.1) and the system models in *MATLAB* including the bond formation model (section 4.1.2), ultrasonic softening model (section 4.1.5) and the dynamical models for the transducer (section 4.1.7), wire (section 4.1.3) and substrate (section 4.1.6) are presented. To reduce computational time high performance computing is utilized; the methodology to run the co-Simulation on a computer cluster is described in section A.4.

4.1 Model setup

The different physical phenomena of the wire bonding process are considered in different sub-models as shown in figure 4.1. In *ANSYS*, the static complex deformation behaviour without ultrasonic excitation is modelled with finite element method using *ANSYS Mechanical*. In *MATLAB*, Reduced Order Models (ROM) are used for full transient simulation of transducer, bond tool, substrate substructure vibration and to calculate the bond formation and ultrasonic softening for all vibration cycles of the bond process. A Graphical User Interface (GUI) allows the user to choose bond parameters, configuration settings of the simulation and post processing options. The sub-models in *MATLAB* and *ANSYS* are coupled by a CORBA-interface between the two software tools to apply the normal force and material softening factor k_{USS} of the wire material to the finite element model. As a result of the finite element simulation, the normal force distribution in the contact between wire and substrate and the vertical displacement z_{WD} of the bond tool are returned to the *MATLAB* simulation. In this co-simulation, *MATLAB* acts as the master program and *ANSYS* as the slave program; the software versions *ANSYS* 18.1 and *MATLAB* 2018b are used.

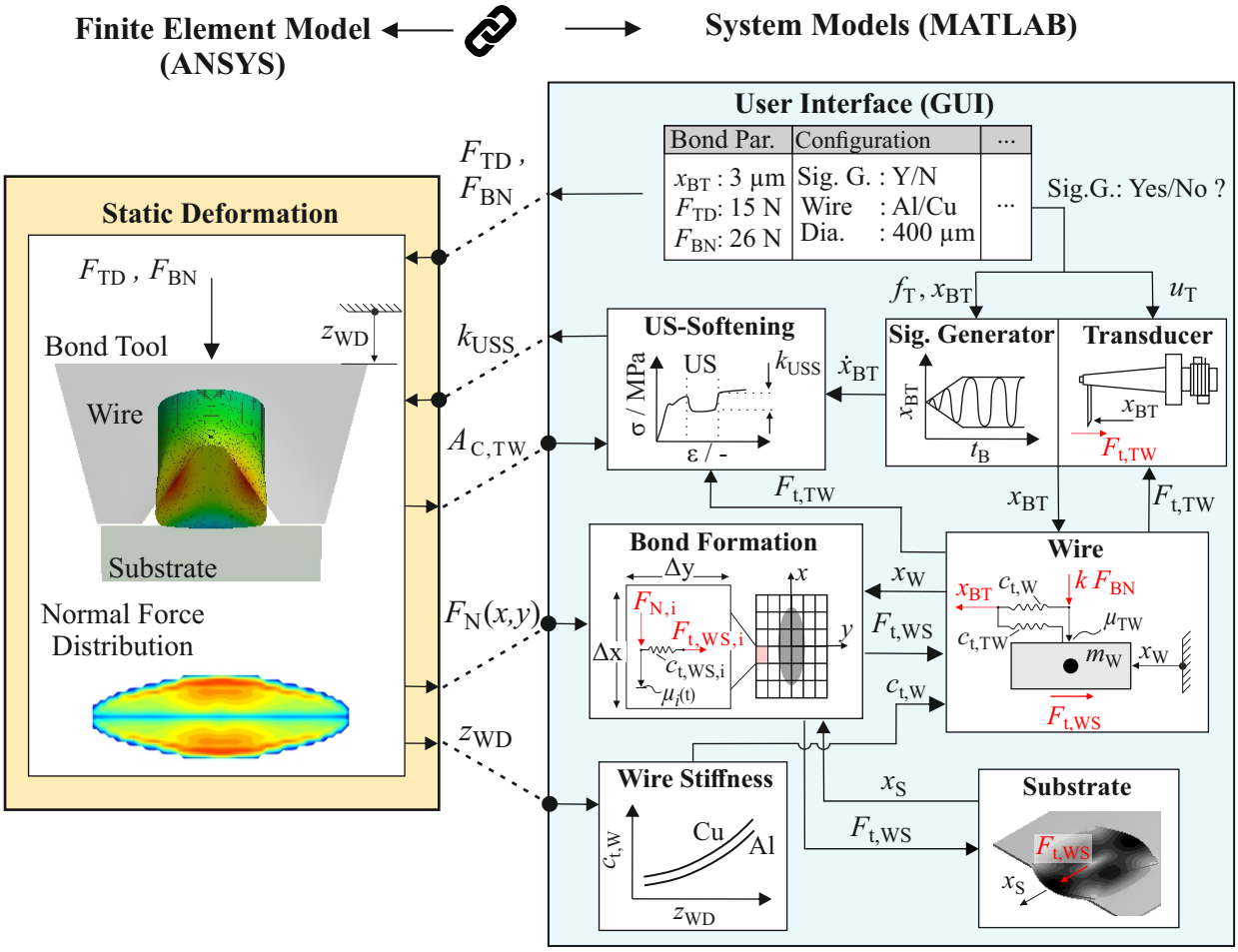

Figure 4.1: Multi scale model approach for the wire bond model using a co-simulation between *MATLAB* and *ANSYS*.

4.1.1 Static deformation model

The finite element model was built in *ANSYS Workbench*, with the benefits of the Graphical User Interface (GUI), geometry import of CAD-models, and automatic mesh generation of complex geometries. The schematic workflow for generating the finite element model for the co-simulation and the mechanical model itself is shown in figure 4.2. A half model of the bond tool, wire and substrate is used with the x-z plane as the symmetry plane; fixed support is defined for the surface on the bottom side of the substrate. The wire is bent, which corresponds to the real shape of the wire before the pre-deformation phase. For the bonding tool, wire and substrate, following geometries are modelled:

- Bonding tool produced by *Small Precision Tools (SPT)* with the type number OSG7-16-M-3,18-2,733-G [120].
- Wire with 400 µm diameter.
- Substrate with 300 µm thickness and 1.5 mm x 0.6 mm top surface dimensions.

The substrate dimensions were chosen such that the contact results are not influenced by the geometry, but also so that the number of mesh elements is not unnecessarily increased; to determine the geometry dimensions of the substrate, the width, height, length and mesh size of the substrate were varied and the simulated contact results were compared to each other. The geometry is imported from a CAD-model into *ANSYS Workbench*

and modified by merging surfaces and edges for easier contact definitions. Within the static structural analysis in *ANSYS Workbench*, contact and boundary settings, the mesh type, element sizes and solver settings are done. The bond tool is modelled as a rigid body, since it is made of tungsten carbide and compared to aluminium or copper wire material, it is about ten times more rigid. The wire and substrate are modeled with non-linear elasto-plastic deformation behaviour; on both, the wire and substrate material, the softening factor k_{USS} is applied from *MATLAB*, which lowers the stress-strain curve of the material model. The contacts between bond tool and wire, and between wire and substrate are modelled with the penalty based *Augmented Lagrange* contact formulation which is suitable for robust convergence behaviour and good accuracy for calculating the normal force distribution between wire and substrate.

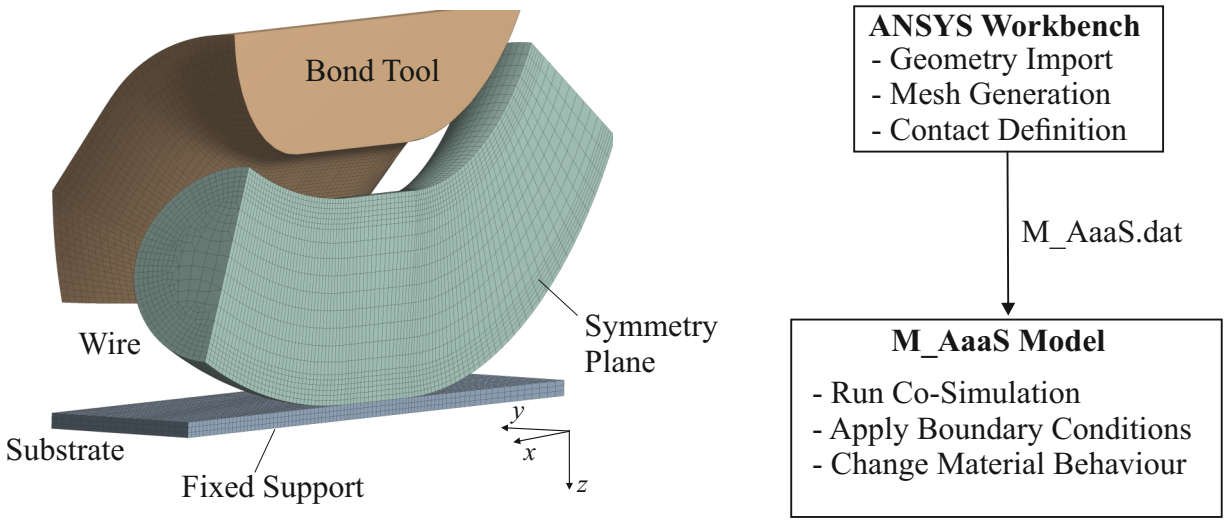

Figure 4.2: Finite element model for the co-simulation.

For meshing, linear hexahedral elements of the element type 185 with mixed u-P formulation [7] and inflation layer for the wire were used. Mid-side nodes of higher order elements are not considered by the contact algorithms, thus increasing the accuracy of the contact results can only be achieved by decreasing the element size in the contact area. For linear hexahedral elements, the accuracy of the calculated stresses is close to those of quadratic elements; for tetrahedral elements, the results can differ significantly as linear tetrahedral elements behave stiffer compared to quadratic elements [140]. The mesh size of the model shown in figure 4.2 has been adapted to the regions of interest with higher density in the contact region between wire and substrate resulting to a mesh with 62881 nodes. The material behaviour under ultrasonic load is adapted by scaling the stress-strain curve with the factor k_{USS}, see section 4.1.5. For this, in *ANSYS* multiple stress-strain curves for the different levels of k_{USS} are stored at different temperatures of the wire material. The stress-strain curve is then scaled within the co-simulation by changing the temperature of the wire material; the corresponding value of the temperature is calculated in *MATLAB*.

When generating the model with *ANSYS Workbench*, a database file (*M_AaaS.dat*) is saved automatically in the solver directory and contains all information like the mesh node coordinates, contact formulations and material properties. The M_AaaS.dat file is then used to perform the co-simulation with *ANSYS Mechanical APDL* using the *ANSYS as a Server* (AaaS) feature described in section 4.2.

4.1.2 Bond formation model

To calculate the distributed bond strength, a discretized friction model shown in figure 4.3 and the difference equation system in equation 4.1 are used. An uniform mesh grid with coordinates of center points of partial contact areas is created within *MATLAB* with input parameters n_x, and n_y the number of partial areas in x- and y- direction respectively and l_x, and l_y the outer dimensions of the grid; the input parameters define the resolution Δx and Δy and total number of the partial areas.

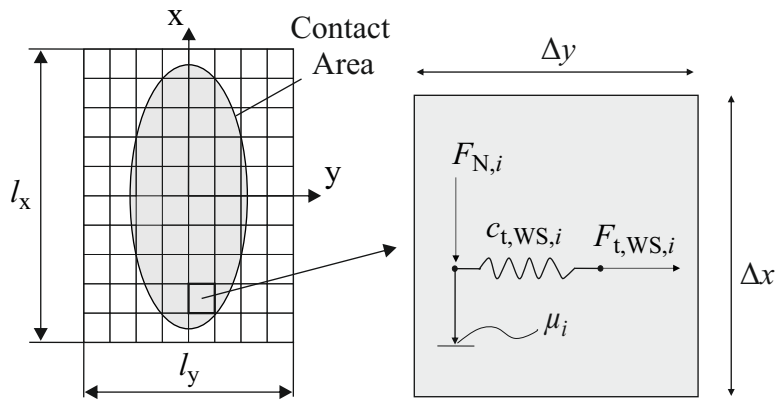

Figure 4.3: Discretised friction model with partial area elements, each modelled using Jenkin elements.

To calculate the partial contact normal forces $F_{N,i}$, the FE-model results are interpolated to the mesh grid of the friction model using the *scatteredInterpolant* function within *MATLAB* and linear interpolation method. Between the updating time steps of the FE-model, the interpolated normal force distribution is normalized to the current bond normal force $F_{BN}(t_{Sim})$ to satisfy static equilibrium condition. As bond formation takes place in sequential steps it is assumed that the whole interface area between wire and substrate can be divided into three parts (figure 4.4):

- Oxide layer area: initial contamination like oxides prevent the bond formation. To remove contamination frictional work W_f is needed to clean the surface.
- Activated area: the clean parts of the interface are activated for bond formation. The activation state $\tau = A_{Activated}/A_{C,WS}$ is increased by cleaning and is mandatory for bond formation.
- Bonded area: frictional work in activated areas leads to bond formation and bonding state $\gamma = A_{Bonded}/A_{C,WS}$ is increased.

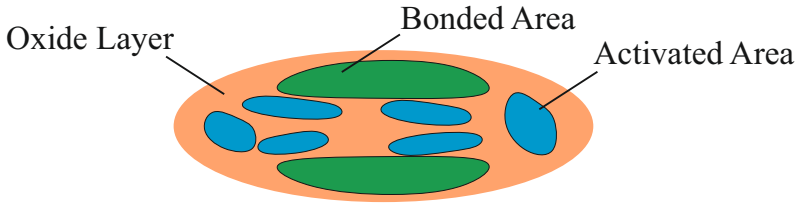

Figure 4.4: Interface of wire and substrate subdivided into areas of oxide layers, activated areas and bonded areas.

The cleaning and bonding behaviour is modelled by the following system of differential equations for the states τ and γ:

$$\begin{aligned} \Delta\tau_{i,n_{\mathrm{Osc}}} &= \alpha \, \frac{\Delta W_{\mathrm{f},i,n_{\mathrm{Osc}}}}{\Delta x \; \Delta y} \; \left[1 - \gamma_{i,n_{\mathrm{Osc}}-1} - \tau_{i,n_{\mathrm{Osc}}-1}\right] - \Delta\gamma_{i,n_{\mathrm{Osc}}} \\ \Delta\gamma_{i,n_{\mathrm{Osc}}} &= \beta \, \frac{\Delta W_{\mathrm{f},i,n_{\mathrm{Osc}}}}{\Delta x \; \Delta y} \; \tau_{i,n_{\mathrm{Osc}}-1}. \end{aligned} \tag{4.1}$$

The changes $\Delta\gamma_{i,n_{\mathrm{Osc}}}$ and $\Delta\tau_{i,n_{\mathrm{Osc}}}$ of states of the i-th area element within one period of the n-th oscillation cycle with period length $T_{\mathrm{P},n_{\mathrm{Osc}}}$ are described by the right hand sides. For the activation state $\tau_{i,n_{\mathrm{Osc}}}$ only the amount of frictional work in the oxide layer area is taken into account. At the same time, when activated areas have been bonded, $\tau_{i,n_{\mathrm{Osc}}}$ decreases by the amount of $\Delta\gamma_{i,n_{\mathrm{Osc}}}$. The coefficients α and β are material dependent model parameters, which are identified from measurements.

Compared to the model approaches presented by Mayer and Schwizer in equation 2.7 and by Gaul in equation 2.8, the bond formation model in equation 4.1 was extended by the cleaning state τ and the size S of the contact area is captured by the constant size $\Delta x \; \Delta y$ of the partial areas. As a discretised friction model is used, the changing size of the interface area $A_{\mathrm{C,WS}}$ during bond formation is captured by the amount of active partial areas in the contact with the information of the area size received from the FE model in the co-simulation.

The single point friction contacts of i-th partial area is modelled by *Jenkin Elements* using the evolution differential equation

$$\dot{F}_{\mathrm{t,WS},i} = c_{\mathrm{WS},i} \; \dot{u} \left(1 - \frac{1}{2}\left(1 + \mathrm{sign}(\dot{u} \; F_{\mathrm{T},i})\right) \left| \frac{F_{\mathrm{T},i}}{\mu_i \; F_{\mathrm{N},i}} \right|^m \right) \tag{4.2}$$

where $\dot{u} = \dot{\mathrm{x}}_{\mathrm{W}} - \dot{x}_{\mathrm{S}}$ is the relative velocity between wire and substrate and $\mu_i \; F_{\mathrm{N},i}$ defines the maximum tangential force $F_{\mathrm{t,WS},i}$ that can be transmitted by the Jenkin element. The exponent m determines the micro-slip behaviour during the transition from sticking to sliding; the larger m is, the sharper the transition is. Details on the evolution differential equation are described in [86, 130]. The stiffness $c_{\mathrm{WS},i}$ is calculated by the shear modulus G, the height h_{I} of the interface layer and the dimensions Δx and Δy of the contact area elements, see figure 4.5 and the description in section 4.1.3.

As oxide layer, activated and bonded show different frictional behaviour, a variable coefficient of friction $\mu_i(\gamma_i, \tau_i, F_{\mathrm{N},i})$ was defined by extending the bond formation model of Gaul et al. [34] to the following equation:

$$\mu_i(\gamma_i, \tau_i, F_{\mathrm{N},i}) = (1 - \gamma_i - \tau_i)\mu_{\mathrm{Ox}} + \tau_i \mu_{\mathrm{Met}} + \gamma_i \, \frac{\tau_{\mathrm{S}} \; \Delta x \; \Delta y}{F_{\mathrm{N},i}}. \tag{4.3}$$

Depending on the states τ_i and γ_i, the value of coefficient of friction μ_i changes. Initially, the coefficient of friction has the value μ_{Ox}. With increasing τ_i the coefficient of friction increases to the final value μ_{Met} for pure metal/metal contact of fully cleaned, but not yet bonded areas. In case of fully bonded partial area elements, μ_i is defined by dividing the maximum tangential force, calculated from shear strength τ_{S} of the material, by the normal force $F_{\mathrm{N},i}$. Thus, the condition

$$F_{\mathrm{t,WS,max}}(\gamma_i = 1, \tau_i = 0) = \tau_{\mathrm{S}}\ \Delta x\ \Delta y \tag{4.4}$$

is satisfied.

This is mandatory to achieve constant boundary condition for bonded areas within contact area between wire and substrate, independently from normal force distribution.

The coefficients μ_{OX}, μ_{MET} and τ_{S} are material dependent and are identified experimentally in section 5.2 and section 5.5.

For simulation of the wire bonding process, the shear force and the shear strength values need to be derived from the simulation results. The shear force is calculated by

$$F_{\mathrm{S}} = \tau_{\mathrm{S}} \sum_{i=1}^{n_{\mathrm{disc}}} \Delta x\ \Delta y\ \gamma_i. \tag{4.5}$$

For the i-th partial area element of the discretised friction model in *MATLAB*, the bonded area is calculated by multiplying the bonding state γ_i with the area size $\Delta x\ \Delta y$ of the partial area element. The bonded areas are then summed over all elements n_{disc} and multiplied with the shear strength of the corresponding wire material. The shear strength is calculated by dividing the shear force with the contact area $A_{\mathrm{C,WS}}$ which is calculated by summation of all partial area elements in the contact between wire and substrate.

4.1.3 Wire and tool-wire contact model

In figure 4.5 the wire model is shown; the wire is modelled as a point mass with coordinate x_{W} and mass m_{W}, which is connected to the tool tip (coordinate x_{BT}) via a friction contact that transmits the tangential force $F_{\mathrm{t,TW}}$ to the wire. The stiffness $c_{\mathrm{t,W}}$ represents the shear stiffness of the wire in direction of the vibration, which depends on the vertical position z_{WD} of the tool tip. Parallel to the spring $c_{\mathrm{t,W}}$, there is the spring $c_{\mathrm{t,TW}}$, which represents the form fit between the bond tool and the wire at the front and back radii; see section 5.6 for the parametrization of the tangential stiffness. On the bottom side, the reaction force $F_{\mathrm{t,WS}}$ from the contact between wire and substrate acts on the wire; $F_{\mathrm{t,WS}}$ is the result of the summation of the single forces $F_{\mathrm{t,WS},i}$, which result from the discretized friction contact for the i-th partial area of the bond formation model. The wire mass m_{W} is calculated from the density of the corresponding material (Al/Cu) and the the volume of the wire corresponding to the tail and the part underneath the v-groove of the bond tool.

The differential equation for the wire mass is:

$$m_{\mathrm{W}}\ddot{x}_{\mathrm{W}} = F_{\mathrm{t,TW}} + F_{\mathrm{t,WS}}. \tag{4.6}$$

The tangential stiffnesses $c_{\mathrm{t,WS},i}$ are calculated by the shear modulus G, the height h_{I} of the interface layer shown in figure 4.5 and the dimensions Δx and Δy of the contact area elements:

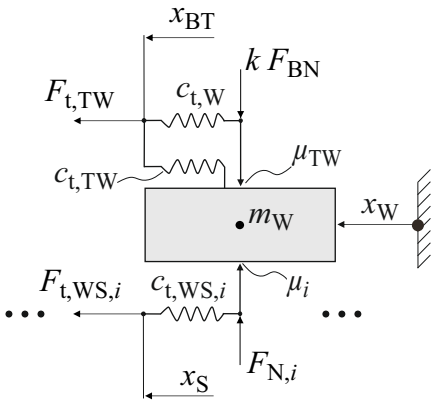

Figure 4.5: Model of the wire as a rigid body and the two frictional contacts between bonding tool and wire and between wire and substrate.

$$c_{t,WS,i} = \frac{G\,\Delta x\,\Delta y}{h_I}. \tag{4.7}$$

The height h_I of the interface layer refers to the height of the metallization, which is 300 µm in case of the investigated DCB from section 3.2.

4.1.4 Normal force magnification between bond tool and wire

The magnification k of the bond normal force in the contact between the tool and the wire mainly depends on the tool opening angle α_{BT} of the v-groove; to identify the factor k, finite element simulations have been carried in this section. In figure 4.6 the reaction forces between bond tool and wire are shown. The bond normal force F_{BN} splits to the two contact points P_1 and P_2, which are merged to the one single point contact of tool and wire in figure 4.5 a).

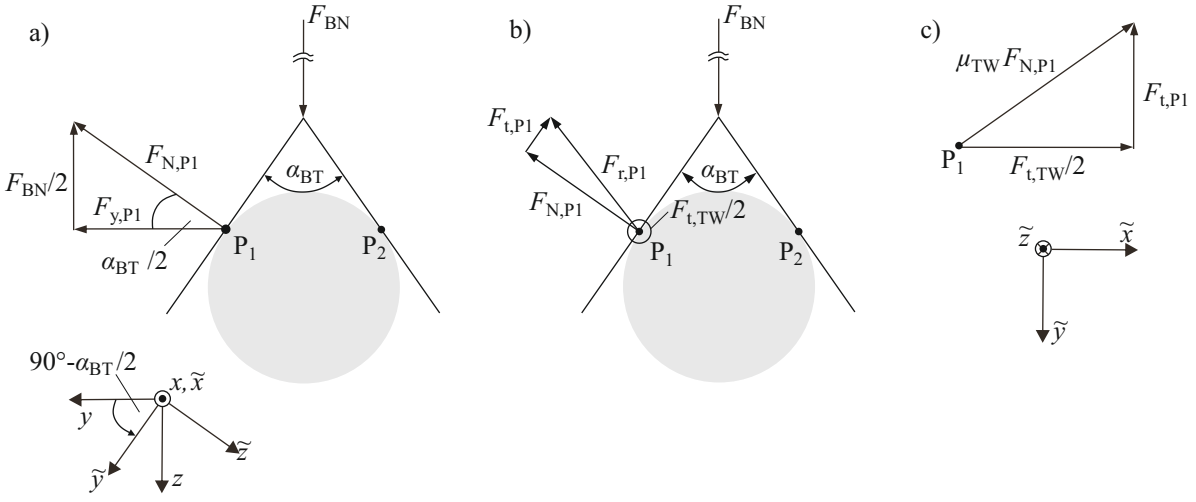

Figure 4.6: Reaction forces between bond tool and wire for a) frictionless contact and b) frictional contact between bond tool and wire. The friction force components in x - and $\tilde{y}$ - direction are shown in c).

When assuming frictionless contact as shown in figure 4.6 a), the magnification factor k can be calculated by

$$k = \frac{F_{\mathrm{N,P1}} + F_{\mathrm{N,P2}}}{F_{\mathrm{BN}}} = \frac{1}{\sin(\frac{\alpha_{\mathrm{BT}}}{2})} \; \forall \; \alpha_{\mathrm{BT}} \in (0, \pi]. \tag{4.8}$$

Neglecting friction in the contact between bond tool and wire represents is inconsistent with transmitting tangential force F_{TW}. In figure 4.6 b) and c) additional forces parallel to the tool flank in direction of $\tilde{y}$ and in x-direction are included. The force in direction of $\tilde{y}$ has a component in the direction of F_{BN}, thus the magnitude of $F_{\mathrm{NP,1}}$ in figure 4.6 b) is reduced.

The following inequality can be derived from figure 4.6 c):

$$F_{\mathrm{t,P1}} \leq \sqrt{\left(\mu_{\mathrm{TW}} \; F_{\mathrm{N,P1}}\right)^2 - \left(\frac{F_{\mathrm{TW}}}{2}\right)^2}. \tag{4.9}$$

If there is no bond tool deflection, F_{TW} is equal to zero $F_{\mathrm{t,P1}}$ is smaller or equal to $\mu_{\mathrm{TW}} \; F_{\mathrm{N,P1}}$. For this case, an inequality for k can be derived from the reaction forces in figure 4.6 b) using the relationship $F_{\mathrm{N,P1}} = k \; \frac{F_{\mathrm{BN}}}{2}$:

$$\begin{aligned} &\frac{F_{\mathrm{BN}}}{2} = F_{\mathrm{N,P1}} \; \sin\left(\frac{\alpha_{\mathrm{BT}}}{2}\right) + F_{\mathrm{t,P1}} \; \cos\left(\frac{\alpha_{\mathrm{BT}}}{2}\right) \\ &\Rightarrow k \geq \frac{1}{\sin\left(\frac{\alpha_{\mathrm{BT}}}{2}\right) + \mu_{\mathrm{TW}} \; \cos\left(\frac{\alpha_{\mathrm{BT}}}{2}\right)} \; \forall \; \alpha_{\mathrm{BT}} \in (0, \pi]. \end{aligned} \tag{4.10}$$

For $F_{\mathrm{TW}} \neq 0$, a closed analytical solution for k cannot be easily found, because F_{TW} is unknown. Similar to the analytical model for ultrasonic friction reduction described in section 2.2.3.2, the force component of F_{TW} is affected by the velocity ratio ξ of the sliding velocity in vibration direction and the sliding velocity in $\tilde{y}$-direction. However, the aim here is to determine a constant and not a time-varying factor k in order to improve numerical convergence and thus reduce the computation time. Therefore a finite element simulation with the wire bond model shown in figure 4.2 was carried out to estimate the magnification factor k numerically. Three different kind of simulations were carried out: with frictionless contact between tool and wire, with frictional contact (μ_{TW} equal to 0.4 [2]) and with frictional contact and a horizontal deflection of x_{BT} equal to 15 µm; a deflection of 15 µm was chosen to ensure, that the transition from stick to slip occurs to receive the maximum transmittable tangential force. The simulation was carried out with a bond normal force of 15 N for copper wire material.

The results are shown in figure 4.7 a); for the simulation with frictionless contact, the results from finite element simulation and the analytical solution of equation 4.8 correlate well; for α_{BT} equal to 70°, k is equal to 1.74. For the simulation with frictional contact but without horizontal deflection the magnification k is equal to 1.2 and for the simulation with frictional contact and horizontal deflection k is equal to 1.5. The magnification increases for the simulation with horizontal deflection compared to the simulation with friction only because the additional force component $F_{\mathrm{TW}}/2$ decreases $F_{\mathrm{t,P1}}$ since the

absolute value of the resulting force vector is limited by the value of μ_{TW} $F_{N,P1}$, see figure 4.7 c). Since only $F_{t,P1}$ and not F_{TW} has a force component in the z-direction and therefore contributes to the reaction force of F_{BN} in addition to $F_{N,P1}$, $F_{N,P1}$ increases when $F_{t,P1}$ is reduced in order to maintain the force equilibrium. As the factor k depends on the tangentially applied force F_{TW} and in order to reduce the complexity of the model, the average value 1.35 between the upper and lower limit if considering friction is assumed for k for the following investigations; otherwise k would be time-variant and would oscillate with F_{TW}.

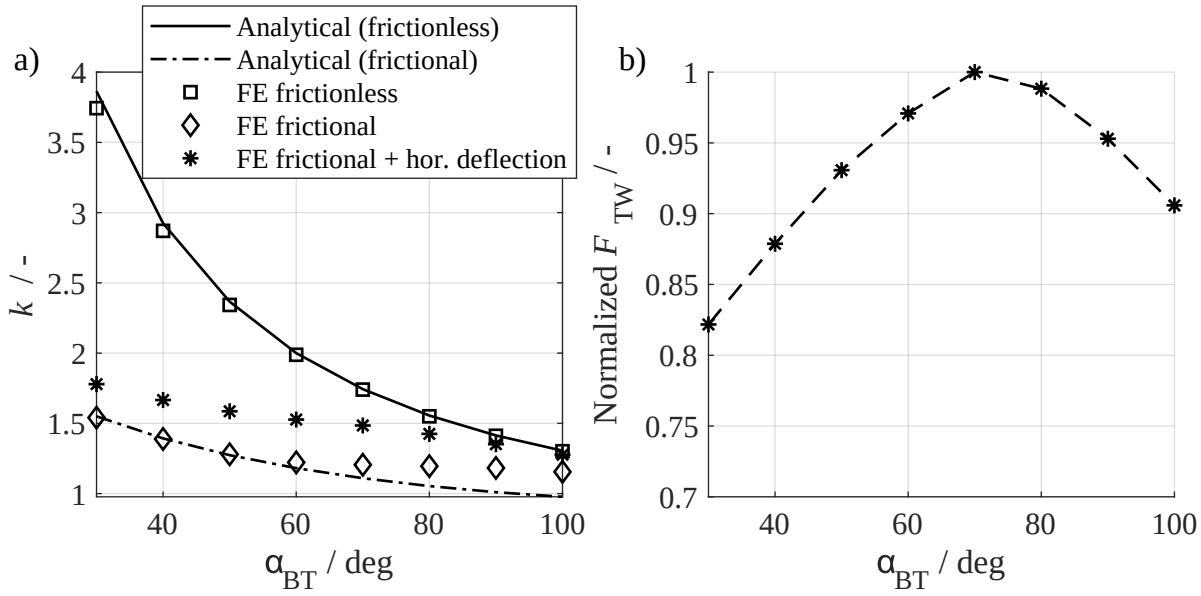

Figure 4.7: Results of finite element simulation for a) the factor k for different contact conditions between bond tool and wire and b) the maximum transmittable and normalized force F_{TW} for frictional contact with horizontal deflection.

Since the maximum transmissible tangential force is an important parameter of the bond tool design, the normalized maximum transmissible force F_{TW} received from the simulation has been plotted in figure 4.7 b); the maximum occurs for the standard angle of α_{BT} equal to 70°, so that this opening angle can be regarded as optimal in this respect. In fact, α_{BT} also has an influence on other process variables such as the vertical deformation behaviour measured as vertical position z_{WD}: the smaller α_{BT} is selected, the faster the tool penetrates into the wire, so that early tool/substrate contacts can occur. Therefore, the choice of α_{BT} is also a compromise between maximum transferable tangential force and acceptable wire deformation behaviour. The influence of α_{BT} on bond quality is rather complex [142].

4.1.5 Ultrasonic softening model

From the state of the art in section 2.2.3, it is known that the ultrasonic softening effect is based on three mechanisms: stress superposition, dynamic impact (friction reduction), and metallurgical volume effects. The separate simulation of the three mechanisms contributing to the ultrasonic softening effect would lead to separate models for the ultrasonic friction reduction, the stress superposition and acoustic softening and consequently to additional model parameters which need to be identified by sophisticated experiments.

First steps in this direction were made in section 5.4.2 and the master thesis of Müller [89], but finally it was not yet possible to quantify all three effects in detail due to metrological limitations (e.g. reliable measurements of reaction forces at high frequencies). Thus, a phenomenological model approach for the ultrasonic softening model was chosen, which is based on the ultrasonic wire bonding tests, where the correlation between wire deformation and evaluation of shear force values was observed.

The ultrasonic softening effect is modelled based on the factor k_{USS} which is used to scale the stress-strain curves of the wire material in such a way that the wire material is softened; this method of modelling the softening effect has previously been published by Althoff et al. [2]. In figure 4.8, exemplary stress-strain curves for different levels of k_{USS} are shown. The scaling factor k_{USS} is calculated within *MATLAB* and is applied to the global wire volume; thus, a homogeneous distribution of the ultrasonic softening effect is assumed. To account for the local distribution of softening across the wire volume, the ultrasonic excitation must be imposed in the FE model in *ANSYS* itself to account for the resulting distribution of ultrasonic loading across the elements of the mesh of the wire volume. With this approach, for example, the local influence of stress distribution as a result of the static and dynamic loading could be taken into account to perform a more detailed analysis of the deformation behaviour over the wire cross section. Within the co-simulation of the wire bond model, the FE-simulation is used to calculate the normal force distribution and contact area size between wire and substrate and additionally the vertical height z_{WD} of the bond tool to simulate tool/substrate contacts; these results are influenced by the global softening behaviour of the wire. Thus, the model approach with the scaling factor k_{USS} applied to the global wire volume is chosen here.

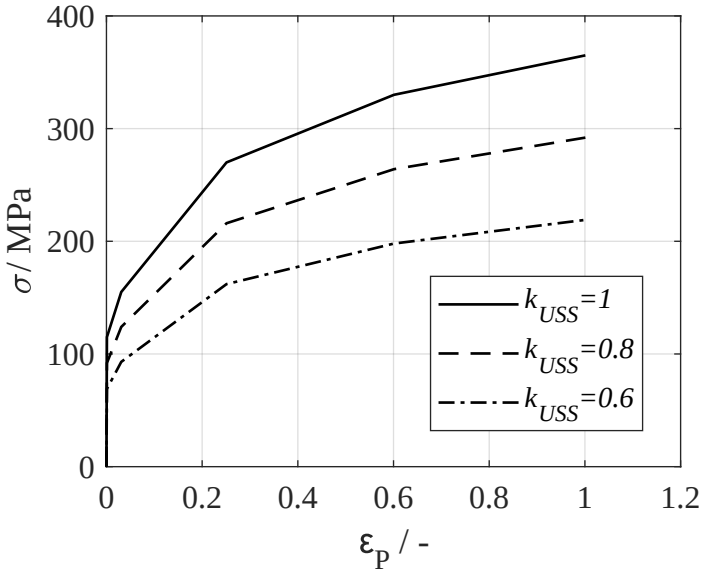

Figure 4.8: Exemplary stress strain curves for different values of k_{USS}.

The central question of modelling the ultrasonic softening effect is: which physical variable in the ultrasonic wire bonding process should be chosen to calculate k_{USS}?

In most of the published results from the state of the art, the vibration amplitude was measured during deformation tests and general result was that the larger the vibration amplitude is, the higher is the resulting softening. Thus, it seems to be obvious, that

the ultrasonic softening effect depends on the vibration amplitude. In spite of this, it is known from ultrasonic wire bonding experiments, that the vibration amplitude decreases with rising bond duration, while the wire deformation continues to increase at constant bond normal force, see figure 3.18 and figure 3.19. Thus, vibration amplitude cannot be the only parameter to be considered. As summarized in the state of the art in section 2.4.2, various modelling approaches based on ultrasonic power per irradiation area (ultrasonic intensity), ultrasonic power per specimen volume, and approaches using ultrasonic energy instead of the power as input variables have been presented in the past. For calculating k_{USS}, the ultrasonic intensity $P_{\mathrm{US,I}}$ transmitted from the bond tool to the wire was chosen as the input variable of the ultrasonic softening model for the following reasons:

- The power and not the energy is used, because the material softening is a transient effect which immediately changes to the quasi-static material behaviour when the ultrasonic excitation is turned off.
- The ultrasonic intensity is chosen for phenomenological reasons: at the beginning of the bonding process, when the ultrasonic power is transmitted through small contact area, most of the softening of the wire occurs. The wire volume underneath the bond tool remains approx. constant. Thus, the ratio between ultrasonic power to the corresponding contact area through which the power is transmitted is suitable.

The ultrasonic power is calculated from the tangential force $F_{\mathrm{t,TW}}$ and the velocity $\dot{x}_{\mathrm{BT}}$ in direction of the bond tool vibration:

$$P_{\mathrm{US}} = \dot{x}_{\mathrm{BT}}\, F_{\mathrm{t,TW}}. \tag{4.11}$$

As shown in figure 4.9, the ultrasonic power P_{US} is transmitted to the wire through the contact area $A_{\mathrm{C,TW}}$ between bond tool and wire. The ultrasonic intensity measured in $\mathrm{W/m^2}$ is defined as ultrasonic power per unit area and is calculated by the following equation:

$$P_{\mathrm{US,I}} = \frac{P_{\mathrm{US}}}{A_{\mathrm{C,TW}}}. \tag{4.12}$$

The ultrasonic intensity splits into the bulk deformation of the wire, the non-conservative power within the frictional contacts between bond tool and wire and between wire and substrate. A small amount of $P_{\mathrm{US,I}}$ is also transmitted through the contact area $A_{\mathrm{C,WS}}$ into the substrate substructure which does not directly contribute to the ultrasonic softening effect, but can be neglected in bond applications like sufficiently fixed DCB-substrates investigated in this PhD thesis.

Based on the findings reported by Siddiq et al. [116], an exponential approach is chosen for the calculation of k_{USS} based on the ultrasonic intensity $P_{\mathrm{US,I}}$:

$$k_{\mathrm{USS}} = 1 - a\, P_{\mathrm{US,I}}^{b}. \tag{4.13}$$

The factor k_{USS} is calculated in *MATLAB* for all time steps, depending on the bond formation and the finite element model is updated when the change of k_{USS} is larger then a specified criteria, see the program sequence plan in figure 4.16. The coefficients

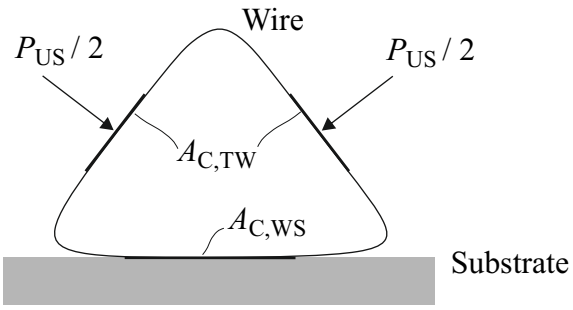

Figure 4.9: Transmission of the ultrasonic power P_{US} to the wire.

a and b are determined in section 5.4.2 by comparing the simulated results of z_{WD} to the measured results from the ultrasonic bonding tests. Since the ultrasonic intensity describes the ratio of the applied power to the active area, but not directly the volume of the sample, it is evident that the model parameters are also dependent on the size of the sample. This means that a certain level of ultrasonic intensity will result in greater softening for a smaller volume of the sample than for a larger volume. For example, if the wire diameter is significantly changed, the model parameters must therefore be newly determined.

4.1.6 Substrate model

For modelling the substrate dynamics, the method of modal superposition is used; the modal description is beneficial in terms of reducing the number of degrees of freedom by approximating the dynamical behaviour of the substrate and substructure with the most relevant modes while neglecting e.g. higher modes with less relevance on the dynamical behaviour for the specific excitation.

The work flow for performing the model order reduction and creating a state space model for the substrate dynamics in *MATLAB* is shown in figure 4.10. In the first step, a CAD-model (here within *SolidWorks*) of the substrate and substructure is created. The geometry is imported into *ANSYS* to perform a numerical modal analysis which results into the eigenvectors of the investigated system. At this step, a wide frequency range in *ANSYS* is used to consider all relevant mode shapes up to 1.5 times the frequency range which should be captured in the simulation. The eigenvectors are then exported from *ANSYS* to *MATLAB* and a state space system is created; details on how a state space system can be created from the eigenvectors are described by Hatch in [46]. The created state space system has a high number of states because of the wide frequency range used; thus, model order reduction (MOR) is done within *MATLAB*.

The equations of motion of the undamped structure are given by

$$\underline{M}\,\underline{\ddot{q}}(t) + \underline{K}\,\underline{q}(t) = \underline{f}(t) \tag{4.14}$$

where $\underline{M}$ is the mass matrix, $\underline{K}$ the stiffness matrix, $\underline{q}(t)$ the coordinate vector and $\underline{f}(t)$ the force vector. Discretization by meshing in *ANSYS* quickly leads to 100.000 degrees of freedom (DOF) or more, thus a reduction of the DOF is necessary for an efficient simulation within *MATLAB*. In order to reduce the number of DOF of the system in

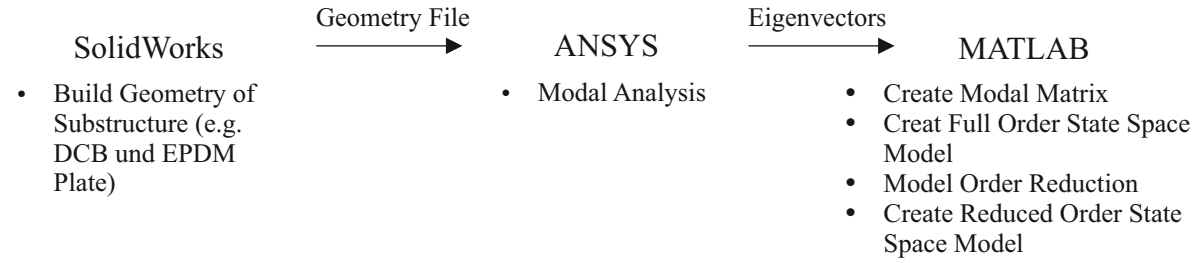

Figure 4.10: Workflow for creation of reduced state space model of the substructure dynamics in *MATLAB*, based on the numerical modal analysis in *ANSYS*.

equation 4.14 to $\tilde{n}_{\mathrm{DOF}} < n_{\mathrm{DOF}}$, a coordinate transformation must be performed with the transformation matrix $\underline{T}$ with the dimension of $(n_{\mathrm{DOF}}, \tilde{n}_{\mathrm{DOF}})$, which transforms the system in equation 4.14 into a reduced basis with $\underline{\tilde{q}}$:

$$\begin{aligned} \underline{q} &= \underline{T}\ \underline{\tilde{q}} \\ \Rightarrow \underline{T}^T\ \underline{M}\ \underline{T}\ \underline{\ddot{\tilde{q}}}(t) + \underline{T}^T\ \underline{K}\ \underline{T}\ \underline{\tilde{q}}(t) &= \underline{T}^T\ \underline{f}(t) \\ \Leftrightarrow \underline{\tilde{M}}\ \underline{\ddot{\tilde{q}}} + \underline{\tilde{K}}\ \underline{\tilde{q}} &= \underline{\tilde{f}}(t). \end{aligned} \tag{4.15}$$

The transformed differential equation in equation 4.15 now has $\tilde{n}_{FHG}$ DOF. As simple as the method of model order reduction may seem, the challenge is to determine a suitable transformation matrix $\underline{T}$. The aim of the reduction is to represent the original system behaviour of equation 4.14 as accurately as necessary with the smallest possible number of DOF $\tilde{n}_{FHG}$. One method to transform the original system and reduce the DOF is the *Modal Superposition* method [46]. The eigenvectors and eigenfrequencies from a numerical modal analysis are needed, which can be exported from *ANSYS* by saving them into text files by user defined commands. Because of the good import possibilities in *MATLAB* and the provenness of this method to represent dynamic deformation behaviour, this method is used to represent the substrate dynamics in the wire bond model. The transformation matrix is the modal matrix $\underline{Q} = [\hat{q}_1, ..., \hat{q}_{n_{Modes}}]$, which consists of the eigenvectors $\hat{q}_j$ and has the dimension $(n_{\mathrm{DOF}}, n_{\mathrm{Modes}})$. In *ANSYS* the modal matrix is mass normalized, which means that the mass matrix is transformed to the identity matrix and it follows:

$$\begin{aligned} \underbrace{\underline{Q}^T\ \underline{M}\ \underline{Q}}_{=\underline{I}}\ \underline{\ddot{\xi}}(t) + \underbrace{\underline{Q}^T\ \underline{K}\ \underline{Q}}_{diag\left(\omega_j^2\right)=\underline{\Omega}^2}\ \underline{\xi}(t) &= \underline{Q}^T\ \underline{f}(t) \\ \Leftrightarrow \underline{\ddot{\xi}}(t) + \underline{\Omega}^2\ \underline{\xi}(t) &= \underline{Q}^T\ \underline{f}(t). \end{aligned} \tag{4.16}$$

The system equations in equation 4.16 are decoupled from each other, so the matrices have diagonal form, with the unit matrix taking the place of the mass matrix and the diagonal matrix with the squared natural frequencies taking the place of the stiffness matrix and where $\underline{\xi}$ is the vector of modal coordinates; equation 4.16 can be extended by a modal damping $diag\,(2D_j\omega_j) = \underline{\Delta}$:

$$\underline{\ddot{\xi}}(t) + \underline{\Delta}\ \underline{\dot{\xi}}(t) + \underline{\Omega}^2\ \underline{\xi}(t) = \underline{Q}^T\ \underline{f}(t) \tag{4.17}$$

For the numerical solution in *MATLAB*, the state space representation is suited due to

its compact form; for the j-th mode, the state space representation is given by:

$$\underbrace{\begin{pmatrix} x_{j,1} \\ x_{j,2} \end{pmatrix}^{\bullet}}_{\underline{\dot{x}}_j} = \underbrace{\begin{pmatrix} 0 & 1 \\ -\omega_j^2 & -2\,D_j\omega_j \end{pmatrix}}_{\underline{A}_j} \underbrace{\begin{pmatrix} x_{j,1} \\ x_{j,2} \end{pmatrix}}_{\underline{x}_j} + \underbrace{\begin{pmatrix} \underline{0}^T \\ \underline{\hat{q}}_j^T \end{pmatrix}}_{\underline{B}_j} \underline{f}(t) \tag{4.18}$$

For describing the dynamical behaviour of the substrate in the bond model, the tangential force $F_{\mathrm{t,WS}}$ between wire and substrate is chosen as the input and the displacement x_{S} and velocity $\dot{x}_{\mathrm{S}}$ at the bond position on the DCB as the outputs:

$$\begin{aligned} \underline{\dot{x}} &= \underline{A}\,\underline{x} + \underline{B}\,F_{\mathrm{t,WS}} \\ \begin{bmatrix} x_{\mathrm{S}} \\ \dot{x}_{\mathrm{S}} \end{bmatrix} &= \underline{C}\,\underline{x}. \end{aligned} \tag{4.19}$$

The model order of the state space system in equation 4.19 depends on the number of modes, that are taken into account; the dimension of the state space model is twice as high as the number of the modes. In order to reduce the simulation time, only those modes, that are relevant for the vibration direction and frequency of the excitation at the bond position should be taken into account. To rate the relevance of the modes, the *Hankel Singular Values* (HSV) are used to rate the controllability and observability of the modes [61, 109]. Here controllability means that the respective mode can be excited by the force $F_{\mathrm{t,WS}}$; if this is not the case, this mode does not play a significant role in the dynamics of the system because it can not be excited by the input of the state space. Observability the influence of the mode on the system output; in this case this is the displacement and velocity at the bond position. For example, if the mode has a vibration node at the bond position, the observability is very low and the mode can be neglected. With the HSV, both, the controllability and observability of the i-th state can be rated; within *MATLAB* the command *balreal* [128] is used to calculate the HSV. If one sets a threshold value for the HSV, the order of the state space can be reduced by the amount of states with HSV lower than the threshold [32].

In figure 4.11 the geometry for the substrate structure is shown as a CAD model in *Solidworks*. Like in the wire bonding experiments in section 3.2, the DCB has the dimensions 55 mm x 39 mm x 0.9 mm and is fixed to the EPDM plate via a bonded contact; the EPDM plate is fixed to an aluminium plate via a bonded contact. In *ANSYS Workbench*, the geometry was meshed with quadratic tetrahedra elements and a numerical modal analysis was performed up to 300 kHz; 3885 modes were identified in this frequency range. After the modal analysis, the eigenvectors were saved as a text file for further processing in *MATLAB*. Additionally, the node numbers at the bond position are written in additional text files for building the state space with the desired inputs and outputs according to equation 4.19. The material properties used for the modal analysis within *ANSYS Workbench* are given in table A.1.

The balanced transformation was then carried out within *MATLAB* and the HSV was determined in order to carry out the model order reduction; the results are shown in figure 4.12. Beginning from the 37th state of the balanced state space, the states were truncated, thus the reduced state space model has the model order of 36 states; compared to the full state space model with 7770 states, the model order could be reduced by a

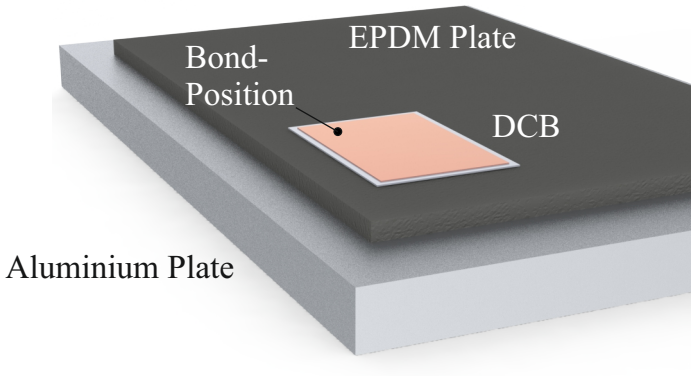

Figure 4.11: Geometry of the substrate substructure with the DCB on an EPDM-plate which is fixed on an aluminium plate; the bond position is marked on the DCB.

factor of 99.5 %. The first 50 HSV of the balanced state space are shown in figure 4.12 a); the first four HSV are not visible, because their values are 10-100 times larger than the remaining HSV and therefore the scale of the y-axis has been adapted to the remaining 46 HSV. Small HSV indicate states, that are either badly controllable or observable. If the HSV are sorted and plotted in a descending order, then large jumps indicate that at this point the either the observability or the controllability of the states has changed significantly. In figure 4.12 a) those jumps occur e.g. at the state numbers 7, 13, 21, and 37. It was found that in the frequency range up to 300 kHz there is a very good agreement with the full state space when cutting off from the 37th state. A comparison of the frequency responses and phase diagrams between the applied tangential force $F_{\mathrm{t,WS}}$ and the resulting displacement amplitude x_{S} at the bond position is given in figure 4.12 b). Especially in the frequency range of the typical bond frequencies of 40 kHz to 100 kHz, a good match of the two frequency responses was achieved. This is also the case in the frequency range of the higher harmonic frequencies that occur in processes with friction. For 60 kHz, these are the frequencies 180 kHz and 300 kHz, where the reduced model also agrees well with the full state space model.

4.1.7 Ultrasonic excitation

The ultrasonic excitation in the bond model can be implemented in many ways: in principle, all models can be implemented which have a displacement as output variable which should correspond to the bond tool amplitude. In the field of modelling ultrasonic transducers, different approaches exist to derive computationally efficient models. For the ultrasonic wire bond transducer, an equivalent model which has been presented by Brökelmann et al. [14, 134] can be used. The model describes the electromechanical behaviour of a piezoelectric elements and the mechanical structure of the transducer close to its resonance frequency and includes a phased locked loop (PLL) controller, which controls the excitation frequency f_{T} to match the resonance frequency of the transducer. Inputs of the transducer model are ultrasonic voltage u_{T} and tangential contact force $F_{\mathrm{T,TW}}$ between bonding tool and wire at the tool tip. The outputs are the excitation frequency f_{T} of the PLL and the resulting tool tip amplitude x_{BT}.

Alternatively a signal generator can be chosen with constant values for with excitation

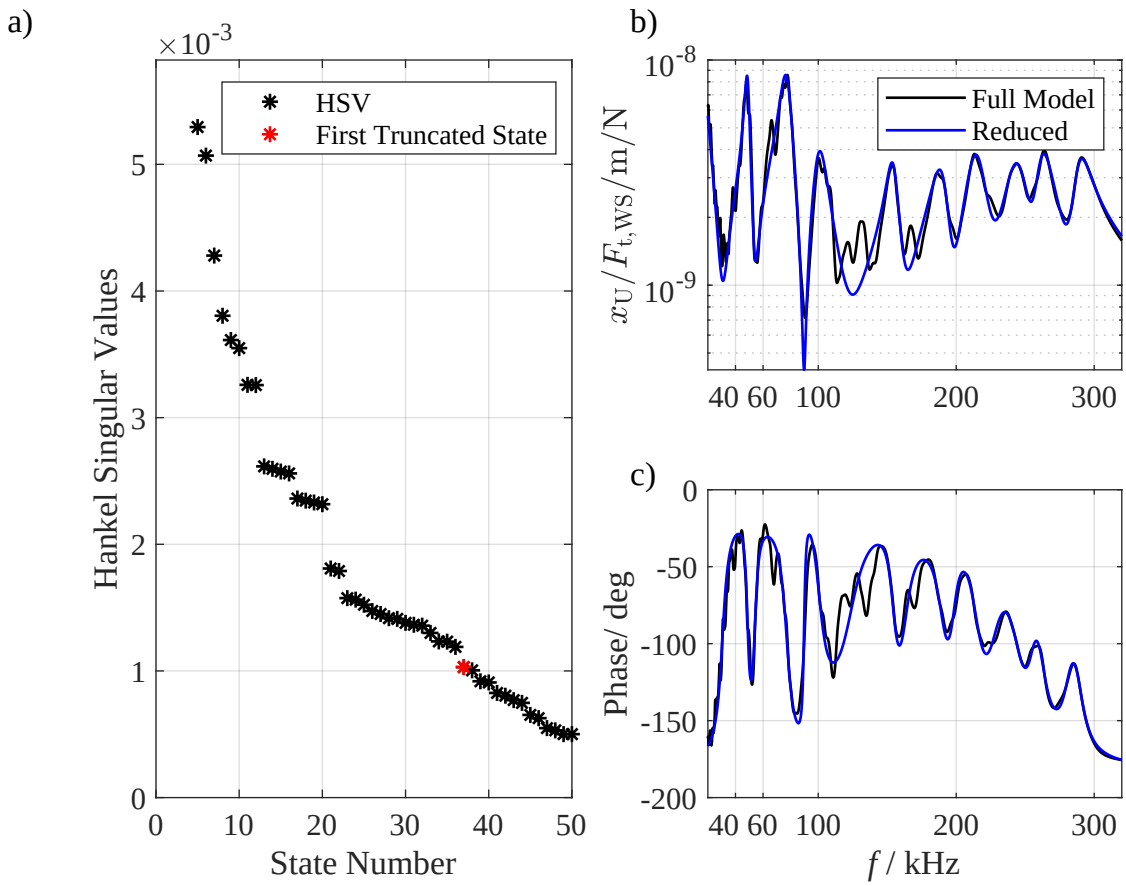

Figure 4.12: Results of the model order reduction based on the balanced transformation with a) the Hankel Singular Values, b) the frequency response and c) the phase diagram.

frequency and vibration amplitude set by the user. This method is chosen in the framework of this PhD, as it allows for exactly matching the amplitudes from the bonding tests to be exactly reproduced with the simulation input. Since the amplitude curves from the parameter studies in section 3.2.4 are known from laser measurements, they can be approximated by specifying amplitude values at characteristic times; this is shown in figure 4.13 for the copper wire. The amplitudes for the signal generator are given at the time points 0 ms, 15 ms, 50 ms and 300 ms for the different bond normal forces F_{BN} and ultrasonic voltages u_{T}. Depending on u_{T} and F_{BN}, there are different curves, e.g. at 20 N and 60 V, where the amplitude first rises to approx. 4.5 µm and then drops relatively quickly and then remains almost constant. On the other hand, the curve at 30 V looks very different: after 15 ms the amplitude reaches a value of approx. 2.5 µm and then rises to approx. 2.7 µm and also remains constant. Both curves can be mapped by the signal generator; if no laser measurements are available for the parameter combination of force and ultrasonic voltage to be simulated, the amplitudes are interpolated from the measured values of the forces and voltages using *scatteredInterpolant* function in MATLAB.

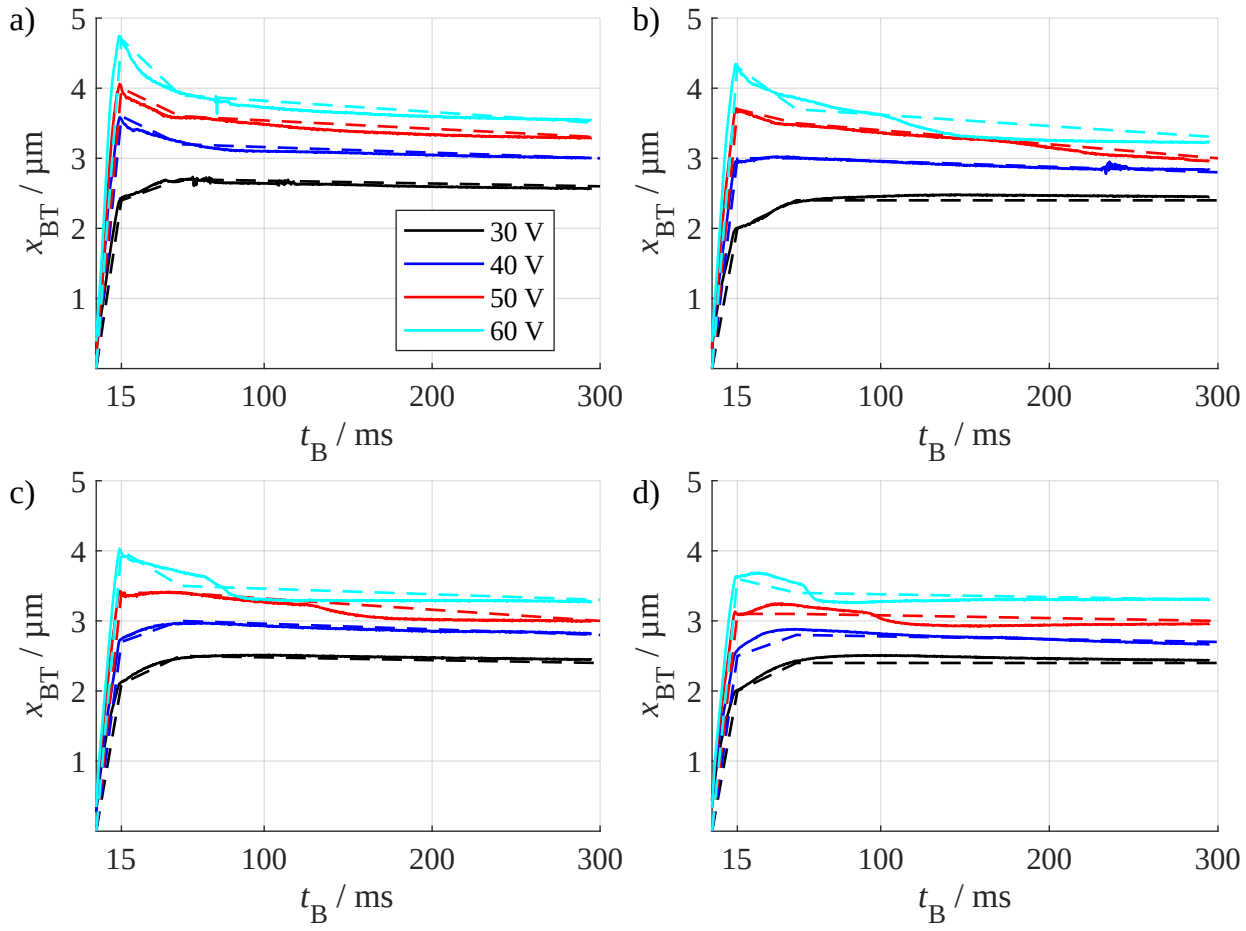

Figure 4.13: Copper wire: measured envelopes of the tool tip vibration (solid lines) and approximated curves by the signal generator in the bond model (dashed lines) for F_{BN} equal to a) 20 N, b) 26 N, c) 32 N and d) 38 N.

4.2 Program structure

Since the programming implementation of the co-simulation reached a high degree of complexity during the development of the bond model, the essential programme structure is summarised in this chapter. A graphical user interface (GUI) is used to set the input parameters for the simulation, such like the solver settings (number of cores for the FE-simulation, solver type, etc.), the bond parameters for a single bond simulation or for parameter sweeps the array with parameter combinations. The settings are stored in the *Cache.m* file, which is loaded by the object *Main* when starting the simulation.

In *MATLAB*, object-oriented programming was used to structure the individual sub-models as sub-objects of a master object - here called *Main*; figure 4.14 gives an overview and description of the objects. There are two categorical types of objects in the bond model: the objects *Main*, *Bondmodel*, and *MAaaS* , which contain the methods for the pre/post-processing and the solution process, and objects that contain the physical models such as the bond formation model and the differential equation systems for the dynamics of the substrate and wire.

In addition to the physical simulation models already presented in section 4.1, the interface to *ANSYS* was developed. In figure 4.14, this includes the *MATLAB-ANSYS as*

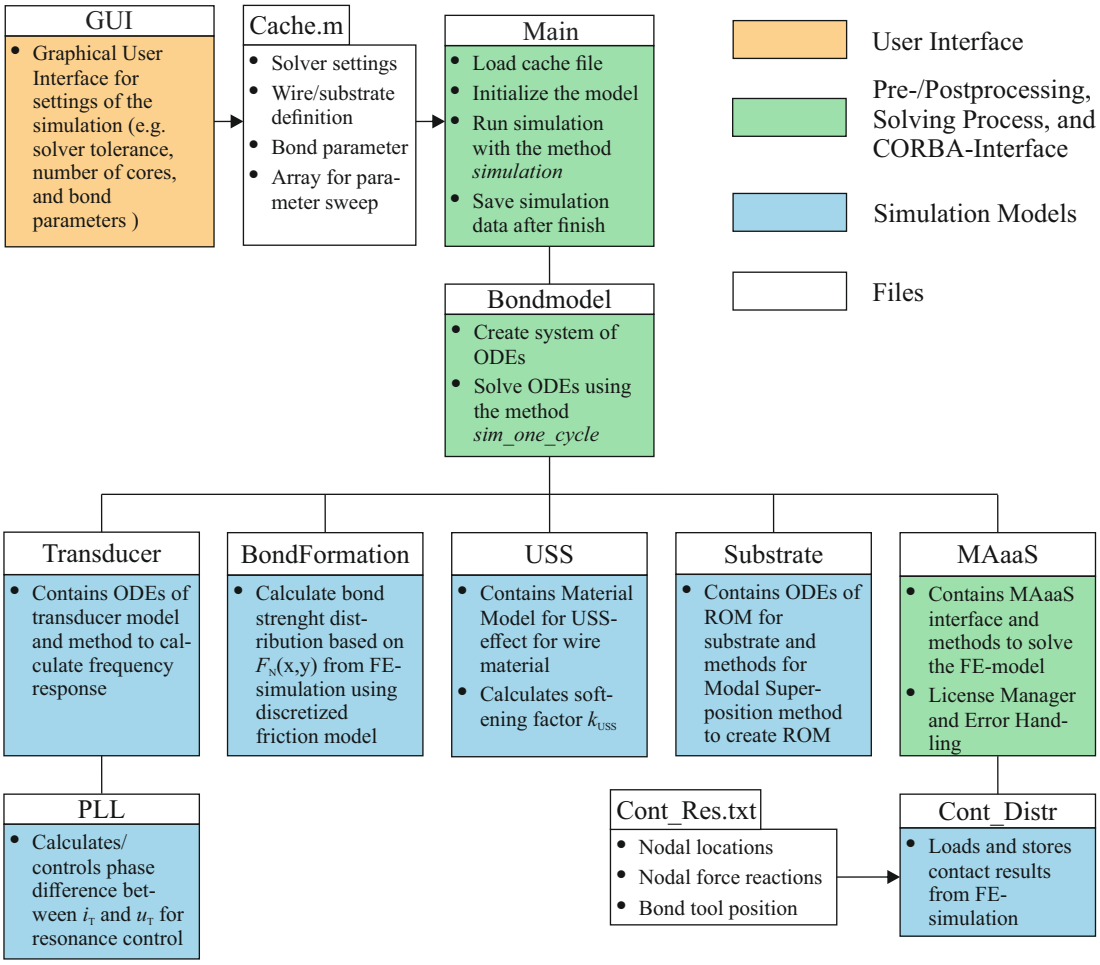

Figure 4.14: Object structure of the bond model within MATLAB.

a Server (MAaaS) object for communication with *ANSYS* and the object *Cont_Distr*, which is required for reading in and loading the contact results.

The *MAaaS* object contains several methods, so that in the following the interface between *MATLAB* and *ANSYS* (section 4.2.1), the multi frame restart option (section 4.2.1.1), the program sequence plan (section 4.2.1.2) are described. The simulation of the parameter studies is carried out on the computer cluster *OCuLUS* (Paderborn University) using the benefits of the HPC resources; the program structure for parallel simulation of the bond model and performance results of HPC are described in the appendix, see section A.4. The interface between *MATLAB* and *ANSYS* in section 4.2.1, the multi frame restart option in section 4.2.1.1 and the paralleled simulation for high performance computing in section A.4 were partially programmed as part of the master thesis of Krieger [62].

4.2.1 MATLAB-ANSYS as a Server (MAaaS) interface

The interface between *MATLAB* and *ANSYS* was programmed within *MATLAB* based on the *ANSYS as a Server* (AaaS) feature, provided by *ANSYS* as a *MATLAB* Toolbox [8] that allows local or remote client applications like *MATLAB* to access and interact with a running session of *ANSYS Mechanical*; the AaaS interface exists alongside the graphical user interface of *ANSYS Workbench* and the batch mode interface. The AaaS

function is different from batch mode in that commands, initialization, and intermediate and final result reporting can be issued to the running session at any time in addition to a predefined file, as long as the *ANSYS* solver has reached a stable point, e.g. after successfully ending an equilibrium iteration. This allows for solution steering and other manipulation without exiting from the running simulation [8]. The interface was programmed in the object *MAaaS* including an error handling to catch messages from the running *ANSYS* session, a license manager to limit the maximum of used licenses of *ANSYS* and *MATLAB* when using High Performance Computing running multiple simulations in parallel, and several methods to run *ANSYS Parametric Design Language* (APDL) commands from *MATLAB* during the simulation.

4.2.1.1 Multi Frame Restart

To reduce simulation time for the simulation of the parameter studies, the multi frame restart option in *ANSYS Mechanical* [6] is used, to calculate the load steps up to a maximum value $F_{\mathrm{TD,max}}$ of F_{TD}, which can than be reused for each simulation unless the fundamental simulation settings of the FE-model like the number of cores, or solver settings are changed. The simulation starts with the initial bond normal force equal to the touch down force $F_{\mathrm{BN}}(t_{\mathrm{Sim}} = 0) = F_{\mathrm{TD}}$; the results of the FE-Model for the set F_{TD} value are needed as the starting point for the co-simulation.

In figure 4.15 a), an illustration of the restart simulation is shown. Depending on the set touchdown force, the corresponding restart point is loaded to continue the FE-simulation at this load step; if the set touchdown force is not available as a restart file, the next smaller restart point is loaded and the difference to the set force is calculated in one load step. For comparison of simulation duration with and without restart, a touchdown force of $F_{\mathrm{TD}} = 20$ N and a bond normal force $F_{\mathrm{BN}} = 30$ N were simulated with the co-simulation of the wire bond model; the results are shown in figure 4.15 b). Without restart option, 12 load steps in *ANSYS* are needed to calculate the initial conditions at 20 N. Using the restart feature, about 50 % of the overall simulation duration of the co-simulation can be saved; especially the first load steps are time consuming, because the contact status between wire and substrate changes quickly with many elements coming into contact, so the time increment for solving the load steps in the beginning is relatively small for convergence reasons and most of the simulation time can be saved here.

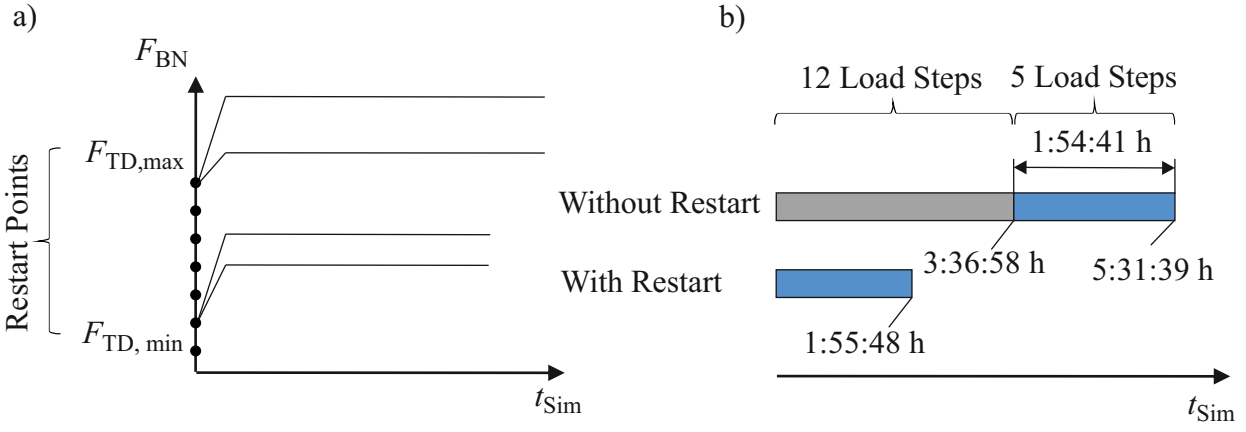

Figure 4.15: a) schematic visualisation of the restart option and b) representative reduction of the simulation time.

4.2.1.2 Program sequence plan to start a AaaS session

The program sequence plan for starting a AaaS session, performing a restart for the finite element model and running the co-simulation is shown in figure 4.16. After starting a wire bond model simulation, first the files for the restart analysis are checked, whether they are matching the simulation settings; when the database of the FE-model or the number of cores were changed or the restart files are simply missing, the restart files are generated and stored for the current and future simulations. When the files are available for the restart analysis, a AaaS session is started by executing following command to run the *ANSYS* Mechanical executable (exe) from command line in the AaaS mode:

```
Path_exe <options> -aas.
```

The command specifies the path to the executable and to the workspace for the FE-simulation, and amongst other things in the options the number of cores, main memory, and parallel processing method (shared memory, distributed memory). After starting the session, automatically a keyfile with the information for *MATLAB* to connect to the AaaS session is created. For this, the Java class ORB is initialized which allows for CORBA objects communicating with each other by connecting „objects making requests“ (clients, here *MATLAB*) with „objects servicing requests“ (servers, here *ANSYS Mechanical*) [91]. After the *MATLAB* client is connected to the running AaaS session, the restart files are loaded into the workspace of the FE-simulation to perform a restart starting from the set value of F_{TD}. In the final step of preparing the wire bond simulation, the object of the class *Main* is generated and the initial values for the values for the bond parameters and solver settings are stored in the object. In the next step, the method *simulation* of the object *Main* runs the co-simulation within *MATLAB*; the pseudo code of the method is shown in algorithm 1. While the simulation time t_{Sim} is smaller than the bond duration t_{B}, one single vibration cycle with period length T_{P} after the other is simulated. Therefore, the method *SOC* of the object *Bondmodel* is used with the input parameters simulation duration T_{P}, vibration amplitude x_{BT}, and bond normal force F_{BN} in case of the signal-generator and u_{T} instead of x_{BT} for the option of the ultrasonic transducer to solve the ODE-system. The FE-simulation is updated, when - compared to the previous updated load step - either the bond normal force F_{BN} or the material softening factor k_{USS} changed more than the criteria $F_{\mathrm{BN,crit}}$ and $k_{\mathrm{USS,crit}}$ and no tool/substrate contacts occurred before. In case of tool/substrate contacts, the bond formation parameter β (see section 4.1.2) is reduced by the factor k_{TSC}. When the FE-model needs to be updated, first the object *USS* is refreshed to calculate the current softening factor k_{USS} for the wire material. Afterwards the next Load Step (LS) is calculated by the method *Solve_Next_LS* of the object *MAaaS* with the input parameters bond normal force F_{BN} and softening factor k_{USS}. Before the next vibration cycle is simulated, the model parameters such like the object *BondFormation* with the new contact normal force distribution and the wire stiffness $c_{\mathrm{t,W}}$ depending on the vertical position z_{WD} are updated. In case of the excitation with the ultrasonic transducer, the object *PLL* is also updated to calculate the excitation frequency f_{T} for the transducer.

The program structure allows for duplicating the simulation to be solved in parallel with different input parameters, by simply copying all model files (restart files, database, and macros of the FE-model, *MATLAB* files of the object classes and additional functions); by this method, all simulations run independently from each other making High Performance Computing (HPC) possible, see section A.4.

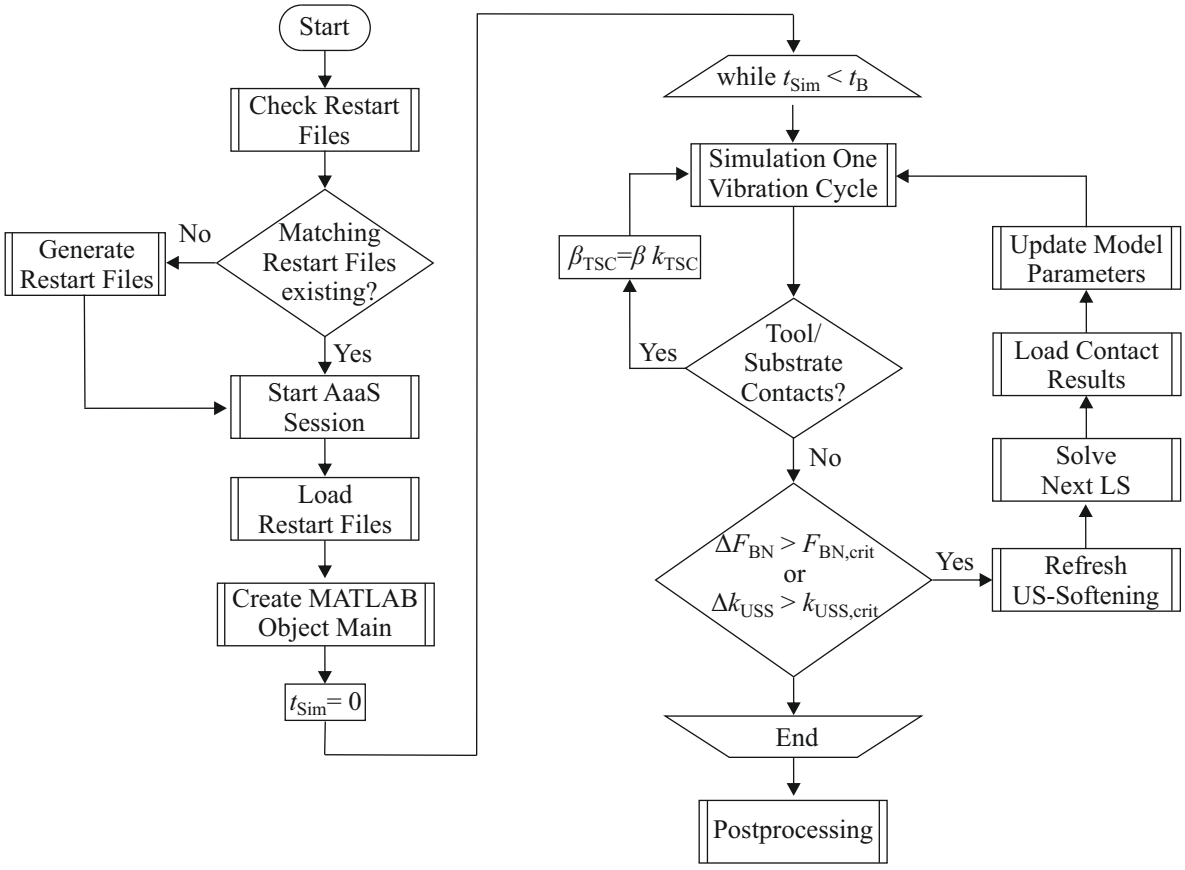

Figure 4.16: Program sequence plan to run one simulation of the wire bond co-simulation

Algorithm 1: Pseudocode of the method *simulation* of object (obj) *main*.

```
function obj = simulation(obj)
while t_Sim < t_B do
    if Exitation=Signalgenerator then
        obj.Bondmodel.SOC([0,T_P],x_BT(t_Sim),F_BN(t_Sim));
    else
        if Exitation=US-Transducer then
            obj.Bondmodel.SOC([0,T_P],u_T(t_Sim),F_BN(t_Sim));
        end
    end
    if (ΔF_BN > F_BN,crit or Δk_USS > k_USS,crit) and z_WD ≤ z_WD,TSC then
        k_USS = obj.Bondmodell.USS.refresh(P_USS(t_Sim));
        obj.Bondmodel.MAaaS.Solve_Next_LS( F_BN,k_USS);
        if z_WD ≥ z_WD,TSC then
            obj.Bondmodel.BondFormation.beta =
            obj.Bondmodel.BondFormation.beta·k_TSC;
        end
    else
        No update of the finite element model necessary.
    end
    obj.Bondmodel.BondFormation.update();
    obj.Bondmodel.SaveData();
end
```

5 Model parameter identification

This chapter describes the experimental identification of the bond model parameters by principle physical tests. The model parameters shall not be identified by fitting the output variables of the model, namely the shear force and strength, to experimental wire bonding results, as this will not allow for use of the model in simulation based process development. Therefore, a versatile test rig is presented in section 5.1, which meets the following requirements:

- Low frequency excitation (frequency up to 1 kHz) to measure tangential and normal forces during the bond process.
- Ultrasonic excitation to measure stress-strain curves of copper and aluminium bonding wire samples for investigation of the ultrasonic softening effect.

In section 5.2, the identification of friction coefficients and the cleaning parameter α is described. In section 5.4, the stress-strain diagrams for the FE model in *ANSYS* are determined from compression tests for the two bonding wires made of aluminium and copper; the tests were carried out both statically and dynamically under ultrasonic influence. The shear strength of the wire is a parameter in the bond formation model and is also needed to calculate a shear force value from the simulated bonded area; therefore, this parameter was determined in section 5.5. A parameter that was not identified from experiments but model-based using the finite element method is the tangential stiffness of the wire in section 5.6.

5.1 Test rig for low frequency wire bonding experiments

Measurements - especially of the frictional energy required for cleaning and bonding - are still a challenging task in ultrasonic wire bonding. The bond duration is so short and the excitation frequency so high, that observation of the bonding process cycle by cycle including high-speed recordings and measuring the tangential force in the interface is very challenging. Althoff et al. [4] presented a tri-axial force sensor to measure normalized tangential forces during the bond formation, but because of the missing dynamic calibration in the ultrasonic frequency range the quantitative measurement of the force components was not directly possible. Harthoorn found in [45], that welding metallic sheets with a vibration frequency of 30 Hz leads to similar results in weld strength with comparable process parameters (vibration amplitude, clamping force, and amount of oscillation cycles) compared to ultrasonic welding experiments with 20 kHz; he also was able to measure the tangential forces with a commercial strain gauge. Thus, the test-rig with low frequency excitation (<1 kHz) was developed for identification of the model parameters like the coefficients of friction, which are derived from measurements of the tangential forces. The construction of the test rig is shown in figure 5.1.

The crosshead of the testing machine (Instron Series 4400) is guided on spindles and can be moved in vertical direction with a settable speed from 1 mm/min to 100 mm/min. A

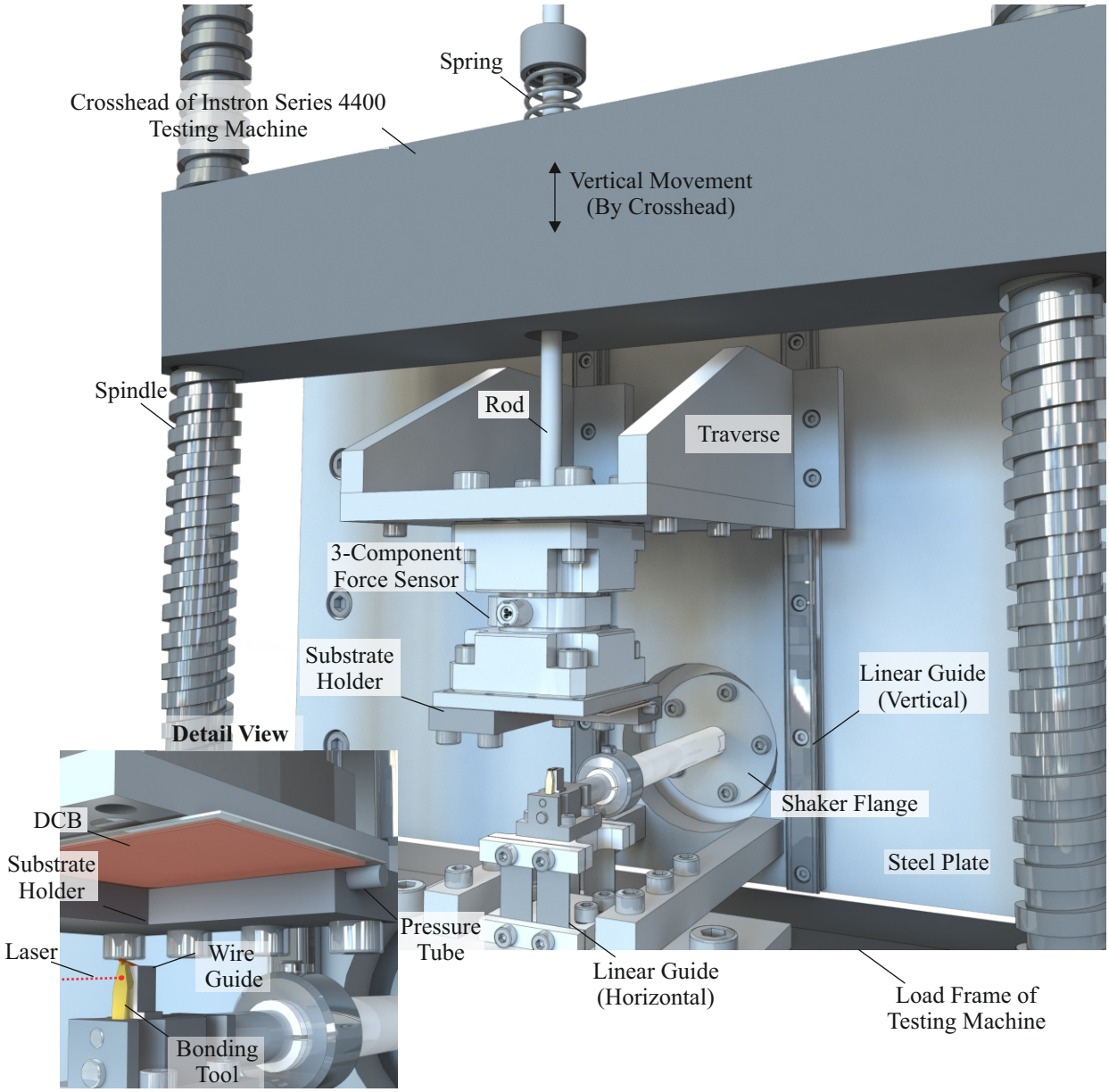

Figure 5.1: Rendered CAD image of the construction of test rig for low frequency wire bonding experiments.

traverse, which is linearly guided in vertical direction on a steel plate, is supported by a rod on a pressure spring above the crosshead; due to its own weight, the traverse achieves the equilibrium position on the spring, so that from the touchdown between wire and substrate onwards there is a linear increase in force according to the spring characteristic curve; this results in a more robust and stable force control for the touchdown and bond normal force compared to a rigid coupling between traverse and crosshead. The maximum normal force is determined by the dead weight (6 kg) of the traverse and the components mounted on it. On the bottom side of the traverse, a piezoelectric three component force sensor (Kistler / 9347C) is mounted to measure the tangential and normal forces.

On the bottom side of the force sensor, a substrate holder is mounted, which fixes the DCB using a pressure hose. When pressure is applied to the tube, it expands inside the

substrate holder housing, fixing the DCB. The substrate holder has a L-shape to make the bond tool tip visible from the front and right hand side for laser measurements and high speed camera recordings. Contrary to typical bonding machines, the orientation of substrate and bonding tool is upside down: the DCB is fixed above the bonding tool with the tool tip pointing upwards, because the bond tool is fixed on a linear guide with flexure hinges mounted on the load frame of the testing machine; thus, the DCB is moved in vertical direction. The bonding tool was shortened to increase the bending stiffness and behind the bonding tool, a wire guide is mounted, which was newly designed for the test rig; both, the substrate holder and the wire guide were produced using a 3d printer using polylactide (PLA) material. The adapter on the linear guide is connected by a rod to the flange of the shaker (Brüel & Kjaer / LDS V455) to excite the linearly guided bond tool; the shaker is placed behind the steel plate.

The control system of the Series 4400 testing machine is originally made up of two major subsystems: a crosshead drive and control system, that applies tensile or compressive loading to a specimen; and a load weighing system, that measures the loading of a specimen, [54]. The crosshead position is controlled by an external control system via GPIB which has been newly developed by Klahold et al. [60] to meet the specifications for the test-rig, see figure A.7 and the description in section A.6.

5.2 Coefficients of friction between tool, wire and substrate

For measuring the coefficients of friction for the contact between bonding tool and wire, the wire was fixed on the substrate by a bond loop that was ultrasonically bonded at the bonding machine and formed as low as possible; the bond tool in the test rig was than positioned in the middle between source and destination bond, so that only the bond tool could slide on the wire, see figure 5.2.

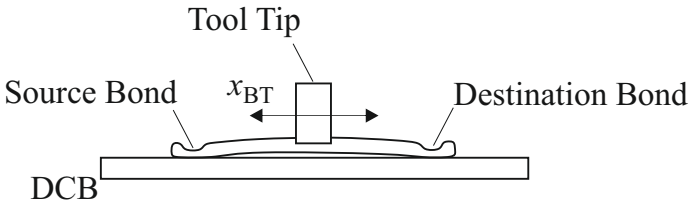

Figure 5.2: Fixation of the bond wire on the DCB substrate by flat loop, which has been ultrasonically bonded.

For measuring the coefficients of friction between wire and substrate, the wire was clamped in the v-groove of the bond tool only so that the wire could slide on the substrate. A test program has been implemented on the control board which allows to set the bond normal force F_{BN}, the excitation frequency, and the number of oscillation cycles for the tests.

In general, the coefficients of friction in both contacts between bonding tool and wire and between wire and substrate vary during the measurements due to frictional processes like fretting and cleaning processes; thus, the number of oscillation cycles were chosen such that a stationary value for the coefficient during the measurement was achieved.

The excitation frequency of the bonding tool was set to 5 Hz to avoid dynamical impacts of resonance frequencies of the test rig on the measurements (especially on the force measurement) and achieve quasi-static conditions for the measurements; the settings for the experiments in the following sections are listed in table 5.1.

Table 5.1: Settings for the experiments.

Contact	Material	Freq./Hz	F_{BN} / N	Oscillations
μ_{TW}	Al	5	3	60
μ_{TW}	Cu	5	5	40
μ_{WS}	Al	5	6	100
μ_{WS}	Cu	5	4.5	100

The amplifier of the shaker was excited with a constant voltage level during the measurement, which had been adjusted before the experiments to achieve a certain amplitude to achieve sliding conditions. Since the voltage level of the shaker was constant, the vibration amplitude of the bond tool generally decreased during the measurements, because the tangential force increased and with that, the mechanical resistance for the bond tool, see figure 5.3. A closed loop control was not used, because the reduction of the vibration amplitude does not affect the identification of the coefficient of friction as long as the sliding mode occurs.

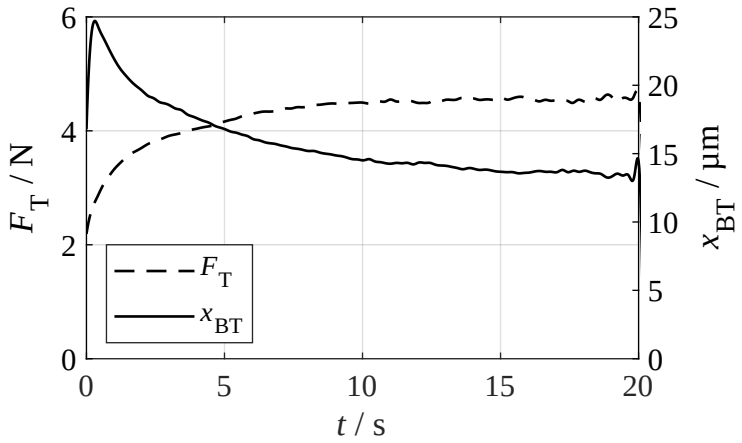

Figure 5.3: Envelopes of the tangential force and vibration amplitude of the tool tip at 4 N normal force for the copper wire fixed on the substrate.

The friction coefficient is determined by evaluating the plateau of the hysteresis; exemplary results are shown in figure 5.4 for the contact between bond tool and copper wire. In figure 5.4 a), a detail view on the measured time series of the tangential force F_{T}, the normal force F_{BN}, and the vibration x_{BT} of the bond tool tip are shown. The stick slip behaviour can be clearly seen in the shape of the time series of the displacement and tangential force; the displacement abruptly increases when sliding occurs (tangential force reaches its maximum). The hysteresis of vibration stroke x_{BT} and tangential force F_{T} in figure 5.4 b) relates clearly to dry friction which is modelled by the *Jenkin Element* in the bond model explained in equation 4.2. The tangential stiffness leads to steadily increasing tangential force in the sticking phase until the transition from stick to slip occurs.

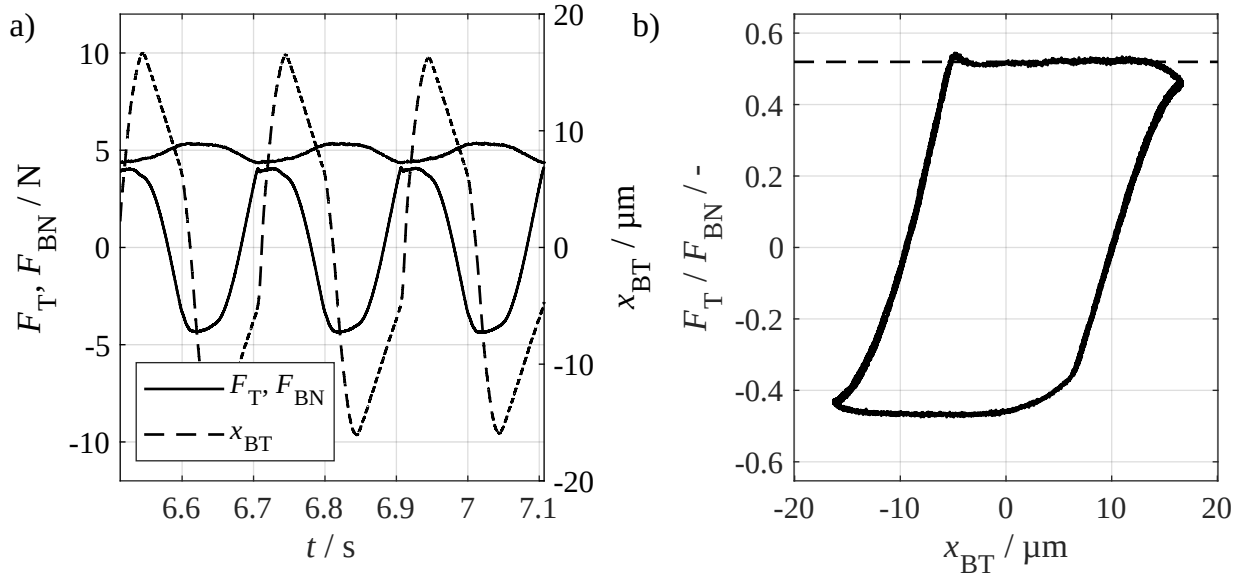

Figure 5.4: a) Exemplary time series of the tangential force, tool tip displacement and bond normal force and b) hysteresis of the tangential force for evaluation of the friction coefficient.

In figure 5.5 the results for the friction coefficient between bonding tool and wire are shown. For the copper wire in figure 5.5 a), μ_{TW} starts at approx. 0.45 and increases to 0.68 at the end of the measurement. The friction coefficient for aluminium wire starts at a higher level at approx. 1.14 and decreases over the duration of the measurement to a level of approx. 0.75, see figure 5.5 b).

The different behaviour of copper and aluminium is caused by oxides on the surface of the wires. While the copper oxides Cu_2O and CuO are rather soft, [40], the aluminium oxide Al_2O_3 is hard and brittle and has proved to crack under the bonding load, [75]. Rabinowicz stated in [101], that oxide layer acts as solid lubricant when oxide hardness is not greater than three times the metal hardness. This is the case for copper, but not for aluminium. As the oxide layers are worn out from the contact during the experiment, frictional behaviour changes over time.

For the copper wire, after 5 s (25 oscillation cycles), the friction coefficient reaches approx. 95 % of the end value and for the aluminium wire, after 10 s (50 oscillation cycles), a value of approx. 105% in relation to the final value is reached. Comparing these results with a typical ultrasonic excitation with a frequency of 60 kHz for heavy wire bonding, the two durations correspond to 0.4 ms and 0.8 ms respectively; typical process times for heavy wire bonding are between 100 ms to 500 ms. This means that even if the friction coefficient between bonding tool and wire changes at the beginning and reaches a stationary final value only after a few oscillation cycles, this value can be assumed to be constant in good approximation. Therefore, the end values of the measurements are used for the parametrization of the model, as they are achieved within fairly short time after 25 (copper) and 50 (aluminium) oscillation cycles.

In figure 5.6 the results of the measurements of the friction coefficient between wire and substrate are shown; the results are plotted over the cumulated dissipated frictional energy W_f per contact area $A_{C,WS}$ as this ratio relates to the cleaning process which

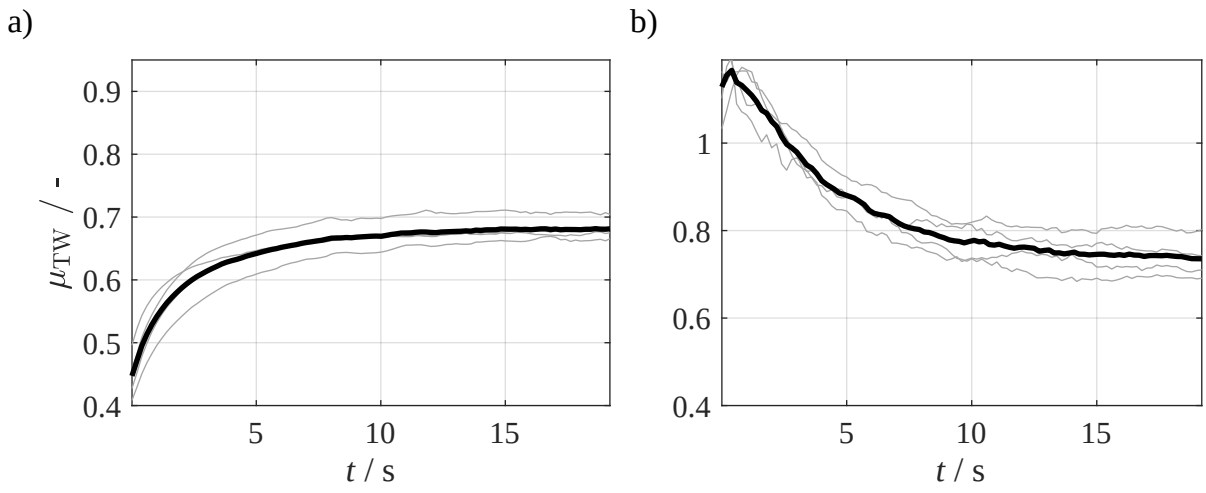

Figure 5.5: Measurements of the friction coefficient between bonding tool and wire for a) the copper wire and b) the aluminium wire. The grey lines relate to the single measurements, the black solid line to the mean time series.

affects the friction coefficient that changes from the initial value of μ_{OX} to μ_{Met} for fully cleaned contact area. During the first measurements, the copper wire in particular hardly deformed at all due to the low normal forces and only a very small line-contact area was obtained, which varied in size and form from experiment to experiment. In order to achieve consistent test conditions, the wire was therefore loaded with a static pre-load of 50 N for the copper wire and 20 N for the aluminium wire before vibration excitation, resulting in a uniform elliptical contact area between wire and substrate; all experiments were performed on DCB substrate. The contact areas have been measured after the experiments using digital microscopy. Due to the pre-deformation of the wire it is assumed that the contact area $A_{C,WS}$ remains constant during the experiments. The friction coefficient for the copper wire in figure 5.6 a) initially starts at μ_{OX} equal to 0.21 and increases up to 0.45; afterwards, slip between bond tool and wire occurred. For the aluminium wire in figure 5.6 b), the friction coefficient has an initial value of μ_{OX} equal to 0.23 and a final value of 0.56, before the bond tool starts sliding on the wire. Tabor stated in [126], that the friction coefficients of metals can be calculated from the ratio of shear strength and yield stress of the softer material; for ideal plastic materials, this ratio is about 0.2 which is in good agreement with the measurements in figure 5.6.

5.3 Bond formation model parameters

With increasing frictional work W_f due to sliding of the wire on the substrate, the friction coefficient increases in figure 5.6. Microscopy observation showed that the contact areas were not fully cleaned and activated after the measurements because the bond tool starts sliding on the wire before the contact could be fully cleaned. The contact areas were classified as 35 % cleaned and activated for the copper wire and 65 % for the aluminium wire. In case of the copper wire, the contact area was partially bright and shiny indicating fretting processes and for the aluminium wire, a thin aluminium layer was left on the DCB substrate within the cleaned and activated areas, thus these areas were segmented

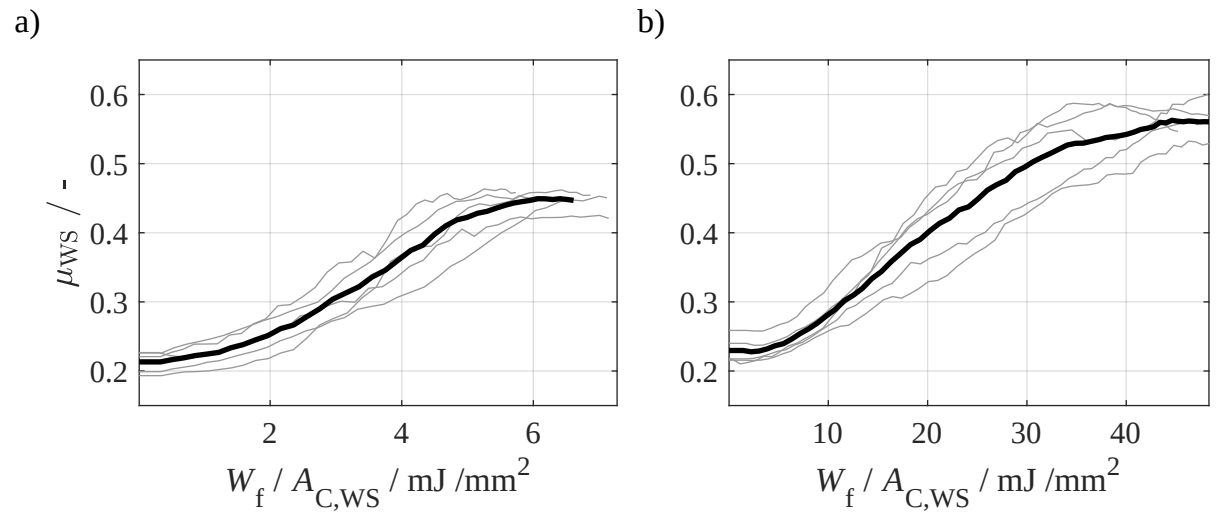

Figure 5.6: Measurements of the friction coefficient between wire and substrate on DCB substrate for a) the copper wire and b) the aluminium wire. The grey lines relate to the single measurements, the black solid line shows the mean value.

from the rest of the contact area to classify the areas using the methods described in [131]. To calculate the coefficient of friction μ_{Met}, the equation 4.3 is reduced by setting γ equal to zero, as no bond formation was observed during the experiments. With the identified values for μ_{Ox} and τ, μ_{Met} can be calculated to 0.9 for copper and 0.75 for aluminium wire, taking into account that about 35 % respectively 65 % of the contact area were cleaned and activated. Liu found in [72], that the coefficient of friction for fully cleaned surface between copper and copper in air is approx. 1 which correlates well with the calculated value from the experiments.

In figure 5.7, the results from figure 5.6 have been normalized to the percentage value of cleaned and activated area which can be referred to the cleaning state τ in the bond formation model in equation 4.1. Within the bond formation model, the model parameter α is from interest, which has been identified in figure 5.7 by evaluating the slope of the curve. In the beginning of the measurements, the cleaning state τ first remains constant and then starts rising after 1.4 mJ/mm^2 for the copper wire and 4.66 mJ/mm^2 for the aluminium wire. The slope of the curve after these starting points is evaluated: for copper, the slope is 86.94 mm^2/J and for aluminium 24.28 mm^2/J; these values are referred as the cleaning parameters α for copper respectively aluminium.

The experimental determination of the coefficient β for the bond formation is significantly more complex than the identification of α for the cleaning state. For the cleaning parameter, the assumption was, that the initial contact area is not activated and bonded, thus the full amount of the measured frictional work W_{f} contributes to the increase of τ. For experimental identification of β, a distinction between frictional work within activated areas (contributing to bond growth) and within contact areas with contaminations (contributing to growth of activation) is necessary. This is not achievable with simple measuring methods such as an optical microscope and shear tests. For this, the experiments would have to be stopped in short time steps to identify the initial, activated and bonded areas. In the next step, the amount of frictional work W_{f} within the activated areas has to be derived; but with the experimental setup used in this section, only the global frictional work transmitted into the system consisting of the two contacts be-

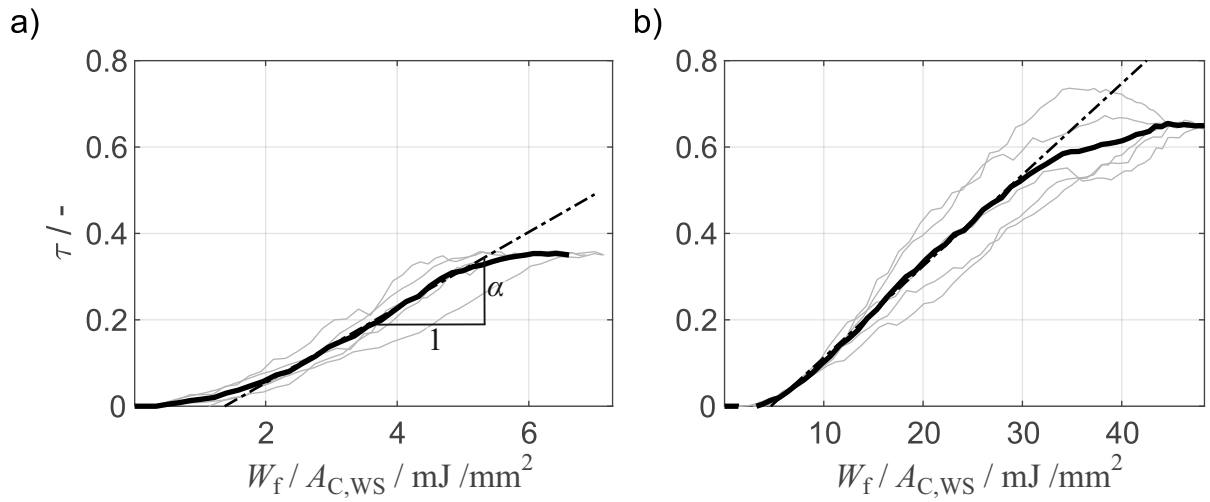

Figure 5.7: Cleaning state τ and the cleaning coefficient α for a) the copper wire and b) the aluminium wire.

tween tool and wire and between wire and substrate can be measured. Thus, the results from the wire bonding experiments in section 3.2 are used to scale β by comparing the measured shear force values with the simulated results, see section A.7 in the appendix. The results of the measurements of the coefficients of friction and cleaning parameters α and the identified values of β are listed in table 5.2.

Table 5.2: Identified coefficients of friction and bond formation parameters.

Material	$\mu_{\mathrm{TW}}/-$	$\mu_{\mathrm{OX}}/-$	$\mu_{\mathrm{Met}}/-$	$\alpha/\mathrm{mm}^2/\mathrm{J}$	$\beta/\mathrm{mm}^2/\mathrm{J}$
Al	0.75	0.23	0.75	24.28	30
Cu	0.68	0.21	0.9	84.94	1.9

5.4 Material behaviour of the bond wire under static and ultrasonic load

Literature values for the material parameters of aluminium and copper summarized in section A.5 differ in a wide range because of the fact that the plastic material behaviour is strongly dependent on the initial state of the material; strain hardening during the manufacture of the specimens can, for example, explain a greater yield strength σ_{Y} compared to a soft-annealed specimen. For this reason, the plastic behaviour of the Al and Cu bond wires must be measured for the bond model, as otherwise any values within the limits of the literature values in table A.3 must be guessed.

To describe the elasto-plastic behaviour of metals, typically tension-compression-tests of defined material samples are made. As material characteristics depend strongly on microstructure, material samples of the same material as the bond wires would be needed, but are not available. Thus, experiments must be done directly with the bond wires. Tension tests are not suitable, as the clamping of the small wire diameter without damaging the wire is a challenging task and often impacts the measurements. Furthermore, the

transmission of the ultrasonic vibration into the thin wire under tensional load becomes even more challenging as the risk that the wire breaks at small elongations is increased. Thus, compression tests are carried out with the 400 µm copper and aluminium wires to a) determine the stress-strain curves for the FE-model and b) investigating the impact of ultrasonic excitation on the forming force during compression of the wire. The results used in section 5.4.2.1 and section 5.4.2.2 were partially produced as part of the master thesis of Müller [89].

The main difference of the setup of the test rig used in this section to the set-up shown in figure 5.1 is that instead of the elastic support on the spring, the traverse is rigidly connected directly to the crosshead of the test rig via a metal rod and the linear guide with the bond tool excited by the shaker was replaced by a transducer, see figure 5.8. The transducer horn is designed for a lambda half mode of vibration and is clamped in the vibration node via a membrane in the transducer holder using a clamping ring; the horn is made of steel. The transducer holder is made of aluminium and is fixed to the test rig by two screws. The transducer (Branson, 902R) with a resonance frequency of 19.8 kHz is screwed to the right end of the horn. The transducer is operated in resonance via a PLL controller which is implemented within the ultrasonic generator (*ATHENA Technologie Beratung GmbH*). The vibration amplitude at the front side of the transducer horn is measured by a laser vibrometer (Polytec OFV 512 with Polytec OFV 5000). The position of the 400 µm wire is shown in the detail view in figure 5.8; a flat surface was milled on the front side of the horn on which the wire can be placed in alignment to the direction of vibration.

In advance of the material tests, the force-displacement curve of the test rig without the wire was measured in order to determine the stiffness of the test rig and the horn themselves, which have to be considered for correction of the measured force-displacement curves.

A non-standard compression test method shown in figure 5.9 was developed to deform the wire while measuring the reaction force F_z: the wire is placed between two parallel surfaces and deformed perpendicular to the wire axis, see figure 5.9 a). On the lower side is the contact surface of the horn of the ultrasonic transducer, which serves as a fixed support in the vertical direction and can transmit an ultrasonic vibration with the displacement x_H to the wire in the horizontal direction. On the upper side is the counter surface to the horn, which moves vertically and between the two surfaces is the wire.

With this experimental setup, force-displacement curves can be measured; for the simulation in *ANSYS*, however, a stress-strain curve is needed. As the cross section of the wires cannot be measured during the experiments, the workflow shown in figure 5.9 b) was applied. The basic assumption is that the stress-strain curve has the shape of a tension curve; that this assumption is valid has already been shown in [106, 145] as the stress strain curves were very similar in tension and compression tests. In *ANSYS* a multi linear material model with five sample points in the plastic region is used for the simulation. The essential adjustment parameters that need to be identified in the material model are therefore the:

- young's modulus E,
- yield point σ_Y,
- and the slope between the sample points in the plastic region of the material model.

These parameters of the material model are adjusted such that the simulated force-

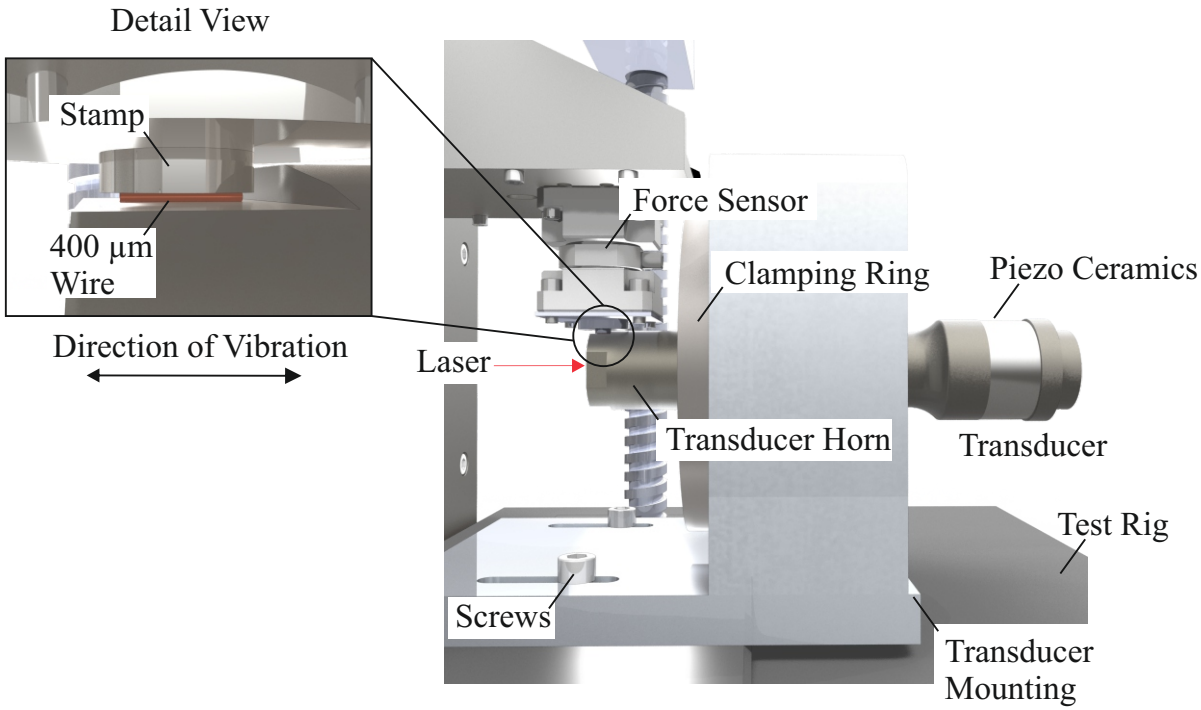

Figure 5.8: Experimental set up for measuring the deformation behaviour under static and ultrasonic load with a detail view on the wire clamped between the stamp and transducer horn; CAD rendered images.

displacement curve fits to the measurement. The FE model consists of two rigid bodies, which represent the force sensor on the upper side and the sonotrode of the transducer on the lower side. The wire itself is modelled as a flexible body and meshed with square tetrahedral elements, which are used for robust convergence behaviour; the mesh density was adjusted so that the force-displacement results were no longer significantly dependent on the mesh density, resulting in a node number of 162093 nodes. The contacts between the rigid bodies and the wire were modelled with the normal Lagrange contact algorithm and a friction coefficient of 0.1.

5.4.1 Static deformation behaviour

In this section, the results from the quasi-static measurements and simulations for the copper and aluminium wire are discussed. In order to have constant initial conditions for the force measurements, the wires were pre-deformed before the actual measurement so that a well defined contact surface was obtained; without this procedure, angular errors between the upper and lower surfaces result in different contact situations in the beginning and the wire immediately deforms plastically. With a constant initial contact surface, this problem is solved so that all force-displacement curves elastically in the beginning. The preformed geometry of the wire is measured under a digital microscope and is mapped in *ANSYS* as the initial state for the geometry. The copper wires are pre-deformed with 80 N and the aluminium wires with 25 N; the wire samples are cut to a length of 3 mm.

In figure 5.10 a) the comparison of simulation and measurement for the copper wire is shown: good agreement between simulation and measurement is achieved, as the

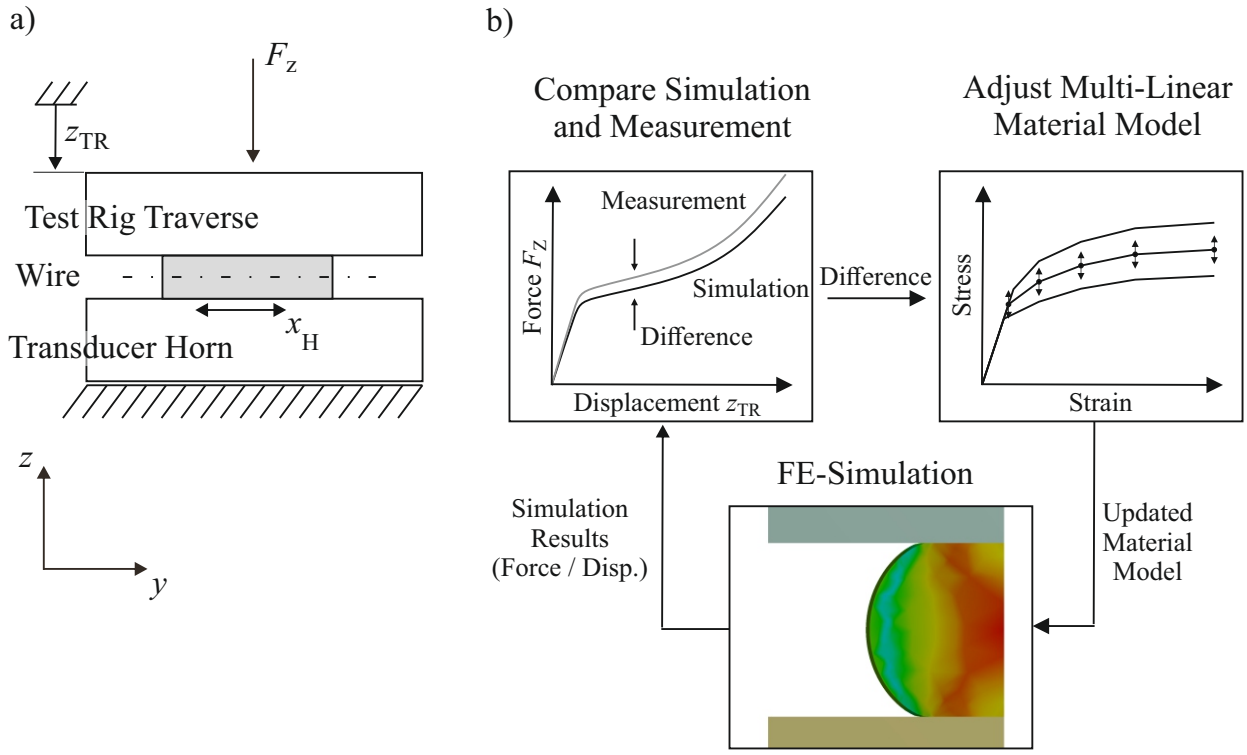

Figure 5.9: a) Principal setup for measuring the reaction force during deformation of the wire and b) iterative workflow for determination of the stress-strain curves for the FE-model from the measured force-displacement curves.

simulated curve lies within the scatter band of six individual measurements. In figure 5.10 b) the corresponding stress-strain curve for the simulation is shown, which was derived according to the procedure in figure 5.9.

The results for the aluminium wire are shown in figure 5.11; for the material model in figure 5.11 b) the qualitative trend of the curve is comparable to the copper model in figure 5.10 b). In general, the values for the individual data points in the plastic range are approx. 70 % smaller for aluminium compared to copper. The comparison between simulation and measurement in figure 5.11 a) also shows good agreement, as the simulated force-displacement curve lies within the limits of the error bar and follows the curve of the mean value of the measurement very closely.

The results of the experimental investigations for the copper and aluminium wire are summarised in table 5.3.

Table 5.3: Identified material parameters of the multi-linear material model.

Copper		**Aluminium**	
E / GPa	σ_Y / MPa	E / GPa	σ_Y / MPa
120	115	70	40
Plastic strain ϵ_P / -	Stress σ / MPa	Plastic strain ϵ_P / -	Stress σ / MPa
0.03	155	0.03	55
0.25	270	0.25	85
0.60	330	0.60	110
1.00	365	1.00	118

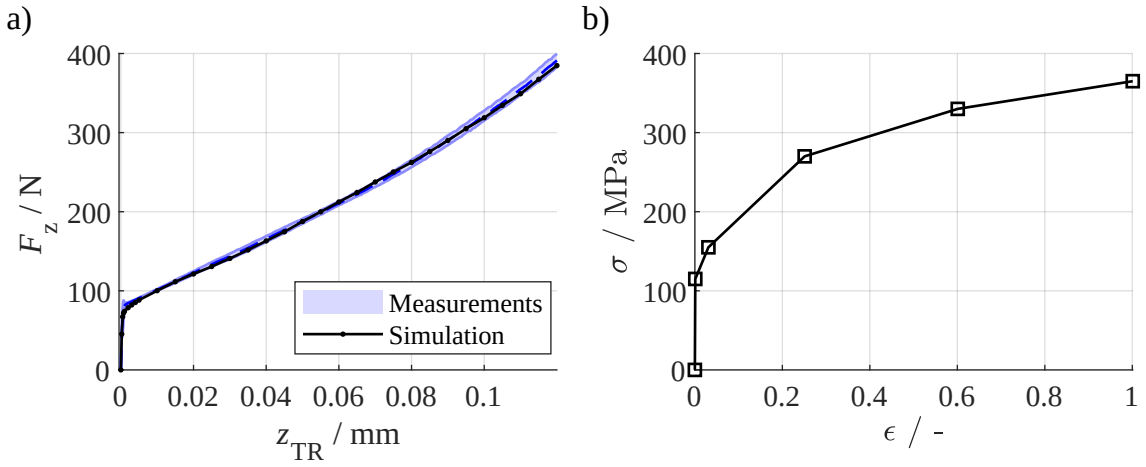

Figure 5.10: Results for the copper wire: a) measured force-displacement curves (six measurements) with 2σ error limits of the shaded error bar and the simulated force-displacement curve and b) corresponding multi-linear stress strain curve for the material model of the simulation.

5.4.2 Material behaviour under ultrasonic excitation

In this section, the results from the force measurements with ultrasonic excitation are discussed. The ultrasonic generator has been driven in the constant current mode to vary the vibration amplitude x_H by setting different current levels. The advantage by setting a value for the current, which is then controlled by the generator to be constant during the tests, is that the actual oscillation amplitude x_H at the horn of the transducer remains approximately constant, as the vibration amplitude is proportional to the current when the transducer is driven in its resonance frequency, which is the case in these experiments. The test procedure is described by the following steps:

1. Positioning the wire at the horn tip and quasistatic pre-deformation of the wire with 80 N for the copper wire and with 25 N for the aluminium wire.
2. Moving the traverse upwards and starting a second test program, which was specifically programmed for these tests:
   a) The traverse moves down until a force of 100 N for the copper wire 30 N for the aluminium wire is reached.
   b) The ultrasonic generator is started and the traverse continues to drive downward.
   c) When either the maximum displacement of z_TR or the maximum fore F_z is reached the traverse stops and moves upwards into the initial position.

The starting levels of 100 N for the copper wire 30 N for the aluminium wire were chosen such that the wire is sufficiently clamped before the ultrasonic excitation starts but as low as possible to investigate a wide range of deformation level of the wire. From literature it is known, that the ultrasonic softening effect is reversible and not directly dependent on the clamping force itself. For the experiments, the same wire samples as for the static deformation tests with 3 mm length from the 400 µm bond wires are used and the traverse speed has been set to 1 mm/min. In the following subsections, the results of the

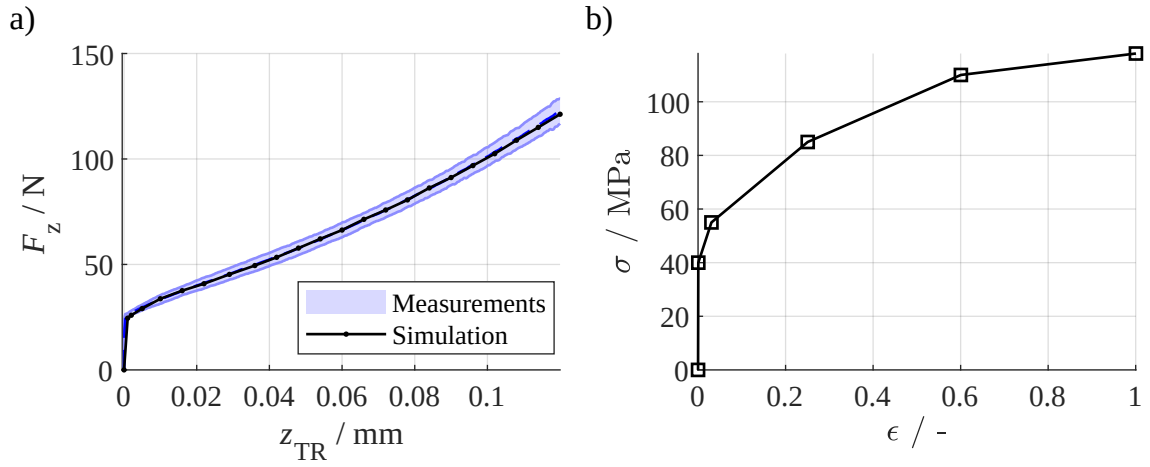

Figure 5.11: Results for the aluminium wire: a) measured force-displacement curves (six measurements) with 2σ error limits of the shaded error bar and the simulated force-displacement curve and b) corresponding multi-linear stress strain curve for the material model of the simulation.

ultrasonic deformation tests are discussed separately for the copper and aluminium wire and are compared to each other in section 5.4.2.3. For all experiments in the following subsections, for each current level, the mean values out of three single measurements are shown.

5.4.2.1 Copper wire

For the copper wire, six equally distanced levels of the current in the range from 50 mA to 300 mA have been investigated; in figure 5.12 the results of the laser-measurements of x_{H} during the compression tests are shown. In figure 5.12 a) the time series of the vibration amplitude during the deformation tests is shown; for each current level, the amplitude keeps constant nearly independently from the vertical load of the test-rig on the transducer-horn. In figure 5.12 b), the mean values of the vibration amplitude over the excitation time are shown; the vibration amplitude increases proportional to the set current levels in the range from 0.4 µm to 3.3 µm.

In figure 5.13, the results from the wire deformation tests with ultrasonic excitation are shown. The maximum travelling distance of the traverse is $z_{\mathrm{TR}} \approx 0.14$ mm where the maximum force for these experiments - which has been set before the tests at the test rig control board - of about 500 N is reached. In figure 5.13 a) the force F_{z} reduces immediately after ultrasonic excitation starts at 100 N. For the first four levels of the current from 50 mA to 200 mA, the force-displacement curves are almost parallel to each other, but not parallel to the static force-displacement curve. For 250 mA, the curve can be divided into two parts: in the first part up to $z_{\mathrm{TR}} = 0.1$ mm, the curve has a smaller slope than the curve for lower current levels, but then the slope immediately increases, which can be interpreted as a hardening effect. For 300 mA, the point of hardening is shifted to approx. $z_{\mathrm{TR}} = 0.125$ mm.

In figure 5.13 b), the ratios between F_{z} with ultrasonic excitation to $F_{\mathrm{z,0mA}}$ without ultrasonic excitation are shown. For all current levels, the curves vary over the vertical

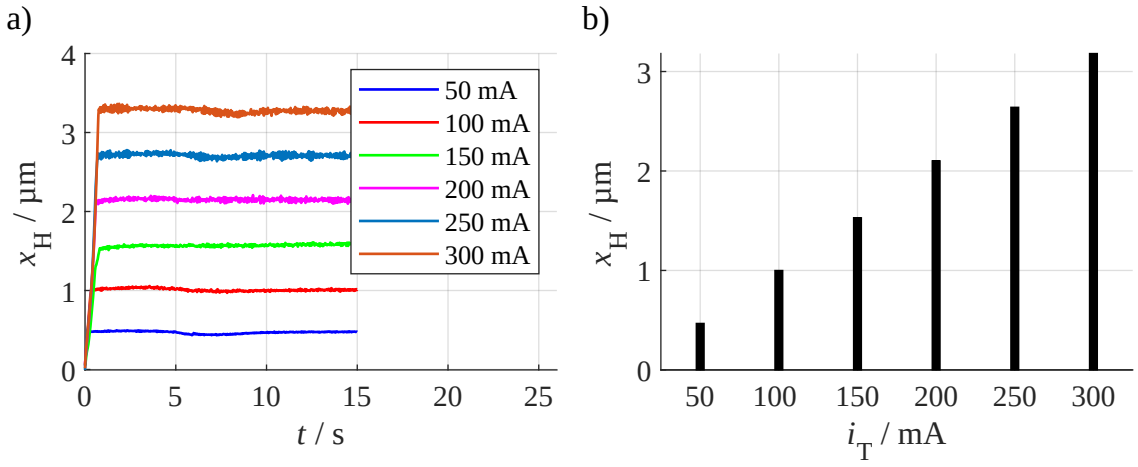

Figure 5.12: Copper wire: a) mean values of three leaser measurements during the compression tests and b) mean values over time of the curves in a).

displacement z_{TR}, thus the ratio F_z / $F_{z,0mA}$ - which can be interpreted as a measure of the material softening - is not constant. When the ultrasonic excitation starts, the material softening immediately starts and depending on the current level, the ratio F_z / $F_{z,0mA}$ drops from 1 to a lower level. Then, with increasing travelling distance z_{TR} of the traverse, the force ratio even further decreases to a minimum, which is reached for the different current levels at different traverse positions z_{TR}. For 50 mA and 100 mA, the transition between increasing material softening to hardening is barely noticeable at $z_{TR} \approx 0.08$ mm, thus the softening can also be interpreted as almost constant over the whole duration until the end of the measurement. For higher current levels from 150 mA to 300 mA, this effect becomes more significant. Comparing the curve from 150 mA to the curve from 200 mA shows that the hardening for 200 mA leads to the two curves lying on each other at the end of the measurement. The measurements of 250 mA and 300 mA differ most significantly from the other current levels; especially for 300 mA, the ratio F_z / $F_{z,0mA}$ decreases to the lowest level of approx 0.4 and then remains on this level for the longest duration and the hardening effect starts only at the end of the measurement.

5.4.2.2 Aluminium wire

In figure 5.14 the results of the laser measurements at the ultrasonic horn tip for the experiments with the aluminium wire are shown; five equally distanced current levels in the range from 30 mA to 150 mA were investigated. The time-series of the vibration amplitude in figure 5.14 a) show that the vibration amplitude remains almost constant over the whole duration of the measurements, such like for the copper wire experiments. The mean values of the vibration amplitude over time are shown in figure 5.14 b); the amplitude linearly increases from 0.3 µm to 1.6 µm with increasing current levels.

In figure 5.15 a), the force-displacement curves with ultrasonic excitation for the aluminium wire are shown. Compared to the experiments with the copper wire, the travelling distance of the test-rig traverse is higher and reaches a maximum of $z_{TR} \approx 0.23$ mm; the reason is, that the maximum force of about 400 N is reached later because the alu-

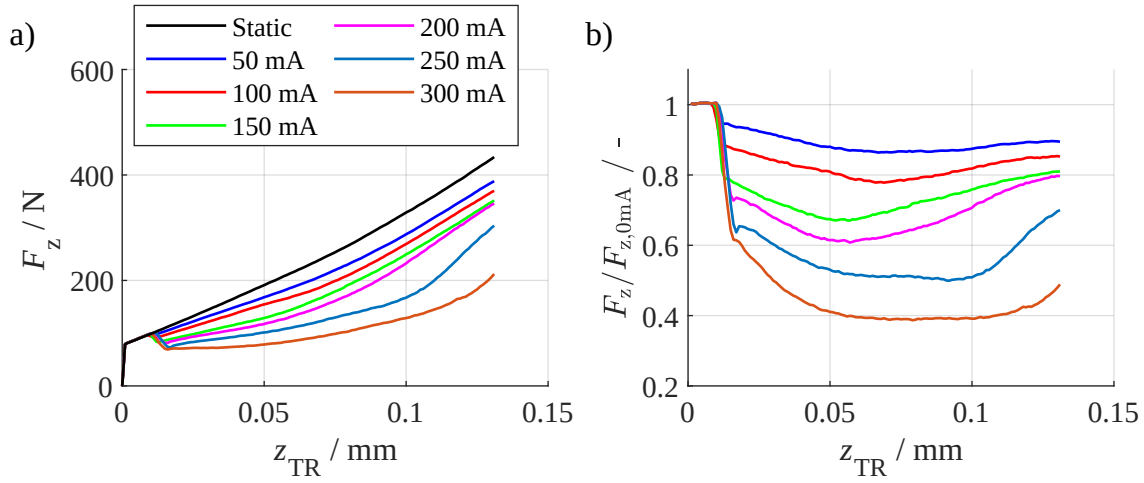

Figure 5.13: Copper wire: a) Force-displacement curves at the different ultrasonic excitation levels and b) ratio between the ultrasonically influenced and static vertical force.

minium material is softer compared to copper. After a certain travel distance of the test-rig traverse, a hardening effect of the wire material is observed for all current levels. In case of current levels from 30 mA to 90 mA, the hardening effect leads to significant increase of the forming force and after a travelling distance of $z_{TR} \approx 0.17$ mm the curves cross the static force-displacement curve, thus the vertical force F_z becomes even larger with ultrasonic excitation compared to the quasistatic force. For 120 mA and 150 mA, the moment when the hardening effect occurs, is shifted to larger travelling distances.

In figure 5.15 b), the ratio F_z / $F_{z,0mA}$ of the vertical force, measured with ultrasonic excitation, to the force without ultrasonic excitation is shown. The softening effect occurs immediately after turning on the ultrasonic excitation. For current levels from 30 mA to 90 mA, before the hardening effect occurs, the ratio remains almost constant; when the material hardening occurs, the ratio increases significantly to values larger than 1. This correlates to the results in figure 5.15 a), where the force-displacement curves crossed the static force-displacement curve when the hardening effect occurs. For 150 mA, the ratio is not constant during the wire deformation, as the ratio F_z / $F_{z,0mA}$ first drops to 0.4 for 120 mA and to 0.22 for 150 mA and then increases to 0.6 and 0.45 respectively before the hardening effect occurs.

5.4.2.3 Discussion of the results and identification of the ultrasonic softening model parameters

For both materials, the ultrasonic softening effect has been investigated, by applying an ultrasonic excitation with different vibration amplitudes during compression tests with 400 µm wire samples. Significant reduction of the vertical force, measured during the compression tests was observed for both materials; a relative force reduction of around 60 % was measured for the largest vibration amplitude for both materials. The mean value of the ratio F_z / $F_{z,0mA}$ plotted over the vibration amplitude x_H during the compression tests for the copper and aluminium wire are shown in figure 5.16. For calculating the mean values, only the part of the curves in figure 5.13 b) and figure 5.15 b) before the

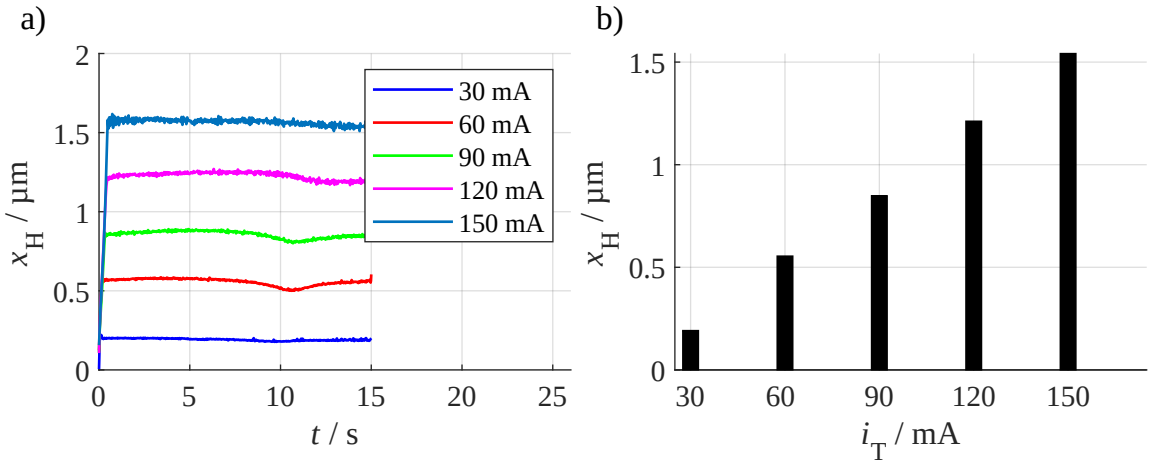

Figure 5.14: Aluminium wire: a) mean values of three laser measurements during the compression tests and b) mean values over time of the curves in a).

material hardening begins was evaluated. For both, the aluminium and copper wire, an almost linear decreasing trend occurs. The slope of the curve for the aluminium wire is twice as high as for the copper wire which means, that the vibration amplitude for the copper wire to reach a certain level of the ratio F_z / $F_{z,0mA}$ is also approx. twice as high as for the aluminium wire.

The vibration amplitude x_{BT} of the bond tool tip from the wire bonding experiments in section 3.2.4.1 was in the range from 1.4 µm to 2.0 µm for the aluminium wire and from 2.5 µm to 3.8 µm for the copper wire; these amplitude ranges are almost captured by the experiments in this section. Thus, it can be explained by the results in figure 5.16, why the vibration amplitude for copper wire bonding must be almost twice as high compared to aluminium wire bonding, as optimal results for aluminium wire were found for x_{BT} = 1.7 µm (u_T = 30 V and F_{BN} = 14 N) and for copper for x_{BT} = 3.5 µm (u_T = 60 V and F_{BN} = 26 N).

In the master thesis of Müller [89], it could be shown, that the measurements from figure 5.13 and figure 5.15 are suitable to model the ultrasonic softening effect; by applying the ratio F_z / $F_{z,0mA}$ as the factor k_{USS} in the finite element model, the simulated reduction of forming force shows good agreement with the measured forming force F_z under ultrasonic load. But for modelling the ultrasonic softening effect, in section 4.1.5 a model approach was derived to calculate the factor k_{USS} using the ultrasonic power transmitted into the wire. In the experiments, however, direct measurement of the tangential force to calculate the power at 20 kHz is not possible with conventional equipment, as this requires dynamic calibration of the force sensors. The force sensor used in the experiments has its first resonance frequency at approx. 3 kHz and is not suitable for measurements in the ultrasonic frequency range. Additionally, in wire bonding sliding friction can occur between the bond tool and the wire with increasing bond strength and tangential forces transmitted to the wire, resulting in an increasing amount of friction reduction, which are not captured systematically in the experiments at the test-rig.

Thus, the correlation between force reduction and vibration amplitude from figure 5.16 alone is not suitable to identify the parameters a and b of the ultrasonic softening as the

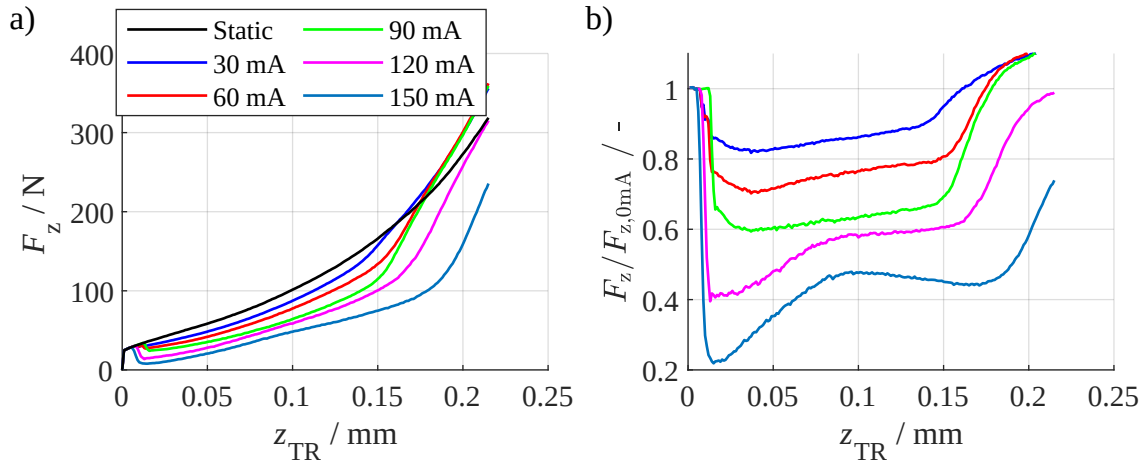

Figure 5.15: Aluminium wire: a) force-displacement curves at the different ultrasonic excitation levels and b) ratio between the ultrasonically influenced and static vertical force.

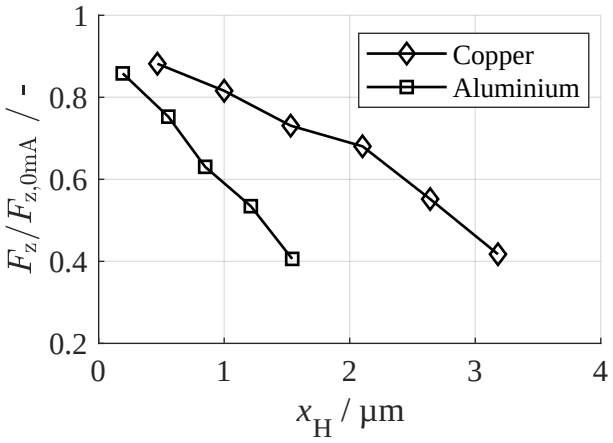

Figure 5.16: Mean values of the ratio F_z / $F_{z,0mA}$ of the vertical force with ultrasonic excitation to the vertical force without ultrasonic excitation for the aluminium and copper wire plotted over the vibration amplitude x_H.

force reduction in the tests is mainly influenced by the effects of stress superposition and acoustic softening. For this reason, the measurements of the vertical tool position z_{WD} from the ultrasonic bonding tests in section 3.2.4 are used to identify the parameters a and b, which were adjusted iteratively such that the vertical deformation $z_{WD,max}$ at the end of the bond process correlates between the simulation and experiment. In figure 5.17 the maximum vertical deformation $z_{WD,max}$ at the end of bond formation is shown for a) the aluminium wire and b) the copper wire, simulated with the identified model parameters listed in table 5.4. For the different levels of ultrasonic voltage and bond normal force, for both materials a good correlation was achieved over a wide range of the different bond normal forces and ultrasonic voltages which were chosen to the levels used in the experimental parameter studies in section 3.2. For the copper wire, at 30

V ultrasonic voltage and from 26 N to 38 N bond normal force, the simulated vertical deformation is slightly lower compared to the experiments; the reason for this is not only the identification of the parameter a and b as the different bond formation behaviour between simulation and experiment also impacts the wire deformation in the bond model. Thus, the sub models of the bond formation model and the ultrasonic softening effect interact with each other as with rising shear force values also the tangential forces increase and with that, the power $P_{\mathrm{US,I}}$ increases.

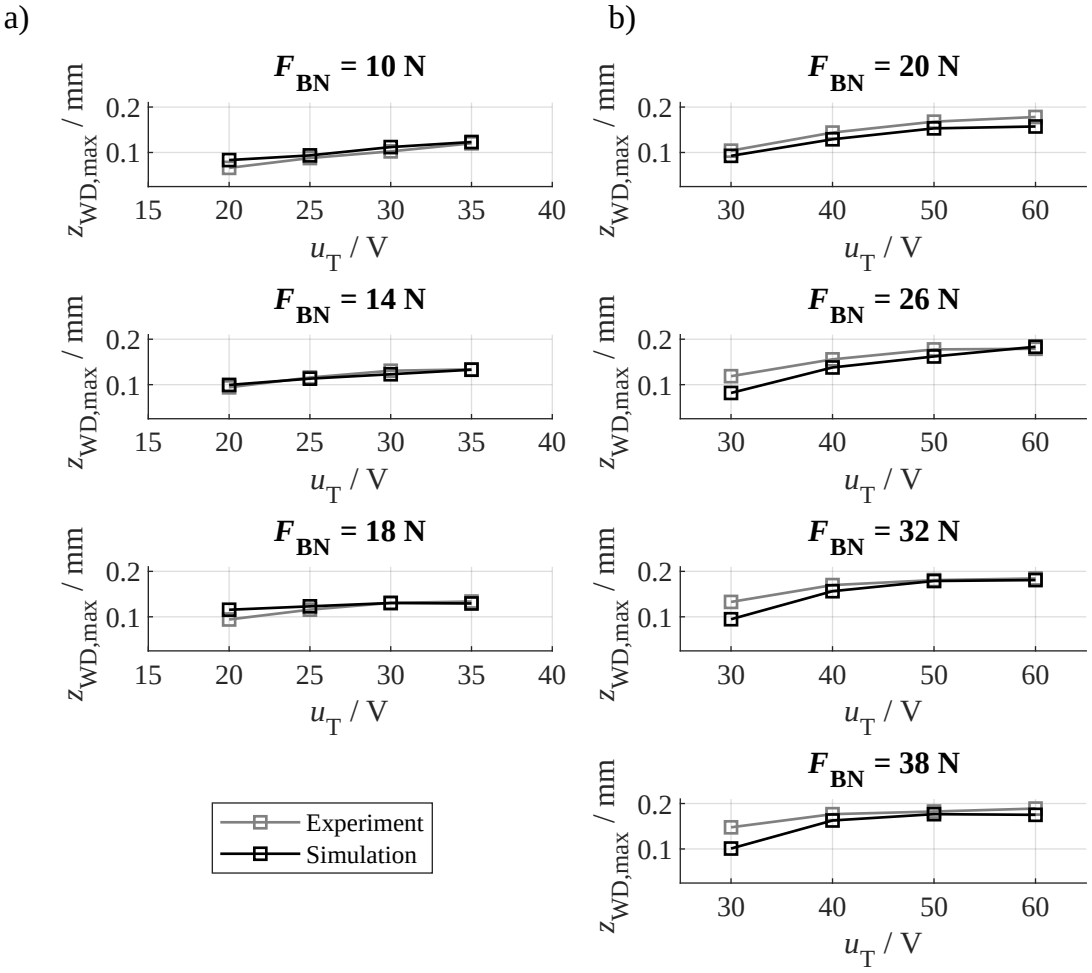

Figure 5.17: Maximum vertical bond tool position $z_{\mathrm{WD,max}}$ for the different levels of bond normal force F_{BN} and ultrasonic voltage u_{T} measured at the bonding machine (grey lines) and from the simulation with the identified model parameters a and b for a) the aluminium wire and b) the copper wire.

5.5 Shear strength of the bond wire

For the shear strength τ_{S}, no information is given either in the data sheets of the wire manufacturers *Tanaka* and *Heraeus* or in the literature in general for aluminium and copper. Since the shear strength is an essential parameter in the bond formation model

Table 5.4: Identified model parameters a and b for the ultrasonic softening model

Copper		**Aluminium**	
a/mm^2/W	b/-	a/mm^2/W	b
0.01988	0.67	0.01003	0.995

in equation 4.3 and is required for the calculation of the shear force from the bonded areas, it must therefore be determined experimentally.

For this purpose, the clamp shown in figure 5.18 a) was built, which fixes the wire upright. The wire is positioned so that one part protrudes over the top edge and can be sheared through by the shear chisel. The shear force F_S is then measured by the shear tester; with the known cross-sectional area $A_S = \pi\ r^2$ of the wire the shear strength τ_S is calculated. The experimental setup is shown in figure 5.18 b); for the experiments, a *Dage Series 4000* pull and shear tester was used.

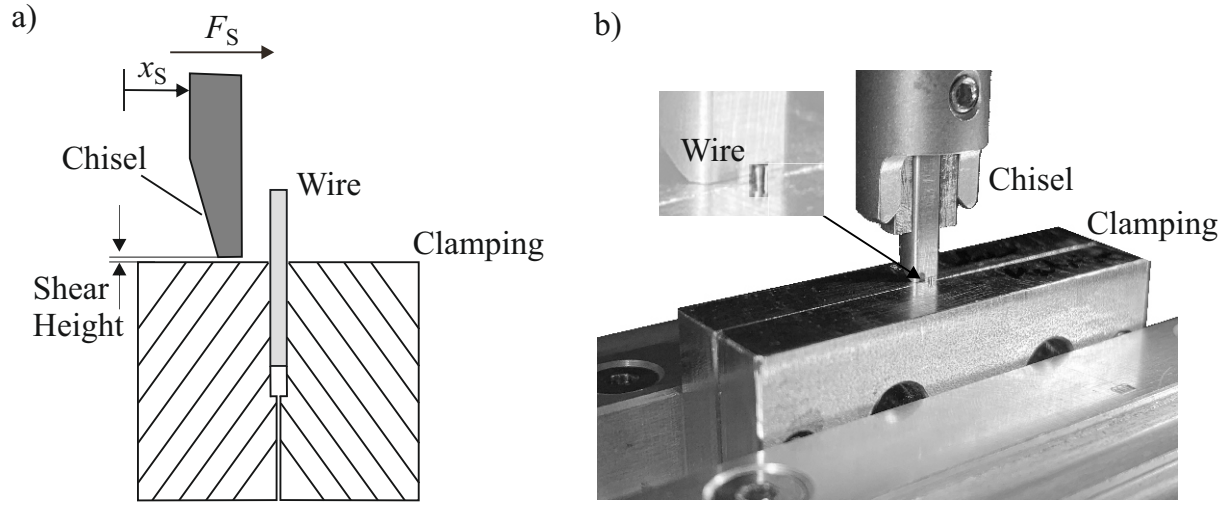

Figure 5.18: a) Clamping for the 400 µm bond wire to measure the shear strength and b) experimental setup in the shear tester.

For each material, 14 wires were sheared with a shear height of 5 µm and test speed of 300 µm/s in order to achieve a clearly reproducible fracture surface after the shear. The results are shown in the box plot in figure 5.19. The median value is 54.38 MPa for aluminium and 178.67 MPa for copper. The outlier values are 63.75 MPa for the aluminium and 166.22 MPa for the copper wire; for the bond model, the median values are used for the simulations.

When comparing the results from figure 5.19 with the shear strengths obtained after the shear tests from the ultrasonic aluminium wire bond tests in section 3.2, it is noticeable that the quasistatic shear strength of 54.38 MPa is significantly lower than the highest shear strength of 82.10 MPa measured in the wire bond shear tests; the corresponding sheared area to the highest shear strength of 82.10 MPa is shown in figure 5.20 a).

The shear strength is calculated from the measured sheared area, which is measured at the digital microscope by manually marking an area with the red lines shown in figure 5.20. No distinction is made between the areas within the marking, but the entire area is used to determine the shear strength. By this method, the calculated shear strength is

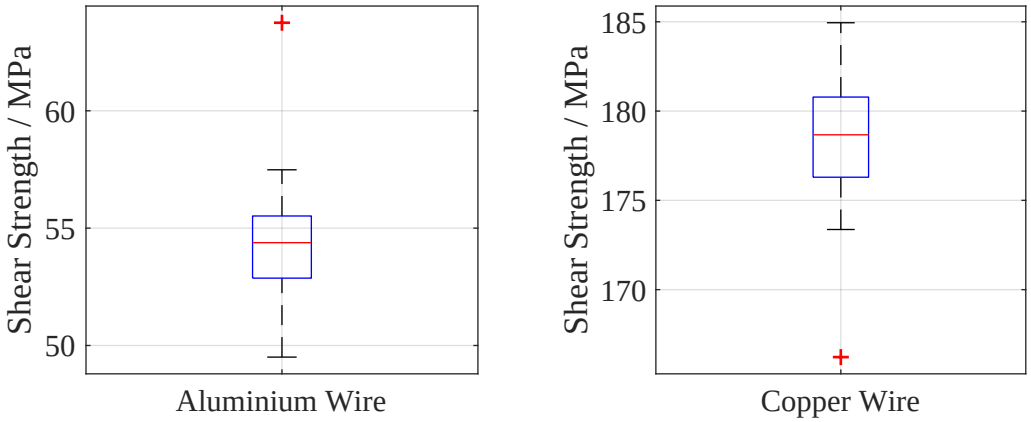

Figure 5.19: Box plots for the results of the shear strength for the aluminium and copper wire; for each material, 14 wires were sheared.

generally less than or equal to the actual shear strength of the wire. Only when the entire surface is 100 % bonded and thus contributes to the bond strength, the maximum shear strength can be determined. In figure 5.20 b) the sheared area with shear code 5 is shown; the corresponding shear strength was 66.78 MPa; although almost only the wire has been sheared, the shear strength is less compared to the shear code 2 shown in figure 5.20 a). Possible reasons for this effect are:

1. The measured sheared area is larger than the real bonded area, because the soft aluminium material has been smeared over the DCB surface during the shear test.
2. The shear strength of the interface area between copper and aluminium is larger compared to pure aluminium, thus the shear strength for shear code 2 is higher.

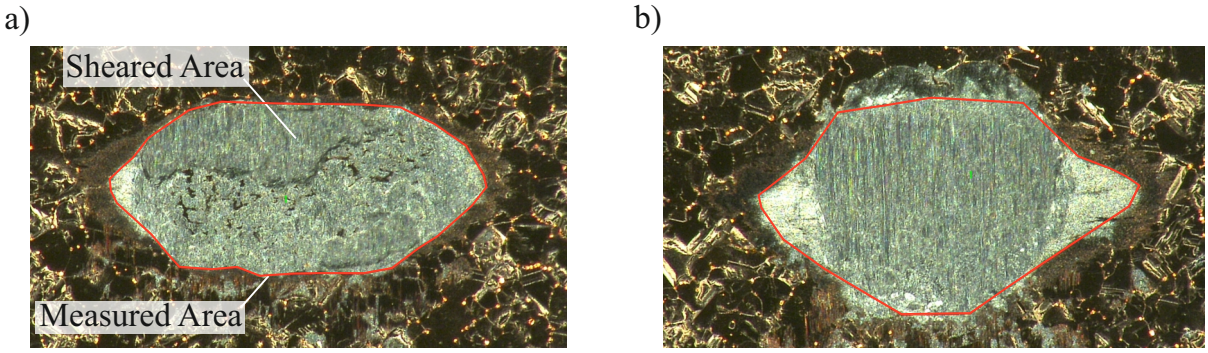

Figure 5.20: Sheared area from the aluminium wire bond experiments with a) $F_{\mathrm{BN}} = 14$ N, $u_{\mathrm{T}} = 25$ V and $t_{\mathrm{B}} = 400$ ms and b) $F_{\mathrm{BN}} = 10$ N, $u_{\mathrm{T}} = 35$ V and $t_{\mathrm{B}} = 400$ ms. The red line was set at the digital microscope for measuring the sheared area.

From the ultrasonic softening experiments in figure 5.15, it is known that material hardening occurs after a certain degree of deformation for the aluminium wire. The material hardening can explain the effect, that the shear strength of aluminium is larger after ultrasonic wire bonding compared to the shear strength which was determined using the shear tests in figure 5.18 of the wire in its original state . The value of the shear strength τ_{S} is used in the bond model to calculate the shear force from the calculated bonded area

and is also a parameter in the bond formation model, see section 4.1.2. For the simulation, the shear strength equal to 82.10 MPa is used for the aluminium wire, because this value considers the material hardening for calculating the shear force values; for copper, the static shear strength of 178.67 MPa is used, as from the bonding experiments, no higher shear strength values were observed, even for shear code 4.

5.6 Tangential wire stiffness

The shear stiffness $c_{\mathrm{t,W}}$ of the wire - which is summarized within the spring in the contact between wire and substrate - depends on the vertical position z_{WD} of the bonding tool. The accurate experimental identification of the tangential stiffness of the wire is very challenging, as in experiments the stiffness of the test rig impacts the measurement. For this reason the FE model from section 4.1.1 has been used to determine the shear stiffness of the wire with 400 µm diameter for aluminium and copper material. Therefore the substrate was modelled as a rigid body, thus only the wire had flexible body behaviour. In the simulation the vertical displacement z_{WD} of the bonding tool was increased from 10 µm to 190 µm in 20 µm steps in relation to the initial position of the undeformed wire; for 190 µm, tool/substrate contact occurred, thus this was the maximum vertical deflection of interest. For each height the bonding tool was deflected once sinusoidally with an amplitude of 3 µm and as a result, the tangential reaction force $F_{\mathrm{t,WS}}$ between wire and substrate was recorded. To determine the tangential stiffness, the slope of the positive flank of the hysteresis was evaluated using linear regression, see figure 5.21 a). The simulation was performed for aluminium and copper wire materials with the material properties shown in table 3.2.

The results for the wire shear stiffness are shown in figure 5.21 b). For both wire materials, the shear stiffness increases progressively as the bonding tool is lowered. When comparing the results at 190 µm to 10 µm, the shear stiffness of the wire at the end is about 16 times higher compared to the beginning.

The results from the FE-simulation were approximated by a polynomial fit of second order:

$$c_{\mathrm{t,W}}\left(z_{\mathrm{WD}}\right) = p_1\, z_{\mathrm{WD}}^2 + p_2\, z_{\mathrm{WD}} + p_3. \tag{5.1}$$

The polynomial coefficients are listed in table 5.5. Within the co-simulation, the polynomial function is implemented in *MATLAB* to calculate the current shear stiffness of the wire depending on the vertical position z_{WD} which is received from the *ANSYS* simulation.

Table 5.5: Polynomial coefficients of the fit to the shear stiffness of the aluminium and copper wire.

	p_1 / N/m/µm^2	p_2 / N/m/µm	p_3 / N/m
Al	247.37	$361.12 \cdot 10^2$	$843.83 \cdot 10^3$
Cu	252.87	$162.58 \cdot 10^3$	$904.72 \cdot 10^3$

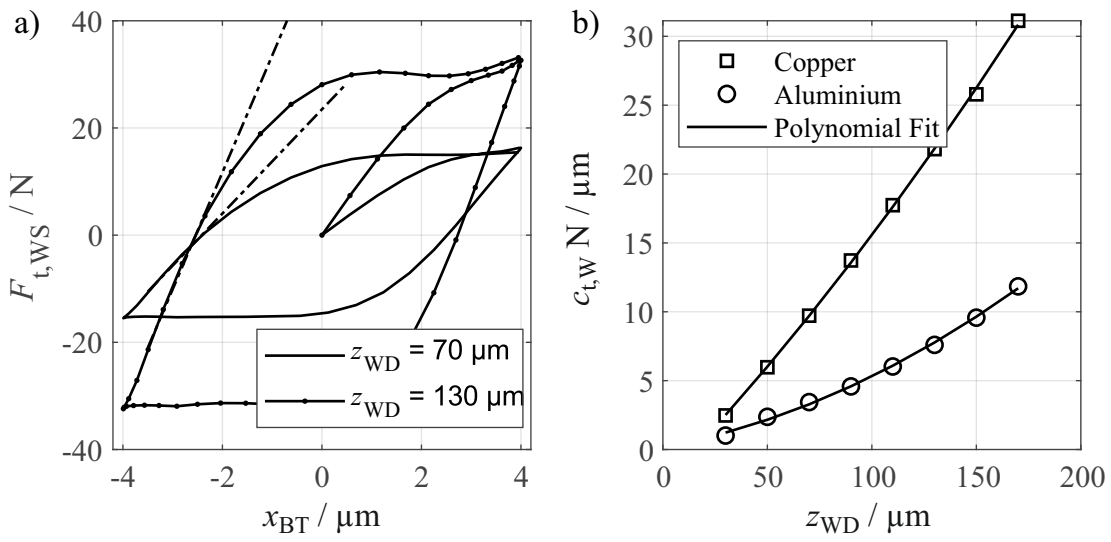

Figure 5.21: a) Hysteresis of the tangential force of the copper wire for two different heights (70 µm and 130 µm) with the slope of $c_{T,W}$ at the left flank. b) Tangential stiffness for the copper and aluminium wire from the FE-simulation and curve of the polynomial best fit.

5.7 Overview of the model parameters

In preparation for the simulation of the parameter studies and further detailed model based analysis of the bond formation in section 6.2, all scalar model parameters are listed in table 5.6. In terms for the clarity of the table, the coefficients of the stress-strain curve for the wire material in table 5.3 and the polynomial coefficients for the tangential wire stiffness $c_{t,W}$ in table 5.5 are not listed separately in table 5.6.

Table 5.6: Model parameters.

Short Description	-	Units	Al wire	Cu wire	Reference
Cleaning parameter	α	mm^2/J	24.28	84.94	table 5.2
Bonding parameter	β	mm^2/J	30	1.9	table 5.2
Fric. coeff. tool/wire	μ_{TW}	-	0.75	0.68	table 5.2
Fric. coeff. wire/DCB	μ_{OX}	-	0.23	0.21	table 5.2
Fric. coeff. wire/DCB	μ_{Met}	-	0.75	0.9	table 5.2
Mag. F_{BN} tool/wire	k	-	1.35	1.35	section 4.1.4
Wire shear strength	τ_S	MPa	82.10	178.67	section 5.5
Shear modulus of metallization	G	MPa	$47 \cdot 10^3$	$47 \cdot 10^3$	[13]
US-Softening parameter	a	mm^2/W	0.01003	0.01988	table 5.4
US-Softening parameter	b	-	0.995	0.67	table 5.4
Metallization height	h_I	µm	300	300	-
Reduction factor for TSC	k_{TSC}	—	0.15	0.50	-
Form fit tool/wire	$c_{t,W}$	N/m	$2.60 \cdot 10^6$	$5.00 \cdot 10^6$	-
Element number	n_x	—	100	100	-
Element number	n_y	—	20	20	-

6 Validation of the wire bond model

The main objective is the model based enhancement of process development in heavy wire bonding by simulation of parameter studies which are otherwise carried out experimentally.

The setup of the simulation is described in section 6.1. In section 6.2 the parameter studies from section 3.2 are simulated with the newly developed process model; the simulated main effects diagrams and shear force values at the different bond durations are compared with the experimental results for validation of the model approach for both, the aluminium and copper wire. In section 6.3, additional results of the predeformation, tangential forces and frictional energy between bond tool and wire, which are only available in the simulation and not from the experiments, are compared between the two wire materials. In section 6.4, the simulation results are discussed.

6.1 Setup for the simulation

Since the program structure of the co-simulation has reached a high degree of complexity, the Graphical User Interface (GUI) shown in figure 6.1 was programmed in order to be able to enter all simulation settings in an easily navigable way. In the panel shown in figure 6.1, the model parameters such like the bond formation model parameters or the coefficients of friction can be entered. In addition, the discretised friction contact can be parametrized and a visualisation of the mesh is given in order to check the mesh density.

In the panel *Excitation*, settings can be made whether the signal generator or the transducer model should be used; also, the frequency for the signal generator can be set. When the transducer model is used, in the panels *Transducer* and *Controller*, additional settings for the transducer model and PLL-controller can be made. Within the panels *Config* and *CoSim*, parameters for the solvers of *MATLAB* and *ANSYS* like the number of cores and time step size can be set. In the panel *Single Bond*, the bond parameters such as F_{TD}, F_{BN}, u_{T}, x_{BT} and t_{B} and in *Parameter Sweep* limits for several parameter combinations of the bond parameters for the simulation of the parameter studies can be made. All settings are then stored in the *cache.mat*-file which is loaded before the simulation of the bond model starts.

6.2 Simulation of the parameter studies

In this section, the results from the simulation of the parameter studies are presented. In order to allow a direct comparison between the results of the simulation and the experiment, the parameter levels from the experiments listed in table 3.3 were chosen for the simulation except for the bond duration as only the maximum level of 300 ms for copper and 400 ms for aluminium need to be simulated, since all the time points before

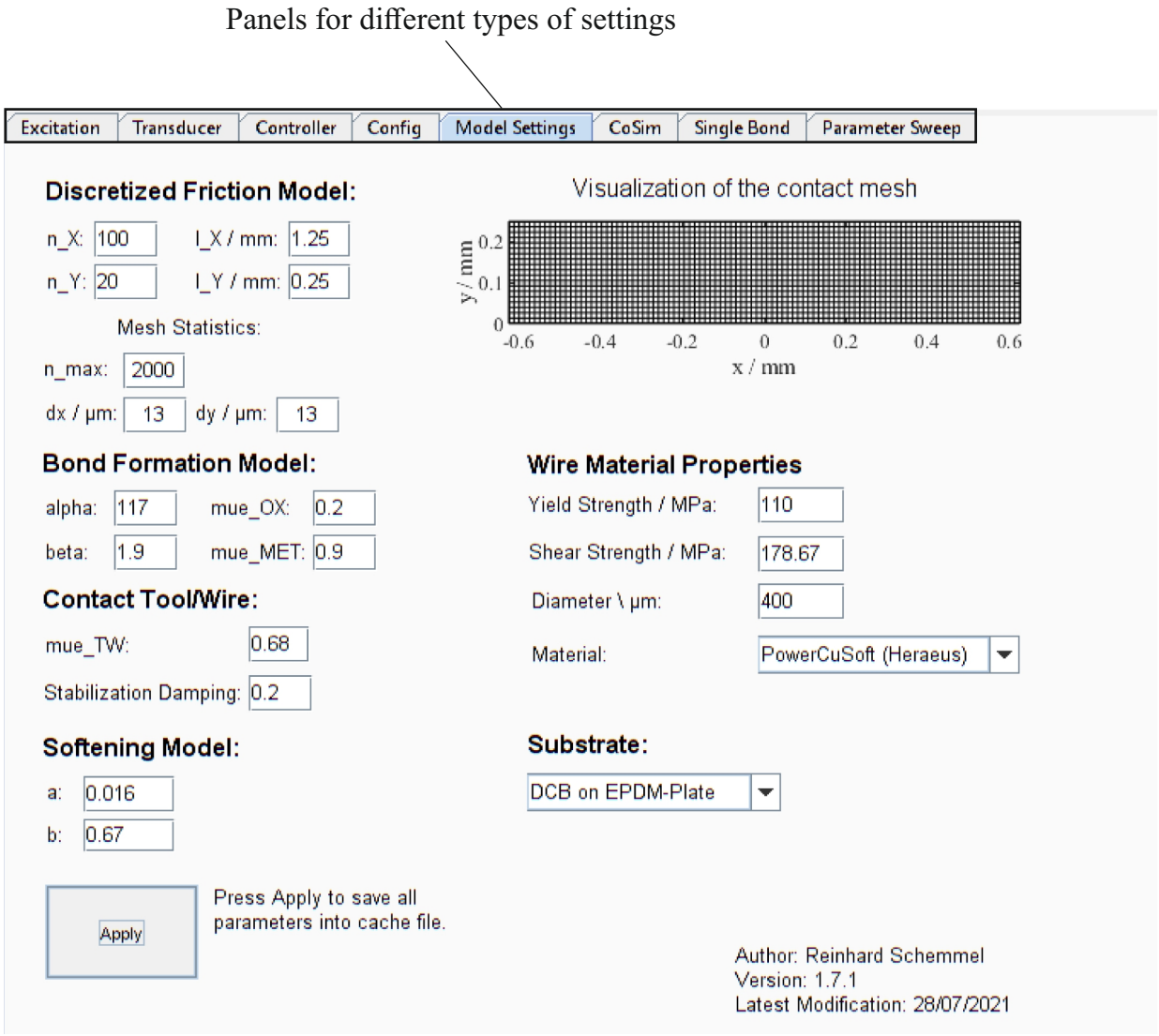

Figure 6.1: Graphical User Interface (GUI) of the bond model with the exemplary panel for the model settings for the copper wire.

are also available after simulation; thus, only 16 instead of 64 parameter combinations for copper and 12 instead of 48 parameter combinations for aluminium were simulated.

6.2.1 Copper wire

In figure 6.2 the simulated main effects diagram for the copper wire is shown; the grey lines in the background are the experimental results from section 3.2. The simulation results for the bond normal force F_{BN} have no significant effect on the shear force as all level means from 20 N to 38 N are close to the overall mean value, indicated by the horizontal dashed line. For the shear strength, increasing the bond normal force has a negative effect in the investigated range from 20 N to 38 N. The bond duration t_{B} has a clear positive effect over the entire range from 70 ms to 300 ms on both, the shear force values and shear strength. This also applies to the ultrasonic voltage u_{T}, which shows the largest positive effect on the shear force and strength values. Good agreement between the results of the simulation and the experiment could be achieved for the trends of the

shear force and the shear strength values. Although, the trends for the shear strength correlate between simulation and experiment as the curves are almost parallel to each other, the simulated shear strength values are shifted towards higher values by a relatively constant factor of 1.35. This effect is explained by the measurement of the contact area of the sheared surfaces: in the outer part of the measured contact areas, dark spots are observed, which can be identified as oxides which do not contribute to the bond strength but were included in the measurements leading to a larger measured contact area. This leads to constantly lower shear strength values in the measurements compared to the simulation; see section 6.4 and figure 6.10 for a detailed comparison of the measured and simulated contact areas and a correction method of the measured shear strength values.

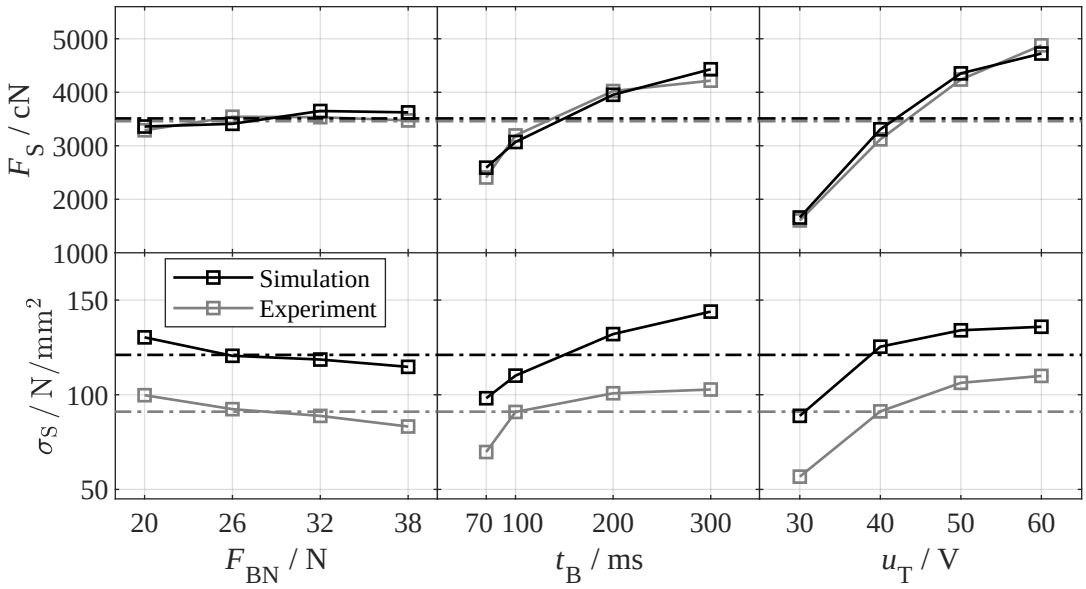

Figure 6.2: Copper wire: simulated main effects diagram; the grey lines are experimental results from section 3.2.

For a more detailed insight, figure 6.3 shows the simulated curves of the shear force values during bond formation and the measured mean shear force values from the experiments at the investigated bond durations for the different levels of bond normal forces and ultrasonic voltages. For u_T equal to 30 V, the simulated curves show a significant flatter trend for all bond normal forces compared to voltages from 40 V to 60 V. This correlates with the experimental results; especially in the beginning up to 70 ms, only very small shear force values lower than 10 N were computed while in the experiments 100 % lift off's occurred as already cutting the wire can lead to a lift off for such small shear force values. For F_{BN} from 26 N to 38 N, at 100 ms and 200 ms the simulated shear force values are slightly smaller than the measured mean shear force values while for 20 N, the simulation fits to the measured values at these bond durations. As for increased bond normal force the sticking force is also increased in the contact between wire and substrate, gross sliding is reduced for the larger bond normal forces which leads to reduced bond growth for the small vibration amplitudes at 30 V in the simulation. In contrast to the voltage of 30 V, for the voltages in the range from 40 V to 60 V, the shear force increases rapidly at the beginning and then reaches a turning point, which is reached more quickly for higher voltage levels. After the turning point, the shear force continues to increase with lower slope, which is the main reason why in the main effects diagram

the bond duration after ultrasonic voltage has the second largest positive effect on the shear force and the shear strength. When tool/substrate contacts occur, the slope of the shear force curves decreases significantly because at this point in the simulation model the parameter β is reduced by the factor k_{TSC} to account for the fact that part of the vibration power is transmitted directly from the bond tool into the substrate and not into the wire. This correlates well with the measurements: for F_{BN} equal to 38 N for example, tool/substrate contacts occurred for ultrasonic voltage equal to 60 V after approx. 100 ms and the growth of shear force values with rising bond duration is significantly decreased for both, simulation and experiment. A direct comparison between the simulated and measured tool/substrate contacts is given in the appendix, see section A.8.

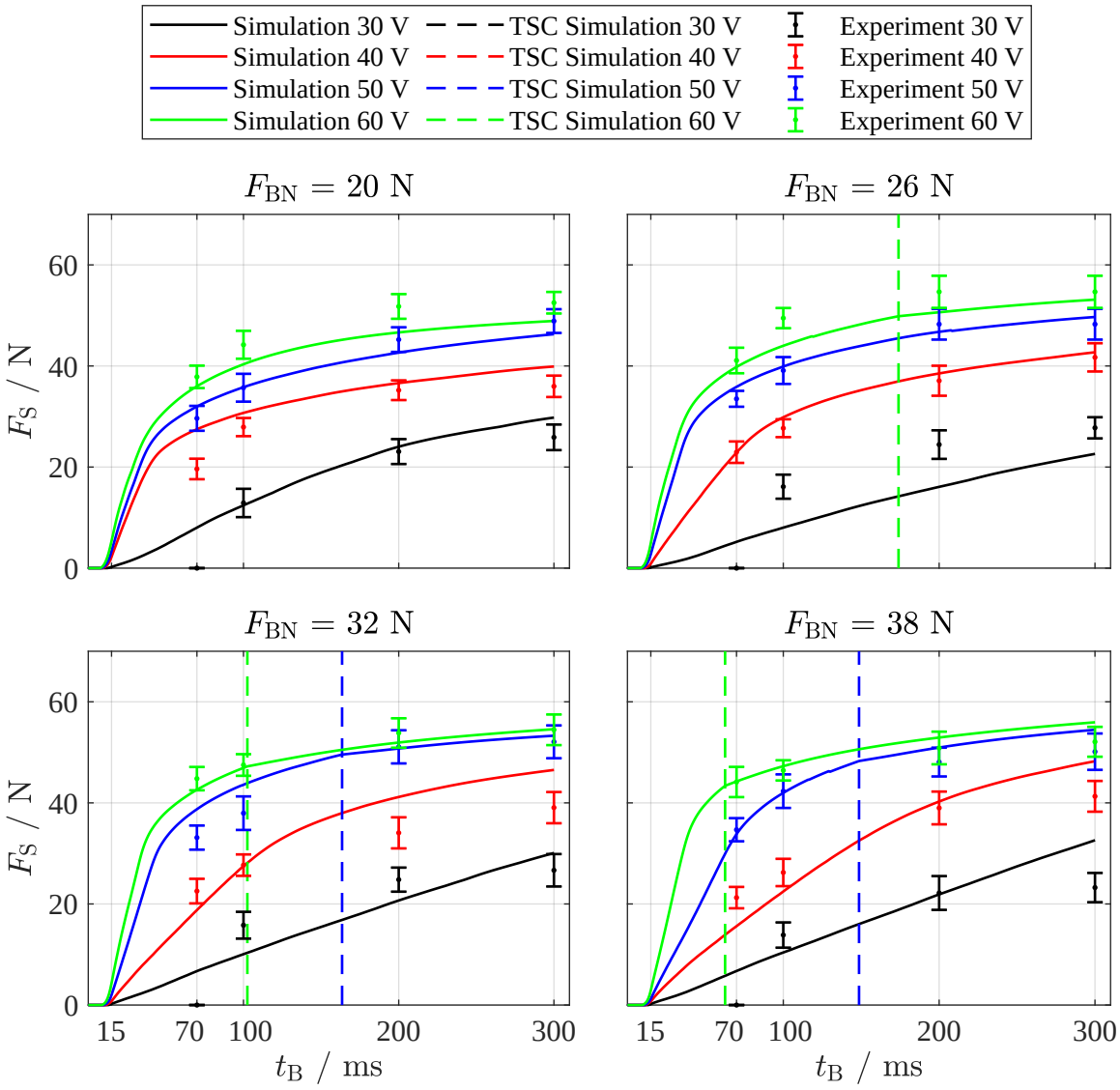

Figure 6.3: Copper wire: simulated shear force values during bond formation for the different levels of ultrasonic voltage and bond normal force with the vertical dashed lines indicating the time of tool/substrate contacts (TSC) in the simulation and the experimental results for the shear force values (mean values ± standard deviation) at the investigated bond durations.

6.2.2 Aluminium wire

In figure 6.4 the simulated main effects diagram for the aluminium wire is shown. As observed from the experiments, the bond normal force F_{BN} has a significant positive effect on the shear force values in the whole range from 10 N to 18 N as the curve shows an almost linear positive trend in the simulation. For the shear strength, in the simulation no significant effect of the bond normal force occurs, while for the experiments a negative trend is observed. The bond duration t_{B} has a positive effect over the entire range from 100 ms to 400 ms on both, the shear force values and shear strength in the simulation. For the shear strength, in the experiments a slight negative effect of the bond duration on the shear strength was observed. For the ultrasonic voltage u_{T}, a positive effect on the shear force values is observed in the simulation. This is in good agreement with the experimental results from 20 V to 30 V; for 35 V, the shear force values decrease in the experiments while for the simulation the curve flattens, but does not decrease. The shear strength increases from 20 V to 25 V in the simulation and then remains almost constant from 25 V to 35 V, while in the experiments, the shear strength decreases from 25 V to 35 V.

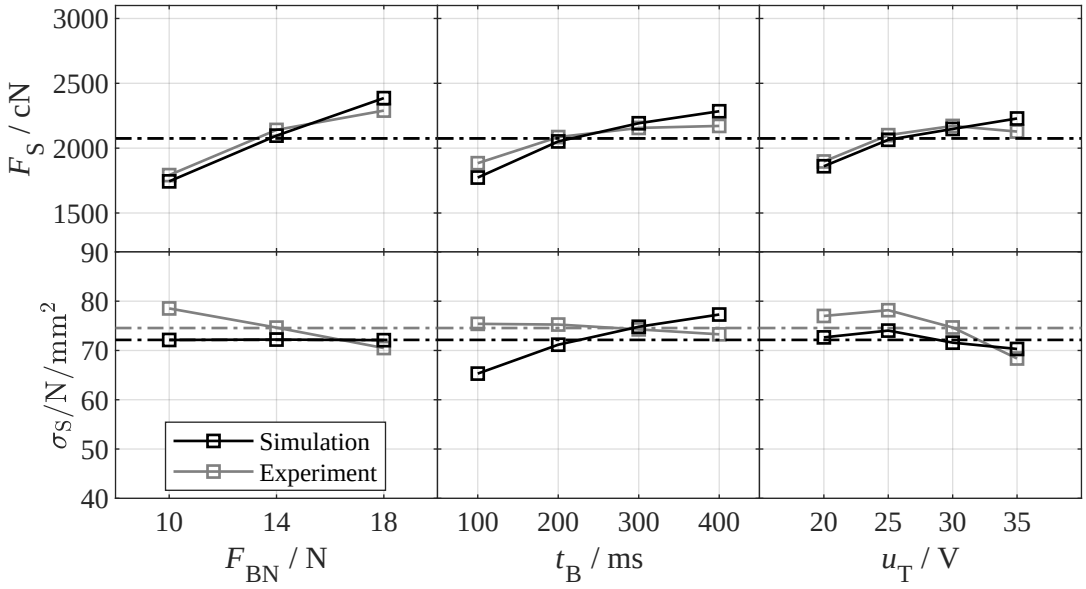

Figure 6.4: Aluminium wire: simulated main effects diagram; the grey lines are experimental results from section 3.2.

In figure 6.5 the simulated shear force during bond formation for the aluminium wire is shown. For F_{BN} equal to 10 N, the curves for the different ultrasonic voltages show good agreement with the measured shear force values. For F_{BN} equal to 14 N, the simulated curve of u_{T} equal to 20 V is slightly lower compared to the levels of mean shear force values from the experiments, while for the higher levels from 25 V to 35 V good correlation between simulation and experiments is achieved. For F_{BN} equal to 18 N, the shear force values for the ultrasonic voltage equal to 35 V decrease after 100 ms in the experiments, while in the simulation the shear force values further increase, although the slope is reduced after occurrence of the tool/substrate contact. This is the reason, why in the main effects diagram, for the ultrasonic voltage the trend does not decrease from 30 V to 35 V as for the experiments. For 18 N bond normal force, the shear forces

for 25 V and 30 V ultrasonic voltage reach even higher shear force values than the curve bonded at 35 V as no TSC or later TSC occur compared to 35 V.

For all investigated levels of the ultrasonic voltage and bond normal force, most of the bond formation occurs within the first 75 ms of bond duration while the first measured shear force values from the experiments are available from 100 ms to 400 ms. The bond normal force has the largest impact on the shear force values, while the curves for the different ultrasonic voltages are grouped together and do not differ that much from each other, as for the copper wire in figure 6.3. Thus, the results from figure 6.5 correlate with the finding from the main effects diagram in figure 6.4.

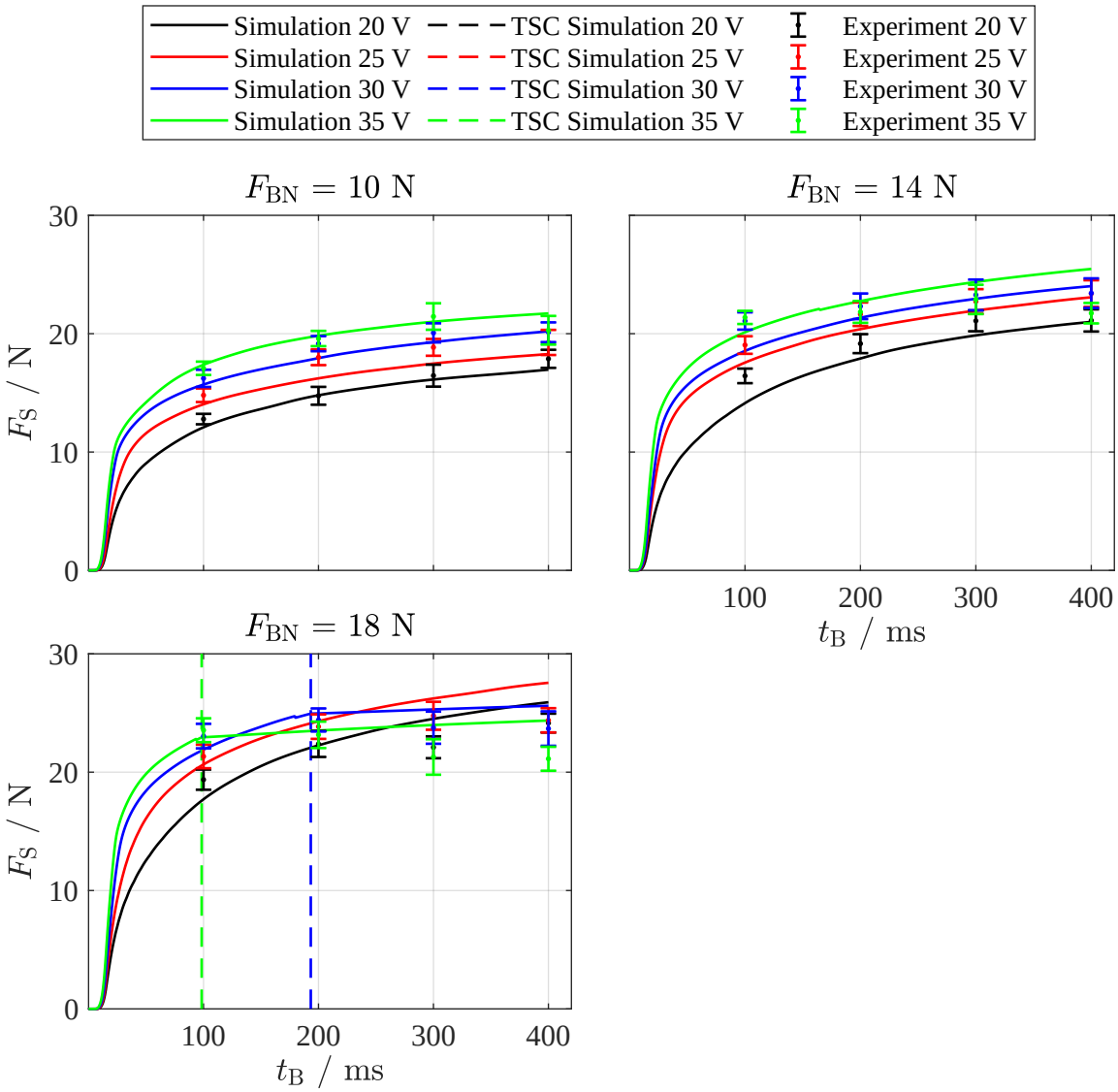

Figure 6.5: Aluminium wire: simulated shear force values during bond formation for the different levels of ultrasonic voltage and bond normal force with the vertical dashed lines indicating the time of tool/substrate contacts (TSC) in the simulation and the experimental results for the shear force values (mean values ± standard deviation) at the investigated bond durations.

6.3 Additional simulation results

In this section, additional simulation results of the wire pre-deformation, the tangential forces and the bond formation are shown; the wire pre-deformation and the tangential forces could not be measured during the wire bonding experiments. Thus, the simulation results give new insights into the wire bonding experiments that are not provided by the experiments.

6.3.1 Pre-deformation

In figure 6.6 a) the vertical bond tool displacement z_{WD} and in figure 6.6 b) the contact area size $A_{\mathrm{C,WS}}$ at the investigated touch down force levels for the aluminium and copper wire are shown. For both materials, an almost linear trend of the curves occurs. For the aluminium wire, significantly larger vertical displacements and contact area sizes were calculated compared to the copper wire. The vertical displacement is approx. 4.5 times and the contact area approx. 2.5 times larger than for the copper wire.

In the experimental investigations on the impact of the touchdown force in section 3.1, it was observed that the vertical displacement z_{WD} increases with decreasing ratio F_{TD} / F_{BN}. This can be explained by the simulation results from figure 6.6 a): within the pre-deformation phase, the vertical displacement of the bond tool is decreased with decreasing ratio F_{TD} / F_{BN} and when ramping up the bond normal force from the touchdown force during the bonding process, the bonding machine captures the resulting vertical displacement. When increasing the ratio F_{TD} / F_{BN}, the resulting deformation occurs within the pre-deformation phase, which is not measured by the bonding machine; thus, the measured vertical displacement z_{WD} at the bonding machine decreases.

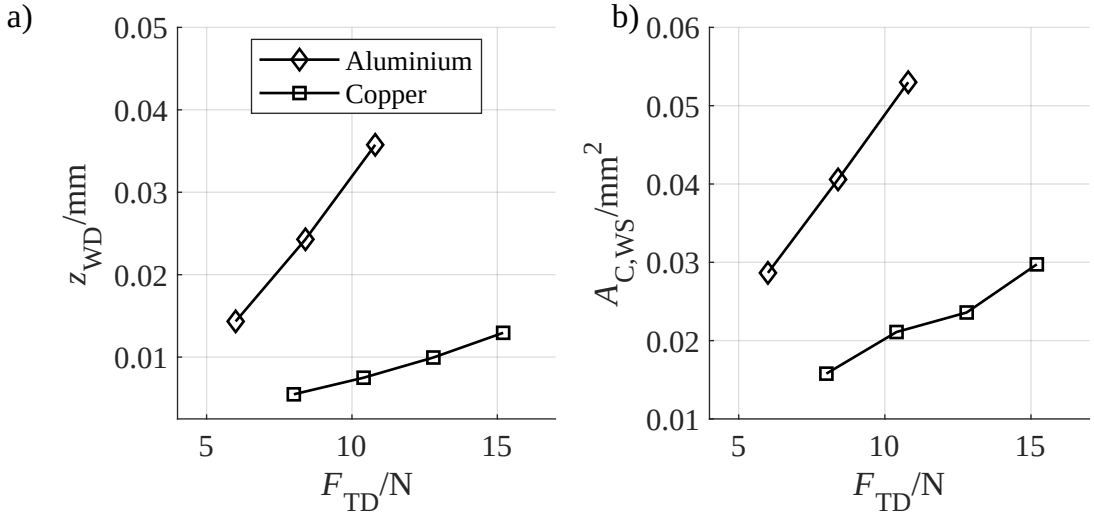

Figure 6.6: Simulation results of the pre-deformation: a) vertical displacement z_{WD} of the bond tool and b) contact area size $A_{\mathrm{C,WS}}$ at the corresponding touchdown forces F_{TD}.

6.3.2 Tangential forces, development of activated and bonded areas and frictional work between bond tool and wire

In figure 6.7 a) the envelopes of the simulated tangential force for the aluminium and copper wire within the first 100 ms of bond formation are shown, as most changes in the characteristics of the curves occur in the beginning of the bond formation. For the copper wire, the transition from micro-slip to gross sliding occurs after approx. 5 ms and immediately the cleaning process begins and the tangential force increases as the coefficient of friction increases from μ_{OX} to μ_{MET}. For aluminium, the curve of the tangential force shows a more continuously and smooth trend. The increase of activated area $A_{\mathrm{Activated}}$ and bonded area A_{Bonded} are shown in figure 6.7 b) for the aluminium wire and in figure 6.7 c) for the copper wire. For the aluminium wire, the growth rate of the activated area during the ramp phase up to 15 ms is less compared to the copper wire; this is because of the five times lower coefficient α for the cleaning and activation state τ compared to the copper wire, see table 5.2. With increasing activated area, with a certain delay, the bond formation begins and activated areas become bonded. In the beginning, the growth rate of the bonding state γ is the largest as the amount of activated areas and the frictional work due to gross sliding are highest in this phase. With increasing bond formation, the mechanical resistance in direction of the vibration increases as the tangential force $F_{\mathrm{t,WS}}$ in figure 6.7 a) continuously increases and the relative motion between wire and substrate is reduced; the bond formation then reaches the turning point, which was also observed in the curves of the shear force values in figure 6.3 and figure 6.5.

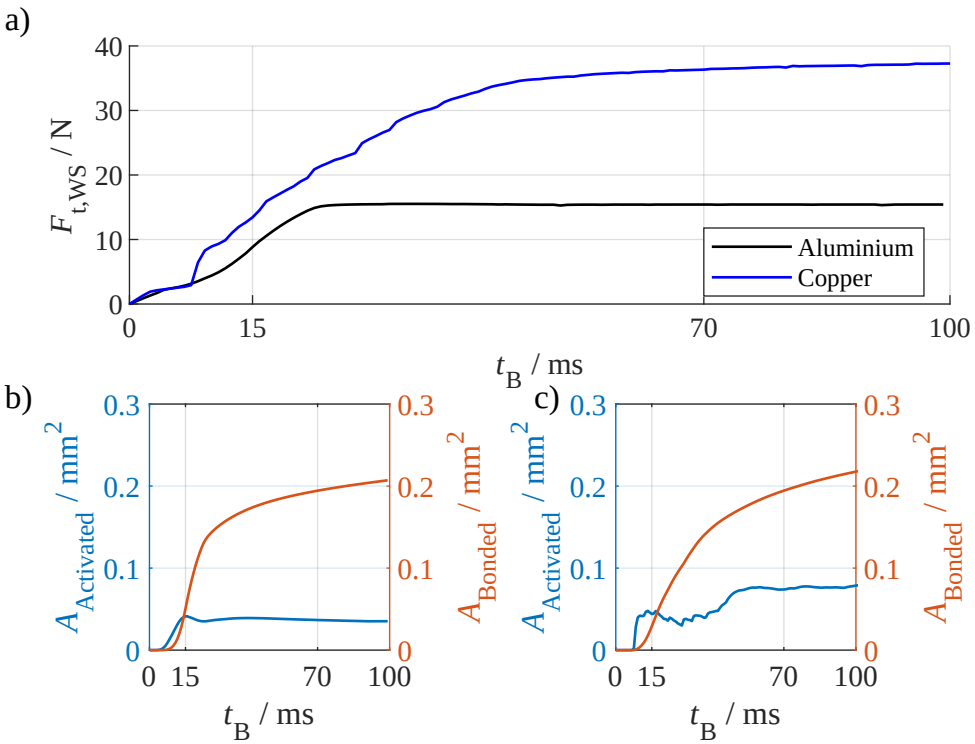

Figure 6.7: a) Envelopes of the tangential force $F_{\mathrm{t,WS}}$ for aluminium ($F_{\mathrm{BN}} = 14$ N and $u_{\mathrm{T}} = 30$ V) and copper ($F_{\mathrm{BN}} = 20$ N and $u_{\mathrm{T}} = 60$ V), and the activated and bonded areas during bond formation for b) copper and c) aluminium wire.

This behaviour can be explained by the hysteresis of the tangential forces $F_{\mathrm{t,WS}}$ between tool and wire and $F_{\mathrm{t,TW}}$ between wire and substrate, see figure 6.8. For the aluminium wire in figure 6.8 a), at 3 ms the wire sticks on the substrate and no relative motion occurs. At 7 ms, gross sliding occurs and for 25 ms, the transition from stick to slip is shifted to a higher level as the cleaning process leads to more activated areas and the coefficient of friction increases from from μ_{OX} to μ_{MET}. At 75 ms bond duration, the relative motion between wire and substrate is significantly reduced and micro-slip behaviour instead of gross sliding is observed. For the contact force $F_{\mathrm{t,TW}}$ between bond tool and and wire, only elastic deformation is observed for the bond durations up to 35 ms as the bond tool sticks on the wire. For 75 ms, relative motion occurs between bond tool and wire occurs. During sliding in the contact between tool and wire, the tangential force $F_{\mathrm{t,TW}}$ steadily increases due to the parallel spring $c_{\mathrm{t,TW}}$ which models the form fit.

For the copper wire in figure 6.8 b), the tangential forces and relative displacements are in general approx. two times larger than for aluminium. The principle frictional behaviour in the contact between wire and substrate is comparable for the two wire materials. In the contact between bond tool and wire, significantly larger relative motion occurs. The contact between tool and wire can transmit tangential force up to a maximum equal to $\mu_{\mathrm{TW}}\ k\ F_{\mathrm{BN}}$. For copper, μ_{TW} is equal to 0.68 and for aluminium equal to 0.75, see table 5.2. Thus, the maximum transmittable tangential force by the frictional contact in the sticking phase depends on the applied bond normal force and is almost independent from the material itself, as the values for coefficients of friction are close to each other and and k is the same as the same bond tool geometry is used for both materials. Due to the larger tangential stiffness $c_{\mathrm{t,W}}$ and larger vibration amplitude x_{BT} of the copper wire compared to aluminium wire, less elastic deformation of the wire and more relative motion between bonding tool and wire occurs for the copper wire. When the bond tool starts sliding on the wire, the ultrasonic power transmitted to the wire is reduced and the growth rate of bonded areas A_{Bonded} in figure 6.7 c) reduces.

From the results shown in figure 6.8 it follows, that the dissipated energy in the contact between bond tool and wire is generally larger for copper wire than for aluminium wire because of the increased relative motion between tool and wire. In figure 6.9, the cumulated dissipated energy W_{f} from the contact between tool and wire is shown for the different levels of bond normal force and ultrasonic voltage. For the aluminium wire, for bond normal forces from 10 N to 18 N and ultrasonic voltages from 20 V to 25 V, almost no relative motion occurred between tool and wire, thus the dissipated energy is close to zero. For ultrasonic voltage from 25 V to 35 V, the dissipated energy almost linearly increases with increased voltage for all three levels of the bond normal force. The maximum of the dissipated energy is approx. 2 J. For the copper wire, only for ultrasonic voltage equal to 30 V and bond normal force from 26 N to 38 N almost no sliding of the bonding tool on the wire occurred and the dissipated energy is close to zero. For higher levels of the voltage, the dissipated energy almost linearly increases for all levels of the bond normal force. The maximum of the dissipated energy is approx. 10 J for the copper.

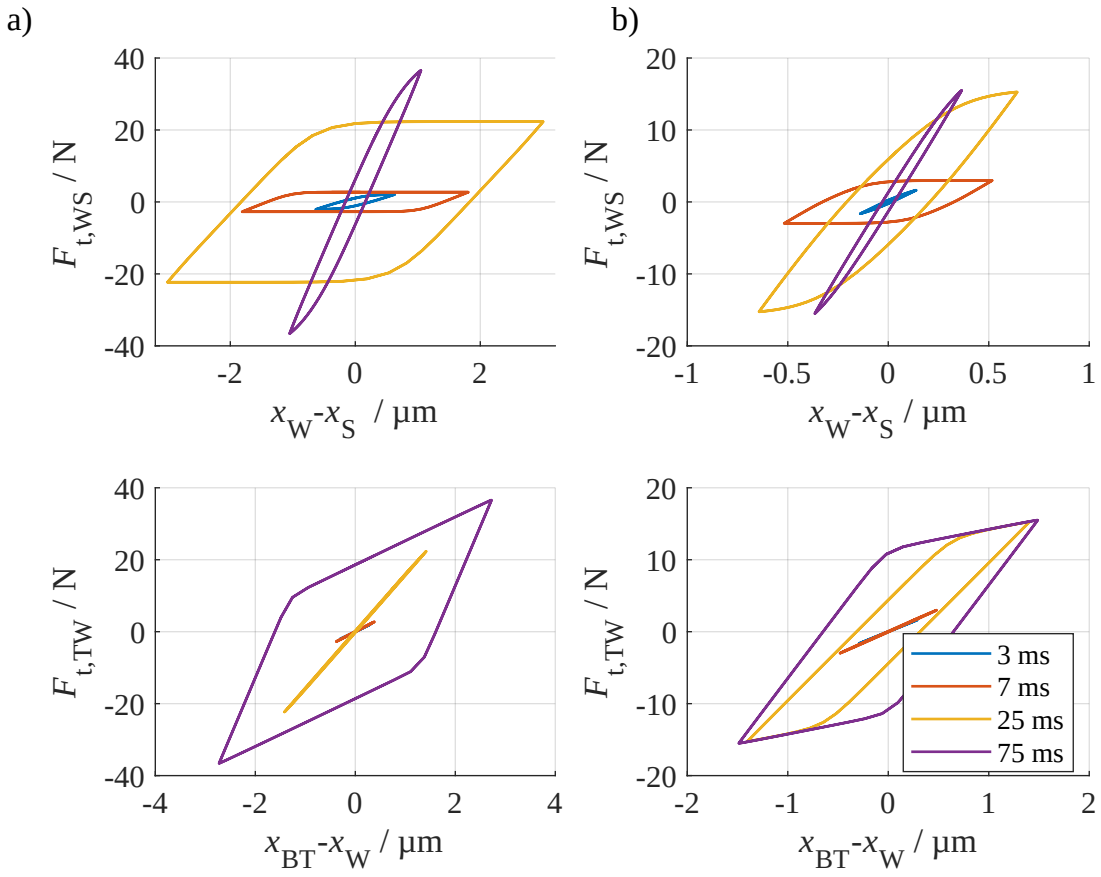

Figure 6.8: Hysteresis of the tangential forces $F_{t,WS}$ (top) between wire and substrate and $F_{t,TW}$ between bond tool and wire (bottom) for a) copper ($F_{BN} = 20$ N and $u_T = 60$ V) and b) aluminium ($F_{BN} = 14$ N and $u_T = 30$ V).

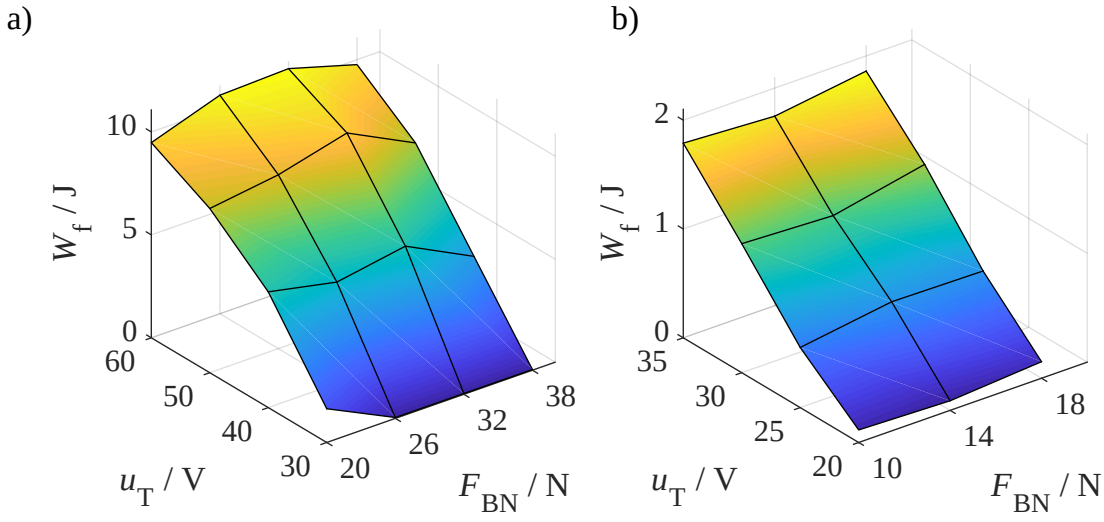

Figure 6.9: Simulation results: dissipated energy W_f due to friction in the contact between bond tool and wire after 300 ms of bond formation for a) copper and b) aluminium wire.

6.4 Interpretation of the simulation results

The comparison between simulated and experimentally determined main effects diagrams for the aluminium and copper wire showed, that the developed bond model is capable to predict the shear force and strength values over wide range of the process parameter, namely the touchdown force, bond normal force, bond duration and ultrasonic voltage. Thus, the basic physical mechanisms leading to bond formation are considered in the multi-scale model approach. Nevertheless, some slight deviations between the results from the simulation and measurements were detected for some parameter combinations which are discussed in the following.

In the main effects diagram of the copper wire in figure 6.2, the simulated shear strength values are shifted to higher levels by a constant factor of approx. 1.35 compared to the measured values. The reason for this could be identified in the determination of the size of the sheared surface: in figure 6.10 sheared surfaces and simulated contact areas for two bond parameter combinations are shown, one with low bond normal force and low ultrasonic voltage and one with increased bond normal force and ultrasonic voltage to capture different wire deformation levels. When comparing the simulated contact areas to the sheared surfaces from the experiments, it is noticeable that the sheared surfaces were constantly determined larger than the simulated contact area. As the red lines are set manually at the digital microscope, the decision was made to draw the line at the border between the original surface of the DCB and the worn surface; especially in the area of the elliptical ring between the red line and the outer line of the simulated contact area, it was unclear whether these parts of the sheared surface contribute to the bond strength or not. The dark spots in the outer parts of the sheared surface are copper oxides which were transported to the outside of the sheared surface during bond formation. Thus it can be assumed, that these parts of the sheared surfaces do not contribute to the shear strength.

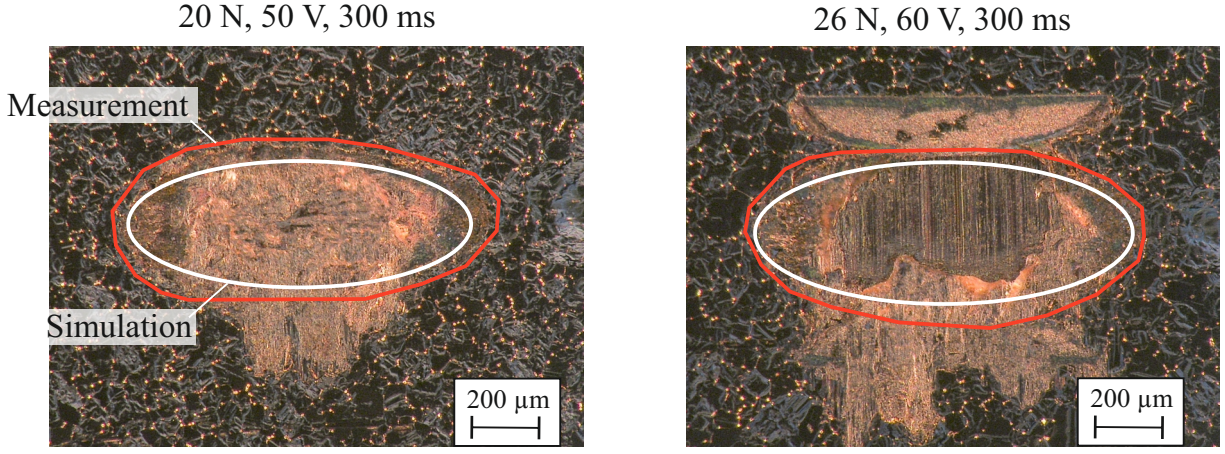

Figure 6.10: Copper wire: microscopy images of the sheared surfaces and simulated contact surface for two representative bond parameter combinations; the red lines were set at the microscope to measure the size of the sheared surface.

When calculating the shear strength by taking the shear force values from the experiments and the contact area size from the simulation, the corrected main effects diagram can be determined and now the values of simulated and measured shear strength correlated with each other, see figure 6.11. Thus, the conclusion from the comparison between

simulation and measurement is, that the measurement of the size of sheared surface is crucial to determine the correct shear strength and in this case, the surface was constantly measured larger than the real contact area contributing to the shear strength.

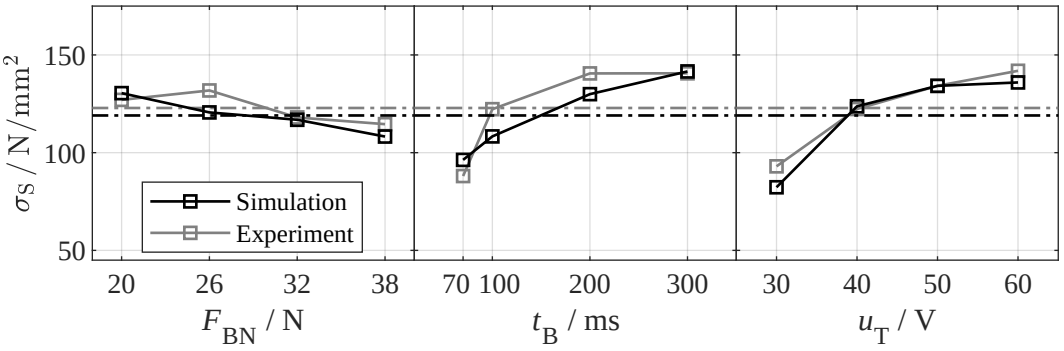

Figure 6.11: Copper wire: corrected simulated main effects diagram from figure 6.2 with shear strength values of the experiments calculated with the nominal contact area $A_{C,WS}$ from the simulation.

For the aluminium wire, the simulation results of the shear force values over the bond durations in figure 6.5 show that most of the bond formation takes place within the first 100 ms. In the experiments, the investigated bond durations were varied from 100 ms to 400 ms; these levels were chosen based on the results from the parameter studies of the copper wire, which were performed before the experiments with the aluminium wire. If the knowledge about the different bonding behaviour between aluminium and copper wire could have been investigated in advance on the basis of simulation, the levels would have been chosen differently. *This shows the great potential of simulation-supported process development.*

In the main effects diagram of the aluminium wire in figure 6.4, slight differences between simulation and experiment occur especially for increased values of the ultrasonic voltage and bond normal force. For further analysis of this effect, in figure 6.12, the sheared surfaces and simulated contact areas for the aluminium wire are shown for two representative bond parameter combinations. For the sheared surface on the left, the differences between the sheared surface from the experiment and the simulated contact area are negligible as the simulated area is only slightly narrower but also slightly longer. For the second parameter combination on the right side with larger bond normal force and higher ultrasonic voltage, the width of the sheared surface is increased significantly and is only limited by the width of the v-groove of the bond tool; also splashing is observed, as parts of the aluminium wire were transported underneath the bond tool. In the simulation, the contact area remains an almost elliptical shape, but the width is also increased compared to the bond parameter combination with lower bond normal force and ultrasonic voltage. Since in the simulation, the wire deformation is computed quasi-statically with the FE-model using the symmetry plane shown in figure 4.2, effects like splashing and unsymmetrical deformation behaviour can not be captured by the model which partly explains the deviations between simulation and experiment especially for the increased bond normal force and ultrasonic voltage where these effects occur.

Besides the size and shape of the sheared surface, the occurrence of the different shear codes and tool/substrate contacts impacts the measured shear force values. In figure 6.13

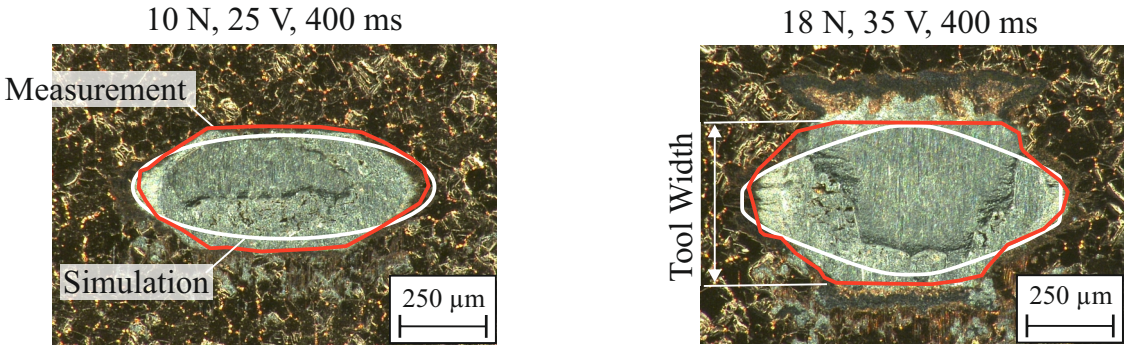

Figure 6.12: Aluminium wire: microscopy images of the sheared surfaces and simulated contact surface for two representative bond parameter combinations; the red lines were set at the microscope to measure the area of the sheared surface.

the simulated and measured shear force values bonded with 35 V ultrasonic voltage and a) 10 N and b) 18 N bond normal force over bond duration are shown. For 10 N bond normal force, the shear code steadily increases from shear code 1 to shear code 4 as do the measured shear force values. This behaviour is in good agreement with the simulated curve of the shear force values. For 18 N bond normal force in figure 6.13 b), shear code 3 is observed for all bond durations and tool/substrate contacts occur after approx. 100 ms. In the simulation, the shear force remains almost constant after the tool/substrate contact, as β is reduced by k_{TSC} equal to 0.15. In the experiments, from 100 ms to 200 ms, the shear force values also remain almost constant with the first occurrence of tool/substrate contacts, but with further increasing bond duration from 200 ms to 400 ms, the measured shear force values even decrease. This can not only be explained by reduced ultrasonic power transmitted to the wire. Since the shear forces in the experiment do not decrease at 10 N bond normal force, although the amplitude x_{BT} is approximately the same in both cases, the decreasing shear values can be explained by the overdeformation and overbonding, which are strongly linked:

- With the occurrence of tool/substrate contacts, sharp edges only at the top side of the sheared surfaces are observed. As the shear direction was from top to bottom in all images, this edge was produced by the shear chisel by pushing wire material in front of the chisel which can influence the fracture dynamics during the shearing process.
- Overbonding occurs, as reported by Pan et al. [94]; due to over deformation of the wire, already bonded parts of the interface can be destroyed leading to reduced shear force values.

Further explanations for slight deviations between the results of the simulation and the experiment for both, the aluminium and copper wire, are:

- Tolerances of the bond tool geometry, especially of the v-groove (foot length, tool opening angle, groove depth), which are specified by the manufacturer [120]. The geometry has an impact on the wire deformation and thus, impacts the bond formation.
- Calibration of the bond head: as a standard bond head for copper ribbon/heavy wire bonding was used for all experiments, especially for the aluminium wire and the low normal forces compared to copper wire, the accuracy of the applied touchdown and bond normal force is strongly dependent on the calibration of the force control

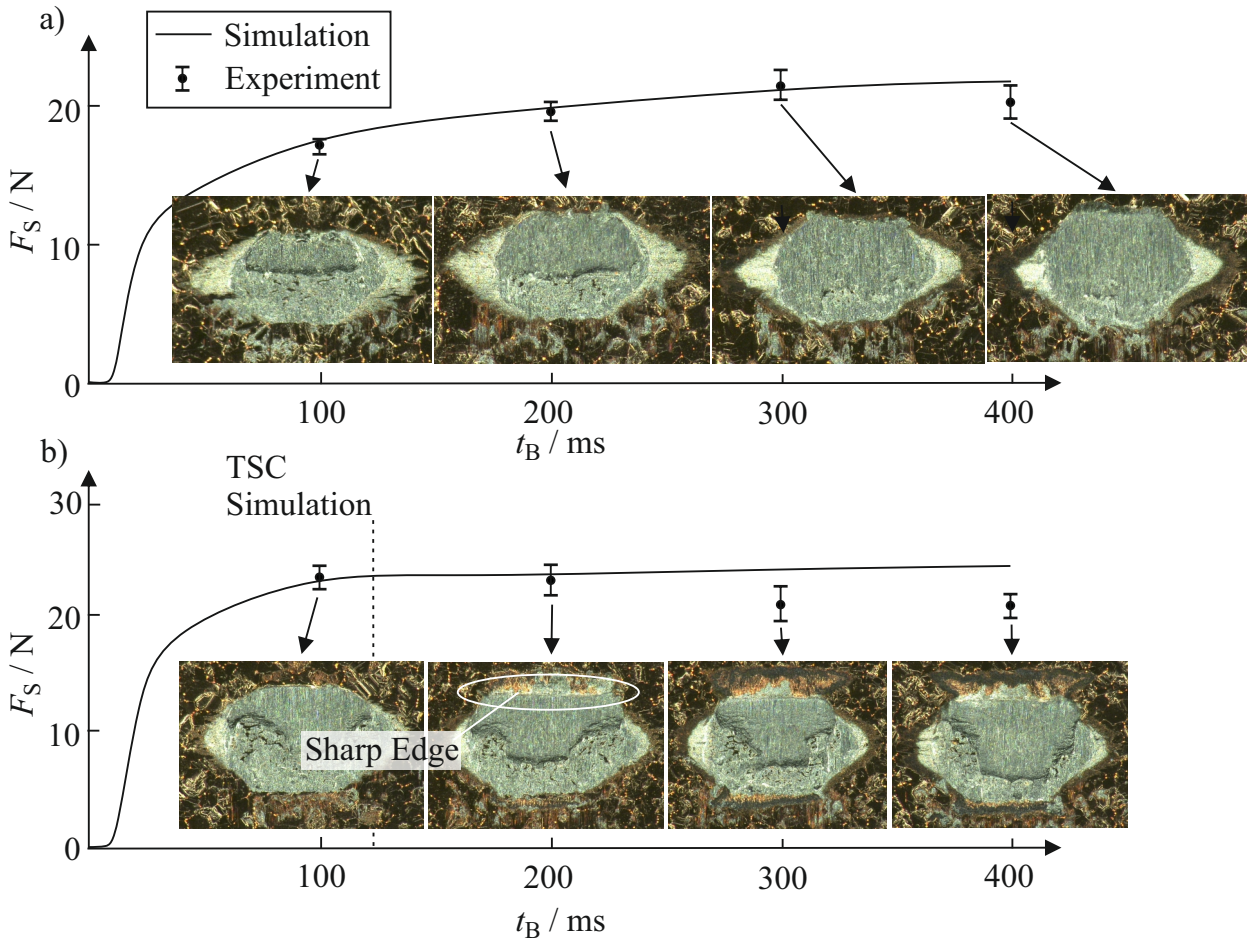

Figure 6.13: Aluminium wire: simulated and measured shear force values over the bond duration bonded with 35 V and bond normal forces equal to a) 10 N and b) 18 N.

unit applying the normal force. Although the calibration has been done before changing the wire material, the real applied normal forces can differ from the set values at the bonding machine, while the simulation is carried out with idealised values from the test plan.

- Angular error in the alignment of the bonding tool to the DCB surface: In the simulation, an ideal, parallel alignment of the surfaces is ensured, while in the experiment, one-sided tool/substrate contacts occur, see figure 6.10.

7 Conclusion and suggested future work

In this thesis, a new model approach based on a co-simulation for the ultrasonic heavy wire bonding process was developed and validated for 400 µm copper and aluminium wire. The gained knowledge is summarized in the following.

In ultrasonic wire bonding experiments the impact of the process parameters on the shear force and shear strength was investigated. In particular, the influence of the touchdown force and the ultrasonic frequency on the shear force and shear strength had not been systematically investigated for ultrasonic heavy wire bonding before:

- A smaller ratio of touchdown force and bond normal force leads to more wire deformation during bonding. For copper wire, a smaller touchdown force than the bonding normal force leads to an improvement in shear force and shear strength.
- The ultrasonic frequency has an impact on the substrate vibration: when the excitation frequency is higher than the resonance frequency of the next closest substrate vibration mode, the substrate vibration is reduced significantly. This is beneficial for the bond result in most cases.

The requirements for modelling the bond process were derived from the ultrasonic bonding tests and a wire bond process model was developed based on a co-simulation between *MATLAB* and *ANSYS*:

- A finite element model was built to simulate the quasistatic complex plastic deformation of the wire, as the wire deformation highly impacts the bond formation. The contact area and the normal force distribution between wire and substrate are calculated and then used for the simulation of bond formation within *MATLAB*. Contrary to previously presented process models of ultrasonic heavy wire bonding, with the co-simulation also the pre-deformation phase can be simulated. Thus, the impact of touch-down force is considered in the co-simulation.
- The dynamical behaviour of the wire, substrate and its substructure are modelled within reduced order models for computational efficiency. Considering the substrate dynamics is mandatory for modelling the impact of substrate resonance effects seen in the ultrasonic bonding tests.
- From modelling the contact between bond tool and wire, new insights into the magnification of bond normal force in the v-groove were gained: additionally to the tool opening angle, also the frictional forces in the contact influence the magnification. Thus, a new analytical model for estimating the magnification factor was derived.

To identify the model parameters such like the friction coefficients and the material models for the aluminium and copper wire, a test-rig based on a universal tensile-compression machine was developed and experiments were carried out:

- An iterative workflow for determination of the quasi-static stress-strain curve of the bond wire has been developed and used to identify the material model for the

FE-model. The material models for the investigated 400 µm wire were not available before, as standard tensile or compression tests are not suitable for the small wire sample size.

- The ultrasonic softening effect has been investigated systematically in compression tests for the 400 µm copper and aluminium wire. For both materials, the forming force can be reduced by approx. 60 %, but for copper, the vibration amplitude for this force reduction is twice as high as for the aluminium wire.
- For the aluminium wire, the observed hardening effect during the compression tests with ultrasonic excitation was significantly larger than for the copper wire.

With the developed and parametrized simulation model, parameter studies were carried out and compared to the experimental results from ultrasonic bonding tests:

- The simulated shear force values were correctly predicted by the simulation in the main effects diagrams for a wide range of 64 parameter combinations for the copper wire and 48 parameter combinations for the aluminium wire. Thus, the multi-scale model approach is suitable to predict the impact of the bond parameters and captures the relevant physical phenomena contributing to the bond formation.
- For the copper wire, the simulated shear strength was shifted to higher levels by a constant factor; by comparing the sheared surfaces with the simulated contact areas, it was found, that the measured areas included unbonded areas at the outer edge of the sheared surface; thus, the measured areas were larger than the real contact area contributing to the shear strength.
- Additional simulation results gave new insights into the activation and bonding of the interface area, tangential forces during bonding and the amount of dissipated energy in the contact between tool and wire making a direct simulation based comparison between the two wire materials possible.
- From the simulation of the parameter studies and the comparison with the experimental results, it became clear that the levels for the bond duration were selected too long for aluminium in the experiments. By using the bond model in advance for simulation based selection of the parameter levels for the experiments, the levels could have been chosen more accurately and additional iterations in the experimental determination of optimal bond parameters can be avoided, which shows the potential of simulation enhanced process development.

The research carried out in this thesis has led to new findings in the field of ultrasonic heavy-wire bonding, which result in the following recommendations for future work:

- The occurrence of the different shear codes has an impact on the measured shear force values. Especially for aluminium, high ultrasonic voltages enhance the occurrence of shear code 4. The different failure modes during shear testing impact the measured shear force values; these effects are not modelled in the current development stage of the bond model and should be considered for increasing the accuracy of predicting the shear force values especially for the aluminium wire, where the different shear codes occur.
- For the aluminium wire, at high levels of ultrasonic voltage and bond normal force, the shear force values decreased with increasing bond duration; this was partly explained by the effect of overbonding due to high deformation levels of the wire, which should be considered in an extended future version of the bond formation model.

- In the ultrasonic softening experiments with 400 µm wire samples, significant differences between the behaviour of aluminium and copper wire were observed. For further investigations, experiments with the frequency used in heavy wire bonding (60 kHz) and modifications of the test-rig construction should be made to investigate the three mechanisms - friction reduction, stress superposition, and acoustic softening - separately. All three effects occur during the bond formation process, thus only when these effects could be investigated directly in the experiments independently from each other, the direct identification of the ultrasonic softening model parameters with the test rig gets possible.
- For modelling the ultrasonic heavy wire bonding process, the accurate representation of the ultrasonic softening effect is indispensable to simulate the influence of the bonding parameters on bond quality; for this, the co-simulation has been developed to directly calculate the softening factor k_{USS} to simulate the wire deformation using the FE-model. At the same time, there is a great savings potential of approx. 50 % of the simulation time if the FE model could be replaced by an analytical model. This model approach can be implemented as a parallel option in the simulation model for time efficient simulations with less computing resources.

Reference

[1] Ahmadi, F. ; Farzin, M. ; Mandegari, M.: Effect of grain size on ultrasonic softening of pure aluminum. In: *Ultrasonics* 63 (2015), pp. 111 – 117. – ISSN 0041–624X

[2] Althoff, S. ; Meyer, T. ; Unger, A. ; Sextro, W. ; Eacock, F.: Shape-Dependent Transmittable Tangential Force of Wire Bond Tools. In: *IEEE 66th Electronic Components and Technology Conference*, 2016, pp. 2103–2110

[3] Althoff, S. ; Neuhaus, J. ; Hemsel, T. ; Sextro, W.: A friction based approach for modeling wire bonding. In: *IMAPS 2013, 46th International Symposium on Microelectronics*. Orlando (Florida), USA, 2013

[4] Althoff, S. ; Neuhaus, J. ; Hemsel, T. ; Sextro, W.: Improving the bond quality of copper wire bonds using a friction model approach. In: *Electronic Components and Technology Conference (ECTC), 2014 IEEE 64th*, 2014, pp. 1549–1555

[5] Anderson, O. L. ; Christensen, H. ; Andreatch, P.: Technique for Connecting Electrical Leads to Semiconductors. In: *Journal of Applied Physics* 28 (1957), pp. 923–923

[6] ANSYS, Inc.: *ANSYS Mechanical APDL Basic Analysis Guide*, Software Documentation, 2018

[7] ANSYS, Inc.: *ANSYS Mechanical APDL Element Reference*, Software Documentation, 2018

[8] ANSYS, Inc.: *ANSYS as a Server: MATLAB Toolbox Setup*, Software Documentation, 2019

[9] Arjmand, E. ; Agyakwa, P. A. ; Corfield, M. R. ; Li, J. ; Mouawad, B. ; Mark Johnson, C.: A thermal cycling reliability study of ultrasonically bonded copper wires. In: *Microelectronics Reliability* 59 (2016), pp. 126–133. – ISSN 0026–2714

[10] ASTM F1269-89: Test Methods for Destructive Shear Testing of Ball Bonds. 2001. – Technical Report

[11] Azadmanjiri, J. ; Berndt, C. ; Kapoor, A. ; Wen, C.: Development of Surface Nano-Crystallization in Alloys by Surface Mechanical Attrition Treatment (SMAT). In: *Critical Reviews in Solid State and Material Sciences* 40 (2015), 02, pp. 164–181

[12] AZO Materials: *Aluminium: Specifications, Properties, Classifications and Classes*. https://www.azom.com/article.aspx?ArticleID=2863. – Last visited: 26.07.2021

[13] AZO Materials: *An Introduction to Copper*. https://www.azom.com/properties.aspx?ArticleID=597. – Last visited: 26.07.2021

[14] Brökelmann, M.: *Entwicklung einer Methodik zur Online-Qualitätsüberwachung des Ultraschall-Drahtbondprozesses mittels integrierter Mikrosensorik*, Heinz Nixdorf Institut, Paderborn, PhD Thesis, 2008

[15] Bruns, J.: *Spannungsanalyse des Ultraschall-Wedge-Wedge-Bondens mit Aluminiumdraht unter Berücksichtigung ultraschallabhängiger Werkstoffdaten bei verschiedenen Frequenzen mit Hilfe der Methode der Finiten Elemente*, Technische Universiät Clausthal, PhD Thesis, 2001

[16] Chan, Y. H. ; Kim, J.-K. ; Liu, D. ; Liu, P. C. K. ; Cheung, Y. M. ; Ng, M. W.: Effects of bonding frequency on Au wedge wire bondability. In: *Journal of Materials Science: Materials in Electronics* 19 (2008), Mar, Nr. 3, pp. 281–288. – ISSN 1573–482X

[17] Charles, H. ; Mach, K. ; Lehtonen, S. ; Francomacaro, A. ; DeBoy, J. ; Edwards, R.: Wirebonding at higher ultrasonic frequencies: reliability and process implications. In: *Microelectronics Reliability* 43 (2003), Nr. 1, pp. 141 – 153

[18] Charles, H. K. ; Mach, K. J. ; Lehtonen, S. J. ; Francomacaro, A. S. ; DeBoy, J. S. ; Edwards, R. L.: High-frequency wirebonding: process and reliability implications. In: *52nd Electronic Components and Technology Conference 2002*, 2002, pp. 881–890

[19] Chauhan, P. ; Zhong, Z. W. ; Pecht, M.: Copper Wire Bonding Concerns and Best Practices. In: *Journal of Electronic Materials* 42 (2013), pp. 2415–2434

[20] Chen, K. ; Zhang, Y. ; Wang, H.: Effect of acoustic softening on the thermal-mechanical process of ultrasonic welding. In: *Ultrasonics* 75 (2017), pp. 9 – 21. – ISSN 0041–624X

[21] Czerny, B. ; Chavan, V. ; Gasser, C. ; Rosc, J. ; Khatibi, G.: Application of in-situ non-invasive failure detection methods for wire bonds. In: *2020 IEEE 8th Electronics System-Integration Technology Conference (ESTC)*, 2020, pp. 1–6

[22] Czerny, B. ; Khatibi, G.: Interface characterization of CuCu ball bonds by a fast shear fatigue method. 114 (2020), pp. 113831. – ISSN 0026–2714. – 31st European Symposium on Reliability of Electron Devices, Failure Physics and Analysis, ESREF 2020

[23] Danfoss Silicon Power GmbH: *Technologie und Innovation (eng. technology and innovation)*. https://www.danfoss.com/de-de/about-danfoss/our-businesses/silicon-power/technology-and-innovation/. – Last visit: 26.07.2021

[24] Das, A. ; Masters, I. ; Williams, D.: Process robustness and strength analysis of multi-layered dissimilar joints using ultrasonic metal welding. In: *The International Journal of Advanced Manufacturing Technology* (2018). – ISSN 1433–3015

[25] Daud, Y. ; Lucas, M. ; Huang, Z.: Modelling the effects of superimposed ultrasonic vibrations on tension and compression tests of aluminium. In: *Journal of Materials Processing Technology* 186 (2007), Nr. 1, pp. 179 – 190. – ISSN 0924–0136

[26] Department of defense (USA): *MIL-STD-883E, Test method standard - microcircuits*

[27] Deshpande, A. ; Tofangchi, A. ; Hsu, K.: Microstructure evolution of Al6061 and copper during ultrasonic energy assisted compression. In: *Materials Characterization* 153 (2019), pp. 240 – 250. – ISSN 1044–5803

[28] Ding, Y. ; Kim, J.-K.: Numerical analysis of ultrasonic wire bonding: Part 2. Effects of bonding parameters on temperature rise. In: *Microelectronics Reliability* 48 (2008), Nr. 1, pp. 149 – 157

[29] Ding, Y. ; Kim, J.-K. ; Tong, P.: Effects of bonding force on contact pressure and frictional energy in wire bonding. In: *Microelectronics Reliability* 46 (2006), Nr. 7, pp. 1101 – 1112. – ISSN 0026–2714

[30] DVS - German Welding Society: *Technical Bulletin DVS 2811 - Test Procedures for Wire Bonded Joints*. 2017

[31] Eacock, F. ; Unger, A. ; Eichwald, P. ; Grydin, O. ; Hengsbach, F. ; Althoff, S. ; Schaper, M. ; Guth, K.: Effect of different oxide layers on the ultrasonic copper wire bond process. In: *IEEE 66th Electronic Components and Technology Conference*, 2016, 2111-2118

[32] Fässler, F. ; Bircher, F.: Flexible Mehrkörpersimulation zur Optimierung moderner Fertigungssysteme / Berner Fachhochschule, Institut für Drucktechnologie. 2010. – Technical Report

[33] Gaul, H. ; Schneider-Ramelow, M. ; Reichl, H.: Analysis of the friction processes in ultrasonic wedge/wedge-bonding. In: *Microsystem Technologies* 15 (2009), May, Nr. 5, pp. 771–775

[34] Gaul, H. ; Schneider-Ramelow, M. ; Reichl, H.: Analytic Model Verification of the

Interfacial Friction Power in Al us w/w Bonding on Au Pads. In: *IEEE Transactions on Components and Packaging Technologies* 33 (2010), Nr. 3, pp. 607–613. – ISSN 1557–9972

[35] Geissler, U. ; Schneider-Ramelow, M. ; Reichl, H.: Hardening and Softening in AlSi1 Bond Contacts During Ultrasonic Wire Bonding. In: *IEEE Transactions on Components and Packaging Technologies* 32 (2009), Dec, Nr. 4, pp. 794–799

[36] Goehre, J. ; Geissler, U. ; Schneider-Ramelow, M. ; Lang, K.: Influence of Bonding Parameters on the Reliability of Heavy Wire Bonds on Power Semiconductors. In: *2012 7th International Conference on Integrated Power Electronics Systems (CIPS)*, 2012, pp. 1–6

[37] Goehre, J. ; Schneider-Ramelow, M. ; Geissler, U. ; Lang, K.-D.: Interface degradation of Al heavy wire bonds on power semiconductors during active power cycling measured by the shear test. In: *2010 6th International Conference on Integrated Power Electronics Systems*, 2010, pp. 1–6

[38] Gogh, B. van ; Benner, T. ; Seppaenen, H. ; Tszeng, C. ; Sepehrband, P.: An Oxide Wear Model of Ultrasonic Bonding. In: *International Symposium on Microelectronics* International Microelectronics Assembly and Packaging Society, 2020, pp. 222–229

[39] Grams, A. ; Prewitz, T. ; Wittler, O. ; Kripfgans, J. ; Schmitz, S. ; Middendorf, A. ; Müller, W. H. ; Lang, K.-D.: Simulation of an aluminum thick wire bond fatigue crack by means of the cohesive zone method. In: *2013 14th International Conference on Thermal, Mechanical and Multi-Physics Simulation and Experiments in Microelectronics and Microsystems (EuroSimE)*, 2013, pp. 1–8

[40] Gross, D. ; Haag, S. ; Reinold, M. ; Schneider-Ramelow, M. ; Lang, K.-D.: Heavy copper wire-bonding on silicon chips with aluminum-passivated Cu bond-pads. In: *Microelectronic Engineering* 156 (2016), pp. 41 – 45

[41] Göhre, J.-M.: *Entwicklung und Implementierung einer verbesserten Lastwechseltestmethode zur experimentellen Bestimmung der Zuverlässigkeit von Dickdrahtbonds in Leistungsmodulen*, Technical University of Berlin, PhD Thesis, 2013

[42] Hagenkotter, S. ; Brokelmann, M. ; Hesse, H.: PiQC - a process integrated quality control for nondestructive evaluation of ultrasonic wire bonds. In: *2008 IEEE Ultrasonics Symposium*, 2008. – ISSN 1051–0117, pp. 402–405

[43] Han, L. ; Zhong, J. ; Gao, G.: Effect of tightening torque on transducer dynamics and bond strength in wire bonding. In: *Sensors and Actuators A: Physical* 141 (2008), Nr. 2, pp. 695 – 702. – ISSN 0924–4247

[44] Harman, G.: *Wire Bonding in Microelectronics*. Bd. third. McGraw-Hill Education, 2010. – ISBN 9780071642651

[45] Harthoorn, J.: *Ultrasonic metal welding*, Technische Hogeschool Eindhoven, PhD Thesis, 1978

[46] Hatch, M.: *Vibration Simulation Using MATLAB and ANSYS*. 2000

[47] Heinen, G. ; Stierman, R. J. ; Edwards, D. ; Nye, L.: Wire bonds over active circuits. In: *1994 Proceedings. 44th Electronic Components and Technology Conference*, 1994, pp. 922–928

[48] Hella KGaA Hueck & Co.: *Mechanical testing of aluminium thick-wire bond connections 125-500 µm: shearing test (Hella-Norm N67090-02)*

[49] Hesse Mechatronics GmbH: *Heavy Wire Bonder Bondjet BJ985*. https://www.hesse-mechatronics.com/en/products/heavy-wire-bonder/bj985/. – Last visited: 14.06.2021

[50] Hu, J. ; Shimizu, T. ; Yang, M.: Investigation on ultrasonic volume effects: Stress superposition, acoustic softening and dynamic impact. In: *Ultrasonics Sonochemistry* 48 (2018), pp. 240 – 248. – ISSN 1350–4177

[51] Hu, J. ; Shimizu, T. ; Yang, M.: Investigation on Material Deformation Characteristics of Ultrasound-assisted Microcompression with Dynamic Force Sensing Technology. In: *Sensors and Materials* 31 (2019), 10, pp. 3111–3119

[52] Hu, J. ; Shimizu, T. ; Yoshino, T. ; Shiratori, T. ; Yang, M.: Evolution of acoustic softening effect on ultrasonic-assisted micro/meso-compression behavior and microstructure. In: *Ultrasonics* 107 (2020), pp. 106107. – ISSN 0041–624X

[53] Hunstig, M. ; Unger, A. ; Brökelmann, M. ; Hesse, H. J.: Process advantages of thermosonic wedge-wedge bonding using dosed tool heating. In: *International Symposium on Microelectronics* 2019 (2019), Nr. 1, pp. 000519–000523

[54] Instron Corporation: *Instron Model 4400 Universal Testing System*. 1995

[55] Kacher, J. ; Robertson, I.: Quasi-four-dimensional analysis of dislocation interactions with grain boundaries in 304 stainless steel. In: *Acta Materialia* 60 (2012), Nr. 19, pp. 6657 – 6672. – ISSN 1359–6454

[56] Kaestle, C.: *Qualifizierung der Kupfer-Drahtbondtechnologie für integrierte Leistungsmodule in harschen Umgebungsbedingungen*, Friedrich-Alexander-Universität Erlangen-Nürnberg, PhD Thesis, 2018

[57] Kästle, C. ; Franke, J.: Comparative Analysis of the Process Window of Aluminum and Copper Wire Bonding for Power Electronics Applications. In: IEEE (Ed.): *Proceeding of the 2014 International Conference on Electronics Packaging (ICEP)*, 2014. – ISBN 978–4–904090–10–7, pp. 335 – 340

[58] Kim, D. ; Willmot, R. ; Peroulis, D.: A high-efficiency low-cost wire-bond loop antenna for CMOS wafers. In: *2009 IEEE Antennas and Propagation Society International Symposium* (2009), pp. 1–4

[59] Kirchner, H. ; Kromp, W. ; Prinz, F. ; Trimmel, P.: Plastic deformation under simultaneous cyclic and unidirectional loading at low and ultrasonic frequencies. In: *Materials Science and Engineering* 68 (1985), Nr. 2, pp. 197 – 206. – ISSN 0025–5416

[60] Klahold, L. ; Schemmel, R.(Supervisor): *Untersuchung und Verbesserung des Touchdown- und Reinigungs-Vorgangs beim Ultraschall-Dickdrahtbonden*, Paderborn University, Master Thesis, 2021

[61] Krenek, K.: *Modellordnungsreduktion großer Systeme unter rotordynamischem Einfluss*, Technische Universität München, PhD Thesis, 2012

[62] Krieger, V. ; Schemmel, R. (Supervisor): *Modellierung des Ultrasonic-Softening-Effektes beim US-Drahtbonden in einer MATLAB/ANSYS Co-Simulation und Entwicklung einer Methode für Parameterstudienauf dem HPC-Cluster "OCuLUS"*, Master Thesis, 2019

[63] Krzanowski, J. E.: A transmission electron microscopy study of ultrasonic wire bonding. In: *IEEE Transactions on Components, Hybrids, and Manufacturing Technology* 13 (1990), March, Nr. 1, pp. 176–181. – ISSN 1558–3082

[64] Kumar, V. ; Hutchings, I.: Reduction of the sliding friction of metals by the application of longitudinal or transverse ultrasonic vibration. In: *Tribology International* 37 (2004), pp. 833–840

[65] L. L. M. Derks, P.: Parameters That Influence the Ultrasonic Bond Quality. In: *ElectroComponent Science and Technology* 10 (1983), 01

[66] Lai, Z. ; Liu, J.: The Nordic Electronics Packaging Guideline, Chapter A: Wire Bonding. 2000. – Technical Report

[67] Langenecker, B.: Effects of Ultrasound on Deformation Characteristics of Metals. In: *IEEE Transactions on Sonics and Ultrasonics* 13 (1966), Nr. 1, pp. 1–8

[68] Levine, L.: The ultrasonic wedge bonding mechanism: Two theories converge. In: *ISHM* Bd. 95, 1995, pp. 242–246

[69] Lin, J. ; Li, J. ; Liu, T. ; Xie, Z. ; Zhu, L. ; Wang, Y. ; Guan, Y.: Investigation on ultrasonic vibration effects on plastic flow behavior of pure titanium: Constitutive modeling. In: *Journal of Materials Research and Technology* 9 (2020), Nr. 3, pp. 4978 – 4993. – ISSN 2238–7854

[70] Littmann, W. ; Storck, H. ; Wallaschek, J.: Reduction of friction using piezoelectrically excited ultrasonic vibrations. In: Inman, D. J. (Ed.) ; International Society for Optics and Photonics (Veranst.): *Smart Structures and Materials 2001: Damping and Isolation* Bd. 4331 International Society for Optics and Photonics, SPIE, 2001, 302 – 311

[71] Liu, S. ; Xie, T. ; Cao, H. ; Shan, X.: Simulation and experimental research on ultrasonic drawing of copper shaped wires. In: *IOP Conference Series: Materials Science and Engineering* 531 (2019), 09, pp. 012025

[72] Liu, T.: Sliding friction of copper. In: *Wear* 7 (1964), Nr. 2, pp. 163 – 174. – ISSN 0043–1648

[73] Liu, Y. ; Liu, Z. ; Wang, X. ; Tao, H.: Experimental study on tool wear in ultrasonic vibration–assisted milling of C/SiC composites. In: *The International Journal of Advanced Manufacturing Technology* 107 (2020), 03

[74] Liu, Y. ; Suslov, S. ; Han, Q. ; Hua, L. ; Xu, C.: Comparison Between Ultrasonic Vibration-Assisted Upsetting and Conventional Upsetting. In: *Metallurgical and Materials Transactions A* 44 (2013), 07

[75] Long, Y. ; Dencker, F. ; Isaak, A. ; Hermsdorf, J. ; Wurz, M. ; Twiefel, J.: Self-cleaning mechanisms in ultrasonic bonding of Al wire. In: *Journal of Materials Processing Technology* 258 (2018), pp. 58 – 66. – ISSN 0924–0136

[76] Long, Y. ; Dencker, F. ; Isaak, A. ; Li, C. ; Schneider, F. ; Hermsdorf, J. ; Wurz, M. ; Twiefel, J. ; Wallaschek, J.: Revealing of ultrasonic wire bonding mechanisms via metal-glass bonding. In: *Materials Science and Engineering: B* (2018). – ISSN 0921–5107

[77] Long, Y. ; Twiefel, J. ; Wallaschek, J.: A review on the mechanisms of ultrasonic wedge-wedge bonding. In: *Journal of Materials Processing Technology* 245 (2017), pp. 241 – 258

[78] Lubliner, J.: *Plasticity Theory*. Dover Publications, 2008

[79] Lum, I. ; Jung, J. P. ; Zhou, Y.: Bonding mechanism in ultrasonic gold ball bonds on copper substrate. In: *Metallurgical and Materials Transactions A* 36 (2005), May, Nr. 5, pp. 1279–1286. – ISSN 1543–1940

[80] Lum, I. ; Mayer, M. ; Zhou, Y.: Footprint study of ultrasonic wedge-bonding with aluminum wire on copper substrate. In: *Journal of Electronic Materials* 35 (2006), Mar, Nr. 3, pp. 433–442. – ISSN 1543–186X

[81] Malekipour, E. ; Heidary, H. ; Shahbazi Majd, N. ; Mazdak, S. ; Sharifi, E.: Effect of resonant frequency variation on the ultrasonically assisted deep drawing process: numerical and experimental study. In: *The International Journal of Advanced Manufacturing Technology* 106 (2020), 01

[82] Mao, X. ; Popov, V. ; Starcevic, J. ; Popov, M.: Reduction of friction by normal oscillations. II. In-plane system dynamics. In: *Friction* 5 (2017), pp. 194–206

[83] Markt & Technik ; Die unabhängige Wochenzeitung für Elektronik (Ed.): *Leistungselektronik*. 2020

[84] Mayer, M. ; Huang, Y.: Numerical analysis of ultra-high frequency wire bonding. In: *Proceedings - 2009 International Symposium on Microelectronics, IMAPS 2009* (2009), 01, pp. 388–393

[85] Mayer, M. ; Schwizer, J.: Ultrasonic Bonding: Understanding How Process Parameters Determine the Strength of Au-Al Bonds. In: *Proc. International Symposium on Microelectronics IMAPS*, 2002, pp. 626–631

[86] Meyer, T. ; Unger, A. ; Althoff, S. ; Sextro, W. ; Brökelmann, M. ; Hunstig, M. ; Guth, K.: Modeling and Simulation of the ultrasonic wire bonding process. In: *2015 17th Electronics Packaging Technology Conference*, 2015

[87] Minitab 18 Support: *Interpret the key results for Main Effects Plot*. https://support.minitab.com/en-us/minitab/18/help-and-how-to/modeling-statistics/anova/how-to/main-effects-plot/interpret-the-results/key-results/. – Last visited: 30.09.2021

[88] Ndip, I. ; Huhn, M. ; Brandenburger, F. ; Ehrhardt, C. ; Schneider-Ramelow, M. ; Reichl, H. ; Lang, K. ; Henke, H.: Experimental verification and analysis of analytical model of the shape of bond wire antennas. In: *Electronics Letters* 53 (2017), Nr. 14, pp. 906–908

[89] Nico Müller, R.: *Experimentelle Ermittlung der Werkstoffeigenschaften von Aluminium und Kupfer zur Modellierung des Ultrasonic-Softening Effektes*, Paderborn University, Master Thesis, 2021

[90] Onuki, J. ; Koizumi, M. ; Ishikawa, I.: Effects of Frequency and Surface Cleanliness of Al–Si Electrode on Ultrasonic Bonding Characteristics of Thick Al Wire Bonding. In: *Materials Transactions, JIM* 37 (1996), Nr. 9, pp. 1492–1496

[91] Oracle: *Online Documentation: Class ORB*. https://docs.oracle.com/javase/7/docs/api/org/omg/CORBA/ORB.html. – Last visited: 14.06.2021

[92] Osterwald, F.: *Verbindungsbildung beim Ultraschall-Drahtbonden: Einfluß der Schwingungsparameter und Modellvorstellungen*, Technical University of Berlin, PhD Thesis

[93] Paderborn Center for Parallel Computing: *Technical documentation Wiki of OCuLUS*. https://wikis.uni-paderborn.de/pc2doc/OCuLUS. Version: 2020. – Last visited: 16.07.2021

[94] Pan, J. ; Fraud, P.: Wire Bonding Challenges in Optoelectronics Packaging, 2004

[95] Pan, J. ; Le, M.-N. ; Van Pham, C.: The Effect of Ultrasonic Frequency on Gold Wire Bondability and Reliability. In: *Journal of Microelectronics and Electronic Packaging* 6 (2009), Nr. 1, pp. 89–95

[96] Pang, C. C. ; Hung, K.-Y. ; Sham, M.-L.: High frequency thermosonic flip chip bonding for gold to gold interconnection. In: *2004 Proceedings. 54th Electronic Components and Technology Conference* Bd. 2, 2004, pp. 1461–1465 Vol.2

[97] Pedersen, K. B. ; Benning, D. ; Kristensen, P. K. ; Popok, V. N. ; Pedersen, K.: Interface structure and strength of ultrasonically wedge bonded heavy aluminium wires in Si-based power modules. In: *Journal of Materials Science: Materials in Electronics* 25 (2014), Jul, Nr. 7, pp. 2863–2871. – ISSN 1573–482X

[98] Pohlman, R. ; Lehfeldt, E.: Influence of ultrasonic vibration on metallic friction. In: *Ultrasonics* 4 (1966), Nr. 4, pp. 178 – 185. – ISSN 0041–624X

[99] Prymetall Norddeutsche Affinerie AG: *Datacheet PNA 209 Cu-PHC*

[100] Qin, I. ; Shah, A. ; Huynh, C. ; Meyer, M. ; Mayer, M. ; Zhou, Y.: Role of process parameters on bondability and pad damage indicators in copper ball bonding. In: *Microelectronics Reliability* 51 (2011), Nr. 1, pp. 60 – 66. – ISSN 0026–2714. – Copper Wire Bonding

[101] Rabinowicz, E. ; Science & Technology, W. S. t. (Ed.): *Friction and Wear of Materials*. Wiley, 1965 (Wiley Series on the Science & Technology)

[102] Ranert, K. ; Schemmel, R. (Supervisor): *Durchführung einer statistischen Versuchsplanung zur Ermittlung optimaler Bondparameter beim Ultraschall-Drahtbonden*, Paderborn University, Studienarbeit, 2020

[103] Rosseels, J.: *Resonant Piezoelectric Motors - Impact of Mechanical Machining Deviations and Methods to Cope with Them*, KU Leuven University, PhD Thesis, 2016

[104] Roth, R. ; Schulze, H. ; Schäffer, C. ; Hille, F. ; Umbach, F. ; Mertens, G. ; Rohn, N. ; Bolowski, D.: Power Cu metallization for future power devices — Process integration concept and reliability. In: *2016 28th International Symposium on Power Semiconductor Devices and ICs (ISPSD)*, 2016, pp. 195–198

[105] Sa'ardin, A. A.: *Characterising the effective material softening in ultrasonic forming of metals*, University of Glasgow, PhD Thesis

[106] Sandström, R. ; Hallgren, J. ; Burman, G. ; Swedish Nuclear Fuel & Waste Management Co. (Ed.): *Stress strain flow curves for Cu-OFP*. 2009

[107] Saraswati ; Theint, E. P. P. ; Stephan, D. ; Goh, H. ; Pasamanero, E. ; Calpito, D. ; Wulff, F. ; Breach, C.: High temperature storage (HTS) performance of copper ball bonding wires. In: *2005 7th Electronic Packaging Technology Conference* Bd. 2, 2005

[108] Sbeiti, M.: *Thermomechanische Beschreibung der Ausbildung einer intermetallischen Phase beim Ultraschall-Wedge/Wedge-Drahtbonden im Rahmen der Theorie der materiellen Kräfte*, Technical University of Berlin, PhD Thesis, 2013

[109] Schemmel, R. ; Unger, A. (Supervisor): *Auswahl, Modellierung und Validierung einer dynamischen Berechnungsmethodik zur Abbildung des Deformationsverhaltens gekoppelter Substrukturen mit nichtlinearem Reibkontakt beim Ultraschall-Drahtbonden*, Paderborn University, Studienarbeit, 2014

[110] Scheuermann, U. ; Junghaenel, M.: Limitation of Power Module Lifetime Derived from Active Power Cycling Tests. In: *CIPS 2018; 10th International Conference on Integrated Power Electronics Systems*, 2018, pp. 1–10

[111] Schinke, B. ; Malmberg, T.: Dynamic tensile tests with superimposed ultrasonic oscillations for stainless steel type 321 at room temperature. In: *Nuclear Engineering and Design* 100 (1987), Nr. 3, pp. 281 – 296. – ISSN 0029–5493

[112] Schneider-Ramelow, M. ; Reliability, F. I. (Ed.) ; Microintegration (Ed.): *Infinite Potential of Wire Bonding: New Research Findings*. https://blog.izm.fraunhofer.de/infinite-potential-of-wire-bonding-new-research-findings/. – Last visited: 26.07.2021

[113] Seppanen, H. ; Kaskela, A. ; Mustonen, K. ; Oinonen, M. ; Haeggstrom, E.: P1E-5 Understanding Ultrasound-Induced Aluminum Oxide Breakage During Wirebonding. In: *2007 IEEE Ultrasonics Symposium Proceedings*, 2007. – ISSN 1051–0117, pp. 1381–1384

[114] Shah, A. ; Schulze, G. ; Brunner, J. ; Qin, I. ; Chylak, B. ; Wong, N.: Advances in Wire Bonding Technology to Overcome Resonance Conditions. In: *2018 IEEE 68th Electronic Components and Technology Conference (ECTC)*, 2018. – ISSN 2377–5726, pp. 1465–1471

[115] Siddiq, A. ; Sayed, T. E.: A thermomechanical crystal plasticity constitutive model for ultrasonic consolidation. In: *Computational Materials Science* 51 (2012), Nr. 1, pp. 241 – 251. – ISSN 0927–0256

[116] Siddiq, A. ; Sayed, T. E.: Ultrasonic-assisted manufacturing processes: Variational model and numerical simulations. In: *Ultrasonics* 52 (2012), Nr. 4, pp. 521 – 529. – ISSN 0041–624X

[117] Siebertz, K. ; Bebber, D. van ; Hochkirchen, T.: *Statistische Versuchsplanung: Design of Experiments (DoE)*. Springer Berlin Heidelberg, 2017 (VDI-Buch). – ISBN 9783662557433

[118] Siu, K. ; Liu, H. ; Ngan, A.: A universal law for metallurgical effects on acoustoplasticity. In: *Materialia* 5 (2019), pp. 100214. – ISSN 2589–1529

[119] Siu, K. ; Ngan, A. ; Jones, I.: New insight on acoustoplasticity – Ultrasonic irradiation enhances subgrain formation during deformation. In: *International Journal of Plasticity* 27 (2011), Nr. 5, pp. 788 – 800. – ISSN 0749–6419

[120] Small Precision Tools (SPT): *Large Wire Bonding Tools*. http://www.smallprecisiontools.com/products-and-solutions/chip-bonding-tools/wedge-bonding-tools/large-wire-bonding-tools/?oid=434&lang=en. – Last visit: 23.04.2021

[121] Sonderforschungsbereich 543 ; University Stuttgart (Ed.): *Abschlussbericht: Ultraschallbeeinflusstes Umformen metallischer Werkstoffe*. 2002

[122] Starcevic, J.: *Tribospektroskopie als neue Methode zur Untersuchung von Reibungsmechanismen: Theoretische Grundlagen und Experiment*, Technische Universität Berlin, PhD Thesis, 01 2008

[123] Stockmeier, T.: From Packaging to "Un"-Packaging - Trends in Power Semiconductor Modules. In: *2008 20th International Symposium on Power Semiconductor Devices and IC's*, 2008. – ISSN 1946–0201, pp. 12–19

[124] Storck, H. ; Littmann, W. ; Wallaschek, J. ; Mracek, M.: The effect of friction reduction in presence of ultrasonic vibrations and its relevance to travelling wave ultrasonic motors. In: *Ultrasonics* 40 (2002), Nr. 1, pp. 379 – 383. – ISSN 0041–624X

[125] Sysprogs: *SmarTTY: A multi-tabbed SSH client with SCP support.* https://sysprogs.com/SmarTTY/. Version: 2020

[126] Tabor, D.: Junction growth in metallic friction: the role of combined stresses and surface contamination. In: *Proceedings of the Royal Society of London A: Mathematical, Physical and Engineering Sciences* 251 (1959), Nr. 1266, pp. 378–393. – ISSN 0080–4630

[127] The MathWorks: *Documentation of MATLAB function ellipticF: Incomplete elliptic integral of the first kind*. https://de.mathworks.com/help/symbolic/ellipticf.html. – Last visited: 26.07.2021

[128] The Mathworks: *Gramian-based input/output balancing of state-space realizations*. http://de.mathworks.com/help/control/ref/balreal.html. Version: 2016. – Last visited: 26.07.2021

[129] Tsai, T.-N.: An adaptive diagnosis system for copper wire bonding process control and quality assessment in integrated circuit assembly. In: *International Journal of Computer Integrated Manufacturing* 26 (2013), Nr. 6, pp. 513–526

[130] Unger, A.: *Modellbasierte Mehrzieloptimierung zur Herstellung von Ultraschall- Drahtbondverbindungen in Leistungshalbleitermodulen*, Paderborn University, PhD Thesis, 2017

[131] Unger, A. ; Schemmel, R. ; Meyer, T. ; Eacock, F. ; Eichwald, P. ; Althoff, S. ; Sextro, W. ; Brökelmann, M. ; Hunstig, M. ; Guth, K.: Validated Simulation of the Ultrasonic Wire Bonding Process. In: *Ultrasonics Symposium (IUS), 2016 IEEE International*. IEEE CPMT Symposium Japan, 2016, pp. 251–254

[132] Unger, A. ; Sextro, W. ; Althoff, S. ; Eichwald, P. ; Meyer, T. ; Eacock, F. ; Brökelmann, M. ; Hunstig, M. ; Bolowski, D. ; Guth, K.: Experimental and Numerical Simulation Study of Pre-Deformed Heavy Copper Wire Wedge Bonds. In: *Proceedings of the 47th International Symposium on Microelectronics (IMAPS)*. San Diego, CA, US, 2014, pp. 289–294

[133] Unger, A. ; Sextro, W. ; Althoff, S. ; Meyer, T. ; Brökelmann, M. ; Neumann, K. ; Reinhart, R. F. ; Guth, K. ; Bolowski, D.: Data-driven Modeling of the Ultrasonic Softening Effect for Robust Copper Wire Bonding. In: *Proceedings of 8th International Conference on Integrated Power Electronic Systems* Bd. 141, 2014, 175-180

[134] Unger, A. ; Sextro, W. ; Meyer, T. ; Eichwald, P. ; Althoff, S. ; Eacock, F. ; Brökelmann, M. ; Hunstig, M. ; Guth, K.: Modeling of the Stick-Slip Effect in Heavy Copper Wire Bonding to Determine and Reduce Tool Wear. In: *2015 17th Electronics Packaging Technology Conference*, 2015

[135] Verma, G. C. ; Pandey, P. M. ; Dixit, U. S.: Modeling of static machining force in axial ultrasonic-vibration assisted milling considering acoustic softening. In: *International Journal of Mechanical Sciences* 136 (2018), pp. 1 – 16. – ISSN 0020–7403

[136] Vinay Kumar Uppinal, V. M. A.: Analysis of Mechanical Properties of Pure Aluminium Based Metal Matrix Composite. In: *International Journal of Innovative Research and Studies* 3 (2014), 04, pp. 703–711

[137] Wang, C. ; Liu, Y. ; Guo, B. ; Shan, D. ; Zhang, B.: Acoustic softening and stress superposition in ultrasonic vibration assisted uniaxial tension of copper foil: Experiments and modeling. In: *Materials & Design* 112 (2016), pp. 246 – 253. – ISSN 0264–1275

[138] Weston, A.: Wire Bonding as a Technique for Semiconductor Device Assembly. In: *Microelectronics International* 2 (1985), Nr. 3, pp. 26–35

[139] Witthauer, A. T. ; Kim, G. Y. ; Faidley, L. E. ; Zou, Q. Z. ; Wang, Z.: Effects of Acoustic Softening and Hardening in High-Frequency Vibration-Assisted Punching of Aluminum. In: *Materials and Manufacturing Processes* 29 (2014), Nr. 10, pp. 1184–1189

[140] Woodward, J. ; Inc., P. (Ed.): *Mid-side nodes: Do they really help?* https://www.padtinc.com/blog/mid-side-nodes-do-they-really-help/. – last checked on 23.04.2021

[141] Xu, H. ; Liu, C. ; Silberschmidt, V. ; Chen, Z. ; Wei, J.: The role of bonding duration in wire bond formation: A study of footprints of thermosonic gold wire on aluminium pad. In: *Microelectronics International* 27 (2010), 01, pp. 11–16

[142] Xu, T. ; Walker, T. ; Poncelet, B. ; Fu, J. ; Luechinger, C.: Consumable and Process Improvement for Large Copper Wire Bonding. In: *International Symposium on Microelectronics* 2016 (2016), 10, pp. 000445–000449

[143] Yao, Z. ; Kim, G.-Y. ; Faidley, L. ; Zou, Q. ; Mei, D. ; Chen, Z.: Experimental Study of High-Frequency Vibration Assisted Micro/Meso-Scale Forming of Metallic Materials. In: *ASME 2011 International Manufacturing Science and Engineering Conference*, 2011

[144] Yao, Z. ; Kim, G.-Y. ; Wang, Z. ; Faidley, L. ; Zou, Q. ; Mei, D. ; Chen, Z.: Acoustic softening and residual hardening in aluminum: Modeling and experiments. In: *International Journal of Plasticity* 39 (2012), pp. 75 – 87. – ISSN 0749–6419

[145] Yapici, G. ; Beyerlein, I. ; Karaman, I. ; Tomé, C.: Tension–compression asymmetry in severely deformed pure copper. In: *Acta Materialia* 55 (2007), Nr. 14, pp. 4603–4613. – ISSN 1359–6454

[146] Yole Développement: *Power Electronics for E-Mobility 2021*, Market and Technology Report - February 2021

[147] Zha, C. ; Chen, W.: Theories and experiments on effects of acoustic energy field in micro-square cup drawing. In: *The International Journal of Advanced Manufacturing Technology* 104 (2019), pp. 4791–4802

[148] Zhao, Y. Y. ; Li, D. ; Zhang, Y. S.: Effect of welding energy on interface zone of Al–Cu ultrasonic welded joint. In: *Science and Technology of Welding and Joining* 18 (2013), Nr. 4, pp. 354–360

[149] Zhou, H. ; Cui, H. ; Qin, Q. H.: Influence of ultrasonic vibration on the plasticity of metals during compression process. In: *Journal of Materials Processing Technology* 251 (2018), pp. 146 – 159. – ISSN 0924–0136

A Appendix

A.1 Additional shear codes from the wire bonding experiments

In figure A.1, the shear codes for the copper wire, produced with F_{BN} equal to 32 N are shown. For u_{T} equal to 60 V, tool/substrate contacts occur for bond durations beginning with 200 ms and for 50 V minor tool imprints are observed for 300 ms. Shear code 4 is observed for u_{T} equal to 60 V and t_{B} equal to 300 ms.

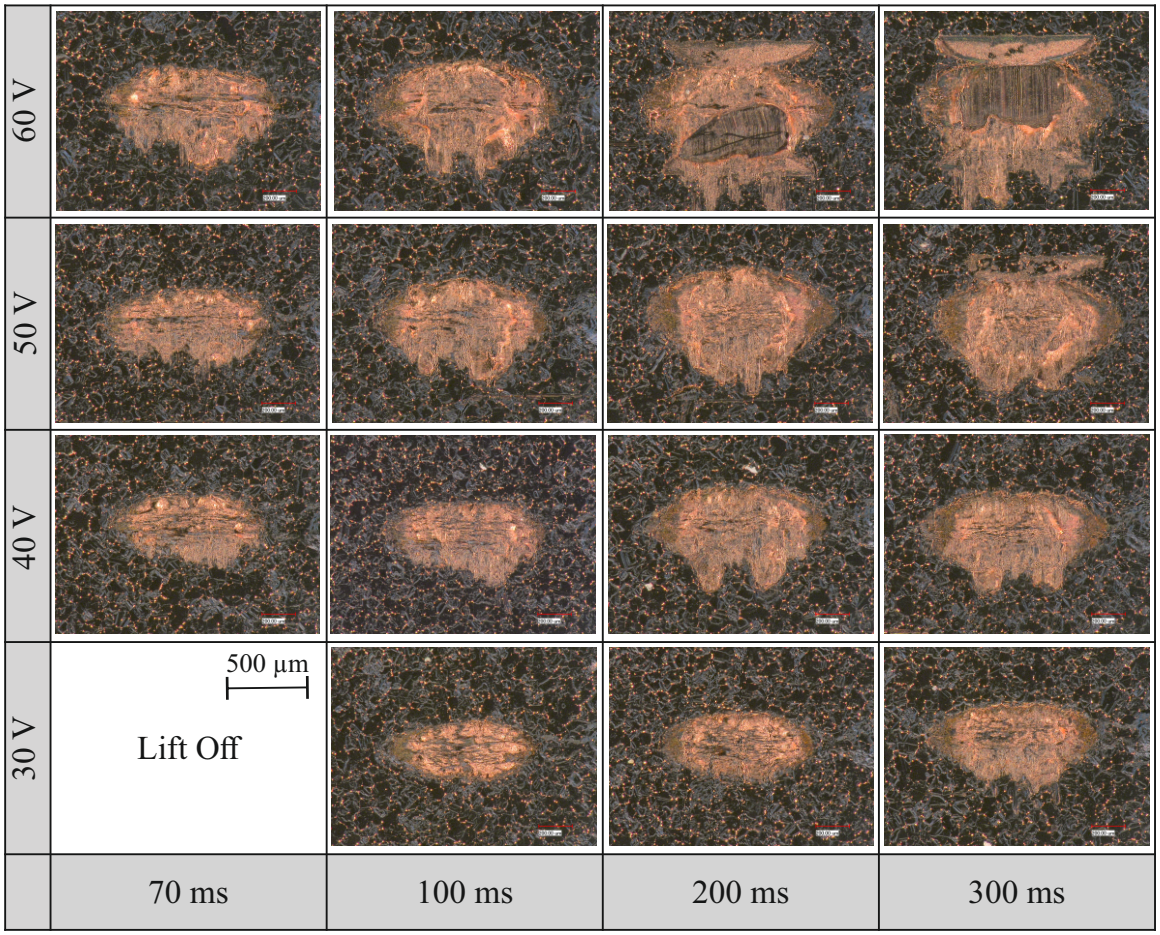

Figure A.1: Copper wire: shear codes bonded at F_{BN} equal to 26 N.

In figure A.2, the shear codes for the copper wire, produced with F_{BN} equal to 32 N are shown. For u_{T} equal to 60 V, tool/substrate contacts occur for bond durations beginning with 100 ms and for 50 V with 300 ms. A small shear nugget is observed for u_{T} equal to 60 V and t_{B} equal to 300 ms.

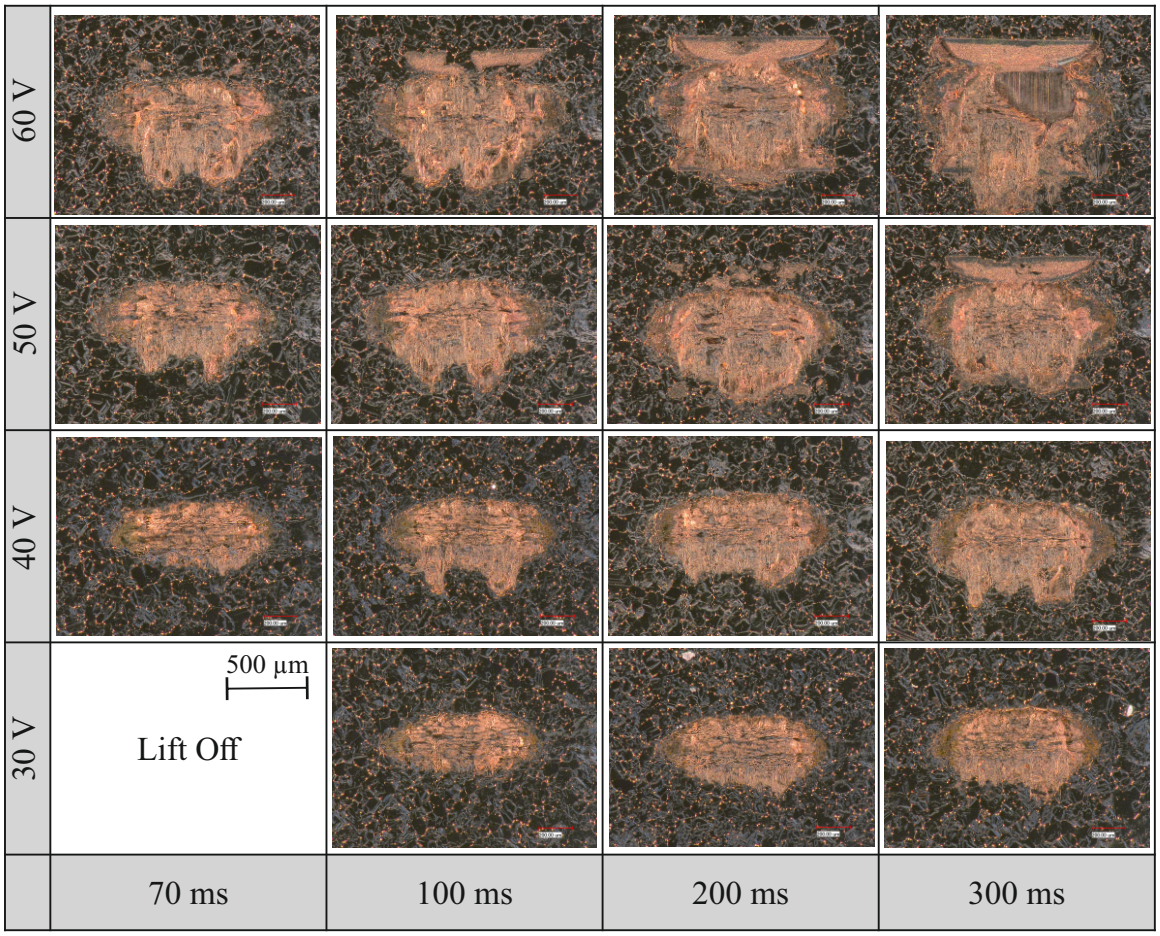

Figure A.2: Copper wire: shear codes bonded at F_{BN} equal to 32 N.

In figure A.3, the shear codes for the aluminium wire, produced with F_{BN} equal to 14 N are shown. For all levels of the ultrasonic voltage and all bond durations, no tool/substrate contacts are observed. For u_T equal to 35 V for bond durations beginning with 200 ms, shear code 4 is observed. For u_T equal to 30 V, the shear code 3 occurs for t_B longer than 300 ms. For u_T equal to 20 V and 25 V, shear code 1 is observed.

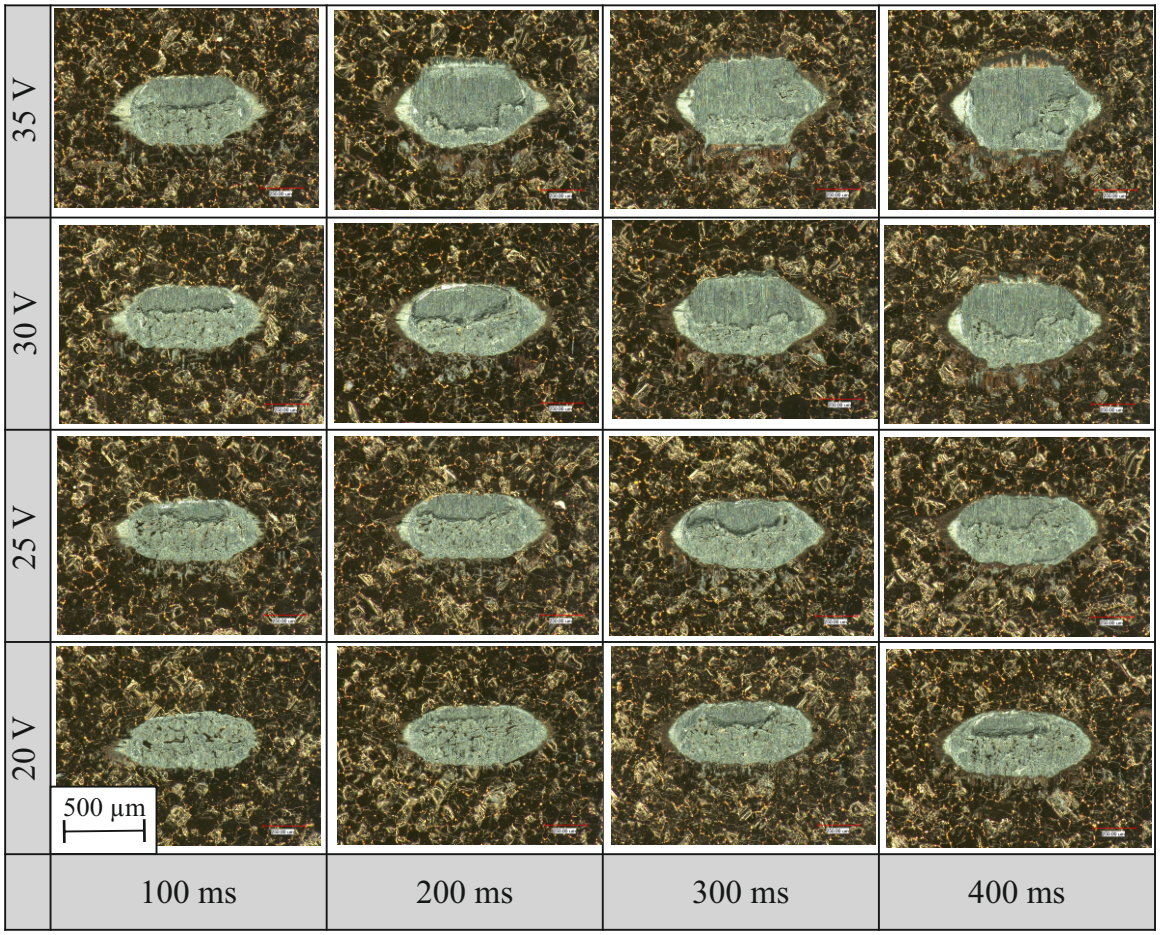

Figure A.3: Aluminium wire: shear codes bonded at F_{BN} equal to 14 N.

A.2 Material properties for the modal analysis of the substrate model

Table A.1: Material properties used for the modal analysis in *ANSYS Workbench* for the modal superposition method of the substrate model.

Material	Density / kg/mm^3	Young's Modulus / N/mm^2	Poisson's ratio / -
Aluminium	2770	70000	0.33
EPDM	1400	9000	0.49
Copper	8300	100000	0.34
Al_2O_3	3950	300000	0.22

A.3 Program structure for high performance computing

For running jobs on the computer cluster OCuLUS, the script OCuLUS_Calculation.sh has been programmed containing the CCS commands to run the simulation on the OCuLUS with Linux operating system figure A.4. Two types of jobs can be requested by the script; either a single job running one simulation of the wire bond model or an array job to run multiple simulations of the wire bond model in parallel with different input parameters for the wire bond model.

The shell script is executed with the inputs for the job request (job duration, number of cores, RAM, number of jobs, the maximum of parallel jobs, and the file system to store temporary simulation files). When the number of jobs is equal to one, than only a single job is requested and the shell script OCuLUS_Single.sh is executed; when the number of jobs is larger than one, an array job is requested and the shell script OCuLUS_Array.sh is executed.

For the single job, the shell script copies the wire bond model files containing the ANSYS database of the FE-model, the restart files, and MATLAB file to a temporary directory on the file system of OCuLUS. Afterwards, the wire bond simulation as described in figure 4.16 is executed by the MATLAB script Single_Bond.m on the node assigned by the Workload Manager with the requested resources (number of cores and RAM size). After the solution process, the results are copied back to the starting path of the simulation and the job is killed, meaning that all files created during the job are deleted from the file system on OCuLUS. The solution results contain the simulation data from the MATLAB and ANSYS solvers needed for the postprocessing step, and a log file, containing all solution information created during the simulation by the ANSYS Mechanical and MATLAB solvers; the log file contains all information for debugging the solving process, if the FE-simulation did not converge, newly implemented function create error messages or for checking all prompts created by ANSYS and MATLAB during simulation.

For the array job, the shell script first creates the directory “IsRunning” in the starting path, where during the array job text messages of the running jobs containing the job ID are created to monitor the amount of the currently running jobs. This is done to manage the maximum number of currently running jobs and by this, the currently used amount of licenses for MATLAB and ANSYS. Typically, different users access a limited number of licenses and for this, a license manager was implemented within MATLAB in the wire bond model, which limits the currently running jobs to a maximum of parallel running jobs defined by the input to the shell script. The Workload Manager assigns the single jobs of the array to the available resources of the OCuLUS; each job is allocated independently and the job ID is assigned to the job by the Workload Manager. Than the wire bond model files are copied to the temporary directory of the single job and the input parameters for the wire bond model are loaded from the parameter array. Afterward, the MATLAB script Single_Bond.m is executed to run a single simulation and after the simulation, the simulation results are copied to the starting path and the job is killed on OCuLUS.

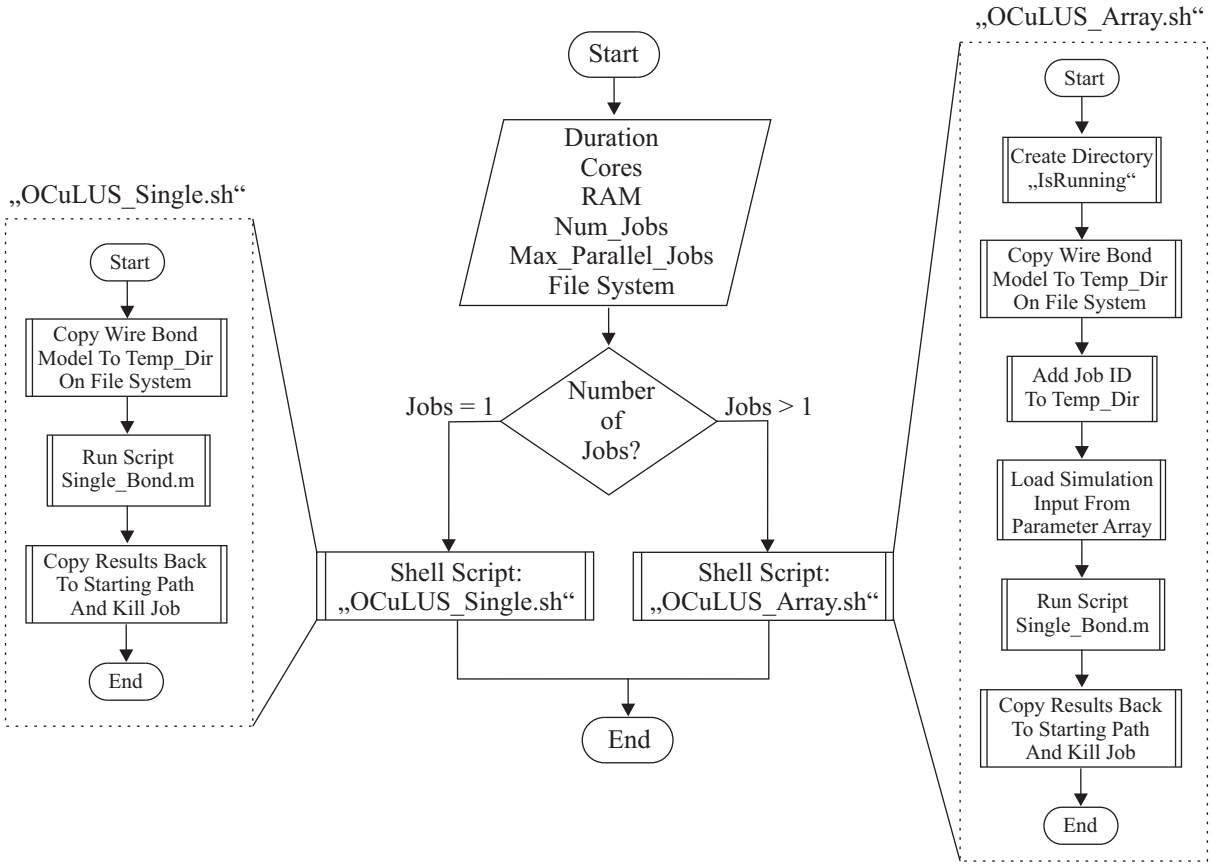

Figure A.4: Program sequence diagram of the shell script OCuLUS_Calculation.sh

A.4 High performance computing results

A typical simulation run of the wire bond model using a Personal Computer (PC) with Intel i7-4790 CPU with four cores and 16 GB Random-Access Memory (RAM) can take up to approx. 8 h simulation duration making parameter sweeps with many simulation runs very time consuming. To reduce computing time, paralleled High Performance Computing (HPC) is utilized using the Owl CLUSter (OCuLUS) of the Paderborn Center for Parallel Computing (PC^2) at Paderborn University [93]. The OCuLUS operating system is Linux (CentOS 6.5) and two frontends are used to communicate with the OCuLUS cluster nodes. To access the frontends Secure Shell (ssh) network protocol is used. For this, when logging in from a windows based system, open source tools can be used; in this contribution the SSH client “SmarTTY” is used [125]. On OCuLUS, OpenCCS is used as Workload Management System to control the usage of the compute nodes and interaction with the system is done by using CCS commands; e.g. specifying the number of cores, memory and simulation duration to be requested for the simulation on OCuLUS. The Workload Management System provides the function for job arrays to run the same program (here the wire bond model) over and over on different input files. Details on the shell scripts and the workflow of submitting the array jobs are described in the appendix section A.3.

The resources of the OcULUS cluster are listed in table A.2. For the wire bond model simulation, the standard node with 16 cores and 64 GB RAM is well suited for the FE simulation because of the large amount of nodes; since the OCuLUS can be accessed by

different users, the waiting time when submitting a job on more exclusive resources can be significantly longer. The OCuLUS provides three types of file systems; a shared file system with access on all systems at the University network, a cluster local parallel file system (PFS) providing fast access and the nodal RAM.

Table A.2: Computing resources of the OcULUS Cluster

Node name	Nodes	CPU-Type	Cores	RAM
Standard	552	Two Intel Xeon E5-2670	16	64 GB
Washington	20	Two Intel Xeon E5-2670	16	256 GB
Tesla	32	Two Intel Xeon E5-2670	16	64 GB
GTX 1080	8	Two Intel Xeon E5-2670	16	64 GB
GTX 2080	1	Two Intel Xeon E5-2670	16	64 GB
SMP	4	Two Intel Xeon E5-2670	16	1000 GB

In figure A.5 computation performance results of the wire bond simulation running a single job on the OCuLUS on the parallel file system (PFS), and directly in the RAM of the node are shown and compared to a PC (Fujitsu Esprimo E900) with Intel i7-4790 CPU with four cores and 16 GB RAM running the simulation on a Solid State Drive (SSD) and Hard Disk Drive (HDD). To compare the results for the different setups, always the same wire bond model (FE-mesh with 119677 nodes) and unchanged input parameters between all simulations were used. Using four cores, the simulation on the PFS on OCuLUS takes 8.13 h and on the PC with the HDD 7.75 h; using the RAM on OCuLUS and the SSD on the PC, the simulation duration can be decreased significantly to 6.66 h and 6.95 h respectively. Using four cores, no significant reduction of simulation duration can be achieved by using the resources on the OCuLUS. Since the used PC is limited to 4 cores, increasing the number of cores is only possible on OCuLUS. Using eight cores, simulation duration can be decreased by 45% with 3.63 h on the RAM and 37% with 4.40 h on the PFS. Further increasing the number of cores to 16 leads to a reduction of simulation duration by 39 % to 2.23 h on the RAM and by 35 % to 2.86 h on the PFS . With 30 cores, the simulation duration on the RAM is 1.73 h and on the PFS 2.42 h. For the simulation of the wire bond model on the OCuLUS, especially using the array job with many jobs running in parallel, the configuration using eight cores and the RAM file system is used for the simulations. Benefits of this configuration are short waiting durations of the Workload Manager, because the standard nodes can be used which have the largest amount of nodes (see table A.2), and significant time reduction of the single wire bond simulation of approx. 50 % compared to the simulation on the PC with the SSD can be achieved. For future simulations, the setting with using eight cores and RAM as the file system for the wire bond simulation is chosen; using these settings, significant time reduction up to 50% compared to the PC can be achieved an additionally, the standard nodes with 16 cores and 64 GB RAM can be used which decreases the waiting time for running the simulation on the OCuLUS.

The results of an array job with 16 jobs using eight cores on the RAM of OCuLUS are shown in figure A.5 on the right side; for the license manager, the settings were chosen such that eight single jobs can run in parallel. The first eight jobs directly start with the simulation and all jobs finish after approx. 4 h; the simulation duration is slightly longer compared to the single job, because preparation of the simulation and how the

Workload Manager distributes the jobs to the resources is different compared to the single job. The remaining eight jobs are waiting for one of the running jobs to finish, to start their own simulation which is controlled by the license manager within the *MAaaS* object. The whole array job has a simulation duration of 9.5 h, meaning that 16 jobs running on the OCuLUS with this configuration take only 2.55 h longer than one single simulation on the available PC with four cores running on the SSD. For the simulation of the parameter studies in chapter 6, 8 cores for each single job are used to run the bond model in parallel.

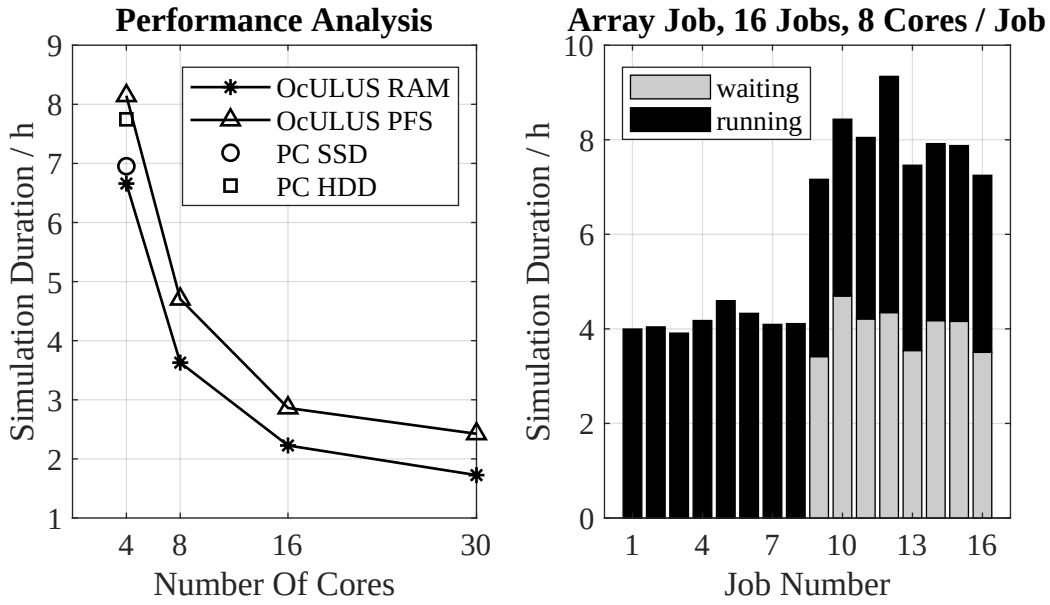

Figure A.5: Simulation Duration of single job, using different number of cores (left) and array job with 16 single jobs on the right.

A.5 Literature values for the material parameters of aluminium an copper

In table A.3 the literature values for the young's modulus and yield strength are shown. Saraswati et al. [107] investigated the stress-strain behaviour of 25 µm copper; they reported results of four wire samples, where the results for the young's modulus and yield strength differed relatively much between the different wire samples. They concluded that the different strengths result mostly from the manufacturing process history, texture formation and purity of the wires. Sandström et al. measured stress strain flow curves of oxygen free copper; their results showed significantly lower values for the yield strength compared to [107]. One possible explanation is, that the samples have not been cold worked before testing. Most sources give a modulus of elasticity of approx. 120 GPa for copper, so that this value can be assumed to be known relatively reliably; only the results for the 25 µm wire reported by Saraswati et al. [107] deviate somewhat from this, which can, however, also be due to the inaccuracy of the measurement for such a thin wire and influences from the measuring apparatus.

Table A.3: Literature values for the material properties of aluminium and copper.

	Copper			**Aluminium**		
Material Type	Ref.	E / GPa	σ_Y / MPa	Ref.	E / GPa	σ_Y / MPa
25 µm Cu bond wire	[107]	79.8-95.8	97.5-171.9	-		
Soft copper tube	[99]	127	< 140	-		
Cu-OFP	[106]	-	55-63	-		
99.99 % Cu	[13]	121-133	45-330	-		
400 µm Al bond wire	-			[39]	70	30
99.99 % Al	-			[12]	68.3	< 90
99.50 % Al	-			[136]	-	50.25

A.6 Control system of the test rig for identification of the model parameters

The functional block diagram of test rig is shown in figure A.6. A motor drives the spindles which are connected to the motor by gears. With an encoder the crosshead speed is measured; on the crosshead control board of the testing machine, a crosshead speed controller regulates the motor speed by comparison between the measured crosshead speed and the set point crosshead speed. The set point for the crosshead speed is transmitted by the IEEE-488 GPIB from the external test rig control board to the crosshead speed controller of the Instron testing machine.

Besides the testing machine itself, different components are added to the test rig for controlling the bond parameters comparable to a typical wire bonding machine. A Polytec OFV 512 laser vibrometer (LV) and a Polytec OFV 5000 vibrometer controller (VC) are used to measure the oscillation of the bonding tool (BT) tip. Compared to a typical bonding machine, where either the transducer voltage u_T or the current i_T are controlled, in this test rig directly the oscillation amplitude of the tool tip can be measured and controlled by the test rig control board. The excitation voltage for the shaker can be either sinusoidal, multi-frequent or other special waveforms can be generated. The three component force sensor (FS) is operated by two Kistler Type 5015A charge amplifier, one for the vertical force and the other one for the horizontal force component in direction of the oscillation. The measured normal force is transmitted to the test rig control board for controlling the bond normal force by setting the crosshead speed.

With a Human Machine Interface (HMI) in the form of a monitor and keyboard, which are connected to the test rig control board by a Video Graphics Array (VGA) and a PS/2 port, the user sets the bond parameters like the bond normal forces $F_{BN,i}$, the interval lengths $t_{I,i}$, and the bond tool amplitude x_{BT}; additionally, the excitation frequency of the shaker f_S can be set up to the limit of the excitation range of the shaker which is about 1000 Hz.

As part of his master thesis [60], Klahold designed and built a control board shown in figure A.7 specifically for the requirements of the test stand; the control board is equipped with:

- Six analogue inputs with 12 bit resolution at +- 10 V (three of the six inputs have a peak detector).
- Two analogue outputs with 12 bit resolution at maximum +- 10 V.

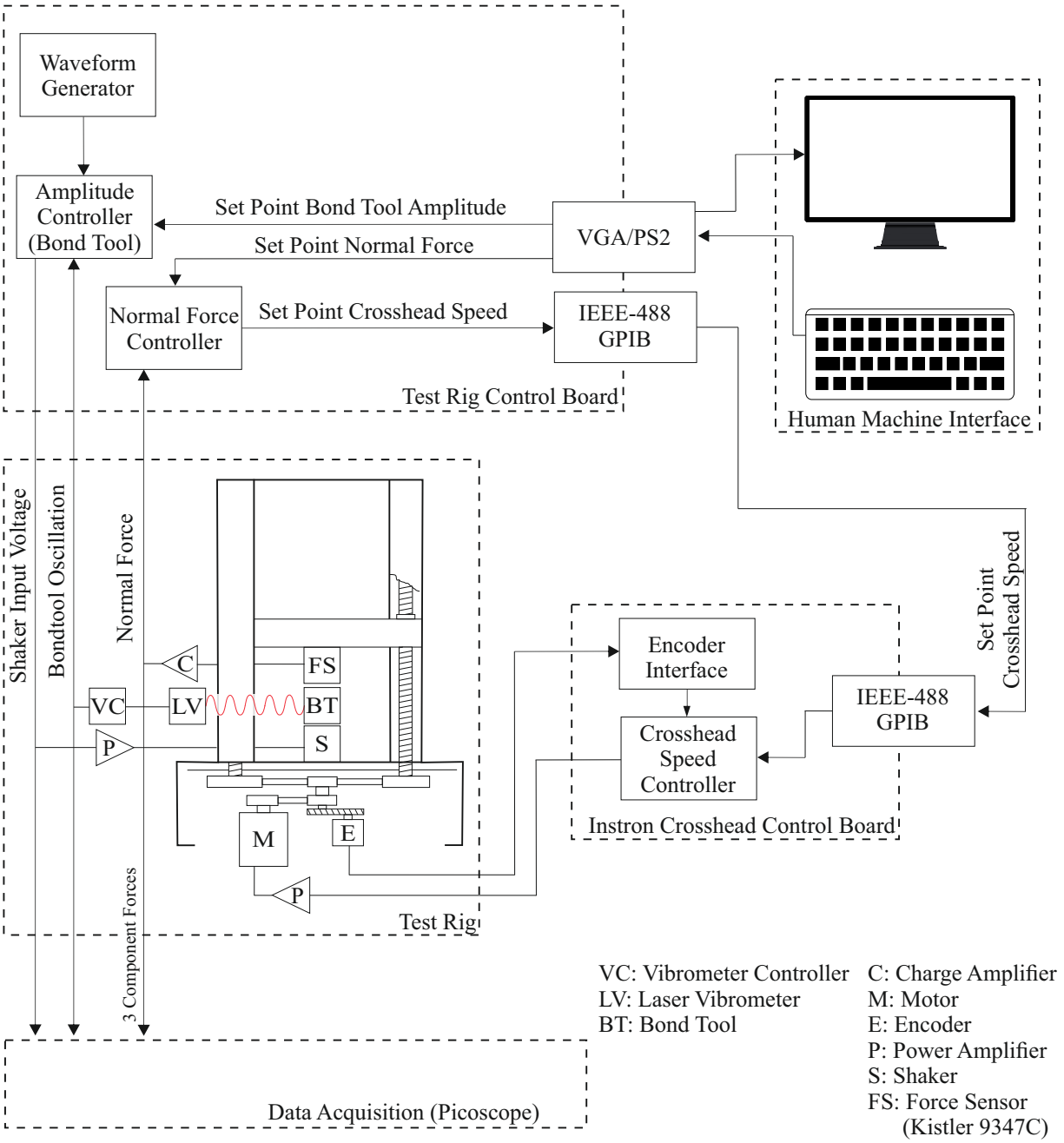

Figure A.6: Functional block diagram of the test rig.

- Two arbitrary function generators with 16 bit resolution at maximum +-10 V controlled by an FPGA.
- Four digital inputs/outputs with 3.3 V to 12 V voltage level.
- Four RS-232 ports.
- One GPIB interface for communication with GPIB devices such as the Instron test machine.
- One SD card slot.
- Two PS/2 ports for keyboard and mouse support.
- One VGA port for the monitor.
- One USB 2.0 port for programming and monitoring the Arduino on the control

board.

Two major functional components of the board are the *Atmel* chip (SAM3X8E), which is also used in the Arduino Due, and an FPGA chip (Spartan 6) from the manufacturer *Xilinx*. The *Atmel* chip was programmed with the Visual-Micro development program which is also used for Arduino controllers. The Spartan 6 FPGA was programmed using the *Planahead* program from *Xilinx*. The circuit diagram and the layout of the board were created with the programme *KiCad*. A four-layer board was created, which was manufactured by *JLCPCB*.

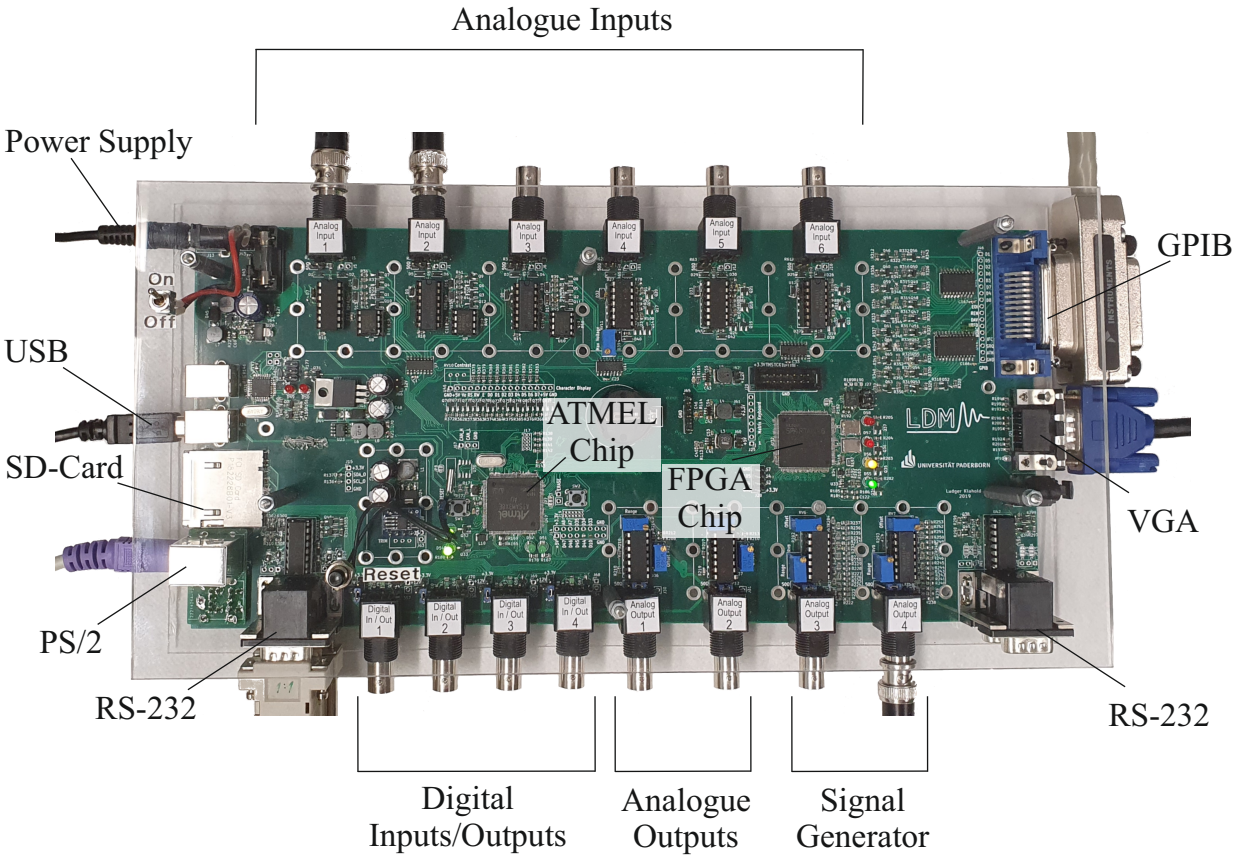

Figure A.7: Control board of the test rig and the description of the most relevant hardware parts.

A.7 Comparison between simulated and measured shear force values for bond model parameter identification

In figure A.8 the comparison between simulated and measured mean shear force values at the end of bond formation after 300 ms for the copper wire and 400 ms for the aluminium wire is shown. Overall, a good agreement between simulation and experiment could be achieved with the identified model parameters for β, listed in table 5.2. Slight deviations occur for the aluminium wire at 35 V ultrasonic voltage and 14 N to 18 N bond normal force; these differences can be explained by complex effect like overbonding and splashing in the experiments, which are discussed in section 6.4.

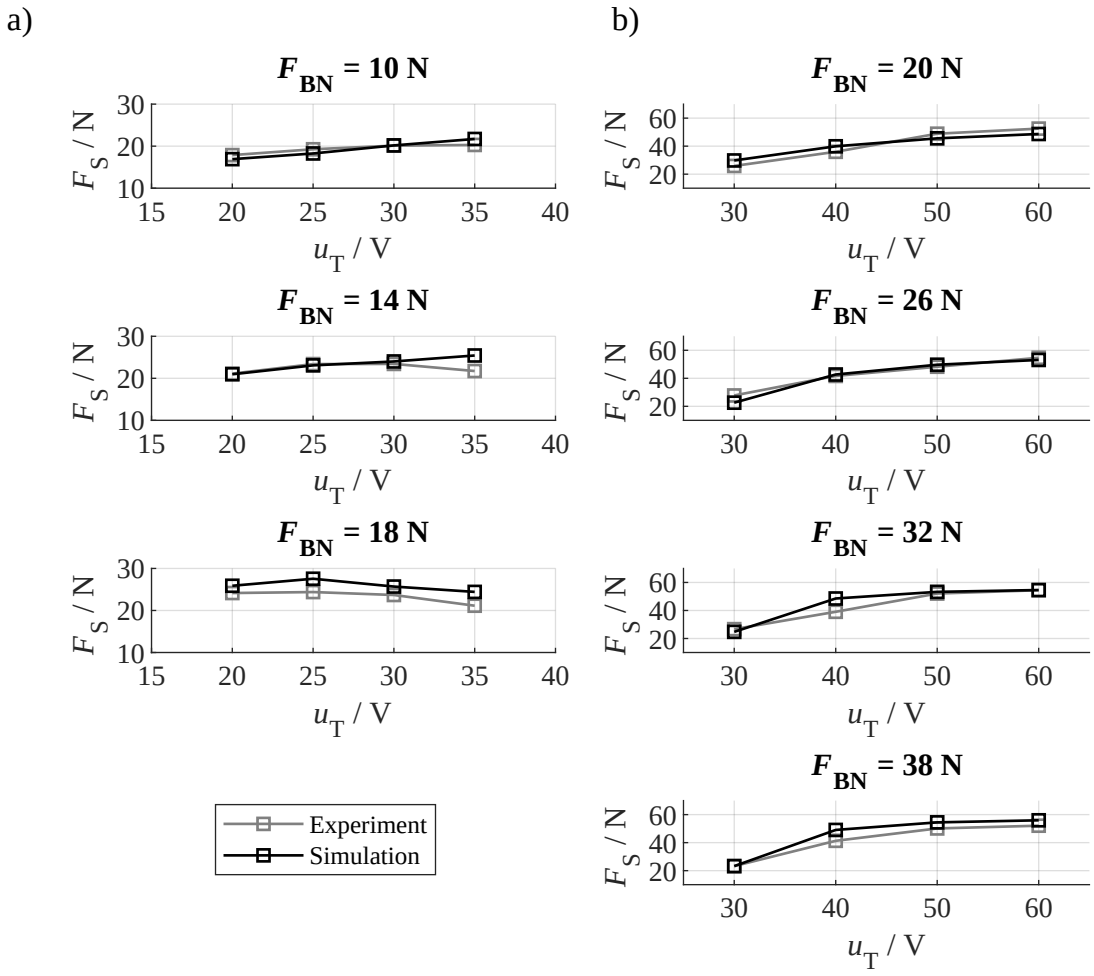

Figure A.8: Shear force values for the different levels of bond normal force F_{BN} and ultrasonic voltage u_{T} from the simulation and experiments with the identified model parameter β for a) the aluminium wire and b) the copper wire.

A.8 Comparison between simulated and measured tool substrate contacts

In figure A.9 the observation whether tool/substrate contacts (TSC) occurred ("Yes") or not ("No") is shown; for all levels of bond normal forces and ultrasonic voltages, the observed TSC from the experiments are captured by the simulation with high accuracy. For F_{BN} equal to 20 N in figure A.9 a), no TSC were detected in the simulation for all bond durations and ultrasonic voltages. This correlates with the observations in the experiments, as only for 60 V slight tool/substrate contacts for approx. 50 % of the bonds were observed. For F_{BN} equal to 26 N in figure A.9 b), TSC occur for the ultrasonic voltage of 60 V after 100 ms; for lower voltages, no TSC occurred in the simulation. In the experiments, TSC were observed for t_{B} equal to 200 ms for ultrasonic voltage equal to 60 V and minor TSC for approx. 60 % of the produced bonds were observed for 50 V. For the bond normal force equal to 32 N in figure A.9 c), TSC occur for all bond durations from 70 ms to 300 ms for the voltage of 60 V in the simulation.

For 50 V, TSC occur after 200 ms and for 40 V for 300 ms. The occurrence of TSC in the experiments is nearly the same as for the simulation; the only difference is, that in the experiments no TSC occur for 40 V and 300 ms. For the largest bond normal force of 38 N, the observation of the TSC is the same as for 32 N in the simulation. In the experiments, TSC occurred already after 100 ms for the voltage of 50 V and after 300 ms for 40 V.

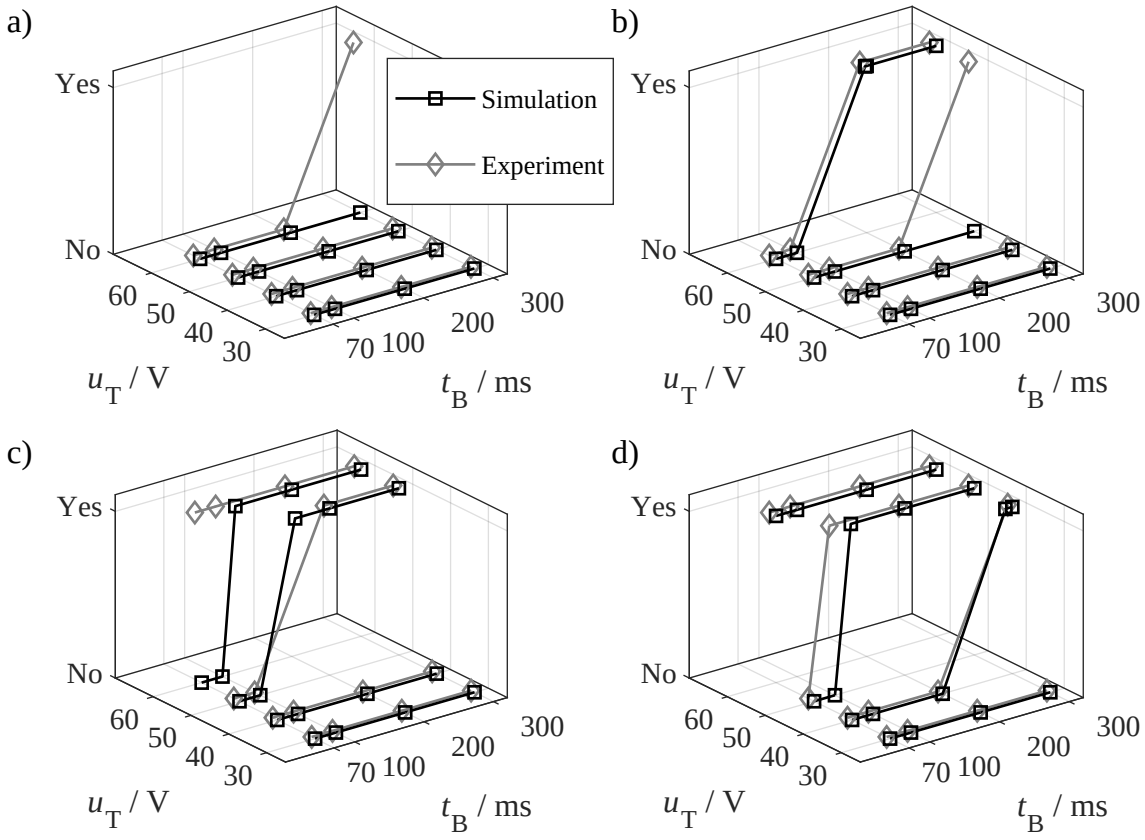

Figure A.9: Copper wire: occurrence (Yes/No) of tool/substrate contacts in the simulation and experiments for a) $F_{BN} = 20$ N, b) $F_{BN} = 26$ N, c) $F_{BN} = 32$ N and d) $F_{BN} = 38$ N.

In figure A.10 the occurrence of TSC for the aluminium wire is shown. For F_{BN} from 10 N to 14 N, no TSC were detected for all bond durations and ultrasonic voltages for both, experiment and simulation. For the bond normal force equal to 18 N and ultrasonic voltage of 35 V, TSC occur in the experiments from 200 ms to 400 ms; in the simulation, the TSC occur at 101 ms. For the ultrasonic voltage equal to 30 V, TSC occurred after 300 ms in the experiments and after 200 ms in the simulation.

Taking into account, that in the experiments, only the occurrence of TSC at the investigated bond durations can be detected, but not the exact time of first TSC which can lay in between two levels of the bond duration, a good accuracy of the prediction of TSC by the simulation was achieved.

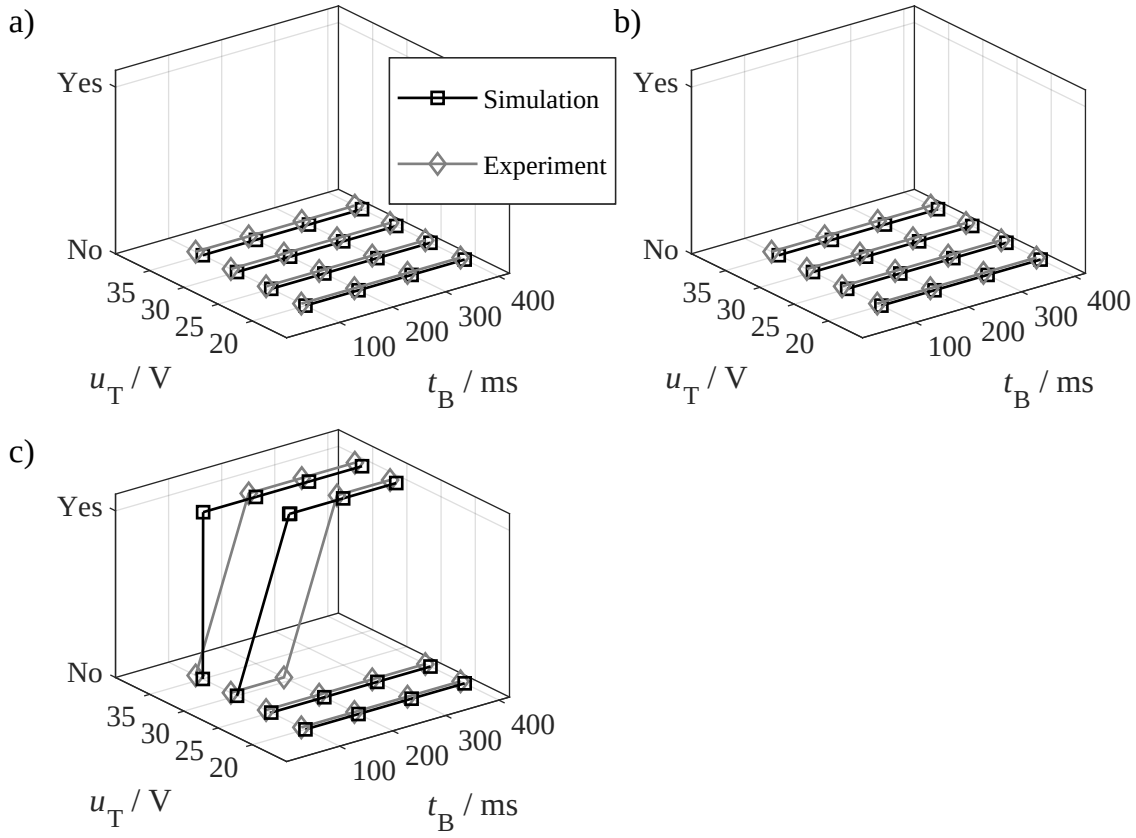

Figure A.10: Aluminium wire: occurrence (Yes/No) of tool/substrate contacts in the simulation and experiments for a) F_{BN} = 10 N, b) F_{BN} = 14 N and c) F_{BN} = 18 N.

Erklärung zur Zitation von Inhalten aus studentischen Arbeiten

In Ergänzung zu meinem Antrag auf Zulassung zur Promotion in der Fakultät für Maschinenbau der Universität Paderborn erkläre ich gemäß §11 der Promotionsordnung und unter Beachtung der Regelung zur Zitation studentischer Arbeiten:

Die von mir vorgelegte Dissertation habe ich selbstständig verfasst, und ich habe keine anderen als die angegebenen Quellen und Hilfsmittel benutzt. Es sind Inhalte studentischen Ursprungs (studentische Arbeiten) in dieser Dissertation enthalten.

Ich habe die verwendeten Arbeiten entsprechend der Regelung „Zitation aus studentischen Arbeiten in Dissertationen“ zitiert.

Paderborn, Februar 2021

Reinhard Schemmel

Im Zusammenhang mit dieser Arbeit betreute studentische Arbeiten

Die nachstehend aufgeführten studentischen Arbeiten wurden im Rahmen der vorliegenden Dissertation am Lehrstuhl für Dynamik und Mechatronik der Universität Paderborn angefertigt. Die Definition der Aufgabenstellung, die Bearbeitung sowie die Auswertung, Interpretation und Visualisierung von Ergebnissen erfolgten unter wissenschaftlicher Anleitung des Autors dieser Arbeit. Die erzielten Ergebnisse sind zum Teil in die Arbeit eingeflossen.

- Martin Greitemann: *Entwicklung eines Schallschutzkonzepts für eine Ultraschallreinigungsanlage,* Studienarbeit, 2017
- Alexander Neufeld: *Konstruktive Erweiterung eines Ultraschall-Bonddemonstrators für das zweidimensionale Drahtbonden,* Studienarbeit, 2018
- Konrad Hesse: *Entwicklung einer FE-basierten Reduktionsmethodik für komplexe piezoelektrische Ultraschallschwinger,* Masterarbeit, 2018
- Ludger Klahold: *Implementierung einer Kraftregelung auf dem Instron 4411 Zugversuchsprüfstand,* Projektarbeit, 2018
- Ludger Klahold: *Entwicklung einer Methodik zur dynamischen Kalibrierung von Kraftsensoren für Ultraschallanwendungen,* Studienarbeit, 2018
- Mateusz Dluzniakiewicz: *Entwicklung einer Methode zur Implementierung des Ultrasonic-Softening-Effekts in ANSYS,* Bachelorarbeit, 2018
- Martin Greitemann: *Entwicklung und Aufbau eines Ultrasonic-Softening- Prüfstands,* Masterarbeit, 2018
- Viktor Krieger: *Aufbau einer Co-Simulation zwischen MATLAB und ANSYS zur dynamischen Analyse beim US-Bonden,* Studienarbeit, 2018
- Claus Scheidemann: *Experimentelle Analyse und Modellierung des Verbindungsaufbaus beim Ultraschall-Dickdrahtbonden,* Masterarbeit, 2019
- Viktor Krieger: *Erarbeitung eines Workflows zum Start einer MATLAB-Simulation auf dem Großrechner „OCuLUS“,* Projektarbeit, 2019
- Viktor Krieger: *Modellierung des Ultrasonic-Softening-Effektes beim US-Drahtbonden in einer MATLAB/ANSYS Co-Simulation und Entwicklung einer Methode für Parameterstudien auf dem HPC-Cluster "OCuLUS",* Masterarbeit, 2019
- Nico Müller: *Experimentelle Untersuchung der Ultraschall-Werkstoffentfestigung,* Studienarbeit, 2020
- Islam Sami Omar Elgmal: *Motion Tracking in Hochgeschwindigkeitsaufnahmen zur Schwingungsmessung beim Drahtbonden,* Masterarbeit, 2020
- Katharina Ranert: *Durchführung einer statistischen Versuchsplanung zur Ermittlung optimaler Bondparameter beim Ultraschall-Drahtbonden,* Studienarbeit, 2020
- Ludger Klahold: *Untersuchung und Verbesserung des Touchdown- und Reinigungs-Vorgangs beim Ultraschall-Dickdrahtbonden,* Masterarbeit, 2021

- Nico Müller: *Ermittlung von Reibungskoeffizienten beim Bondprozess für Aluminium und Kupfer Draht,* Projektarbeit, 2021
- Nico Müller: *Experimentelle Ermittlung der Werkstoffeigenschaften von Aluminium und Kupfer zur Modellierung des Ultrasonic-Softening Effektes,* Masterarbeit, 2021